GEOCHEMISTRY AND RESONANCE IONIZATION OF PLATINUM-GROUP ELEMENTS

Thesis by

Joel David Blum

In Partial Fulfillment of the Requirements

for the Degree of

Doctor of Philosophy

California Institute of Technology

Pasadena, California

1990

(Submitted May 23, 1990)

ACKNOWLEDGEMENTS

I thank Professor G.J. Wasserburg for having the insight to steer me in the right directions and for sharing with me his infectious enthusiasm for science. He has tutored me in the principles of scientific experimentation and interpretation, and has taught me the art of effectively communicating the results of my research. Professors E.M. Stolper, G.R. Rossman, D.S. Burnett, T.J. Ahrens and G.A. Blake are thanked for their continued interest and helpful comments on my research, and willingness to let me use their laboratory facilities. Drs. I.D. Hutcheon, J.T. Armstrong, D.A. Papanastassiou, J.R. Beckett, G.S. Mattioli, A.E. Blum, M.J. Pellin and D.M. Gruen taught me a wide variety of experimental techniques and spent countless hours discussing all aspects of my research. I thank my fellow graduate students for companionship and for creating an environment highly conducive to scholarship. Finally, I thank my wife Cynthia for her continuous support (both spiritual and financial) and our daughter Hazel Claire for making the last year so rewarding.

ABSTRACT

Experimental studies were conducted with the goals of 1) determining the origin of Pt-group element (PGE) alloys and associated mineral assemblages in refractory inclusions from meteorites and 2) developing a new ultrasensitive method for the *in situ* chemical and isotopic analysis of PGE. A general review of the geochemistry and cosmochemistry of the PGE is given, and specific research contributions are presented within the context of this broad framework.

An important step toward understanding the cosmochemistry of the PGE is the determination of the origin of PGE-rich metallic phases (most commonly ϵRu-Fe) that are found in Ca, Al-rich refractory inclusions (CAI) in C3V meteorites. These metals occur along with γNi-Fe metals, Ni-Fe sulfides and Fe oxides in multiphase opaque assemblages. Laboratory experiments were used to show that the mineral assemblages and textures observed in opaque assemblages could be produced by sulfidation and oxidation of once homogeneous Ni-Fe-PGE metals. Phase equilibria, partitioning and diffusion kinetics were studied in the Ni-Fe-Ru system in order to quantify the conditions of opaque assemblage formation. Phase boundaries and tie lines in the Ni-Fe-Ru system were determined at 1273, 1073 and 873K using an experimental technique that allowed the investigation of a large portion of the Ni-Fe-Ru system with a single experiment at each temperature by establishing a concentration gradient within which local equilibrium between coexisting phases was maintained. A wide miscibility gap was found to be present at each temperature, separating a hexagonal close-packed ϵRu-Fe phase from a face-centered cubic γNi-Fe phase. Phase equilibria determined here for the Ni-Fe-Ru system, and phase equilibria from the literature for the Ni-Fe-S and Ni-Fe-O systems, were compared with analyses of minerals from opaque assemblages to estimate the temperature and chemical conditions of opaque assemblage

formation. It was determined that opaque assemblages equilibrated at a temperature of ~770K, a sulfur fugacity 10 times higher than an equilibrium solar gas, and an oxygen fugacity 10^6 times higher than an equilibrium solar gas.

Diffusion rates between γNi-Fe and εRu-Fe metal play a critical role in determining the time (with respect to CAI petrogenesis) and duration of the opaque assemblage equilibration process. The diffusion coefficient for Ru in Ni (D_{Ni}^{Ru}) was determined as an analog for the Ni-Fe-Ru system by the thin-film diffusion method in the temperature range of 1073 to 1673K and is given by the expression:

$$D_{Ni}^{Ru}\ (cm^2\ sec^{-1}) = 5.0(\pm 0.7) \times 10^{-3} \exp(-2.3(\pm 0.1) \times 10^{12}\ erg\ mole^{-1}/RT)$$

where R is the gas constant and T is the temperature in K. Based on the rates of dissolution and exsolution of metallic phases in the Ni-Fe-Ru system it is suggested that opaque assemblages equilibrated after the melting and crystallization of host CAI during a metamorphic event of $\geq 10^3$ years duration. It is inferred that opaque assemblages originated as immiscible metallic liquid droplets in the CAI silicate liquid. The bulk compositions of PGE in these precursor alloys reflects an early stage of condensation from the solar nebula and the partitioning of V between the precursor alloys and CAI silicate liquid reflects the reducing nebular conditions under which CAI were melted. The individual mineral phases now observed in opaque assemblages do not preserve an independent history prior to CAI melting and crystallization, but instead provide important information on the post-accretionary history of C3V meteorites and allow the quantification of the temperature, sulfur fugacity and oxygen fugacity of cooling planetary environments. This contrasts with previous models that called upon the formation of opaque assemblages by aggregation of phases that formed independently under highly variable conditions in the solar nebula prior to the crystallization of CAI.

Analytical studies were carried out on PGE-rich phases from meteorites and the products of synthetic experiments using traditional electron microprobe x-ray analytical techniques. The concentrations of PGE in common minerals from meteorites and terrestrial rocks are far below the ~ 100 ppm detection limit of the electron microprobe. This has limited the scope of analytical studies to the very few cases where PGE are unusually enriched. To study the distribution of PGE in common minerals will require an *in situ* analytical technique with much lower detection limits than any methods currently in use. To overcome this limitation, resonance ionization of sputtered atoms was investigated for use as an ultrasensitive *in situ* analytical technique for the analysis of PGE. The mass spectrometric analysis of Os and Re was investigated using a pulsed primary Ar^+ ion beam to provide sputtered atoms for resonance ionization mass spectrometry. An ionization scheme for Os that utilizes three resonant energy levels (including an autoionizing energy level) was investigated and found to have superior sensitivity and selectivity compared to nonresonant and one and two energy level resonant ionization schemes. An elemental selectivity for Os over Re of $\geq 10^3$ was demonstrated. It was found that detuning the ionizing laser from the autoionizing energy level to an arbitrary region in the ionization continuum resulted in a five-fold decrease in signal intensity and a ten-fold decrease in elemental selectivity. Osmium concentrations in synthetic metals and iron meteorites were measured to demonstrate the analytical capabilities of the technique. A linear correlation between Os^+ signal intensity and the known Os concentration was observed over a range of nearly 10^4 in Os concentration with an accuracy of $\sim \pm 10\%$, a minimum detection limit of 7 parts per billion atomic, and a useful yield of 1%. Resonance ionization of sputtered atoms samples the dominant neutral-fraction of sputtered atoms and utilizes multiphoton resonance ionization to achieve high sensitivity and to eliminate atomic and molecular interferences. Matrix effects should be small compared to secondary ion mass

spectrometry because ionization occurs in the gas phase and is largely independent of the physical properties of the matrix material. Resonance ionization of sputtered atoms can be applied to *in situ* chemical analysis of most high ionization potential elements (including all of the PGE) in a wide range of natural and synthetic materials. The high useful yield and elemental selectivity of this method should eventually allow the *in situ* measurement of Os isotope ratios in some natural samples and in sample extracts enriched in PGE by fire assay fusion.

Phase equilibria and diffusion experiments have provided the basis for a reinterpretation of the origin of opaque assemblages in CAI and have yielded quantitative information on conditions in the primitive solar nebula and cooling planetary environments. Development of the method of resonance ionization of sputtered atoms for the analysis of Os has shown that this technique has wide applications in geochemistry and will for the first time allow *in situ* studies of the distribution of PGE at the low concentration levels at which they occur in common minerals.

PREFACE

This thesis draws together the results and implications of the research projects that I have completed in the course of my doctoral work. The six chapters represent a general review of the geochemistry and resonance ionization of Pt-group elements, and include reference to my research as well as the research of others. Appendices I through VI are original research articles addressing the details of the specific experiments that I have completed and their implications.

TABLE OF CONTENTS

CHAPTER 1. INTRODUCTION

The Pt-group elements (PGE: Ru, Rh, Pd, Os, Ir and Pt) include the six group VIII transition metals that lie in the second and third rows of the periodic table below Fe, Co and Ni (Fig. 1.1). In their metallic form, the PGE (along with their periodic table neighbors Mo, W and Re) are among the most refractory materials known, and yield important information on high temperature solar nebular processes. Re is a group VII transition metal that has many chemical similarities to the PGE (particularly under reducing conditions) and will, therefore, be included with them in many of the following discussions. The PGE are generally classified as siderophile elements because they tend to associate with the common transition elements Ni, Co and Fe in iron meteorites and presumably in the earth's core. However, at the elevated sulfur fugacities prevalent in the earth's crust and upper mantle the PGE also become concentrated into sulfides, and are useful as tracers of the separation of metallic and/or sulfide phases during geologic processes.

The PGE are of considerable economic importance and have a wide range of industrial uses. They are "noble" metals in the sense that the massive metal resists oxidation and are used as corrosion-resistent coatings, in dental applications, and in jewelry. When finely divided, the PGE are chemically reactive and are used as catalysts in the chemical and petroleum refining industries and in automotive exhaust systems. The high melting temperatures of the PGE also make them widely useful in high temperature electronic and industrial applications. World demand for the PGE exceeded 2.5×10^8 g in 1987 (Loebenstein, 1989).

PGE are mined primarily from magmatic sulfide ore deposits associated with mafic and ultramafic igneous rocks. Minor production of PGE also comes from alluvial deposits

Fig. 1. Periodic table of the elements with Groups listed at the top of each column. The platinum-group elements are in the second and third rows of Group VIIIB and are designated by thick solid lines. The other refractory siderophile elements are designated by thin double lines.

PERIODIC TABLE OF THE ELEMENTS

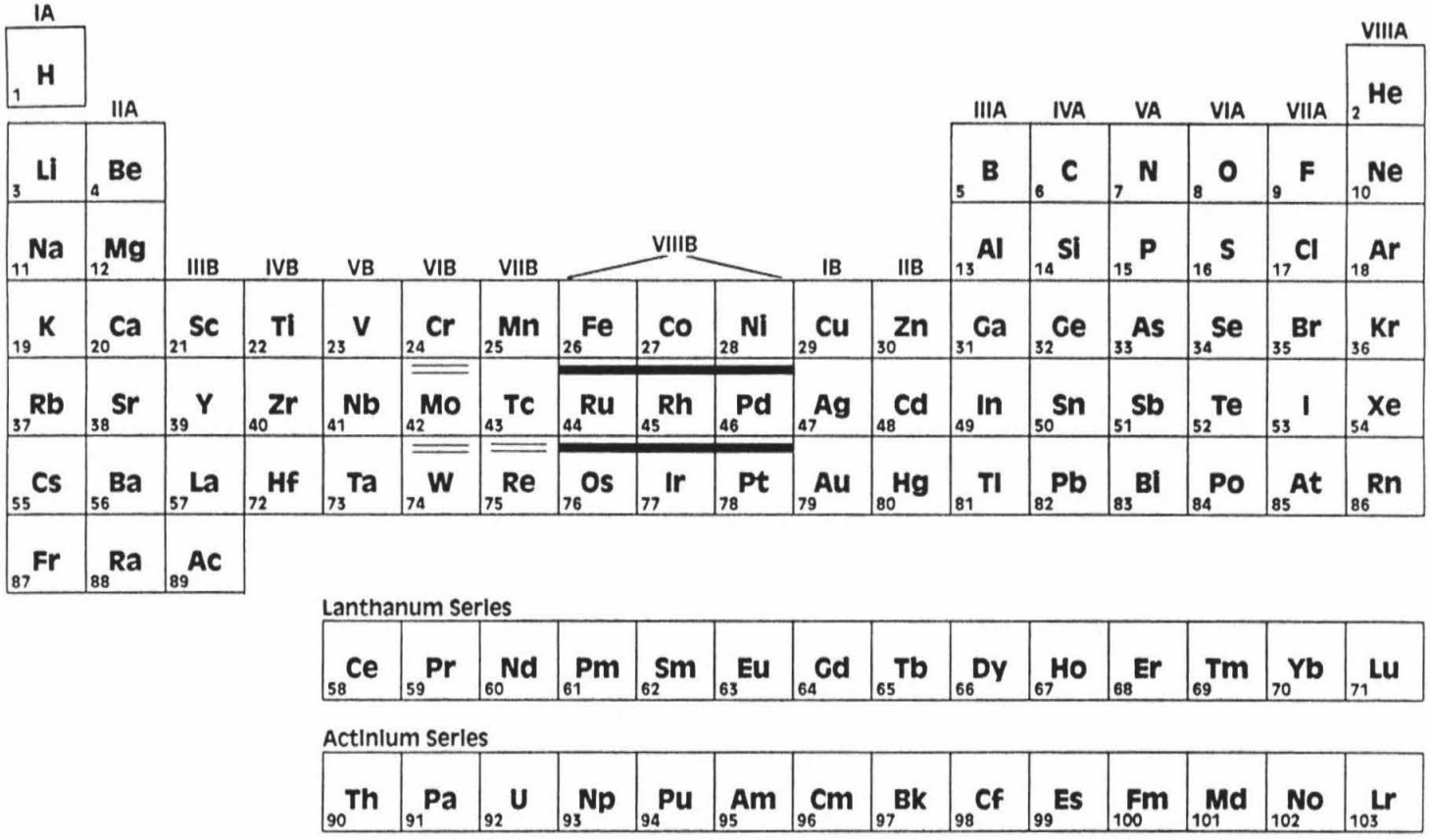

derived from the weathering of mafic and ultramafic igneous rocks and concentration of native alloys from them. Detailed statistics on the supply and demand for PGE can be found in Loebenstein (1989). Approximately 48% of PGE production comes from the Republic of South Africa (primarily from the Merensky Reef in the Bushveld Complex), ~43% of production comes from the U.S.S.R. (primarily from the Noril'sk-Talnakh region of Siberia) and ~5% of production comes from Canada (primarily from the Sudbury District) (Loebenstein, 1989; Naldrett, 1981). Mining of the J-M Reef in the Stillwater Complex of Montana, U.S.A., began in 1977 but is not yet a major source of PGE. The J-M Reef grades as high in Pt and four times as high in Pd as the Merensky Reef over a mining width twice as great but has a more complex structure due to extensive faulting.

Methods of isolating, separating and analyzing the PGE are presented in a series of papers published by Beamish and coworkers, mainly in the journal *Talanta*. The papers provide the basis for the book, *The Analytical Chemistry of the Noble Metals* (Beamish, 1966). Two subsequent books (Beamish and Van Loon, 1972, 1977) provide updated information on analytical methodologies. Crockett and Cabri (1981) provide a brief review of the various analytical techniques for the PGE. Cabri (1988) summarized the status of *in situ* microbeam analytical techniques for the PGE.

By studying the distribution and chemical behavior of the PGE in geological materials, several important problems in geochemistry can uniquely be addressed including 1) the condensation of refractory solids from the solar nebula, 2) the mechanisms by which trace metals are concentrated during magmatic differentiation and planetary metamorphism and 3) core formation in planetesimals, the moon and the earth. Numerous analytical and petrographic studies of the PGE have been carried out in order to address each of these

problem areas. However, due to a lack of diffusion, phase equilibria and partitioning data in PGE-rich systems and the severe limitations of available analytical methods, there are still many basic unanswered questions in PGE geochemistry.

In this thesis, a few key research areas where chosen in which experimental data could potentially elucidate uncertain, yet important, aspects of the geochemistry of PGE. Experimental studies were used to address specific problems including 1) the origin of PGE-rich alloys which occur in meteorites and have been proposed to be the earliest nebular condensates, 2) the behavior of PGE-rich alloys during planetary metamorphism and 3) the role of PGE-rich phases and chromite in the partitioning of PGE during mantle partial melting and crustal magmatic differentiation.

Analytical studies were carried out on PGE-rich phases from meteorites and the products of synthetic experiments using traditional electron microprobe x-ray analytical techniques. The high detection limits for PGE ($\sim$ 100 ppm) relative to the concentrations usually observed in typical rocks ($<$ 6 ppb) have, however, limited the scope of analytical studies to the very few cases where PGE are unusually enriched. To study the behavior of PGE during the more common geologic processes that largely control their terrestrial distribution will require an *in situ* analytical technique with much lower detection limits than any methods currently in use. To overcome this limitation, resonance ionization of sputtered atoms was investigated for use as a new ultrasensitive *in situ* analytical technique for the analysis of PGE in natural samples and experimentally synthesized phases.

Details of specific research projects completed during my thesis studies are presented as original research articles in Appendices I through VI. Appendix I presents diffusion, phase equilibria and PGE partitioning experiments in the Ni-Fe-Ru system. This work demonstrates

that PGE-rich metallic phases can be formed by subsolidus exsolution reactions from an initially homogeneous Ni-Fe-PGE metal. Appendices II and III present analytical studies of PGE-rich metallic phases from refractory meteorite inclusions. The conditions under which the inclusions and their host meteorites were melted and subsequently metamorphosed are quantified by comparison with experimental data from the Ni-Fe-Ru, Ni-Fe-O-V and Ni-Fe-S systems. Appendix IV presents a preliminary experimental investigation of the solubility and diffusion of the PGE in iron sulfide and chromite at magmatic temperatures, and a discussion of the possible importance of these phases in the terrestrial fractionation of PGE.

Appendices V and VI diverge from the theme of PGE geochemistry to the theme of PGE analytical chemistry. They describe the development of resonance ionization of sputtered atoms as a new method for *in situ* analysis of the PGE. It is demonstrated that this method is capable of quantitative PGE analyses at concentrations many orders of magnitude lower than the minimum detection limits of the electron microprobe. With this method we now have the potential to explore many aspects of PGE geochemistry that were previously inaccessible to analytical study. Appendix VI also includes a discussion of the application of resonance ionization of sputtered atoms as a new type of highly efficient and elementally selective ion source for an isotope ratio mass spectrometer.

The chapters of this thesis represent a general review of the geochemistry and resonance ionization of PGE emphasizing those areas in which I have made a contribution. Chapter 2 draws together some basic information on the chemistry and natural abundances of PGE. Chapter 3 summarizes the cosmochemistry of PGE and Chapter 4 discusses the geochemical behavior of PGE in refractory meteorite inclusions. Chapter 5 considers the available data on the terrestrial fractionation of PGE and the applications of the Re-Os geochronometer.

Finally, Chapter 6 reviews the use of resonance ionization of sputtered atoms for the chemical and isotopic analysis of PGE.

CHAPTER 2. CHEMISTRY AND NATURAL ABUNDANCES

This chapter summarizes some of the basic features of Pt-group element chemistry, and presents data on their cosmic and terrestrial abundances. It is not meant to be a comprehensive review, but rather to provide background information and references that are pertinent to the specific discussions of PGE geochemistry in the chapters and appendices that follow. PGE have a remarkable tendency to form their own alloy and sulfide phases in nature rather than dissolving as trace constituents in major minerals. These PGE alloys and compounds typically occur as minute particles (≤ 1 μm) containing two or more of the PGE and variable amounts of Fe and Ni. The binary phase equilibria of pairs of PGE and of each PGE with Fe and Ni are reviewed below and provide a basis for understanding the separation of PGE into the variety of phases observed in nature. Clues to the concentration mechanisms for PGE in meteorites and terrestrial rocks come from consideration of basic chemical stability data, as well as meteoritic and terrestrial abundance patterns.

2.1 ALLOYS

Among the elements, the most notable feature of the PGE is their high melting temperatures, which range from 3045°C for Os to 1554°C for Pd (Table 2.1). Os is the third most refractory element following only W (3410°C) and Re (3170°C). As can be seen on Table 2.1, the melting and boiling points as well as the hardness of the PGE decrease with increasing atomic number along both the second and third rows of the periodic table. Thus, Ru and Os are the most refractory and the hardest, whereas Pd and Pt are the least refractory and the softest.

The binary phase equilibria for pairs of PGE have been determined to varying degrees of completeness. A compilation of all available binary phase diagrams is provided by Massalski

Table 2.1 Some chemical properties of the PGE and Re.

	Ru	**Rh**	**Pd**	**Os**	**Ir**	**Pt**	**Re**
Atomic number	44	45	46	76	77	78	75
Atomic wt (AMU)	101.1	102.9	106.4	190.2	192.2	195.1	186.2
Melting point (°C)	2310	1963	1554	3045	2447	1772	3170
Boiling point (°C)	4080	3700	2900	5020	4500	3800	5630
Crystal structure	HCP	FCC	FCC	HCP	FCC	FCC	HCP
Atomic radius (Å)	1.33	1.35	1.38	1.34	1.36	1.37	1.37
Valence electrons	$4d^7 5s$	$4d^8 5s$	$4d^{10}$	$5d^6 6s^2$	$5d^7 6s^2$	$5d^9 6s$	$5d^5 6s^2$
Oxidation states	2,3,4 6,8	1,3,4 5	2,4	2,3,4 6,8	1,2,3 4,6	2,4	2,3,4 5,6,7
Ionization pot. (eV)	7.4	7.5	8.3	8.6	9.0	9.0	7.9
Density (g/cm^3)	12.5	12.4	12.0	22.6	22.7	21.5	21.0
Hardness (vickers)	200-350	100-120	40-42	300-670	200-240	40-42	~250

HCP=hexagonal close-packed, FCC=face-centered cubic.

(1986). Many of the PGE pairs have only been studied at temperatures close to their melting points, and there are no studies of PGE systems containing three or more components. Nevertheless, it is clear that the crystal structures of the metals play a dominant role in the phase equilibria, and rules relating the binary mixing properties to crystal structure can be stated. Ru and Os (which lie below Fe on the periodic table) and Re (which lies below Mn) have a hexagonal close-packed structure, whereas Rh, Pd, Ir and Pt (which lie below Co and Ni) have a face-centered cubic structure (Table 2.1). The common crystal structure between Ru, Os and Re results in a complete solid solution between these elements at near-liquidus temperatures; the behavior at lower temperatures has not been determined experimentally. Similarly, complete solid solution at high temperature is observed in binary mixtures of the elements Rh, Pd, Ir and Pt. Miscibility gaps are known to occur in each of these binary systems at temperatures below $\sim 1000°C$. The Pt-Ir phase diagram is shown in Fig. 2.1 as a general example of phase equilibria between two PGE with the same crystal structure.

Binary mixtures between the hexagonal close-packed and face-centered cubic PGE display limited solid solution and always have a miscibility gap that extends from lower temperatures ($< 1000°C$) up to the liquidus. The solubilities of each of the end-member elements in the other element of the binary pair vary from $< 5\%$ in the Os-Pd system to $> 30\%$ in the Os-Ir system. The Pt-Ru phase diagram is shown in Fig. 2.2 as an example of phase equilibria between two PGE with differing crystal structure. No ordered intermetallic compounds are known in any of the binary PGE systems.

Binary phase equilibria in PGE-Fe and PGE-Ni systems have been determined to varying degrees of completeness and are compiled by Massalski (1986). Although some of the binary phase diagrams are unknown or only poorly constrained, they too appear to obey simple rules

Fig. 2.1 Pt-Ir phase diagram as compiled by Massalski (1986). The following notation is used in Figs. 2.1 through 2.7. Dashed lines are used for uncertain or speculative phase boundaries, liquid phases are designated by L, complete solid solutions are designated by (A,B) and terminal solid solutions are designated by (A) or (B). Ordered phases are designated by A_XB_Y and Greek letters are used to designate high- and low-temperature forms.

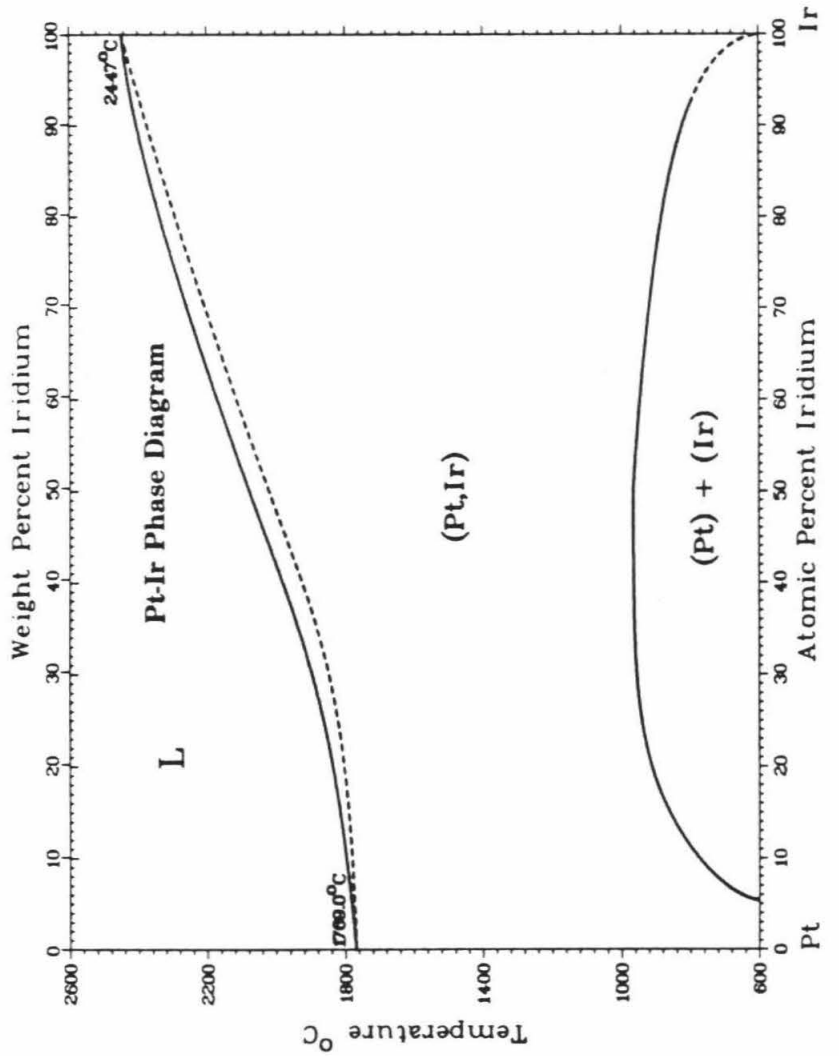
Weight Percent Iridium
Pt-Ir Phase Diagram
L
(Pt,Ir)
(Pt) + (Ir)
2447°C
1769.0°C
Temperature °C
Atomic Percent Iridium
Pt
Ir

Fig. 2.2 Pt-Ru phase diagram compiled by Massalski (1986). Nomenclature as in Fig. 2.1.

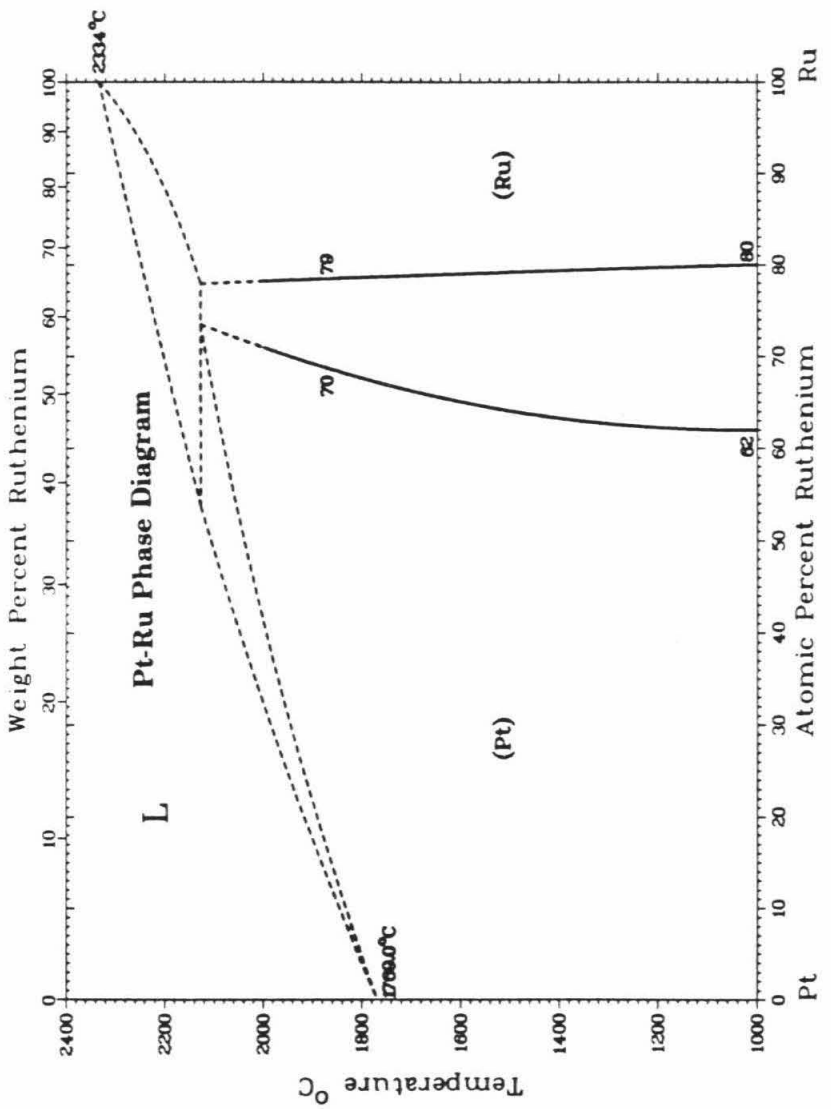
Pt-Ru Phase Diagram
L
(Pt)
(Ru)
2334°C
1769.0°C
79
80
70
62
Weight Percent Ruthenium
Atomic Percent Ruthenium
Temperature °C
Pt
Ru
0
10
20
30
40
50
60
70
80
90
100
2400
2200
2000
1800
1600
1400
1200
1000

based upon the crystal structures of the various PGE. The crystal structure of Fe is face-centered cubic at $T > 912°C$ and body centered cubic at $T < 912°C$. The crystal structure of Ni is face-centered cubic. The hexagonal close-packed PGE (Ru, Os and Re) display limited solid solution and miscibility gaps at all temperatures when alloyed with either Fe or Ni. The Fe-Ru and Ni-Ru diagrams are shown in Figs. 2.3 and 2.4 as examples of the forms of these binary diagrams.

The face-centered cubic PGE (Rh, Pd, Ir and Pt) display complete solid solution with both Fe and Ni at high temperatures and develop miscibility gaps only at temperatures below 600 to 1300°C for alloys with Fe, and temperatures below 200 to 700°C for alloys with Ni. The only ordered intermetallic phases reported are in the Fe-Pd ($FePd$, $FePd_3$), Fe-Pt (Fe_3Pt, $FePt$, $FePt_3$) and Ni-Pt (Ni_3Pt, $NiPt$) systems. The Fe-Pt and Ni-Pt diagrams are shown in Figs. 2.5 and 2.6 as examples of the general forms of these diagrams.

Naturally occurring PGE alloys usually also contain both Fe and Ni and therefore Fe-Ni-PGE ternary systems must be considered. The Fe-Ni binary, which bounds these ternary systems, is shown in Fig. 2.7 for reference. Fe and Ni display complete solid solution at high temperatures and develop miscibility gaps and intermetallic compounds at lower temperatures. Ternary Fe-Ni-PGE phase equilibria have been studied previously only in the Fe-Ni-Pt system and then only at 600°C (Stevens *et al.*, 1978). As can be seen in Fig. 2.8, a continuous tetragonal solid solution forms between the ordered phases $FePt$ and $NiPt$, and cubic solid solutions extend from the ordered phases Fe_3Pt and $FePt_3$ toward more Ni rich compositions. Disordered face-centered cubic and body-centered cubic solid solutions are also observed (Fig. 2.8). Ternary phase equilibria in the Fe-Ni-Ru system were determined in this study between 600 to 1000°C and are discussed in detail in App. I. The 600°C section is shown in Fig. 2.9 for comparison with the Fe-Ni-Pt system. Whereas the traditional phase

Fig. 2.3 Fe-Ru phase diagram compiled by Massalski (1986). Nomenclature as in Fig. 2.1.

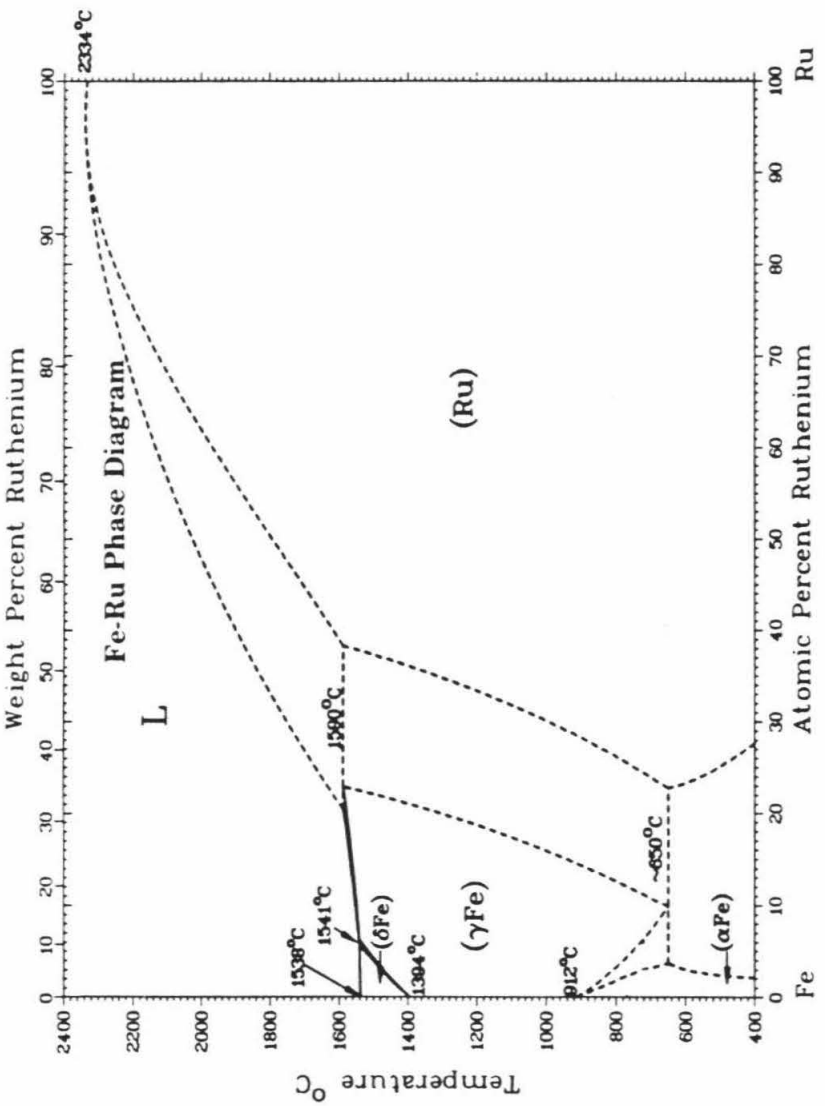
Fe-Ru Phase Diagram
Weight Percent Ruthenium
Atomic Percent Ruthenium
Temperature °C
Fe
Ru
L
(Ru)
(γFe)
(δFe)
(αFe)
2334°C
1538°C
1541°C
1394°C
1590°C
912°C
~650°C

Fig. 2.4 Ni-Ru phase diagram compiled by Massalski (1986). Nomenclature as in Fig. 2.1.

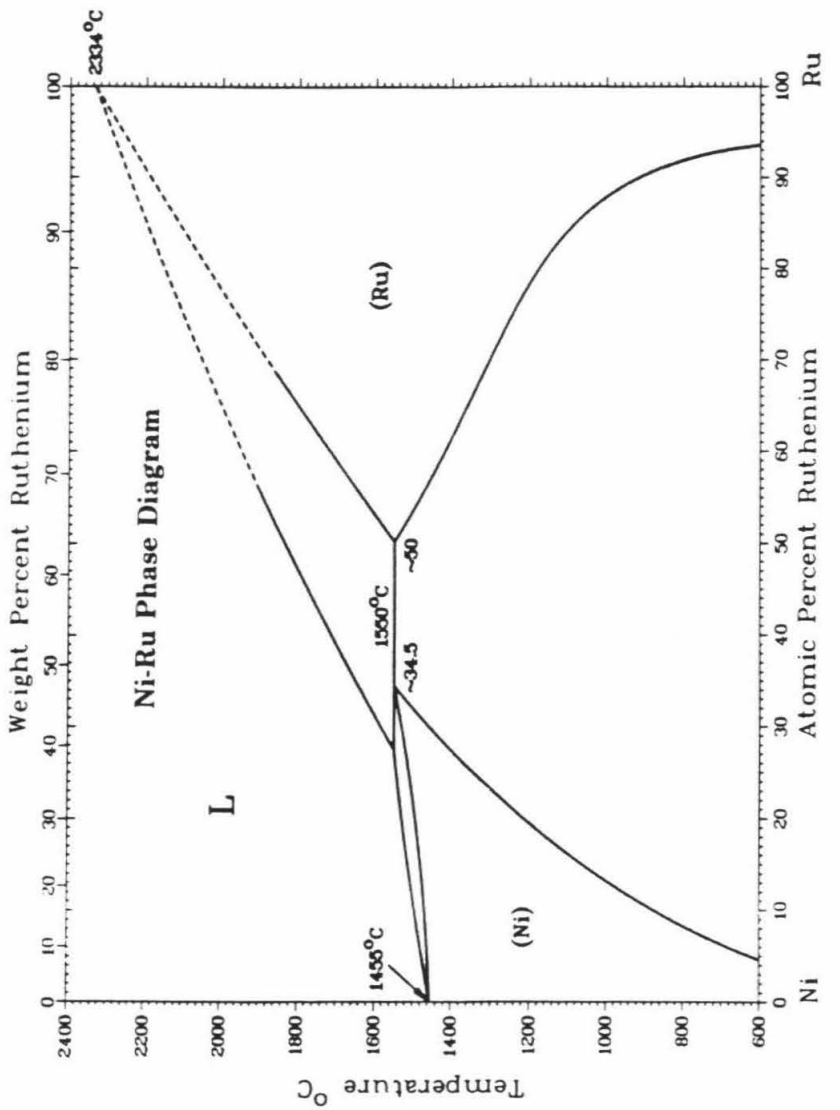
Ni-Ru Phase Diagram
Weight Percent Ruthenium
Atomic Percent Ruthenium
Temperature °C
Ni
Ru
L
(Ru)
(Ni)
2334°C
1555°C
1455°C
~50
~34.5
0
10
20
30
40
50
60
70
80
90
100
2400
2200
2000
1800
1600
1400
1200
1000
800
600

Fig. 2.5 Fe-Pt phase diagram compiled by Massalski (1986). Nomenclature as in Fig. 2.1. Note the existence of three ordered phases.

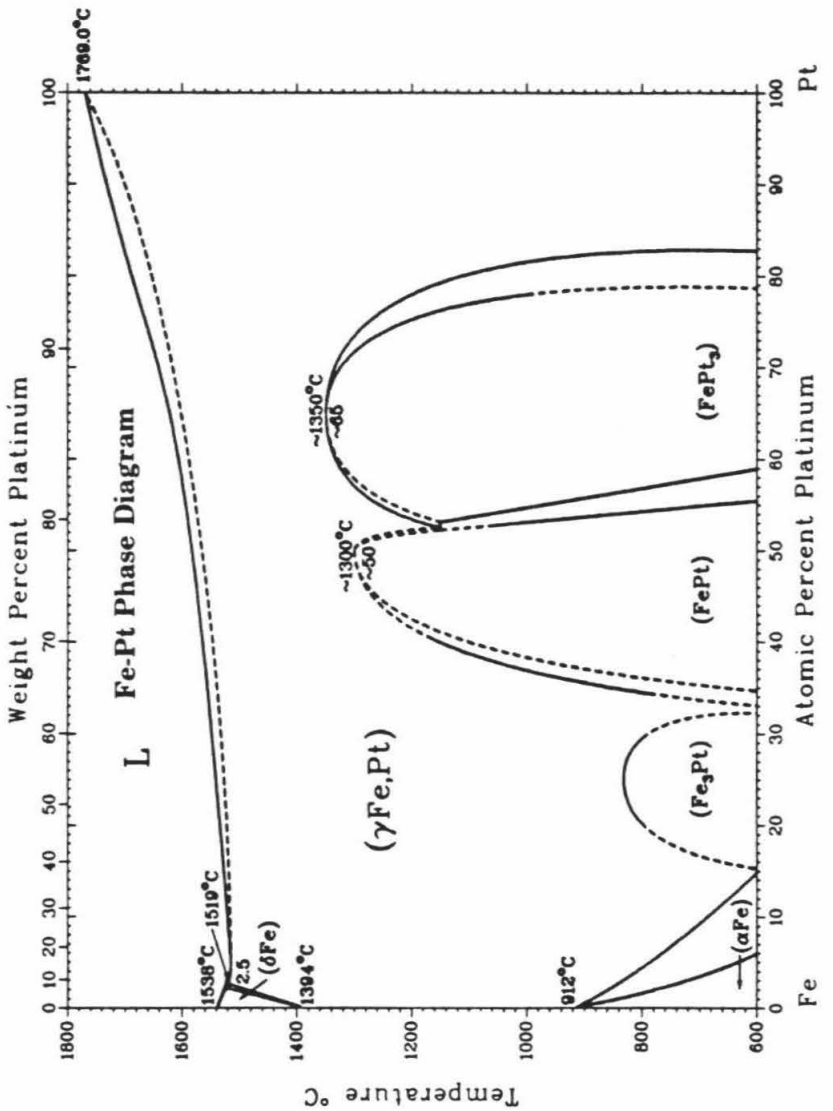
Fe-Pt Phase Diagram
L
(γFe,Pt)
(δFe)
(αFe)
(Fe3Pt)
(FePt)
(FePt2)
1769.0°C
1538°C
1519°C
2.5
1394°C
912°C
~1350°C
~65
~1300°C
~50
Weight Percent Platinum
Atomic Percent Platinum
Temperature °C
Fe
Pt

Fig. 2.6 Ni-Pt phase diagram compiled by Massalski (1986). Nomenclature as in Fig. 2.1. Note the existence of two ordered phases.

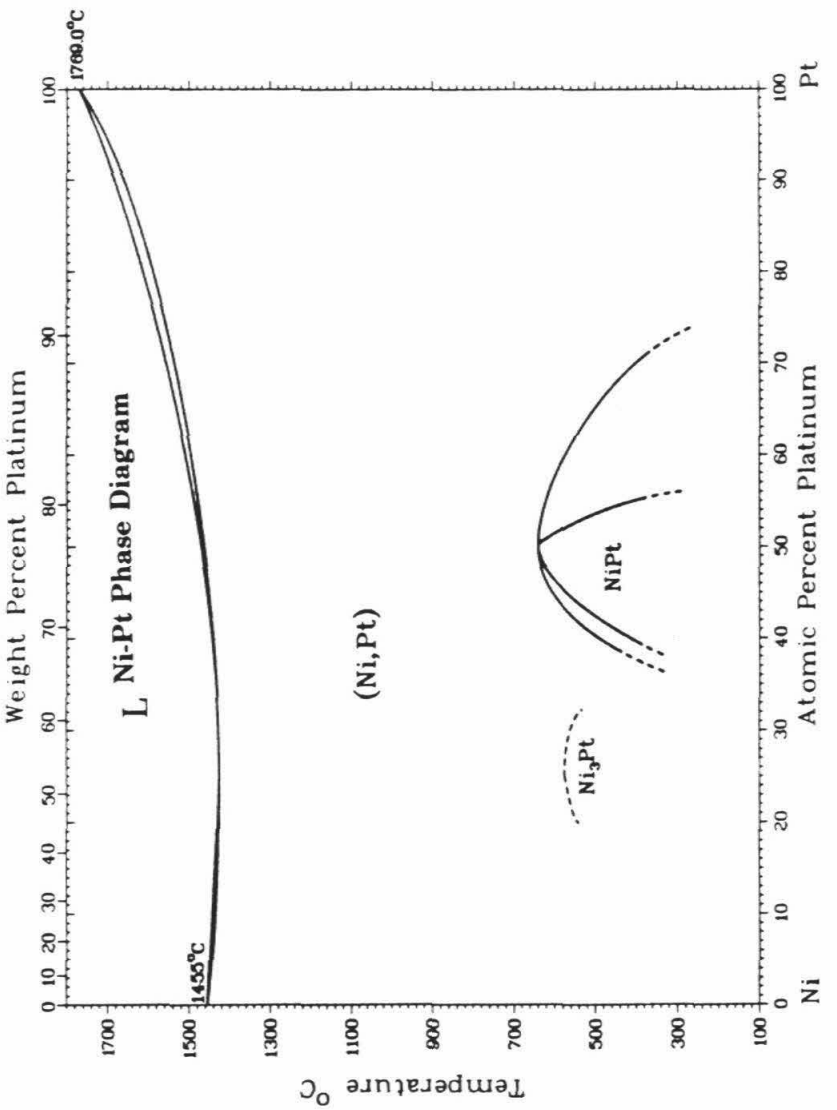
Ni-Pt Phase Diagram
L
(Ni,Pt)
NiPt
Ni3Pt
1769.0°C
1455°C
Weight Percent Platinum
Atomic Percent Platinum
Temperature °C
Ni
Pt

Fig. 2.7 Fe-Ni phase diagram compiled by Massalski (1986). Nomenclature as in Fig. 2.1. Note the existence of three ordered phases.

Fe-Ni Phase Diagram

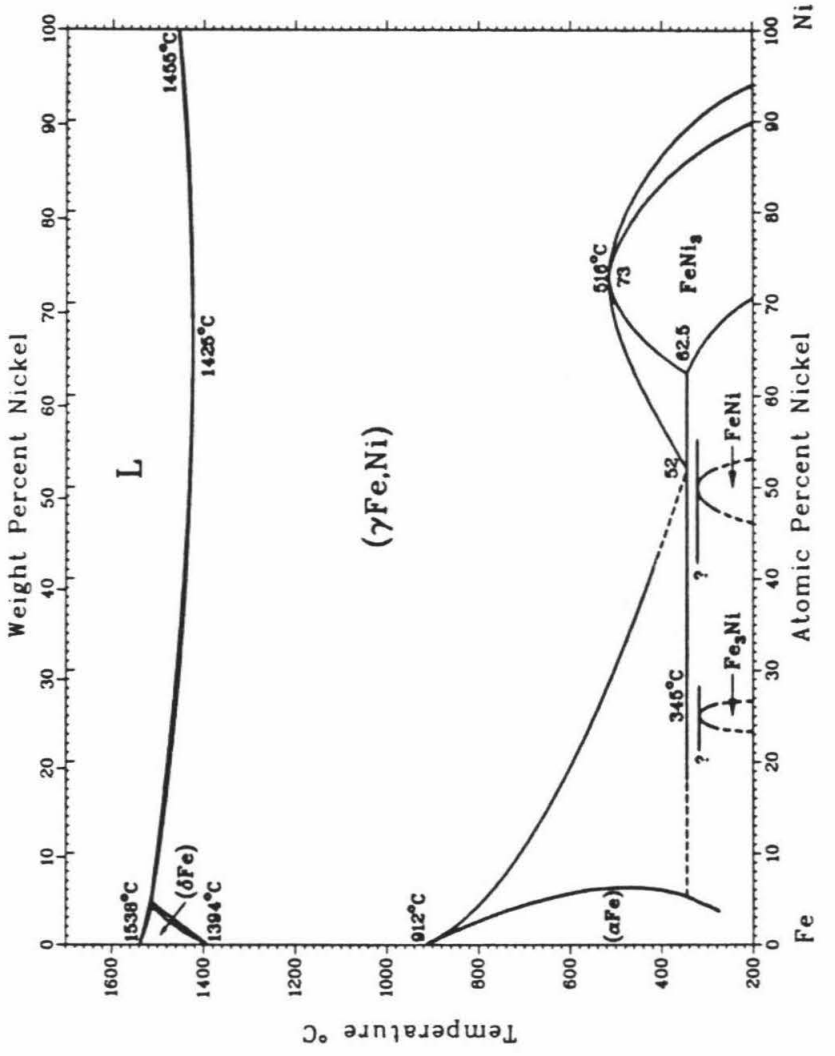

Fig. 2.8 Fe-Ni-Pt phase diagram at 600°C from Stevens *et al.* (1978). All solid solution fields are labeled. Tetragonal and cubic fields are ordered phases whereas face-centered cubic (fcc) and base-centered cubic (bcc) fields are disordered phases. Unlabeled fields are two and three phase regions.

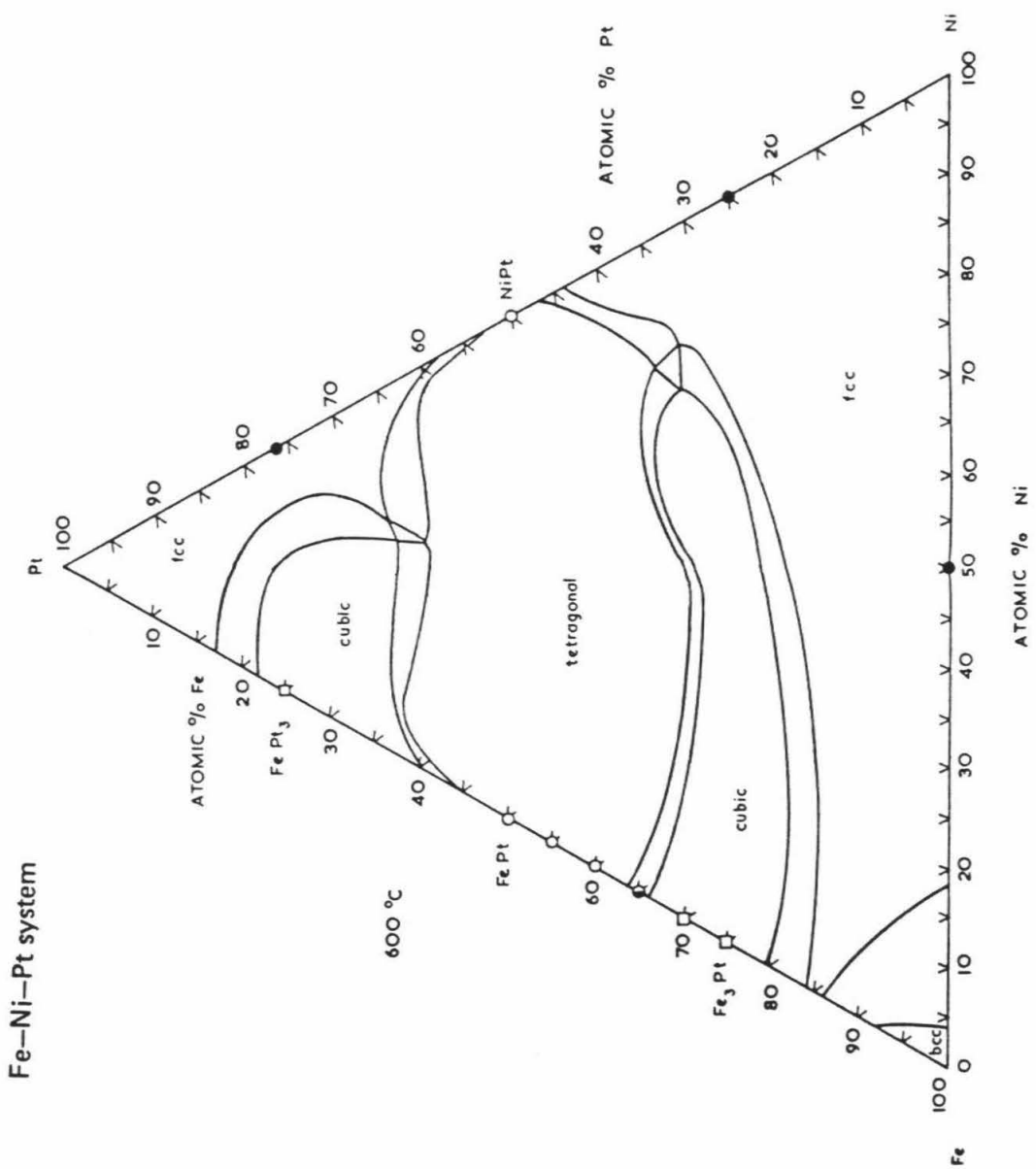
Fe–Ni–Pt system
Pt
Ni
Fe
ATOMIC % Fe
ATOMIC % Pt
ATOMIC % Ni
600 °C
fcc
cubic
tetragonal
cubic
fcc
bcc
NiPt
Fe Pt3
Fe Pt
Fe3 Pt

Fig 2.9 Ni-Fe-Ru phase diagram at 600°C from App. I. Hexagonal close-packed ϵRu-Fe and face-centered cubic γNi-Fe solid solutions fields are labeled. Two-phase (2ϕ) and three-phase (3ϕ) regions are designated. Tie-lines are drawn in two-phase regions.

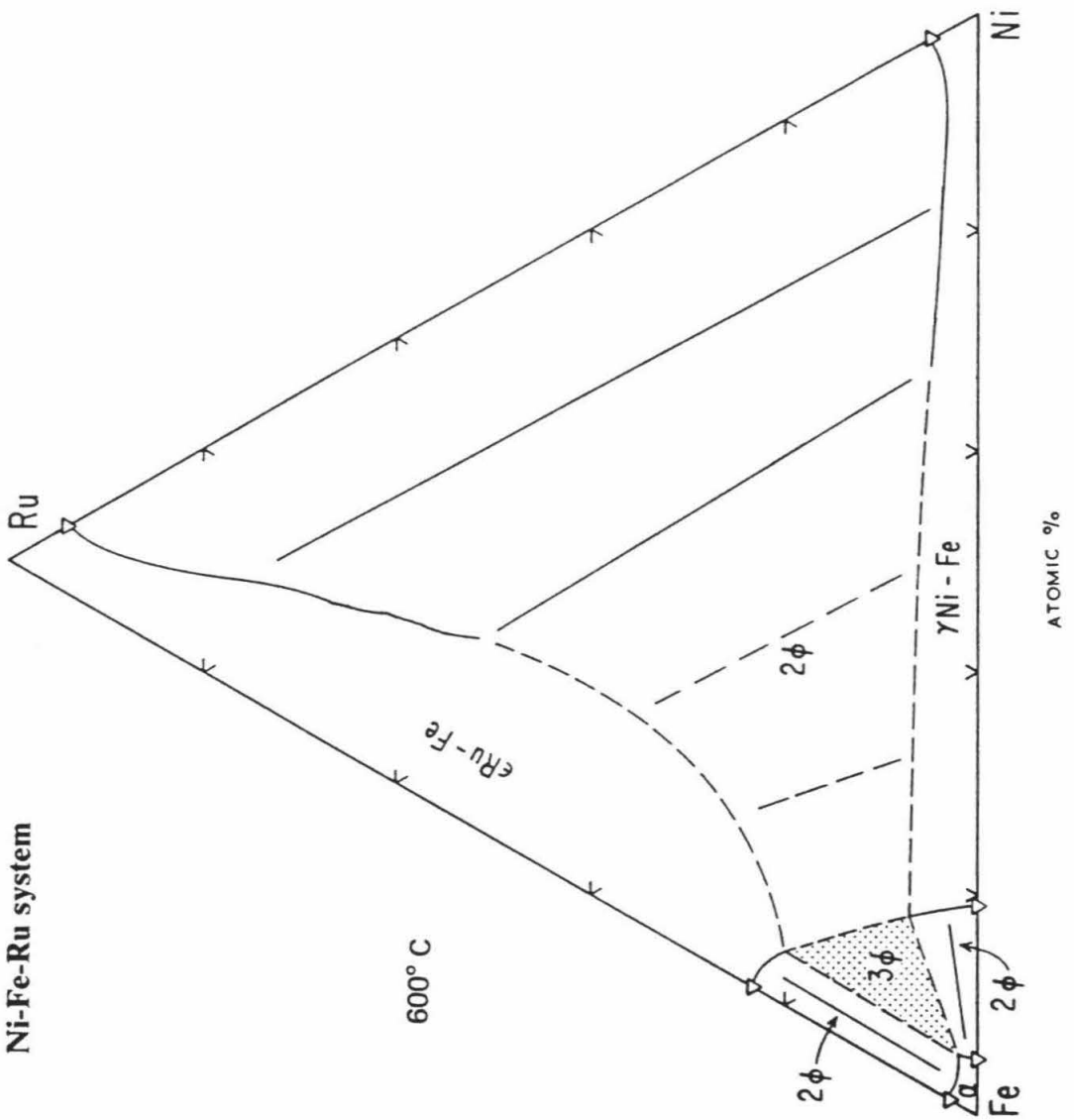
Ni-Fe-Ru system
600° C
Ru
Ni
Fe
εRu - Fe
γNi - Fe
2ϕ
3ϕ
2ϕ
2ϕ
α
ATOMIC %

equilibria methodology used in the study of the Fe-Ni-Pt system required the preparation and annealing of many different alloy compositions, a large portion of the Ni-Fe-Ru system was investigated in this study with a single experiment at each temperature by establishing a concentration gradient within which local equilibrium between coexisting phases was maintained. A wide miscibility gap is present in the Fe-Ni-Ru system at each temperature studied and separates a hexagonal close-packed Ru-Fe phase from a face-centered cubic Ni-Fe phase.

2.2 SULFIDES

The sulfur fugacity (fS_2) of a given geologic environment has a strong influence on the chemical behavior of the PGE and determines whether they exist as alloy or sulfide minerals. Therefore, it is important to summarize the thermodynamic data for metal-sulfide stabilities of PGE. Metal-sulfide stability curves were calculated as a function of temperature using thermodynamic data from Barton and Skinner (1979), Svendsen (1979), Hultgren *et al.* (1973) and Mills (1974). The curves are plotted on a log fS_2 versus 1/T diagram in Figure 2.10. The fS_2 necessary to form a PGE sulfide is considerably higher than needed to form FeS and increases in the order Ru⇒Pt⇒Ir⇒Os. There are insufficient data to include Rh and Pd within this ordering.

A wide variety of PGE sulfide compounds have been synthesized and are listed on Table 2.2. The experimental data are reported in the materials science and chemistry literature and have been compiled in several binary phase diagram reference volumes (Hansen and Anderko, 1958; Elliot, 1965; Shunk, 1969; Moffatt, 1979). Naturally occurring sulfide minerals include laurite (RuS_2; Leonard *et al.*, 1969), prassoite ($Rh_{17}S_{15}$; Geller, 1962), vysotskite (PdS; Cabri *et al.*, 1978), erlichmanite (OsS_2; Snetsinger, 1971), xingzhongite [(Ir,Cu)S;

Fig. 2.10 Plot of log fS_2 versus reciprocal temperature with metal-sulfide stability curves for Fe, Ru, Pt, Ir and Os. Calculated using data from Barton and Skinner (1979), Svendsen (1979), Hultgren *et al.* (1973) and Mills (1974).

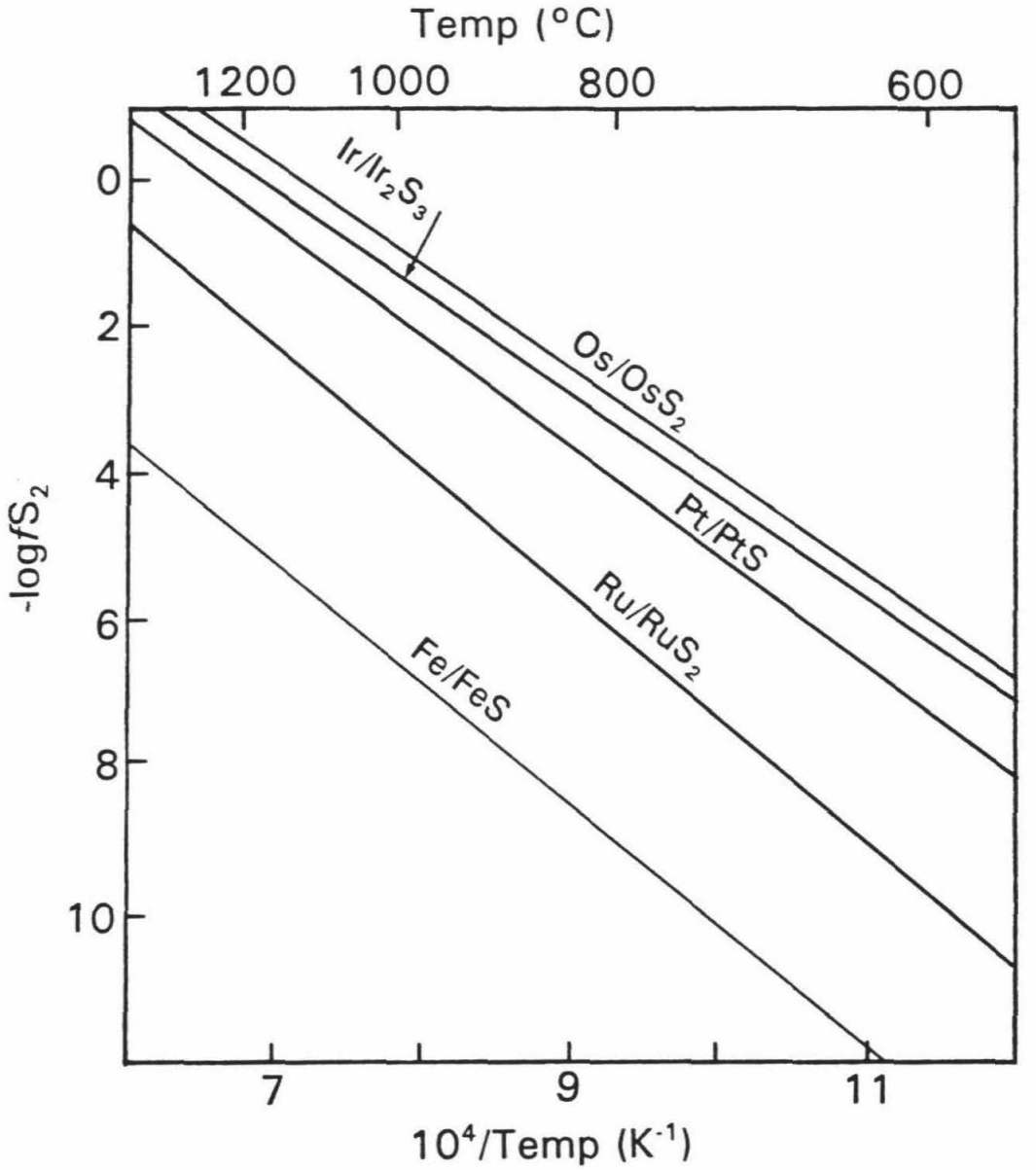
Temp (°C)
1200
1000
800
600
0
2
4
6
8
10
-logfS2
Ir/Ir2S3
Os/OsS2
Pt/PtS
Ru/RuS2
Fe/FeS
7
9
11
10^4/Temp (K^-1)

Table 2.2 Synthetic oxide and sulfide compounds of the PGE and Re.

	Ru	**Rh**	**Pd**	**Os**	**Ir**	**Pt**	**Re**
Oxide formed by heating in air	RuO_2	Rh_2O_3	PdO	OsO_4	IrO_2	PtO_2	Re_2O_7
Other known oxides	Ru_2O_3 Ru_2O_5 RuO_3 RuO_4	RhO_2 Rh_2O_5	--	Os_2O_3 OsO_2 OsO_3	Ir_2O_3 IrO_3	PtO Pt_3O_4	ReO_2 ReO_3
Known sulfides	RuS_2	$Rh_{17}S_{15}$ Rh_3S_4 Rh_2S_3 RhS_3 Rh_6S_7	Pd_4S Pd_3S $Pd_{16}S_7$ PdS PdS_2	OsS_2	IrS Ir_2S_3 IrS_2 Ir_3S_8 IrS_3	Pt_3S PtS PtS_2	ReS_2 Re_2S_7

Peng *et al.*, 1978], braggite [(Pt,Pd)S; Cabri *et al.*, 1978], cooperite (PtS_2; Cabri *et al.*, 1978), and malanite [$(Pt,Ir)_2CuS_4$; Peng *et al.*, 1978]. Naturally occurring alloys, tellurides and arsenides are also observed for many of the PGE; a comprehensive glossary of the chemical and mineralogical properties of these minerals is given by Cabri (1981).

2.3 OXIDES

The PGE display a wide range of oxidation states in their chemical compounds (Table 2.1). In Table 2.2 the oxide compound that forms by heating each metal in air is given as well as other known oxides. OsO_4, which forms by the oxidation of Os metal powder in air at room temperature, is by far the most volatile of the PGE oxides. It forms a colorless solid which melts at 40°C and boils at 101°C. It has a characteristic chlorine-like odor and is extremely toxic (McLaughlin, 1946; Sax, 1968). It is reduced to a black dioxide when it comes in contact with organic matter and can cause severe damage to the eyes and respiratory system. In contrast, Pt can be heated in air to its melting point with only a slight loss of Pt as the volatile PtO_2.

Several PGE-bearing spinel compounds that contain PGE as major cations have been synthesized at high temperatures under very oxidizing conditions, and are reported in the materials science literature (Krutzsch and Kemmler-Sack, 1983; Greenwood, 1968; Muller and Roy, 1969, 1971). Most of the compounds combine one or two first row transition metals with a PGE. Spinels synthesized with the $X^{2+}Y^{3+}{}_2O_4$ structure include $(Ni,Ru)Fe_2O_4$, $(Mg,Ru)Fe_2O_4$, $RuCo_2O_4$ and $IrCo_2O_4$. Spinels synthesized with the $X^{2+}{}_2Y^{4+}O_4$ structure (inverse spinels) include Mg_2PdO_4, Mg_2PtO_4, Cd_2PtO_4 and Zn_2PtO_4.

Recently, Capobianco and Drake (1990) crystallized geologically important $MgAl_2O_4$ spinels at 1450°C in an air atmosphere in the presence of silicate liquid and Ru, Rh and Pd.

Approximately 0.4% Rh and 0.8% Ru dissolved in the spinel phase but Pd solubility was below the 25 ppm detection limit. The finding that PGE are soluble in $MgAl_2O_4$ under highly oxidizing conditions is not surprising considering the variety of PGE spinel compounds that are known to be stable under these conditions.

A key question that remains is whether or not PGE are soluble in geologically important spinels under the much more reducing conditions that prevail during magmatic processes in the crust and upper mantle. This would help to resolve debates over the role of Cr-rich spinel in the partitioning of PGE during mantle partial melting and magmatic crystallization (*e.g.*, Talkington *et al.*, 1984; Auge, 1988). Preliminary experiments designed to test the solubility and mobility of PGE in Cr-rich spinels under geologically realistic conditions are reported in App. IV.

All of the PGE form halogen complexes in one or more oxidation states with F, Cl, Br and I (Cotton and Wilkinson, 1980). The most interesting are the hexaflourides, of which only that of Pd is yet unknown. They are prepared by flourination of the metals at elevated temperatures. The hexaflourides decrease in stability in the order Re⇒Os⇒Ir⇒Pt⇒Ru⇒Rh, dissociating into flourine and lower flourides (Cotton and Wilkinson, 1980). It has been suggested that IrF_6 is an important volatile species in magmatic systems, and that it is responsible for the 10^4 enrichments of Ir (with respect to magma) in airborne particulate matter from some Hawaiian volcanic eruptions (Zoller *et al.*, 1983). Flourine-rich volcanic gases collected from Merapi volcano are enriched in Re by a factor of 10^5 (Symonds *et al.*, 1987), suggesting that volatile flourides may be capable of concentrating Re and other PGE in addition to Ir in magmatic systems.

The aqueous solution chemistry of each PGE is dominated by the tendency to form stable complex ions in preference to simple cationic species. Since this study is concerned

exclusively with the high temperature behavior of PGE, the details of PGE complexes will not be discussed. There is an extensive literature on the low temperature chemistry of PGE complexes which has been reviewed by Griffith (1967), Hartley (1973) and Crockett (1981). The limited data on the marine chemistry of PGE has recently been reviewed by Goldberg *et al.* (1988).

2.4 PARTITION COEFFICIENTS

Very little is known about the partitioning of PGE between mineral phases under conditions relevant to geochemical systems. Partitioning of PGE as a function of temperature, fO_2 and fS_2 is not well understood. Analyses of iron meteorites, magmatic sulfides and chromitites has established that the PGE are compatible with metallic iron, iron-sulfides and chromite relative to silicate liquids. However, experimental studies have been so limited in scope that they have done little more than to confirm these general observations.

The partitioning of Ir and Re between iron metal containing 22% S and basaltic glass was measured by Jones and Drake (1986) at 1270°C and $\log fO_2 = -13$. The silicate/metal partition coefficient ($D_{S/M}$) for Ir was determined to be $5x10^{-4}$ to $5x10^{-6}$ and $D_{S/M}$ for Re was determined to be $5x10^{-3}$ to $5x10^{-5}$. It is not known how much these values vary for the other PGE or the effect of S content, temperature or fO_2. Silicate/sulfide partition coefficients for PGE have not been studied experimentally; empirical estimates based on the study of ore deposits range from 10^{-2} (Ross and Keays, 1979) to 10^{-5} (Campbell and Barnes, 1984).

A study of the partitioning of Ru, Rh and Pd between $MgAl_2O_4$ spinel and a $CaO+MgO+Al_2O_3+SiO_2$ liquid in an air atmosphere at 1450°C has yielded silicate/spinel partition coefficients of 0.04, 0.01 and >50, respectively (Capobianco and Drake, 1990). It is not clear whether these experiments, which were run under highly oxidizing conditions, are

directly relevant to partitioning under the much more reducing conditions prevalent in the crust and upper mantle. They do, however, suggest that spinel compatibility might play a role in the fractionation of PGE during magmatic processes.

The partitioning of Os and Re was measured between chromian diopsidic pyroxene and a Fe-free basaltic liquid contained in a Pt crucible in an air atmosphere (Watson *et al.*, 1987). Silicate melt/pyroxene partition coefficients of ~ 10 and ~ 20 were determined for Os and Re, respectively. However, due to the oxidizing conditions and presence of Pt metal, the relevance of this experiment to equilibrium or to natural conditions is questionable.

2.5 COSMIC ABUNDANCES AND CONDENSATION TEMPERATURES

The concentrations of most PGE and Re have been measured in C1 chondrite meteorites using neutron activation analysis. Rh has not been measured but has been estimated based on analyses of H-chondrites assuming that the relative abundances of the PGE are constant in H-chondrites and C1 chondrites. The first measurements of the PGE (except Rh) were made by Crockett *et al.* (1967), and the first measurements of Re were made by Morgan and Lovering (1967). The original values, averages compiled by Cameron (1972), averages compiled by Anders and Grevesse (1989), and estimates based on abundances in the solar photosphere (Anders and Grevesse, 1989) all agree to $\sim \pm 15\%$. The average cosmic abundances of each of the PGE relative to Si are given in Table 2.3 and vary by a factor of five from 0.344 Rh atoms/10^6 Si to 1.86 Ru atoms/10^6 Si.

Following the approach of Larimer (1967), Scott (1972) first calculated the temperatures at which each of the PGE (and other refractory metals) become stable solid phases relative to an equilibrium gas of solar composition at a total pressure of 10^{-4} atm (Table 2.3). Grossman (1973) repeated the calculation for a few of the PGE at a total pressure of 10^{-3} atm

Table 2.3 Cosmic abundances and nebular condensation temperatures (in K) for the PGE and Re.

	Ru	**Rh**	**Pd**	**Os**	**Ir**	**Pt**	**Re**
Cosmic abundance (atoms/10^6 Si) [1]	1.86	0.344	1.39	0.675	0.661	1.34	0.0517
Condensation temp pure metals ($P_T = 10^{-4}$ atm) [2]	1540	1285	940	1840	1550	1325	1775
Condensation temp pure metals ($P_T = 10^{-3}$ atm) [3]	1613	1346	1050	1917	1636	1415	1838
50% condensation temp into alloy with complete solid solution ($P_T = 10^{-3}$ atm) [3]	1642	1475	1415	1897	1683	1490	1905

[1] Anders and Grevesse (1989); [2] Scott (1972); [3] Palme and Wlotzka (1976).

and Palme and Wlotzka (1976) repeated the calculation for all of the PGE under these conditions (Table 2.3). Palme and Wlotzka (1976) also calculated the condensation temperature for each of the PGE for 50% condensation of each element into an alloy containing 13 metals assuming ideal solid solution (Table 2.3). The 50% condensation temperatures for the PGE range from ~1900°C for Os to ~1400°C for Pd, following a trend similar to the relative melting and boiling temperatures of the PGE given in Table 2.1. The compositions of possible condensate alloys are discussed further in Chapter 3.

2.6 METEORITIC AND TERRESTRIAL ABUNDANCES

Average abundances of PGE (and Re) in several types of meteoritic and terrestrial materials are given along with the sources of data in Table 2.4. In many cases averages were taken from review papers in which all available data were compiled. When such sources were not available, data were taken from analytical studies in which the maximum number of PGE were analyzed. C1 chondrites were included because they are the best estimates of the PGE content of the bulk earth. Ca, Al-rich refractory inclusions from C3 meteorites (CAI) were included because they may be representative of high-temperature nebular condensates. The PGE contents of samples of iron meteorites vary by as much as 10^4 within meteorite groups (*e.g.*, Scott and Wasson, 1975; Pernicka and Wasson, 1987). This variation has been attributed to fractional crystallization of metallic iron during the crystallization of the cores of asteroid size bodies (Scott, 1972). The average values for IIIAB iron meteorites given in Table 2.4 are an estimate of the bulk composition of the metallic parent melt from which the IIIAB iron meteorites crystallized that was calculated using a fractional crystallization model (Willis, 1980; Willis and Goldstein, 1982).

Abundances of the PGE in terrestrial rocks are not well known because the concentrations

Table 2.4 Average PGE (and Re) concentrations in some representative rock-types in ppb.

Rock-type	**Ru**	**Rh**	**Pd**	**Os**	**Ir**	**Pt**	**Re**
C1 chondrite [1]	710	130	560	490	480	990	37
CAI [2]	10450	1240	1160	6920	7510	10740	780
IIIAB Fe-meteorite† [3,4]	710	--	450	530	530	1100	48
Spinel lherzolite xenoliths [5]	--	--	5.5	3.3	3.4	--	0.17
Ophiolite complexes							
Peridotites [6,7]	6.1	3.0	6.7	5.1	3.8	9.1	2.4
Chromitites [8]	180	11	4.8	--	91	17	--
Komatiites [6,9]	--	--	8.6	1.6	1.2	14	1.1
Oceanic basalts [6,10]	--	--	≤1.8	≤0.025	≤0.037	--	0.93
Continental basalts [6]	--	--	8.3	--	0.092	--	--
Granitic rocks [6,7]	--	--	≤0.4	≤0.06	0.03	≤0.5	0.6
K-T boundary sed. [11] (3 mm basal clay layer)	--	--	110	46	57	131	2.7

-- indicates no data available.
†based on model-dependent calculation.
[1] Anders and Grevesse (1989); [2] Mason and Taylor, 1982; [3] Willis (1980); [4] Willis and Goldstein, 1982; [5] Morgan (1986); [6] Crockett (1981); [7] Morgan and Lovering (1967); [8] Page *et al.* (1982); [9] Walker *et al.* (1988); [10] Hertogen *et al.* (1980) [11] Kyte *et al.* (1985).

in almost all rocks are very low and thus difficult to measure. Pd and Ir are the most commonly analyzed PGE in terrestrial samples because these elements are the most sensitive of the PGE to neutron activation analysis. Os and Re have also been analyzed in a variety of rocks because of interest in Re-Os isotope systematics. The concentrations of Ru, Rh and Pt in many rock-types are largely unknown. An exception to the general lack of data on PGE concentrations are mafic/ultramafic layered intrusions such as the Stillwater Complex which host PGE ore deposits and have been extensively analyzed for all of the PGE. The concentrations of PGE in layered intrusions is discussed in section 5.4.

The data from Table 2.4 were normalized to C1 chondrite values and plotted on Figs. 2.11 for comparison. The PGE are plotted in the order of decreasing melting temperature, which seems to correlate with their behavior during terrestrial fractionation. Re is plotted last (after Pd) because it behaves much more similarly to Pd than it does to Os during terrestrial fractionation.

The concentrations in CAI of the highly refractory elements Os, Ir, Ru, Rh, Pt and Re are 10 to 20 x chondritic (Fig. 2.11). Pd is considerably lower at ~ 2 x chondritic, reflecting its lower condensation temperature. The estimated group IIIAB iron meteorite parent liquid is approximately chondritic in composition indicating that all of the PGE partition strongly into metallic liquids during core formation on planetesimals preserving chondritic ratios (Fig. 2.11).

The normalized concentrations of each of the PGE (and Re) in spinel lherzolite xenoliths and ophiolitic peridotites are relatively constant at $\sim 10^{-2}$ x chondritic (Fig. 2.11). This suggests that the sub-continental and sub-oceanic upper mantle has approximately the same PGE (and Re) content. Komatiites, which are generally believed to be magmas produced by high degrees of partial melting in the mantle, also have $\sim 10^{-2}$ x chondritic concentrations but

Fig. 2.11 Average concentrations of PGE and Re from Table 2.4 normalized to C1 chondrite concentrations in representative meteoritic and terrestrial materials. The PGE are plotted in order of decreasing melting point. Re is plotted after Pd because it behaves more similarly to Pd than any of the other PGE during terrestrial fractionation. Lines connecting the elements are dashed where data for a particular element are unavailable. Arrows (↓) attached to symbols designate maximum values. Data sources are given in Table 2.4. See text for discussion.

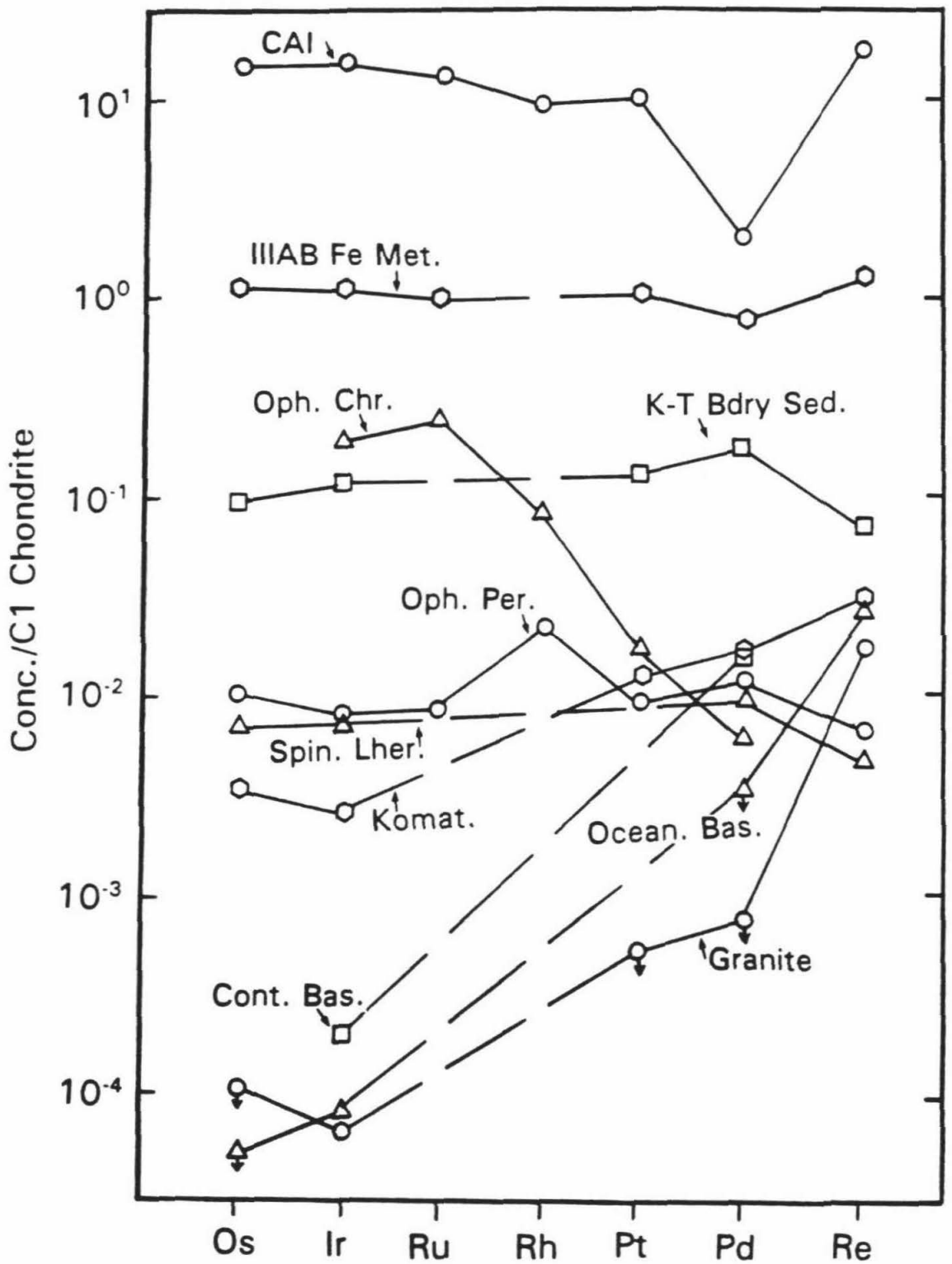
CAI
IIIAB Fe Met.
Oph. Chr.
K-T Bdry Sed.
Oph. Per.
Spin. Lher.
Komat.
Ocean. Bas.
Granite
Cont. Bas.
Conc./C1 Chondrite
10¹
10⁰
10⁻¹
10⁻²
10⁻³
10⁻⁴
Os
Ir
Ru
Rh
Pt
Pd
Re

are slightly depleted in Os and Ir relative to Pd and Re. The depletion of Os and Ir relative to Pd and Re is far more pronounced in magmas formed by lower degrees of mantle partial melting including continental basalts, oceanic basalts and granitic rocks (Fig. 2.11). Chromitites from ophiolitic complexes have a pattern that is complementary to crustal rocks with large enrichments in Ir and Ru relative to Pt and Pd (Fig. 2.11). The patterns suggest that Os, Ir and Ru are compatible in the mantle in chromitites, whereas Rh, Pt, Pd and Re are less compatible and are extracted from the mantle to a much greater extent during crust formation.

Since the initial discovery of high concentrations of Ir in Cretaceous-Tertiary (K-T) boundary sediments and the proposition that the massive terminal Cretaceous extinctions resulted from an asteroidal impact (Alvarez *et al.*, 1980), many workers have investigated the relative concentrations of PGE in K-T boundary sediments. The measured concentrations of Os, Ir, Pt and Re in a basal clay layer 0 to 0.3 cm above the K-T boundary from Caravaca, Spain, are plotted on Fig. 2.11; relative concentrations from other K-T boundary sections are very similar. The flat chondrite normalized pattern is similar to patterns in C1 chondrites, Fe meteorites and mantle peridotites but distinct from the steeply sloped patterns of crustal materials including continental and oceanic basalts. Although this does not resolve the dispute over whether the PGE were derived from asteroids (Alvarez *et al.*, 1980) or the earth's mantle (Officer and Drake, 1985), it does argue against an origin from basaltic volcanics or crustal sediments.

CHAPTER 3. COSMOCHEMISTRY

3.1 REFRACTORY METEORITE INCLUSIONS

The solid bodies that we now observe in the solar system are generally believed to have formed by complex processes that, in many cases, involved material which passed through a high temperature gaseous phase in part of the solar nebula. As the nebula cooled, condensation progressed from the most refractory to the least refractory materials. Lord (1965) first pointed out that with a knowledge of the relative abundances of elements in the solar system and equilibrium thermodynamic data, both the type of condensing phases and the order of condensation could be determined. The calculations of Lord (1965) showed that high-temperature solid condensates would include refractory Ca, Al and Ti compounds. The more comprehensive equilibrium calculations of Grossman (1972) demonstrated that the chemistry and mineralogy expected from high-temperature solid condensates from a gas of solar composition closely resembled the Ca, Al-rich refractory inclusions (CAI) from C3V meteorites. While Grossman (1972) considered CAI and their mineral constituents to be the result of condensation from a vapor, it is now generally agreed that this model is not tenable. However, the major element bulk chemistry of CAI are consistent with the idea of Lord (1965) and Grossman (1972) that they are comprised of early condensate material.

Extensive petrologic, trace element and isotopic studies have since been carried out on CAI from Allende and other carbonaceous chondrites and have provided important clues into the details of how they formed (*cf.* Grossman, 1980; MacPherson *et al.*, 1988). These investigations have demonstrated that many CAI have undergone melting, recrystallization and metamorphic alteration in the nebula or in planetary bodies, but the basic premise that the starting materials for CAI condensed from the early solar nebula has survived detailed

scrutiny. Although the condensate origin for CAI has become a well accepted hypothesis, it must be remembered that the thermodynamic equilibrium between a nebular gas and condensed phases is equivalent for partial condensation and partial evaporation (Kurat *et al.*, 1975; Hashimoto *et al.*, 1979). Therefore, an origin for CAI as volatilization residues of chondritic material is a viable alternative to condensation.

Trace element analyses of CAI have demonstrated that they are enriched relative to cosmic proportions in the elements that are most refractory in a gas of solar composition. Reflecting this trend is a 10 to 20 x enrichment of the PGE in CAI (with the exception of the less refractory PGE Pd) relative to C1 chondrites (Grossman and Ganapathy, 1976; Mason and Taylor, 1982; Fig. 2.11). This is consistent with the high condensation temperatures of all of the PGE (except Pd) in a gas of solar composition (Table 2.3).

An important observation is that although the PGE (except Pd) are uniformly enriched in most CAI, they are highly fractionated into a variety of compositions of μm-sized alloy grains, each containing only a few of the PGE. These PGE alloys most commonly occur in 10-1000 μm multiphase opaque assemblages which also contain Ni-Fe alloys, sulfides and oxides. PGE alloys are also sometimes found as small (0.5-5 μm) grains isolated in the silicate phases of CAI (Wark, 1986; Bischoff and Palme, 1987).

The pattern of PGE fractionation in CAI is demonstrated by the neutron activation data of Bischoff and Palme (1987) for a bulk CAI and individual opaque assemblages separated from the same CAI. The data were normalized to C1 chondrites and are plotted on Fig. 3.1. Two large (20-50 μm) opaque assemblages that were each mechanically separated have highly fractionated PGE patterns with $\sim 10^4$ x chondritic W, Re Os and Ir, but only $\sim 10^3$ x chondritic Mo, Ru and Pt. However, when an aggregate of five "tiny" opaque assemblages along with adhering silicate material were analyzed together, they averaged out to a flat

Fig. 3.1 Chondrite normalized concentrations of refractory elements in one bulk sample, one aggregate of five opaque assemblages and two mechanically separated opaque assemblages from Allende CAI A37 (data from Bischoff and Palme, 1987). See text for discussion.

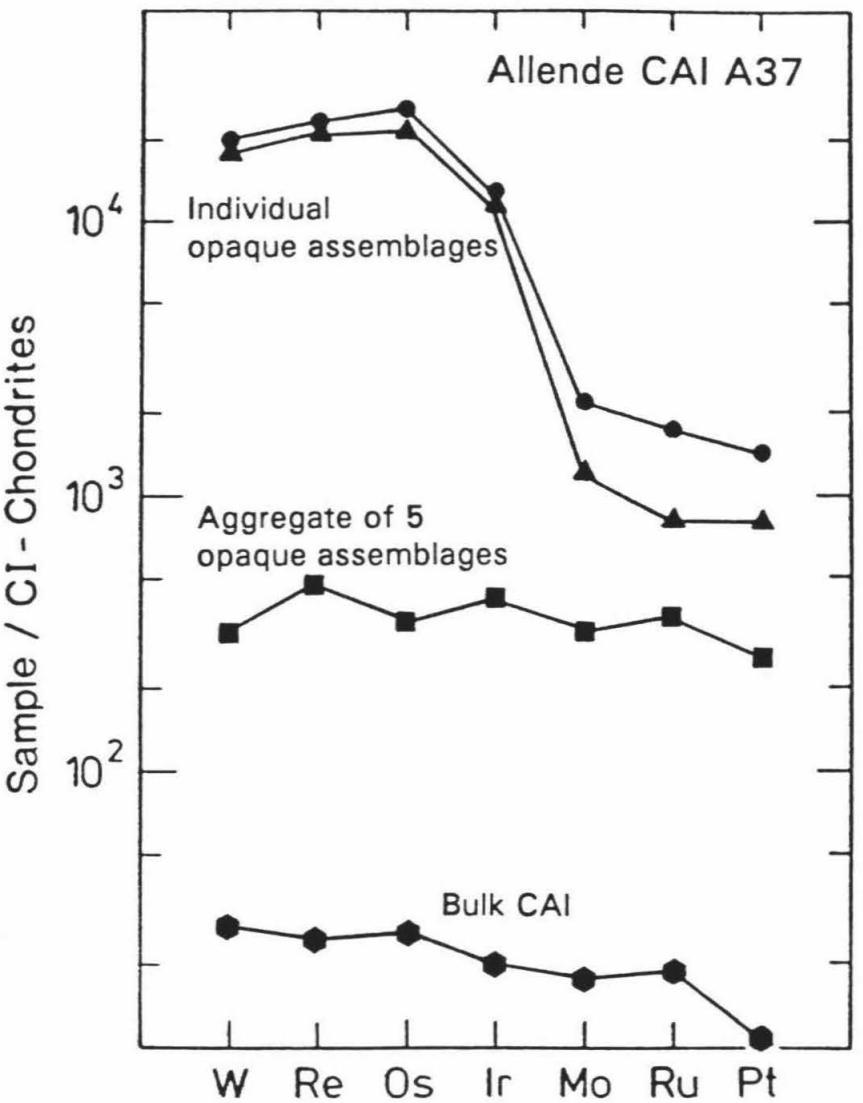
Allende CAI A37
Individual
opaque assemblages
Aggregate of 5
opaque assemblages
Bulk CAI
Sample / CI - Chondrites
10^4
10^3
10^2
W
Re
Os
Ir
Mo
Ru
Pt

chondritic pattern (at somewhat lower concentration due to dilution by silicate). This indicates that some opaque assemblages have abundance patterns that are complimentary to the patterns of the two individual opaque assemblages on Fig. 3.1. Finally, when the bulk CAI was analyzed the contributions from all of the opaque assemblages in it averaged to a relatively "flat" chondrite normalized pattern at the 10 to 20 x chondritic level (Fig. 3.1). Any explanation for the origin of PGE-rich alloys in CAI must explain why such compositionally diverse grains tend to average to a composition for each bulk CAI that is uniformly enriched in PGE relative to chondritic.

Owing in part to the extremely refractory nature of the PGE alloys observed, early workers suggested that the individual metal grains in opaque assemblages were the oldest solid materials in the Solar System and had formed either as condensates in expanding supernova envelopes (outside the Solar System) or as the earliest high-temperature nebular condensates (El Goresy *et al.*, 1978). The opaque assemblages in which PGE alloys are found were also assumed to be exotic and to have formed by condensation of metals, sulfides and oxides from the solar nebula before the crystallization of host CAI (El Goresy *et al.*, 1978; Armstrong *et al.*, 1985, 1987). If this were the case it would require a wide range in temperature, fO_2 and fS_2 in the solar nebula, and that the nebula was turbulent enough to mix together grains formed under highly variable conditions.

It was implied that PGE-rich alloys in opaque assemblages might have an extraordinary isotopic composition, as they would reflect a single pre-solar stellar source. To test this possibility, Hutcheon *et al.* (1987) measured Ru isotope ratios of PGE alloys from opaque assemblages and isolated PGE alloy grains to a precision of $\pm 8^{\circ}/_{\circ\circ}$ using the ion microprobe. Poths *et al.* (1987) measured Ru isotopes in magnetic and nonmagnetic fractions of refractory meteorite inclusions to a precision of $\pm 1^{\circ}/_{\circ\circ}$ by thermal ionization mass spectrometry. In

both studies Ru was found to be isotopically normal within the resolution of each of the analytical techniques, suggesting that PGE alloys are not composed of isotopically exotic material from extra-solar sources, but instead contain the normal solar mixture of isotopic abundances homogenized from various nucleosynthetic sources.

As a result of the exotic history originally proposed for opaque assemblages, they are often referred to in the literature as "Fremdlinge," which is German for strangers or foreigners. The term "Fremdlinge" carries an inappropriate genetic connotation. Instead, I will refer to these multiphase objects by the simple descriptive name "opaque assemblages."

3.2 KINETICS OF GRAIN CONDENSATION

Several workers have considered the question of whether the PGE in CAI could have condensed directly from the solar nebula. For the purpose of this discussion one must differentiate between condensation of the individual metallic phases in opaque assemblages, condensation of each opaque assemblages as a single precursor alloy, and condensation of the bulk PGE content of entire CAI. Palme and Wlotzka (1976) assumed that individual metallic phases in opaque assemblages condensed directly from the nebula and used the kinetic theory of gases to calculate whether μm-sized PGE alloy grains, such as those rich in Os which are often observed in opaque assemblages, could grow by condensation from a nebular gas in a reasonable time period. Based on the number density and mean velocity of Os atoms in the nebula at a total pressure of 10^{-3} atm and at a temperature of 2000K, they derived the following expression for the minimum time needed to grow a cluster of N atoms (τ_N):

$$\tau_N(\text{sec}) = (2.5\text{x}10^{10})\,(n_{O_s})^{-1} \int_{n_i^\circ}^{N} n_i^{-2/3}\, dn_i = (7.5\text{x}10^{10})\,(n_{O_s})^{-1}\,(N)^{1/3}$$

where n_{O_s} is the Os atom density in atoms/cm^3 in the original nebular gas and n_i° is the number of Os atoms in the first Os cluster formed ($n_i^\circ << N$).

From this expression one can calculate that at least 10^3 years are needed to grow a typical 1 μm grain of Os (10^{15} atoms) in the nebula. It would take approximately the same amount of time to condense these 10^{15} Os atoms into a 5 μm alloy grain containing 1% Os. At a total nebular pressure of 10^{-3} atm, n_{O_s} is 10^5 atoms/cm^3 and, therefore, for each 1μm Os grain that condensed a 10^4 m^3 volume of nebular gas would have to be entirely depleted of Os.

One can use the timescale necessary to grow Os grains by condensation to explore whether the metallic phases in opaque assemblages were more likely to have formed in the solar nebula or in a supernova envelope. Estimates for the "cooling time" for various portions of the solar nebula are very uncertain but are generally much shorter than the calculated 10^3 years. For instance, cooling between 1500K and 1700K is believed to have occurred in a time on the order of 1 year (Cameron, 1962; Larimer and Anders, 1967). Supernovae, however, cool at even faster rates and because of their low density are much less appropriate environments for condensation of PGE than the solar nebula. According to the grain growth equation of Palme and Wlotzka (1976) and the supernova density and thermal history suggested by Lattimer *et al.* (1978), an average Os atom will have only 10^{-12} collisions with another Os atom during the entire cooling history of a supernova envelope (Anders, 1987). Abundant elements such as Mg or Al can yield μm-sized condensates in the few months available for condensation (Lattimer *et al.*, 1978), but rare elements such as the PGE cannot.

If the PGE alloys observed in opaque assemblages did form by condensation from the solar nebula, it must have been under conditions highly conducive to nucleation and at low supersaturation, so that atoms could chose their preferred condensation sites and form a variety of PGE-rich phases rather than forming a single alloy (Blander and Katz, 1967). As

pointed out by Anders (1987), it is difficult to imagine how the required high temperatures were sustained in the nebula for so long ($> 10^3$ years), and it is even more difficult to see how the nebular composition could have been regulated to maintain low supersaturation. If the condensate grains contained only 10^6 Os atoms, the equation above indicates that condensation could take place on a ~ 1 year timescale. In this case, the observed 1 μm PGE-rich alloy grains would have had to form out of billions of tiny particles by some secondary collection process. Therefore, it would be the bulk PGE content of CAI that reflects the nebular condensation process rather than the individual metallic phases or bulk opaque assemblages that are presently observed in CAI.

3.3 COMPOSITION OF CONDENSATE ALLOYS

Palme and Wlotzka (1976) calculated the composition of a single homogeneous equilibrium condensate alloy as a function of temperature at a total nebular pressure of 10^{-3} atm. The result of this calculation is shown graphically on Figs. 3.2 and 3.3 (modified from Palme and Wlotzka, 1976). The fractions of each element condensed as a function of temperature are plotted on Fig. 3.2 for condensation of 13 siderophile metals into an alloy containing all 13 metals, assuming ideal solid solution. The temperatures at which 50% of each metal is condensed (see Table 2.3) decreases in the order:

$$W \Rightarrow Re \Rightarrow Os \Rightarrow Ir \Rightarrow Mo \Rightarrow Ru \Rightarrow Pt \Rightarrow Rh \Rightarrow Co \Rightarrow Ni \Rightarrow Fe \Rightarrow Pd \Rightarrow Cr.$$

The total condensate composition is shown as a function of temperature in Fig. 3.3. The initial equilibrium condensate is an alloy of mostly Os, W and Re. As the temperature decreases, significant fractions of the other metals condense in the condensation order given above. Once a solid alloy has condensed, each metal will dissolve in the grain at a composition level that balances the partial pressure of each element in the nebular gas. Since

Fig. 3.2 Calculated condensation curves for Mo, Ir, Ru, Rh, Pt, Ni, Fe, and Au condensing from a solar gas with total pressure of 10^{-3} atm into an alloy of 13 metals (Os, Re, W, Mo, Ir, Ru, Rh, Pt, Ni, Fe, Co, Pd and Au). Ideal solid solution was assumed for all metals. Modified from Palme and Wlotzka (1976). See text for discussion.

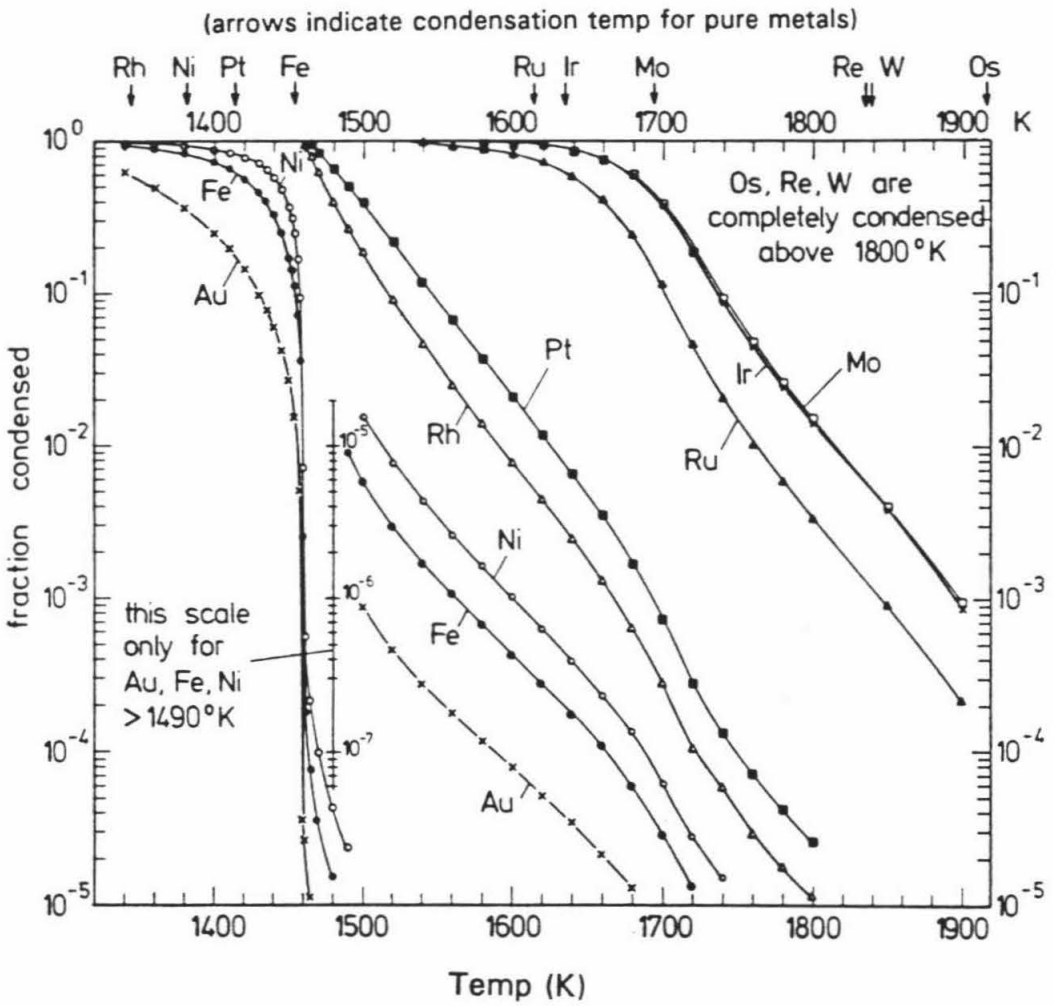
(arrows indicate condensation temp for pure metals)
Rh Ni Pt Fe Ru Ir Mo Re W Os
1400 1500 1600 1700 1800 1900 K
Os, Re, W are completely condensed above 1800 °K
Au
Fe
Ni
Pt
Rh
Ir
Mo
Ru
this scale only for Au, Fe, Ni > 1490 °K
fraction condensed
Temp (K)

Fig. 3.3 The condensation curves from Fig. 3.2 renormalized to weight fractions. The composition of an alloy in equilibrium with a solar gas at a given temperature can be read from this diagram. Modified from Palme and Wlotzka (1976). See text for discussion.

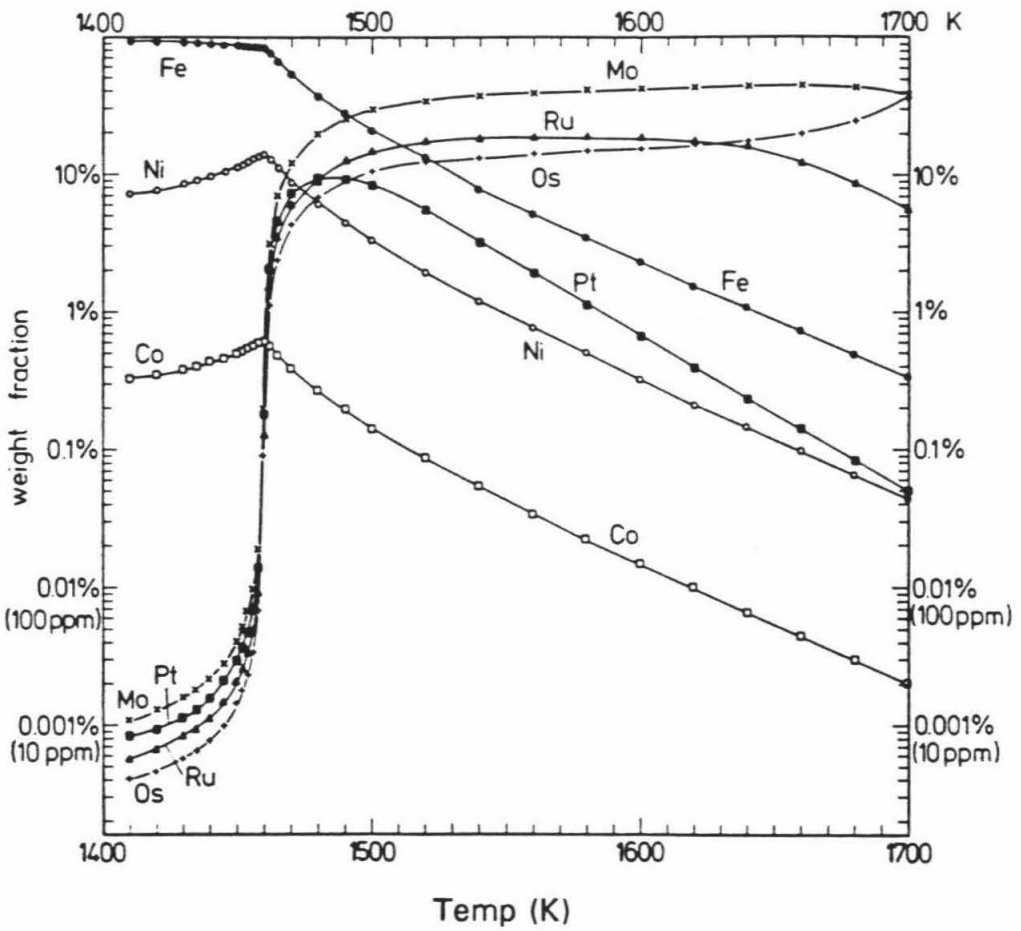
1400
1500
1600
1700 K
Fe
Mo
Ru
Ni
Os
10%
1%
Pt
Fe
Co
Ni
0.1%
weight fraction
0.01%
(100ppm)
Co
Pt
Mo
0.001%
(10 ppm)
Ru
Os
1400
1500
1600
1700
Temp (K)

Fe and Ni are highly abundant elements, they have high partial pressures in the nebula. Therefore, even a small fraction condensed leads to substantial concentrations of Fe and Ni in even the highest temperature condensates. As the temperature decreases, the concentration of Fe and Ni in the refractory alloys increases until the alloys are nearly 100% Fe+Ni, at a temperature just above the condensation temperature of pure Fe. Thus, the amount of Fe+Ni relative to PGE in a condensate alloy indicates the temperature at which it ceased to be in equilibrium with the solar nebula. As can be seen on Fig. 3.2, at all temperatures below 1466K W, Re, Mo and all of the PGE (except Pd) are fully condensed and would be found in a condensate alloy in cosmic relative abundances. Since Pd condenses at a lower temperature than Fe and Ni it will be depleted relative to cosmic abundances in all high temperature condensates. At temperatures above $\sim$1500K depletions of Rh and Pt relative to their cosmic abundances would be observed, and at temperatures above $\sim$1600K depletions of Ru would also be observed.

The average abundances of all of the PGE in bulk CAI are plotted on Fig. 2.11 normalized to C1 chondrites and show that Pd is depleted by a factor of $\sim$10 relative to the other PGE and Rh and Pt are depleted by a factor of $\sim$2. The depletion of Pt by a factor of $\sim$2 is also illustrated on the bulk CAI pattern from Fig. 3.1. Thus, the relative abundances of PGE in bulk CAI are consistent with alloy condensation at a temperature $\geq$1500K but $\leq$1600K. However, to explain the highly variable refractory siderophile patterns in individual opaque assemblages by condensation is far more difficult. Fegley and Palme (1985) attempted to do this by calculating the abundance patterns of condensate alloys at fO_2's more oxidizing than an equilibrium solar gas. Fig. 3.4 shows the relative abundances of W, Re, Os, Ir, Mo, Ru and Pt in a condensate alloy at 1600K for increasing values of H_2O/H_2 (which corresponds to increasing fO_2). The pattern on the far left is for a solar gas and shows depletions in Pt and

Fig. 3.4 The calculated ratios of W, Re, Ir, Mo, Ru, and Pt to Os in a condensate alloy in equilibrium with a solar gas at 1600K (from Fegley and Palme, 1985). The assumptions made in this calculation are the same as in Figs 3.2 and 3.3 except that the calculation is repeated at increasingly higher values of fO_2. See text for discussion.

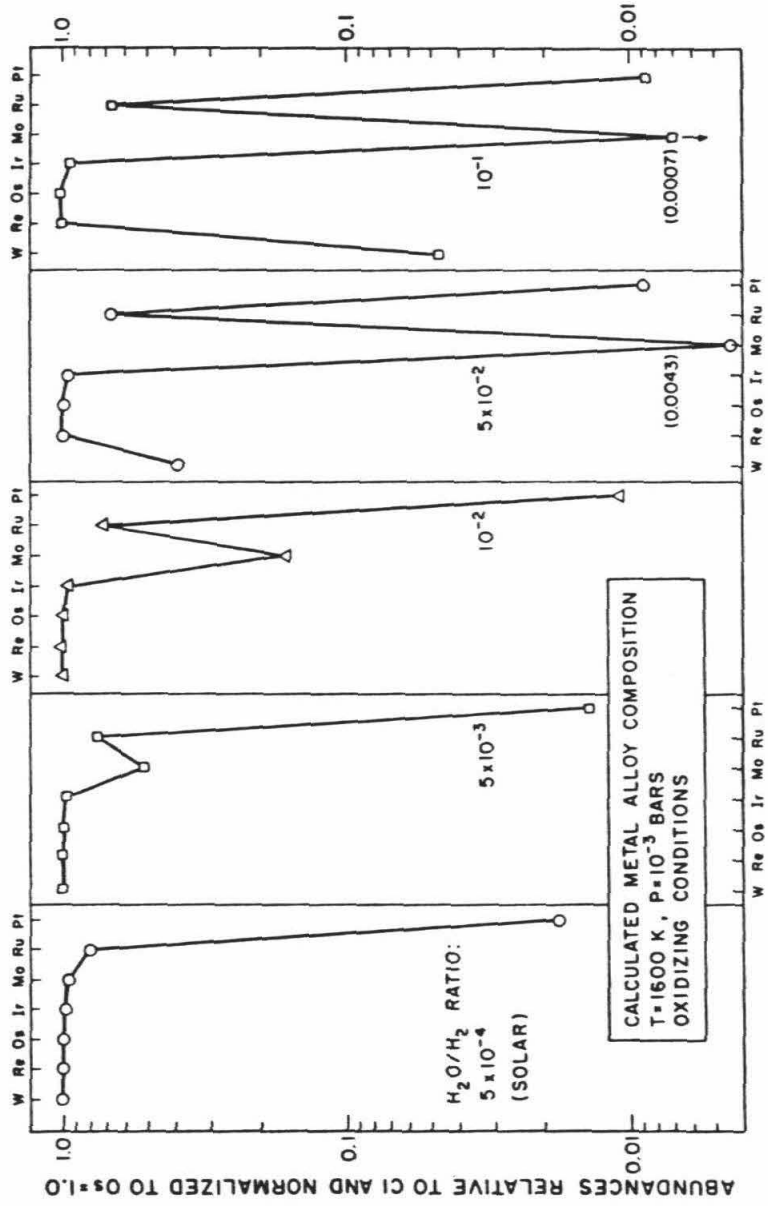
ABUNDANCES RELATIVE TO CI AND NORMALIZED TO Os=1.0
1.0
0.1
0.01
W Re Os Ir Mo Ru Pt
H_2O/H_2 RATIO:
5×10^{-4}
(SOLAR)
5×10^{-3}
10^{-2}
5×10^{-2}
10^{-1}
(0.0043)
(0.0007)
CALCULATED METAL ALLOY COMPOSITION
T=1600 K, P=10^{-3} BARS
OXIDIZING CONDITIONS
Increasing fO_2 →

Ru at 1600K similar to those calculated by Palme and Wlotzka (1976; Fig. 3.3). With increasing H_2O/H_2 (and fO_2) depletions in Mo and W develop as a result of the greater stability of Mo and W oxides relative to the PGE oxides (Fig. 3.4). Fegley and Palme (1985) matched the compositions of calculated condensate alloys to the compositions of some opaque assemblages that display depletions in W and Mo relative to cosmic values. This was done by allowing both the temperature of removal of the alloy from the nebular gas and the H_2O/H_2 ratio of the nebular gas to vary during condensation. They argued that the non-solar refractory siderophile patterns that are sometimes observed for opaque assemblages were the result of condensation at fO_2's 10^3 to 10^4 times more oxidizing than an equilibrium solar gas. For example, to match the refractory siderophile element composition of the LEO-1 opaque assemblage reported by Palme *et al.* (1982), Fegley and Palme required condensation to cease at 1620K and for the nebular gas H_2O/H_2 ratio to be considerably higher than solar value of $2x10^{-2}$ (Fig. 3.5). The depletions of the less refractory elements Ru and Pt are roughly matched in Fig. 3.5 by ending condensation at a temperature high enough that they have not fully condensed. The depletions in W and Mo are roughly matched in Fig. 3.5 by condensation under oxidizing conditions which results in W and Mo remaining in the vapor phase as volatile oxides.

Although the model of Fegley and Palme (1985) successfully reproduces refractory siderophile abundance patterns of individual opaque assemblages, there are alternate explanations for these non-solar patterns which include 1) redistribution of W and Mo as gaseous hydroxides during low-temperature alteration (*e.g.*, Beckett *et al.*, 1988) and 2) redistribution of W, Mo, Ru and Pt (which form sulfides at lower fS_2's than Re, Os or Ir) by low-temperature sulfidation of alloys during planetary metamorphism (App. III). Each of the alternate explanations could result in W, Mo, Ru and Pt redistribution from individual opaque

Fig. 3.5 Measured and calculated relative refractory siderophile element abundances in an opaque assemblage from the Leoville meteorite (LEO-1) (from Fegley and Palme, 1985). Solid lines connect the neutron activation analyses of the opaque assemblage from Palme *et al.* (1982). Dashed lines connect points calculated for an alloy condensed from the nebula under non-solar oxidizing conditions at 1620K. See text for discussion.

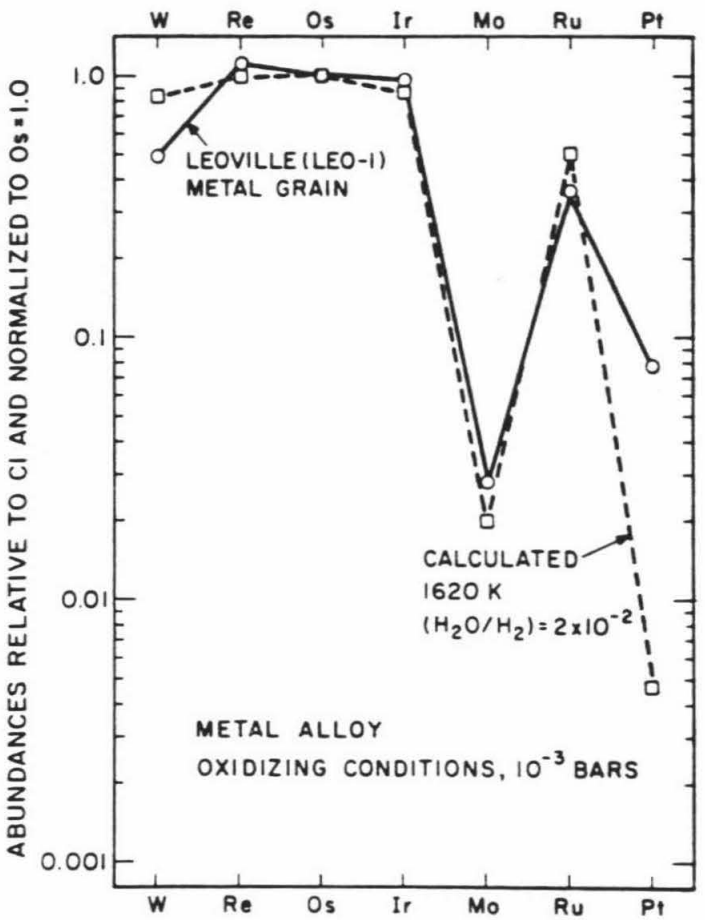
W
Re
Os
Ir
Mo
Ru
Pt
1.0
0.1
0.01
0.001
ABUNDANCES RELATIVE TO CI AND NORMALIZED TO Os=1.0
LEOVILLE (LEO-1)
METAL GRAIN
CALCULATED
1620 K
(H2O/H2)=2x10-2
METAL ALLOY
OXIDIZING CONDITIONS, 10-3 BARS

assemblages to other portions of a CAI. This provides an explanation for the highly fractionated non-chondritic refractory siderophile compositions of individual opaque assemblages while maintaining compositions of bulk CAI that are uniformly enriched relative to chondritic values.

Serious difficulties arise when one looks beyond the relative refractory siderophile abundances of individual opaque assemblages and attempts to explain the bulk composition of opaque assemblages or the metallic phases within them by alloy condensation. Palme and Wlotzka (1976) pointed out that for a condensate alloy to contain several tens of percent Fe and several percent Pt (as is observed in most opaque assemblages) the temperature interval for the removal of the opaque assemblage alloys from the nebula would have to fall in the very narrow temperature interval of 1462 to 1466K, at the point on Fig. 3.3 where the refractory siderophile contents begin to fall dramatically with temperature.

In App. III, the composition of opaque assemblages and the metallic phases within them are compared with the range of alloy compositions that could theoretically be produced by nebular condensation. Wark (1986) gives the compositions of refractory siderophile-rich alloys that occur as isolated grains in CAI unassociated with opaque assemblages. Whereas the relative proportions of the refractory siderophile elements can be reproduced by condensation calculations (Palme and Wlotzka, 1976; Fegley and Palme, 1985) the ratio of Ni:Fe and the ratio of (Ni+Fe):(refractory siderophiles) cannot be produced by direct condensation.

The Ni/(Ni+Fe) ratio can only reach a maximum of 0.20 in alloy condensates, and only at the highest condensation temperatures (Palme and Wlotzka, 1976; Kelly and Larimer, 1978; Grossman *et al.*, 1979). This maximum Ni/(Ni+Fe) ratio of 0.20 is lower than 1) the bulk Ni/(Ni+Fe) ratio of $\sim$0.40 most commonly observed for bulk opaque assemblages, 2) the

Ni/(Ni+Fe) ratio of 0.67 most commonly observed in alloys from opaque assemblages, and 3) the Ni/(Ni+Fe) ratio of most of the isolated alloy grains which ranges from 0.10 to 0.67 (Wark, 1986). With decreasing temperature, the Ni/(Ni+Fe) ratio is expected to decrease from 0.20 to the cosmic value of 0.06 at temperatures below the condensation temperature of pure Fe.

The concentration of each refractory siderophile element in a condensing alloy is expected to drop rapidly from the 1 to 10% level at high temperatures to the 10 ppm level below the condensation temperature of Fe (Fig. 3.3). Therefore, even the unusually Fe-rich alloys from opaque assemblages in the Leoville meteorite (described in App. III), which have nearly cosmic Ni/(Ni+Fe), could not have formed by condensation. The low condensation temperature necessary to produce the cosmic Ni/(Ni+Fe) refractory siderophile contents would result in an alloy with only ~10 ppm of each PGE, much lower than the 1 to 5% levels observed. It appears that the only way the composition of metal from the Leoville opaque assemblages could have formed by condensation is if it represents a mixture of alloys formed during two intervals of condensation; i.e., a mixture of a high-temperature condensate (high refractory siderophiles) and a lower-temperature condensate (low Ni/(Ni+Fe)).

3.4 CONDENSATE ALLOYS DURING METEORITE PETROGENESIS

Sharp phase boundaries are found between metallic Ni-Fe phases and PGE-Fe phases in opaque assemblages in CAI. Following a report of such contacts between Pt-rich metal and Ni-rich metal by El Goresy *et al.* (1978), Arrhenius and Raub (1978) calculated the constraints that these contacts placed on the cooling history of CAI. Arrhenius and Raub assumed that these metals were early nebular condensates and that they had been aggregated before the melting of refractory inclusions, as suggested by El Goresy *et al.* (1978). Using

the diffusion coefficient for Pt in Ni, Arrhenius and Raub (1978) calculated that the sharp phase boundaries could not have existed at CAI liquidus or condensation temperatures (1600-1700K) for more than a fraction of a second, and could not have existed at 900K for more than one day without developing measurable diffusion gradients due to the dissolution of Pt in the γNi-Fe phase. They concluded that CAI must have melted and recrystallized during extremely short thermal pulses.

Recent studies of opaque assemblages in CAI (Armstrong *et al.*, 1985, 1987) have not confirmed the original report (El Goresy *et al.*, 1978) of Pt-rich metallic phases in contact with Ni-Fe-rich metallic phases (as a rule, Pt-rich metallic phases are surrounded by sulfide); however, the approach taken by Arrhenius and Raub (1978) is still useful and can be used to interpret the commonly observed boundaries between εRu-Fe and γNi-Fe in opaque assemblages. Using diffusion coefficients for Ru in Ni as a function of temperature from App. I as a simplified analog for the diffusion of Ru in Ni-Fe in opaque assemblages, I have calculated isothermal survival times for sharp boundaries between εRu-Fe grains and surrounding γNi-Fe. Details of the calculations are given in App. III. The main conclusion is that once εRu-Fe and γNi-Fe are juxtaposed, the sharp metallic phase boundaries observed between these phase can only be maintained for <4 seconds at 1673K, <28 seconds at 1473K or <2 weeks at 873K. This result is similar to that of Arrhenius and Raub (1978) and suggests that if εRu-Fe and γNi-Fe formed separately by condensation and were later juxtaposed, the host CAI must have melted and cooled during extremely short thermal pulses.

It has been inferred based on experimental studies that during the melting and crystallization of the silicate minerals in CAI that host opaque assemblages, a maximum temperature between 1700 and 1550K was reached (Stolper, 1982), and crystallization occurred during slow cooling at a rate of 0.5-20Khr^{-1} (Stolper and Paque, 1986). For even

the lowest maximum temperature and fastest cooling rate considered plausible, nearly complete homogenization of ϵRu-Fe and γNi-Fe would have occurred. Therefore, if ϵRu-Fe and γNi-Fe alloys in opaque assemblages had formed by nebular condensation, the sharp contacts between them would not have survived melting and crystallization of the host CAI.

In summary, each of the arguments that have been discussed in this chapter to test the proposed nebular (or supernova) condensation origin for PGE-rich alloys in CAI have argued to the negative. The kinetics of PGE grain condensation require unreasonably long durations of time at high temperatures, the compositions of calculated alloy condensates do not correspond to observed compositions of opaque assemblages or the metallic phases within them, and sharp boundaries observed between ϵRu-Fe and γNi-Fe phases could not have survived the cooling history of the host CAI minerals. In the following chapter an alternative scenario for the origin of PGE-rich metallic phases in opaque assemblages from CAI will be proposed.

3.5 RE-OS COSMOCHRONOMETER

Before concluding this chapter on the cosmochemistry of PGE, a short review of the use of the ^{187}Re-^{187}Os isotopic pair for the determination of the age of r-process (rapid neutron capture) nuclei is appropriate. This isotopic pair is useful in cosmochemistry because the 42 Æ halflife of ^{187}Re is considerably longer than the age of the solar system but only several times longer than the estimated age of the galaxy. ^{187}Re is produced during nucleosynthesis by the r-process, whereas ^{187}Os and ^{186}Os are produced by the s-process (slow neutron capture). Therefore, the ^{187}Re-^{187}Os pair is free from the uncertainties of the r-process production rates, which must be estimated for most other isotopic pairs. It is a relatively straightforward problem to calculate the time between the formation of the Galaxy and the

formation of the Solar System for the limiting cases of sudden and steady-state nucleosynthesis if one knows 1) the ratio of ^{187}Os to ^{186}Os produced during nucleosynthesis, 2) the decay rate of ^{187}Re, and 3) the Re/Os and $^{187}Os/^{186}Os$ ratios at the time of formation of the Solar System (Clayton, 1964). Luck and Allegre (1983) most recently determined parameters 2 and 3 above from isotopic measurements of meteorites, and estimated parameter 1 from the neutron capture cross-sections of ^{187}Os and ^{186}Os as a function of temperature after including the contributions from a ~ 9.8 keV excited state of ^{187}Os. Based on these data Luck and Allegre calculated the extreme limits on the age of the Galaxy as 10.6 and 16.8 Æ for sudden and steady-state nucleosynthesis, respectively. Yokai *et al.* (1983) pointed out that there are additional uncertainties in this calculation because at the extreme temperatures of a stellar environment 1) the β^- decay rate of ^{187}Re may be substantially greater than in the laboratory, 2) ^{187}Re may be produced from ^{187}Os by electron capture, and 3) there may be previously unrecognized s-process branchings in the W-Os region. Nevertheless, a treatment of these additional factors by Yokai *et al.* (1983) results in an age for the Galaxy of 11 to 15 Æ, in agreement with previous results but with somewhat greater uncertainty.

CHAPTER 4. GEOCHEMISTRY OF PT-GROUP ELEMENTS IN CAI

Pt-group elements in Ca, Al-rich refractory inclusions (CAI) are highly concentrated into metallic phases which occur along with sulfides and oxides in multiphase opaque assemblages. The opaque assemblages occur as inclusions in the major silicate minerals including melilite, fassaite and anorthite. Based on the extremely high melting and condensation temperatures of the PGE, many workers have assumed that PGE-rich metals found in CAI are primordial in origin and formed by high temperature condensation in supernovae or in the solar nebular (*e.g.*, El Goresy *et al.*, 1978; Blander *et al.*, 1980; Armstrong *et al.*, 1985). However, as discussed in the previous chapter, direct condensation from a supernova or the solar nebular does not appear to be a likely explanation for the origin of these PGE-rich metallic phases.

Since little was known previously about subsolidus phase equilibria or diffusion kinetics in PGE-rich metallic systems it was difficult to assess the plausibility of forming PGE-rich metallic phases by processes other than condensation. To test whether PGE-rich metallic phases observed in CAI could have formed by subsolidus reactions I have 1) conducted diffusion and phase equilibria studies in Ni-Fe-PGE systems, and 2) performed detailed analytical studies of PGE-rich phases in CAI for comparison with the experimental results. The experimental methods and results are presented in App. I, and the analytical data for PGE-rich phases in opaque assemblages are presented in App. III. In this chapter, I will first describe the opaque assemblages from CAI that were studied in App. III and provide reproductions of scanning electron micrographs that are of higher quality than was possible in published articles. The reader should note that I will not reiterate the contents of App. I, II and III but will instead summarize the predicted geochemical behavior of PGE during the multistage evolution of CAI based on the model for the origin of opaque assemblages developed in App. II and III. The constraints that this model places on the conditions under

which CAI were melted and subsequently equilibrated will be reviewed, and previous models will be compared with the model presented here.

4.1 DESCRIPTION OF OPAQUE ASSEMBLAGES

Opaque assemblages in CAI are generally spheroidal, 10-1000 μm in diameter and consist primarily of γNi-Fe, magnetite (Fe_3O_4), pentlandite [$(Fe,Ni)_9S_8$], pyrrhotite ($Fe_{1-x}S$) and apatite [$Ca_5(PO_4)_3$ (F,OH,Cl)]. They also contain minor amounts of phases rich in refractory siderophile elements which include Pt-group element-rich metallic phases (most commonly ϵRu-Fe), molybdenite (MoS_2) and scheelite-powellite solid solution [$Ca(W,Mo)O_4$]. Five opaque assemblages from Type B CAI in C3V chondrites were chosen for detailed study. Type B inclusions contain melilite, fassaite, anorthite and spinel as the major mineral phases (*e.g.*, Grossman, 1980). They are from Allende samples JIM (Brandstätter and Kurat, 1983), USNM 5241 ("WILLY" and "F3"; Armstrong *et al.*, 1985) and EGG3 (Meeker *et al.*, 1983), and from Leoville sample UNM 575 (Kracher *et al.*, 1985).

The individual opaque assemblages will be referred to as "JIM-OA1," "WILLY," "F3," "EGG3-OA1" and "LEO575-OA1" respectively. The Allende meteorite belongs to the "oxidized subgroup" of C3V meteorites, which generally contains Ni-rich γNi-Fe alloys, whereas the Leoville meteorite belongs to the "reduced subgroup," which generally contains Fe-rich γ and α Ni-Fe alloys (McSween, 1977). The α, ϵ and γ designations for the metallic solid solution fields in the Ni-Fe-Ru-rich system are based on compositional data rather than direct determination of crystal structure.

JIM-OA1 has a cross-sectional diameter of $\sim$30 μm and consists of the phases γNi-Fe, pyrrhotite, ϵRu-Fe, apatite, molybdenite and magnetite in order of decreasing abundance. The ϵRu-Fe phase occurs within γNi-Fe, pyrrhotite and magnetite, but not within apatite or

molybdenite (Fig. 4.1). Typically, ϵRu-Fe grains within γNi-Fe range in size from 0.3 to 1.0 μm, whereas those within pyrrhotite range from 0.1 to 0.3 μm. One unusually large (3×5 μm) ϵRu-Fe grain occurs in JIM-OA1 adjacent to γNi-Fe, pyrrhotite and magnetite (Fig. 4.1).

Willy has a cross-sectional diameter of ~150 μm and consists of the phases magnetite, γNi-Fe, pyrrhotite, scheelite, apatite, ϵRu-Fe and molybdenite in order of decreasing abundance (Armstrong *et al.*, 1985). Magnetite and γNi-Fe are the two main phases and each account for $\sim45\%$ of the cross-sectional area. ϵRu-Fe grains are typically ~1 μm in diameter and occur surrounded by γNi-Fe and magnetite. A portion of Willy which shows the magnetite outer rim and intergrown magnetite, γNi-Fe, pyrrhotite and ϵRu-Fe is shown in Fig. 4.2.

F3 has a cross-sectional diameter of ~30 μm and consists of the phases magnetite, γNi-Fe, apatite and ϵRu-Fe in order of decreasing abundance (Fig. 4.3). ϵRu-Fe grains are typically ~1 μm in diameter and occur in contact with both γNi-Fe and magnetite.

EGG3-OA1 has an irregular shape and is 5×15 μm in cross-section (Fig. 4.4). The Ni-rich mineralogy of EGG3-OA1 is typical of opaque assemblages in the CAI EGG3 and consists of very Ni-rich γNi-Fe, heazlewoodite (Ni_3S_2), apatite, molybdenite and ϵRu-Fe.

LEO575-OA1 has a cross-sectional diameter of about 15 μm and has a Fe-rich mineralogy typical of opaque assemblages from the Leoville meteorite. It consists of the phases V-rich magnetite, αFe (kamacite), ϵRu-Fe and γNi-Fe (taenite) (Fig. 4.5). The ϵRu-Fe and γNi-Fe phases occur as ~1 μm wide lamellae in the αFe phase and V-rich magnetite occurs as a partial rim around all of the metallic phases.

Fig. 4.1 Scanning electron microscope backscattered electron image of JIM-OA1. ru = ϵRu-Fe, ni = γNi-Fe, po = pyrrhotite, mo = molybdenite, ap = apatite and mt = magnetite. Scale bar is 10 μm.

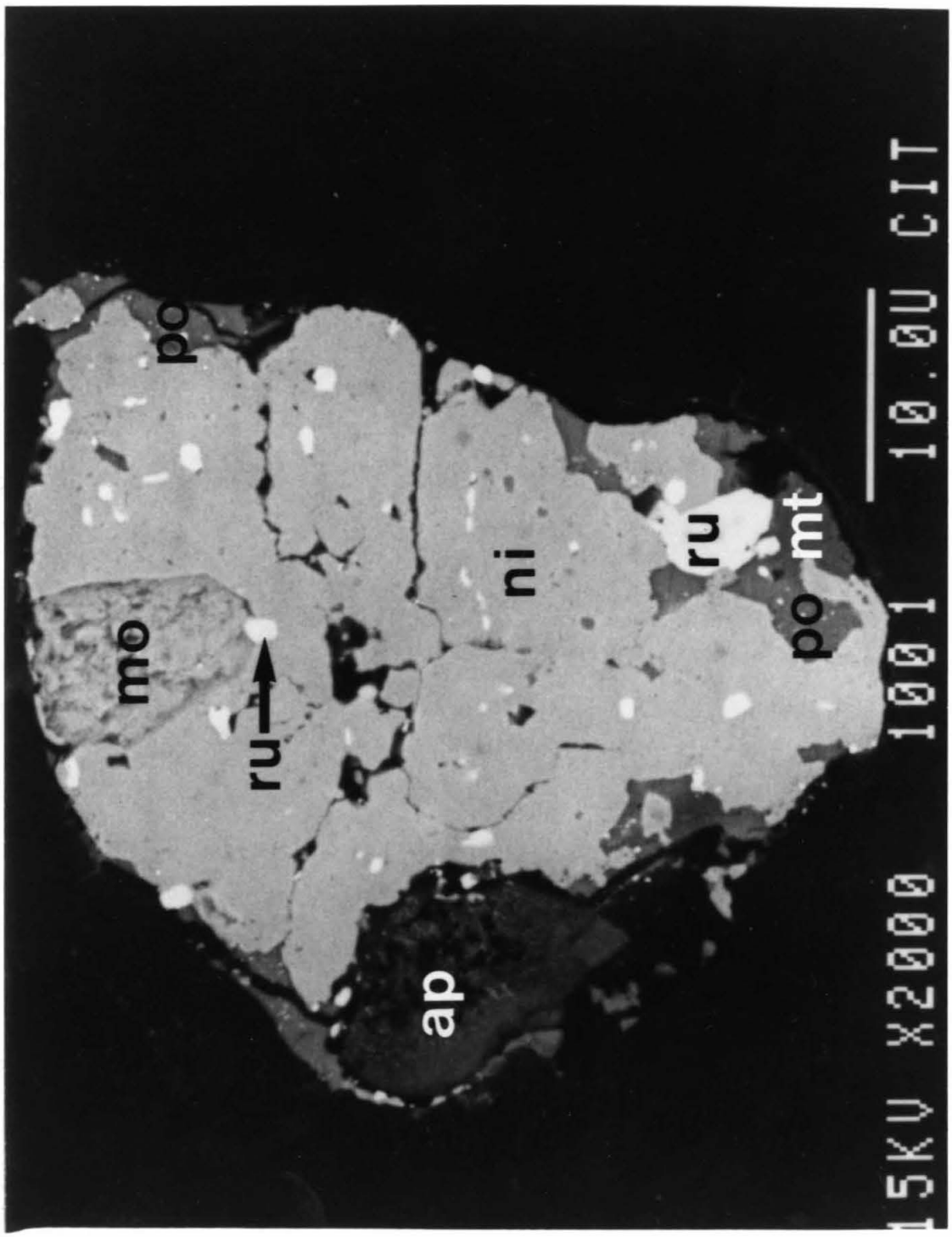
po
mo
ru
ni
ru
po mt
ap
15KV X2000 1001 10.0U CIT

Fig. 4.2 Scanning electron microscope backscattered electron image of Willy. ru = ϵRu-Fe, ni = γNi-Fe, po = pyrrhotite and mt = magnetite. Scale bar is 10 μm.

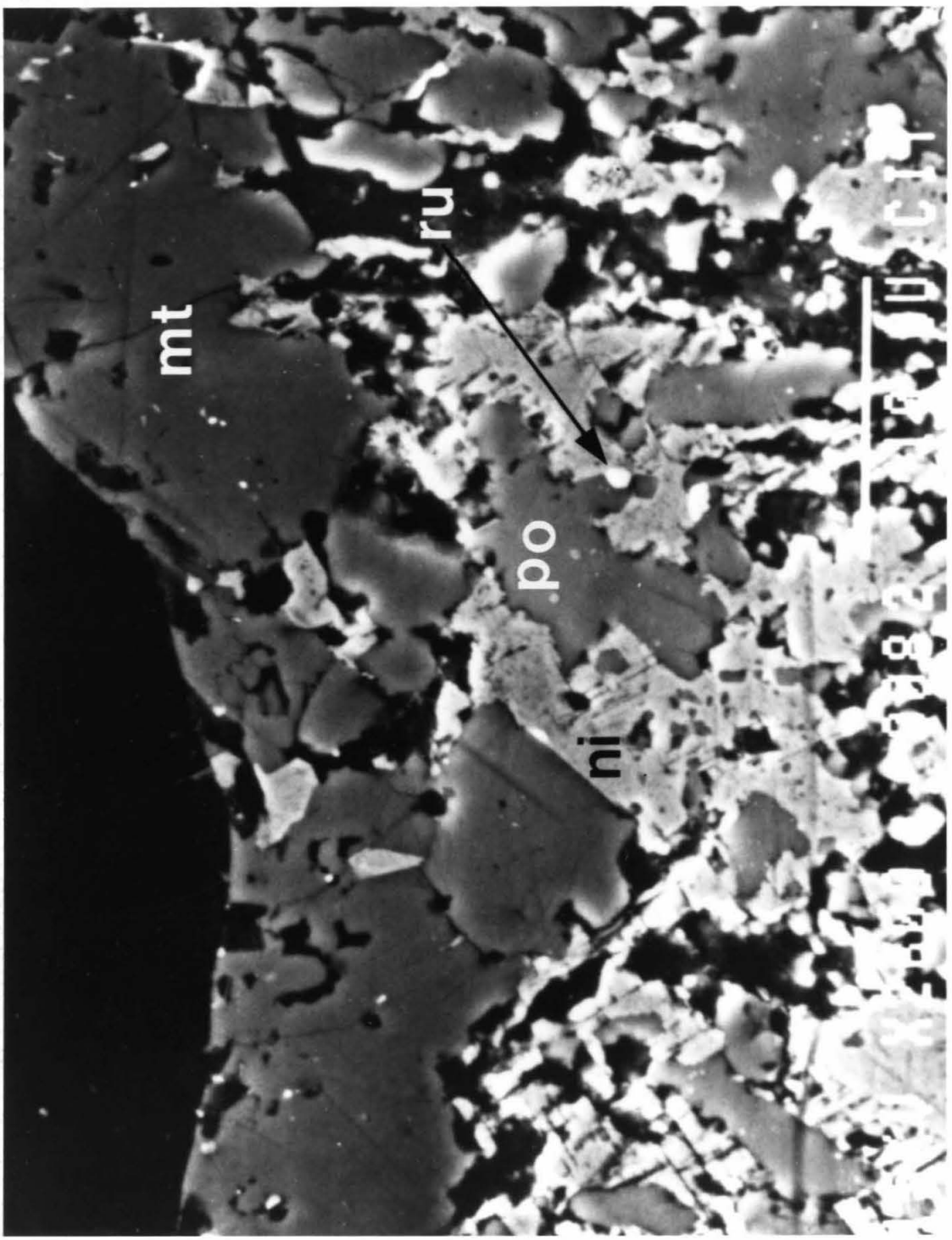
mt
ru
po
ni

Fig. 4.3 Scanning electron microscope backscattered electron image of F3. ru = ϵRu-Fe, ni = γNi-Fe, ap = apatite and mt = magnetite. Scale bar is 10 μm.

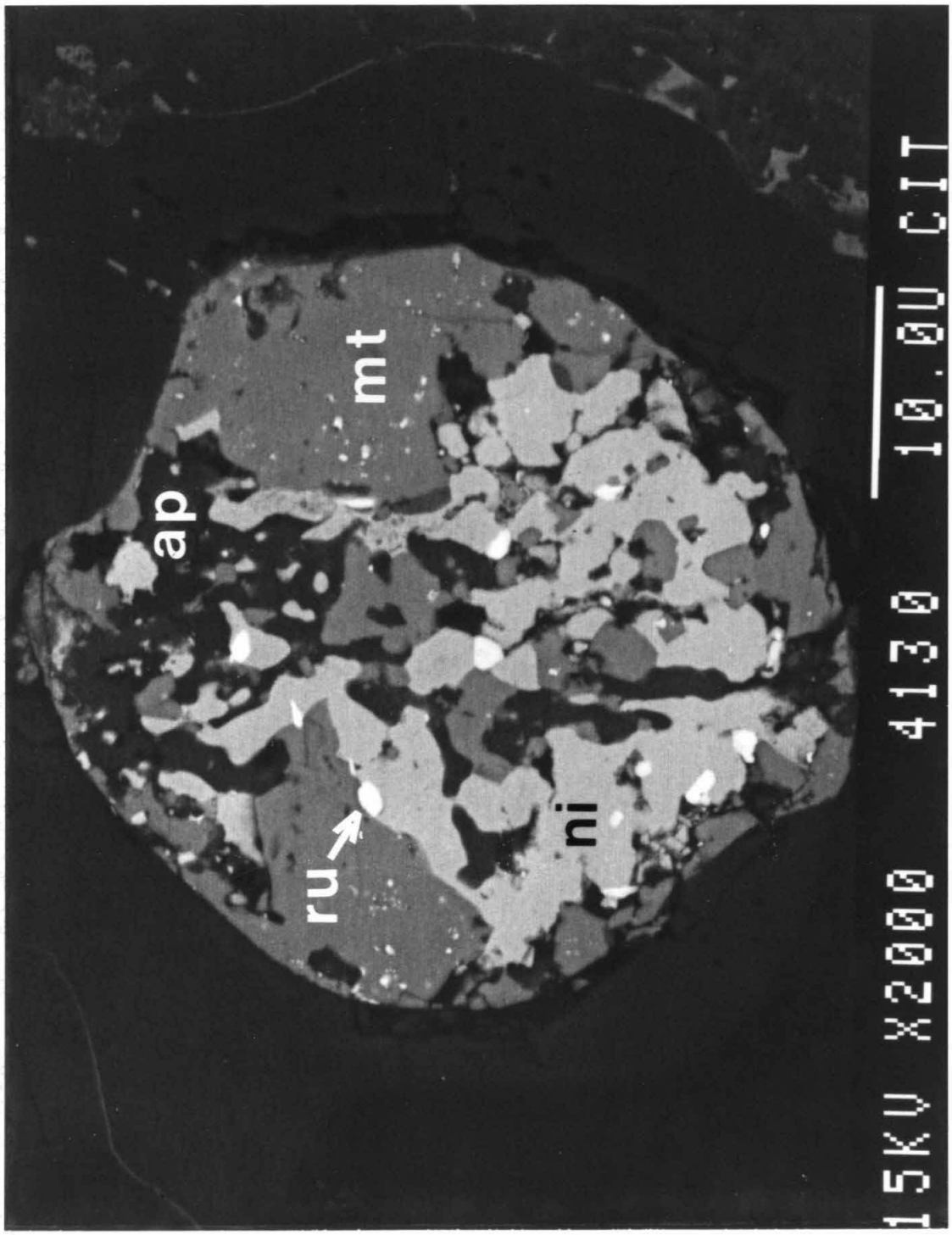
ap
mt
ru
ni
15KV X2000 4130 10.0U CIT

Fig. 4.4 Scanning electron microscope backscattered electron image of EGG3-OA1. ru = ϵRu-Fe, ni = γNi-Fe, hz = heazlewoodite, mo = molybdenite, ap = apatite and mt = magnetite. Scale bar is 1 μm.

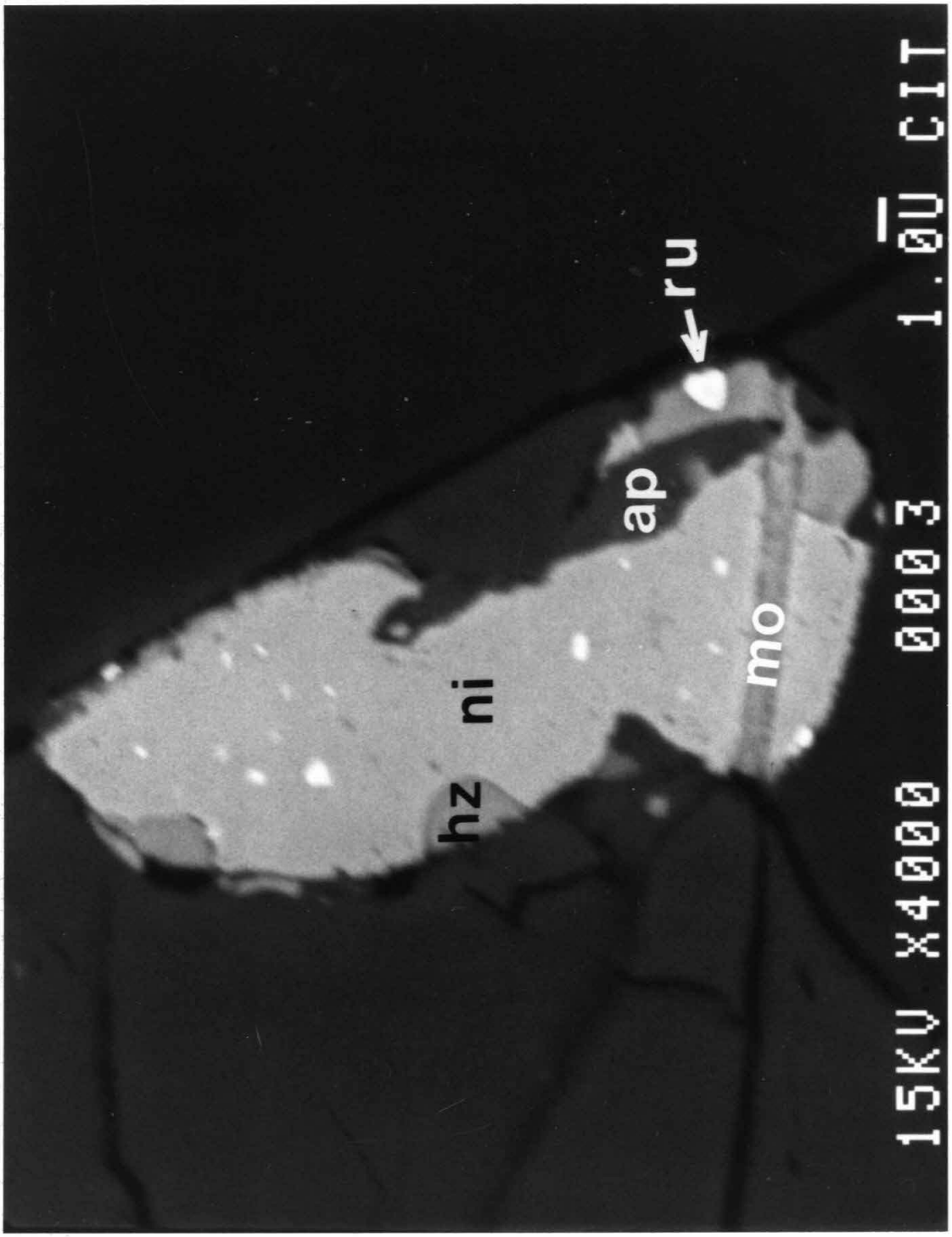
hz
ni
ap
ru
mo
15KV X4000 0003 1.0U CIT

Fig. 4.5 Scanning electron microscope backscattered electron image of LEO-OA1. ru = ϵRu-Fe, ni = γNi-Fe, fe = αFe (kamacite) and mt = magnetite. Scale bar is 1 μm.

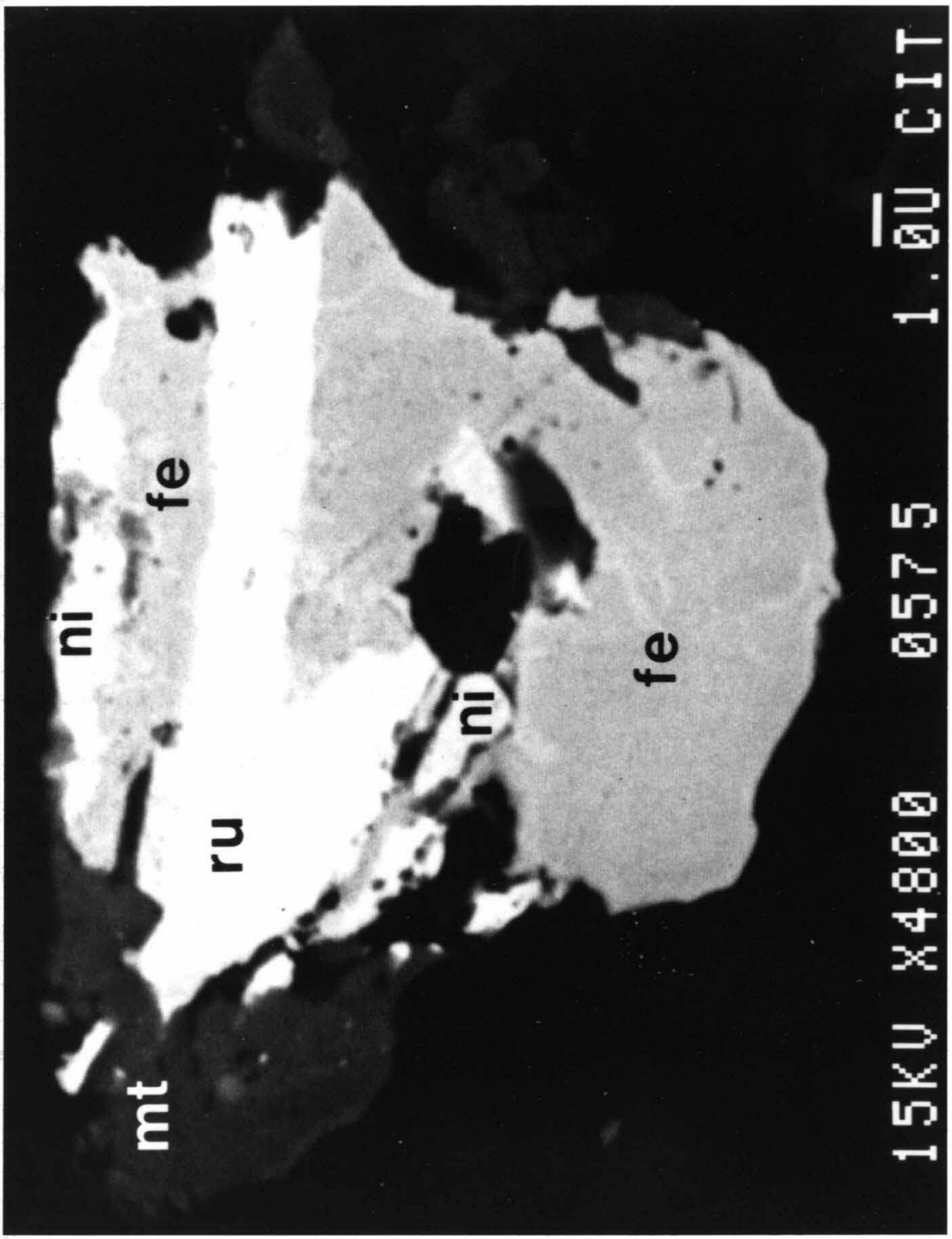
mt
ni
fe
ru
ni
fe
15KV X4800 0575 1.0U CIT

4.2 CONDENSATION AND MELTING IN THE NEBULA

Condensation calculations presented by Palme and Wlotzka (1976) and discussed in the previous chapter indicate that in a nebular environment the PGE would most likely condense along with Fe and Ni as alloys. Unless the alloys were removed from the nebular gas at a temperature above 1466K, the composition of the alloy would be predominantly $Fe_{94}Ni_6$ with the PGE homogeneously dissolved at ppm concentration levels. These alloys would contain approximately chondritic proportions of all of the PGE (except Pd) and would condense in the same temperature interval as the refractory silicate and oxide phases from which CAI were formed (Grossman, 1972). Subsequent to condensation, many CAI melted in the solar nebula forming rounded silicate droplets that slowly cooled and crystallized. Comparisons of CAI silicate mineral textures, crystallization sequences, and major element zoning patterns indicate that maximum temperatures of about 1670 to 1770K were reached, and that cooling during crystallization proceeded at a relatively slow rate of about 0.5 to 20K per hour (Stolper and Paque, 1986). Spinel would have been the only major phase in CAI not to have completely melted under these conditions (Stolper, 1982). The fO_2 in the solar nebula during the crystallization of CAI is believed to have been very reducing and has been quantified from the Ti^{3+}/Ti^{4+} ratios in fassaites (Beckett *et al.*, 1988) and the fO_2 calculated for an equilibrium solar gas composition (Grossman, 1972). At the estimated temperature and fO_2 during CAI melting, an immiscible Fe-Ni liquid phase would be expected to separate from the silicate liquid. This immiscibility can be predicted because the fO_2 was far more reducing than the iron-wüstite buffer, and has also been demonstrated experimentally in solar furnace experiments in which Allende meteorite powders were melted under reducing conditions and Fe-rich metal droplets were formed by reduction (King, 1983).

During the stage when CAI were partially molten, Fe and Ni would form the major

constituents of molten alloys. All other elements that are siderophile at a reducing ambient fO_2 would be expected to partition strongly into the metallic liquid. If opaque assemblages acquired their bulk compositions from precursor metal droplets, then one would expect opaque assemblages to be enriched in all of the siderophile elements. Consistent with this idea is the observation that refractory siderophiles such as PGE, Mo, W and Re are highly concentrated in opaque assemblages from CAI to $\sim 10^4$ x chondritic values. The concentration of refractory siderophiles into metal droplets in CAI is somewhat analogous to planetary core formation on a smaller scale. Silicate/metal partition coefficients ($D_{S/M}$) have been determined experimentally for a few refractory siderophile elements as a function of fO_2 and are known to decrease linearly with decreasing fO_2 on a plot of log fO_2 versus log $D_{S/M}$ (Schmitt *et al.*, 1989). Although experiments have not been performed at fO_2's as low as a solar gas, extrapolation of data from higher fO_2's indicates that values of $D_{S/M}$ are $< 10^{-4}$ for Ir and Re (Jones and Drake, 1986) as well as for W and Mo (Schmitt *et al.*, 1989). The low $D_{S/M}$ values for the four elements that have been studied are consistent with the extreme concentration of PGE, Re, Mo and W into opaque assemblages in CAI.

Elements that are only moderately siderophile (such as V) would partition more equally between metal droplets and silicate melt at fO_2's close to that of a solar gas. Based on thermodynamic data one can estimate the partition coefficient for V between silicate and metal liquids. To a first order, partitioning of V between alloy and silicate at conditions of CAI melting would be determined by the reaction $V + \frac{1}{2}O_2 \Rightarrow VO$. The equilibrium constant can be calculated for the V/VO reaction from thermodynamic data (Chase *et al.*, 1985). By fixing the fO_2 equal to that of a solar gas, a silicate/metal partition coefficient of 20 for V at 1600K is calculated (App. III).

Two opaque assemblages from CAI have been analyzed by analytical SEM in detail to

determine total V concentrations (Armstrong *et al.*, 1987), and one bulk opaque assemblage has been analyzed for V by neutron activation (Grossman *et al.*, 1986). If these three opaque assemblages originated as alloys, their initial V contents would have been 1.1, 2.6 and 5.5 wt% respectively. The V content of the host CAI silicate minerals (and spinel) has not been determined, but the average bulk CAI V content is ~620 ppm (Wänke *et al.*, 1974). We can estimate the V content of the host silicates by difference using the estimate of Armstrong *et al.* (1985), which suggests that opaque assemblages originally comprised about 0.1 wt% of CAI. In this case, the average silicate host concentration of V is ~590 ppm and the apparent silicate/metal partition coefficient for V in CAI is 20 to 100, in agreement with the prediction of 20 calculated above. Thus, the partitioning behavior of V and refractory siderophiles is consistent with silicate-metal equilibration in CAI at an fO_2 equal to an equilibrium solar gas.

During cooling of CAI, Ni-Fe metal droplets and spinel would be the first phases to crystallize. The common occurrence of opaque assemblages in embayments in spinel (Fig. 4.6) suggests that some spinel crystallized after the formation of metallic droplets. Many CAI have coarse-grained melilite rims that have very few inclusions of spinel or opaque assemblages. If crystallization proceeded from the outside of CAI inward, advancing melilite crystal faces might have pushed early crystallized spinel and metal toward the center of the inclusion where melilite, fassaite and anorthite subsequently crystallized around them, resulting in the textures observed in CAI. If CAI continued to cool at a solar gas fO_2 V dissolved in the metallic phase would be expected to oxidize and diffuse out of the metal due to the difference in the slopes of the V/VO buffer and the solar gas curve (App. III). This may explain the observations of Armstrong *et al.* (1985, 1989) that many opaque assemblages have rims of V-rich fassaite (Fig. 4.6) and that V is often highly enriched in spinels in the vicinity of opaque assemblages.

Fig. 4.6 Scanning electron microscope backscattered electron image of F3 (large bright object) and a smaller unnamed opaque assemblage both of which occur in embayments in a spinel (sp) crystal. A vanadium-rich fassaite (vfs) rim can be seen surrounding F3. vfs rims a common feature of opaque assemblages and suggests that vanadium was oxidized from the opaque assemblage metal and reacted with surrounding fassaite to form the vfs rim. Scale bar is 10 μm.

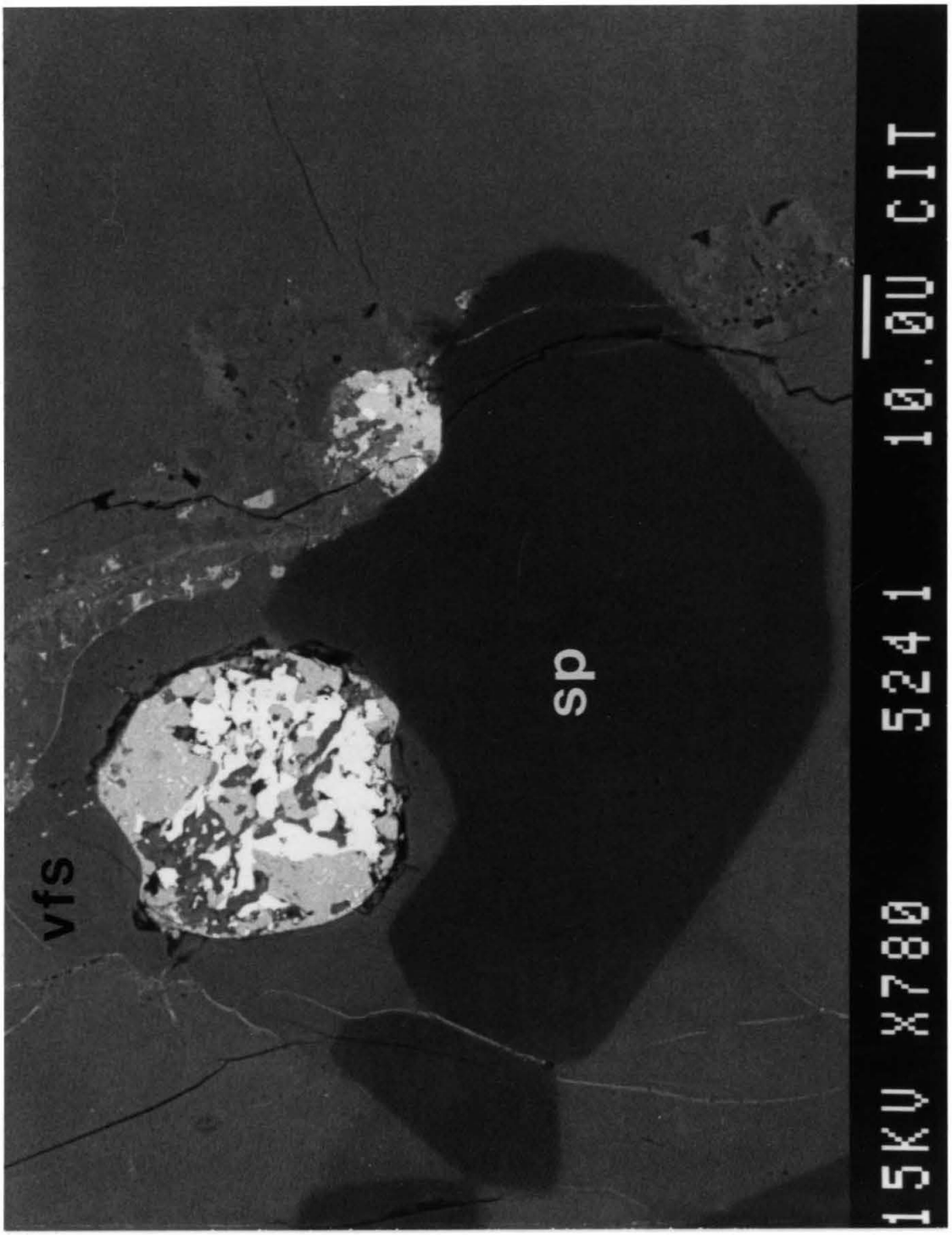
vfs
sp
15KV X780 5241 10.0U CIT

As indicated above, many compositional and textural aspects of opaque assemblages can be explained if they formed from metallic Ni-Fe droplets. However, since most opaque assemblages observed in CAI contain Ni-Fe oxides, Ni-Fe sulfides and PGE-rich metals in addition to Ni-Fe metals, previous workers have assumed the opaque assemblages formed independently from host CAI and acquired their bulk compositions by accretion of grains in the solar nebula prior to the melting of CAI. Contrary to this scenario is the thermodynamic prediction that during the melting and crystallization of CAI the low fO_2 and fS_2 of the solar nebula would not have allowed the stabilization of any of the oxides or sulfides observed in opaque assemblages. Preexisting sulfur would have been vaporized into the nebular gas and preexisting Fe-oxides would have been reduced to metallic iron. Additionally, the various metallic phases would have been homogenized by solid state diffusion as discussed in Chapter 3. However, if one is to argue that opaque assemblages originated as metallic droplets during CAI melting, it must be demonstrated that the complex metal-oxide-sulfide mineralogy that now characterizes opaque assemblages can be formed by the reequilibration of metallic droplets.

4.3 EXSOLUTION OF METALLIC PHASES

To form a data base with which to compare experimental phase equilibria, detailed analyses were made of coexisting metal, oxide and sulfide phases from the five opaque assemblages contained within CAI that were described above. The compositions of coexisting phases are tabulated in App. III. Particular emphasis was placed on the determination of the origin of refractory PGE-rich alloys because it has previously been argued that these phases provide evidence for the primitive nature of opaque assemblages, since it was supposed that they could form only by extremely high temperature condensation processes (El Goresy *et al.*,

1978; Blander *et al.*, 1980; Armstrong *et al.*, 1985).

To address the problem of whether PGE-rich alloys could be formed by a process other than condensation, homogeneous Ni-Fe-PGE alloys were synthesized and then annealed at subsolidus temperatures under both oxidizing and reducing conditions (App. I). Even in the most preliminary experiments (App. II) PGE-rich metal of the appropriate composition formed by exsolution, and the intergrown textures of PGE-rich metal, Ni-Fe metal and magnetite that are characteristic of opaque assemblages were reproduced experimentally (Fig. 4.7). More refined experiments allowed the determination of phase boundaries and tie-lines in the Ni-Fe-Ru phase diagram as a function of temperature as well as the partitioning behavior of Ir and Pt between phases in this system (App. I). Isothermal sections of the Ni-Fe-Ru phase diagram at 1070K, 870K and 770K are shown in Fig. 4.8 with the compositions of metallic phases from the five opaque assemblages studied projected onto this plane for comparison. Metallic phases in the opaque assemblage from the Leoville meteorite appear to have exsolved at a temperature of $\sim$870 K, and that metallic phases in four opaque assemblages from the Allende meteorite exsolved at a temperature of $\sim$770 K (Fig. 4.8; App. III).

Diffusion rates determined for Ru diffusion in Ni (App. I) were used to calculate the timescale for diffusion limited exsolution of PGE-rich metallic phases from a homogeneous alloy. The calculation is presented in App. III and indicates that $\geq 10^3$ years would be needed for diffusion-limited exsolution of the observed ϵRu-Fe grains from surrounding γNi-Fe at a temperature of 770 K (App. III).

4.4 OXIDATION AND SULFIDATION OF METALS

Phase compositions of coexisting Ni-Fe metal and Ni-Fe sulfide can also be used to

Fig. 4.7 Scanning electron microscope backscattered electron image of an experimental run-product from the experiments described in App. I. mt = magnetite, ni = γNi-Fe and ru = ϵRu-Fe. Note the striking similarity in texture between this sample and the opaque assemblage Willy shown in Fig. 4.2. Both images display a mt rim surrounding intergrown mt, ni and ru. Scale bar is 10 μm.

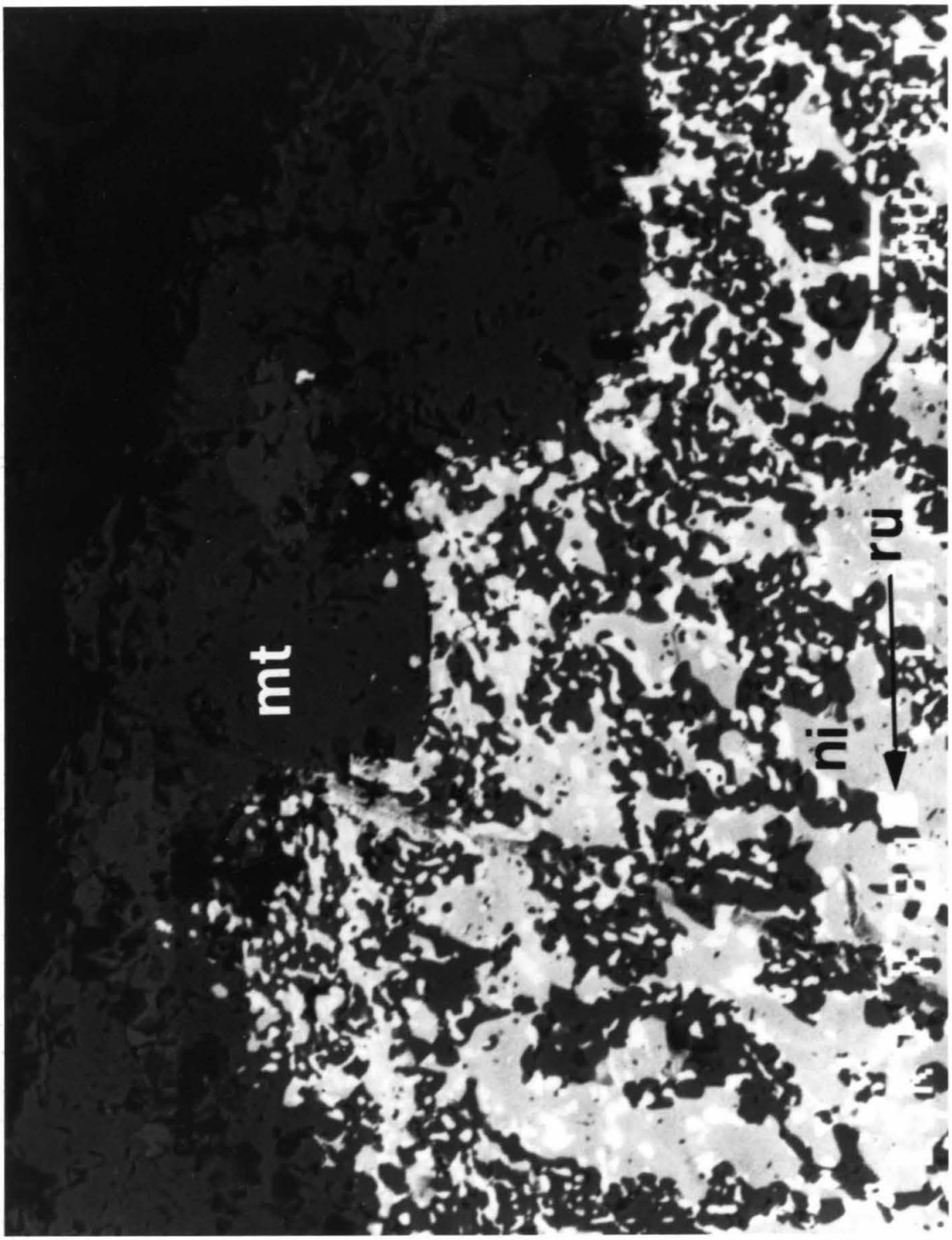
mt
ni
ru

Fig. 4.8 Compositional regions of metallic phases in opaque assemblages from App. III plotted on isothermal sections of the Ni-Fe-Ru plane along with phase equilibria from App. I. at a) 1073K, b) 873K and c) 773K. Phase boundaries and tie-lines are solid near regions where there is experimental data; dashed phase boundaries and tie lines are estimated or schematic. The 773K diagram is speculative and is intended to be diagrammatic only. Two- and three-phase regions are denoted by 2ϕ and 3ϕ respectively and three-phase regions are also stippled. Single-phase solid-solution regions include face-centered cubic γNi-Fe, hexagonal close-packed ϵRu-Fe and base-centered cubic αFe. Asterisks represent bulk alloy compositions for each opaque assemblage estimated from point-counting. The oxidation arrow in (c) connects the approximate total bulk compositions (including alloys, sulfides and oxides) of JIM-OA1, WILLY and F3 (diamond) with the approximate bulk alloy compositions.

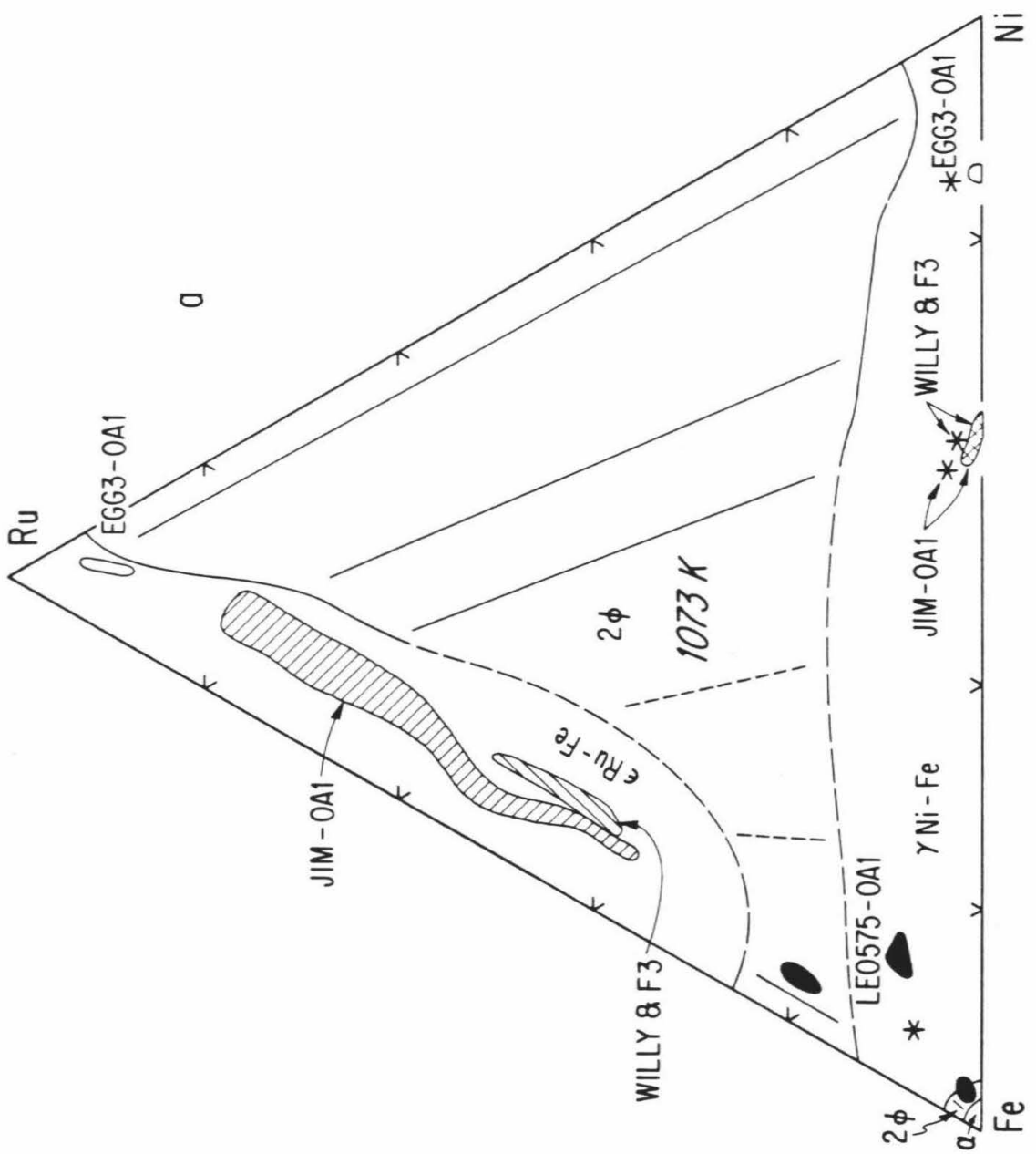
Ru
Ni
Fe
EGG3-OA1
JIM-OA1
WILLY & F3
LE0575-OA1
JIM-OA1
WILLY & F3
EGG3-OA1
1073 K
2φ
εRu-Fe
γ Ni-Fe
2φ
α

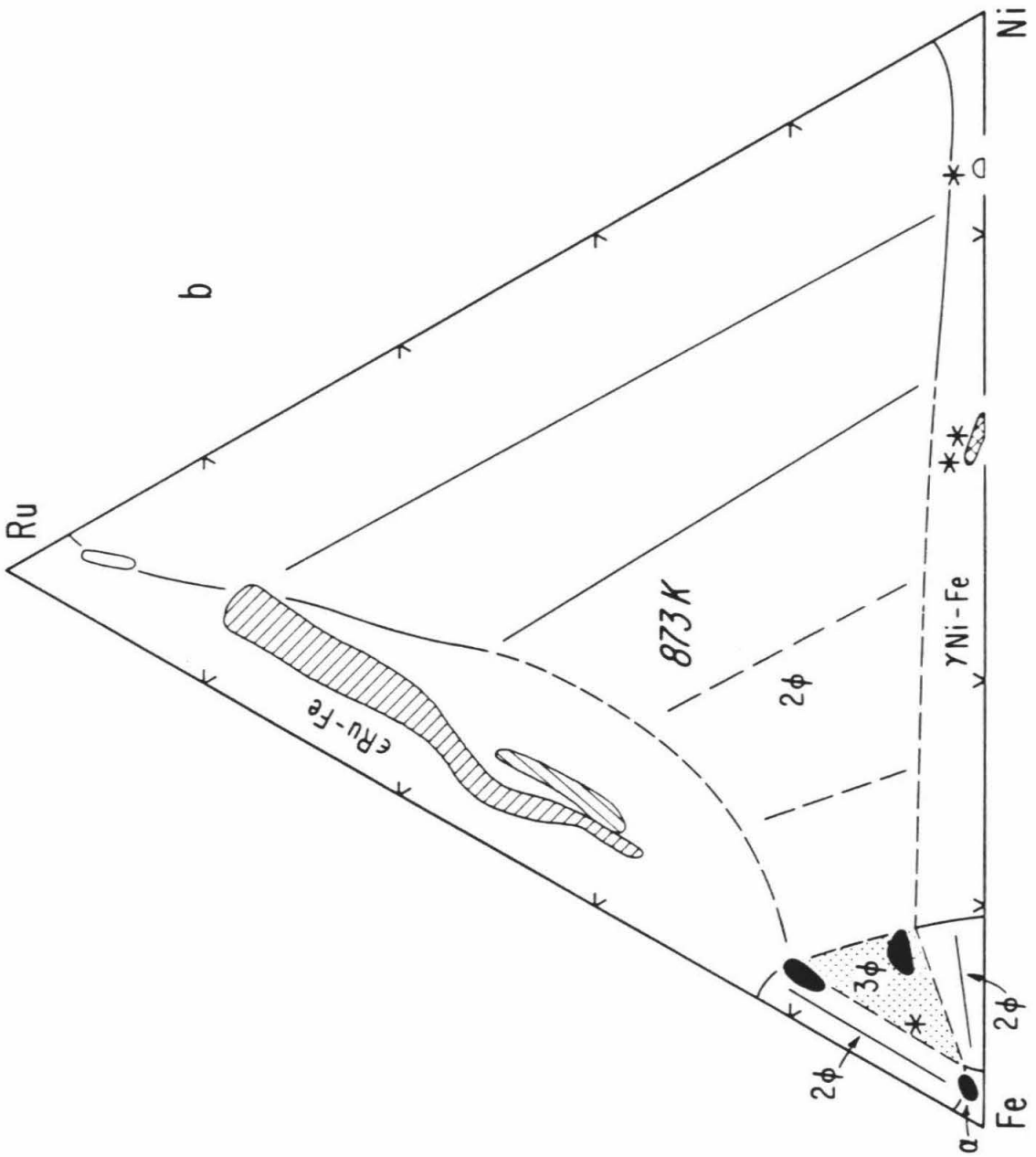
b
Ru
Ni
Fe
873 K
εRu-Fe
γNi-Fe
2ϕ
3ϕ
2ϕ
2ϕ
α

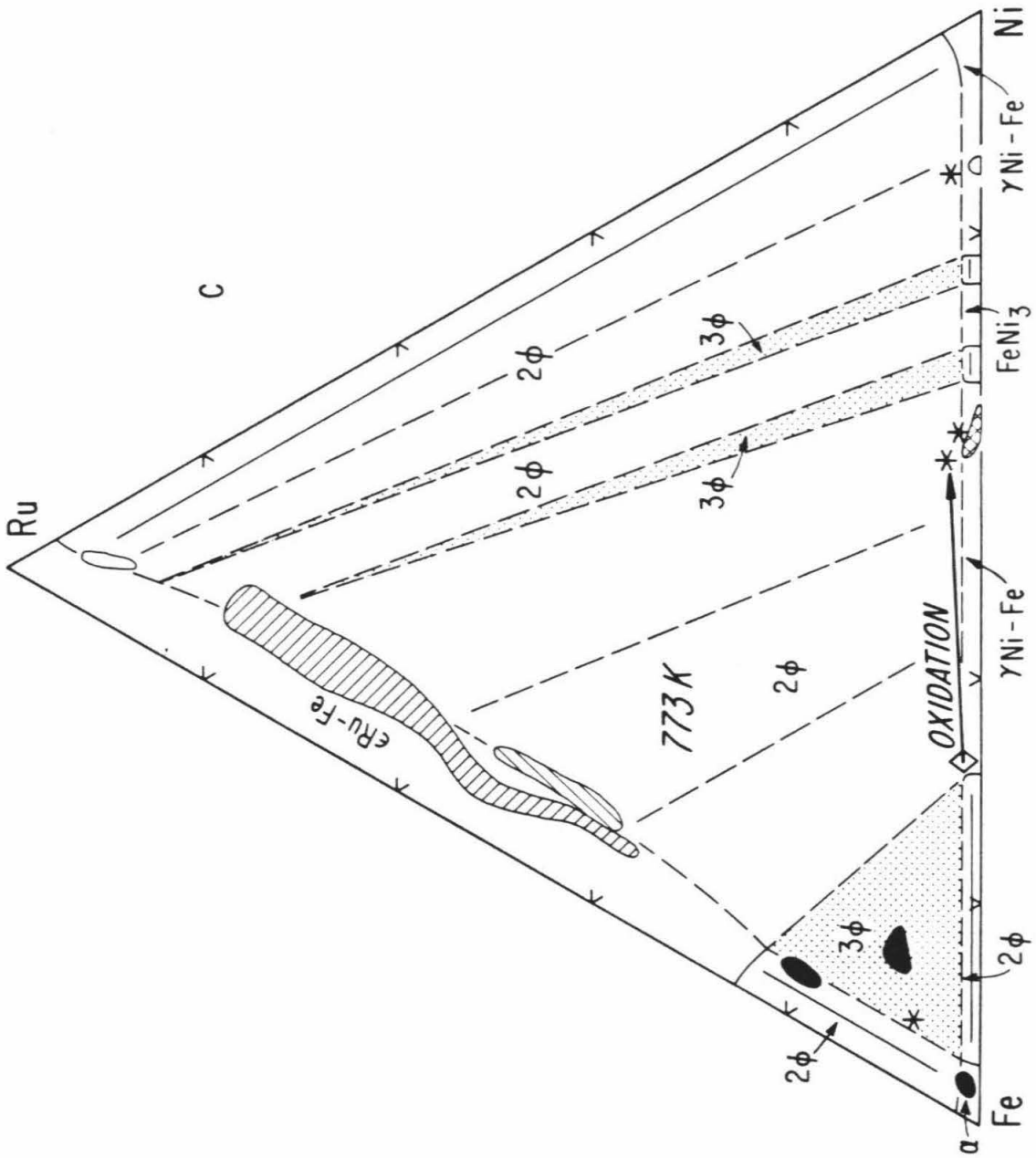
Ru
C
Ni
Fe
α
εRu-Fe
γNi-Fe
FeNi3
γNi-Fe
OXIDATION
773 K
2φ
3φ
2φ
3φ
2φ
3φ
2φ
2φ

calculate a temperature of equilibration using phase equilibria data from the literature. Several different Ni-Fe-S phase assemblages are observed in opaque assemblages. For each mineral assemblage the coexisting mineral compositions are consistent with tie lines and phase boundaries in the experimental system and suggest equilibration at ~770 K (App. III), consistent with the results from the Ni-Fe-Ru system. The fS_2 of equilibration of Ni-Fe metal with Ni-Fe sulfides of the compositions observed in opaque assemblages can be calculated from the reactions $Fe + \frac{1}{2}S_2 \Rightarrow FeS$ and $3Ni + S_2 \Rightarrow Ni_3S_2$ assuming ideal solution in the alloys and sulfides. The fS_2 calculated for both Fe-rich and Ni-rich assemblages are identical and about one log unit above the equilibrium solar gas fS_2 at 770 K (Fig. 4.9; App. III). The position of the Mo/MoS_2 stability curve below, and the Ru/RuS_2 and Pt/PtS stability curves above the estimated conditions of equilibration are consistent with the phase assemblages observed in opaque assemblages. Mo occurs exclusively as a sulfide, whereas Ru and Pt occur exclusively as metals. In contrast, highly metamorphosed C4 to C6 chondrites which experienced higher temperatures and fS_2's than the C3 chondrites studied here, contain PGE as $(Ru,Os,Ir)S_2$ and PtS phases, rather than PGE-rich metals (Geiger and Bischoff, 1989).

The fO_2 for the equilibration of opaque assemblages can be calculated from the compositions of coexisting Ni-Fe metal and magnetite from the reaction $3Fe + 2O_2 \Rightarrow Fe_3O_4$ again assuming ideal solution in the alloys and oxides. This treatment indicates that the fO_2 of equilibration was six log units above the solar gas curve at 770 K (Fig. 4.10; App. III).

It has been argued in this chapter that the phases in opaque assemblages from CAI are the expected results of exsolution, oxidation and sulfidation of homogeneous liquid metallic droplets formed by immiscibility in CAI silicate liquid. In addition to CAI, chondritic meteorites contain olivine chondrules, which in turn also contain opaque assemblages with identical Ni-Fe metal, oxide and sulfide phases as opaque assemblages from CAI (App. III).

Fig. 4.9 Plot of logarithm of fS_2 *versus* reciprocal temperature for equilibria relevant to opaque assemblage origin. Solar gas curve is from Fuchs and Blander (1977). Stability curves are calculated from thermodynamic data compiled by Barton and Skinner (1979) except for the Ru/RuS_2 curve, which is from Svendsen (1979). The curve labeled Ni-Fe alloy/Ni-Fe sulfide is broken into four segments (A-D) based on Ni-Fe-S phase equilibria from the compilation of Hsieh *et al.* (1982) at $T \geq 973K$ and from Misra and Fleet (1973) at $T \leq 873K$. For each line segment, a different alloy assemblage of sulfides may be in equilibrium with Ni-Fe alloy: A: FeS, Ni-S melt; B: FeS, Ni_3S_2, Ni-S melt; C: FeS, Ni_3S_2; and D: FeS, Ni_3S_2, $(Fe,Ni)_9S_8$. The position of the Ni alloy/Ni-Fe sulfide curve is calculated from the compositions of phases in opaque assemblages (see text). Region I is the fO_2 - T space for equilibration of opaque assemblages determined in App. III.

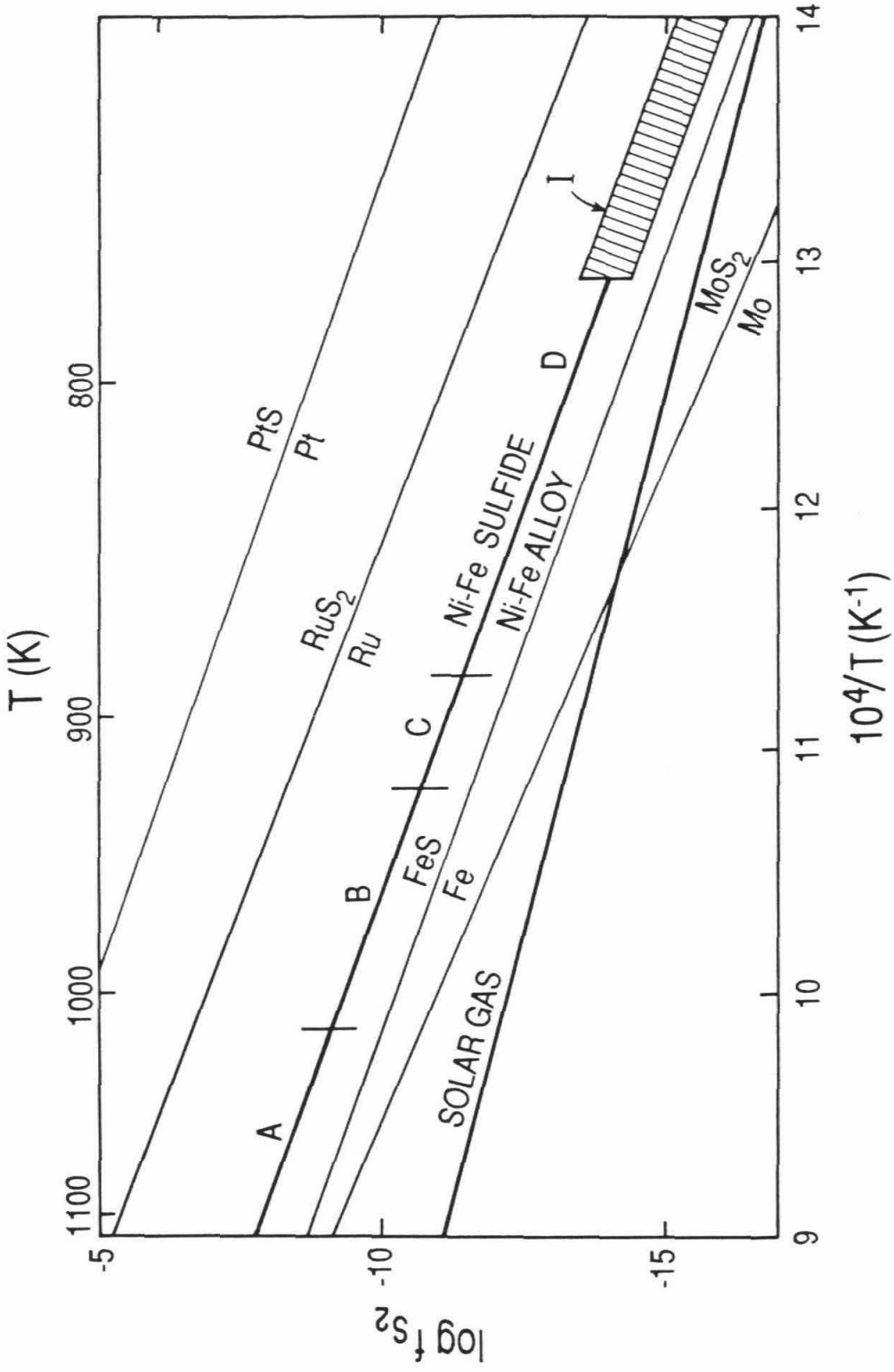
T (K)
1100
1000
900
800
-5
-10
-15
log f_{S_2}
9
10
11
12
13
14
$10^4/T\ (K^{-1})$
PtS
Pt
RuS_2
Ru
FeS
Fe
SOLAR GAS
Ni-Fe SULFIDE
Ni-Fe ALLOY
MoS_2
Mo
A
B
C
D
I

Fig. 4.10 Plot of the logarithm of fO_2 *versus* reciprocal temperature for equilibria relevant to opaque assemblage origin. The solar gas curve is at $P_T = 10^{-3}$ atm (Grossman, 1972) and the V/VO and Ni/NiO curves are calculated from thermodynamic data (Chase *et al.*, 1985). Curve (a) is Fe/Fe_3O_4, curve (b) is $Ni_{67}Fe_{33}/Fe_3O_4$, and curve (c) is $Ni_{85}Fe_{15}/Fe_3O_4$ (McMahon and Haggerty, 1980). Lines (a), (b) and (c) end at the highest temperature at which the alloys are stable with magnetite. Region I is the fO_2 - T space for partitioning of V between alloy and silicate liquids as calculated in App. III. Region II is the fO_2 - T space for the crystallization of fassaite in CAI based on reactions involving Ti^{3+}/Ti^{4+} ratios in fassaites (Beckett *et al.*, 1988). Region III is the fO_2 - T space determined in App. III for equilibration of opaque assemblages.

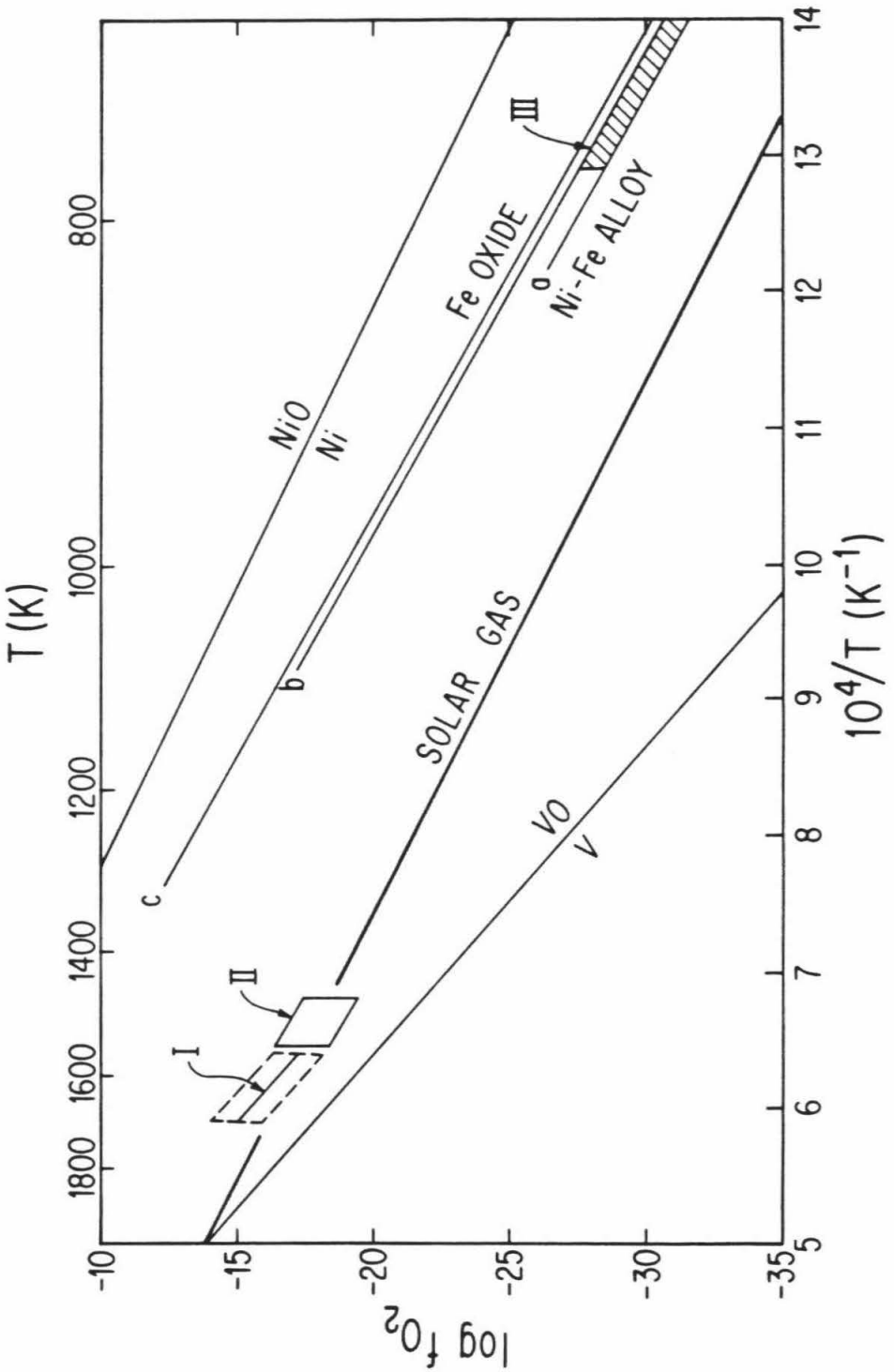
T (K)
1800
1600
1400
1200
1000
800
log f_{O_2}
-10
-15
-20
-25
-30
-35
$10^4/T$ (K^{-1})
5
6
7
8
9
10
11
12
13
14
NiO
Ni
Fe OXIDE
Ni-Fe ALLOY
SOLAR GAS
VO
V
I
II
III
a
b
c

Fig. 4.11 Scanning electron microscope backscattered electron image of an opaque assemblage from an Allende olivine chondrule. ni = γNi-Fe, pn = pentlandite, ap = apatite and mt = magnetite. Scale bar is 100 μm.

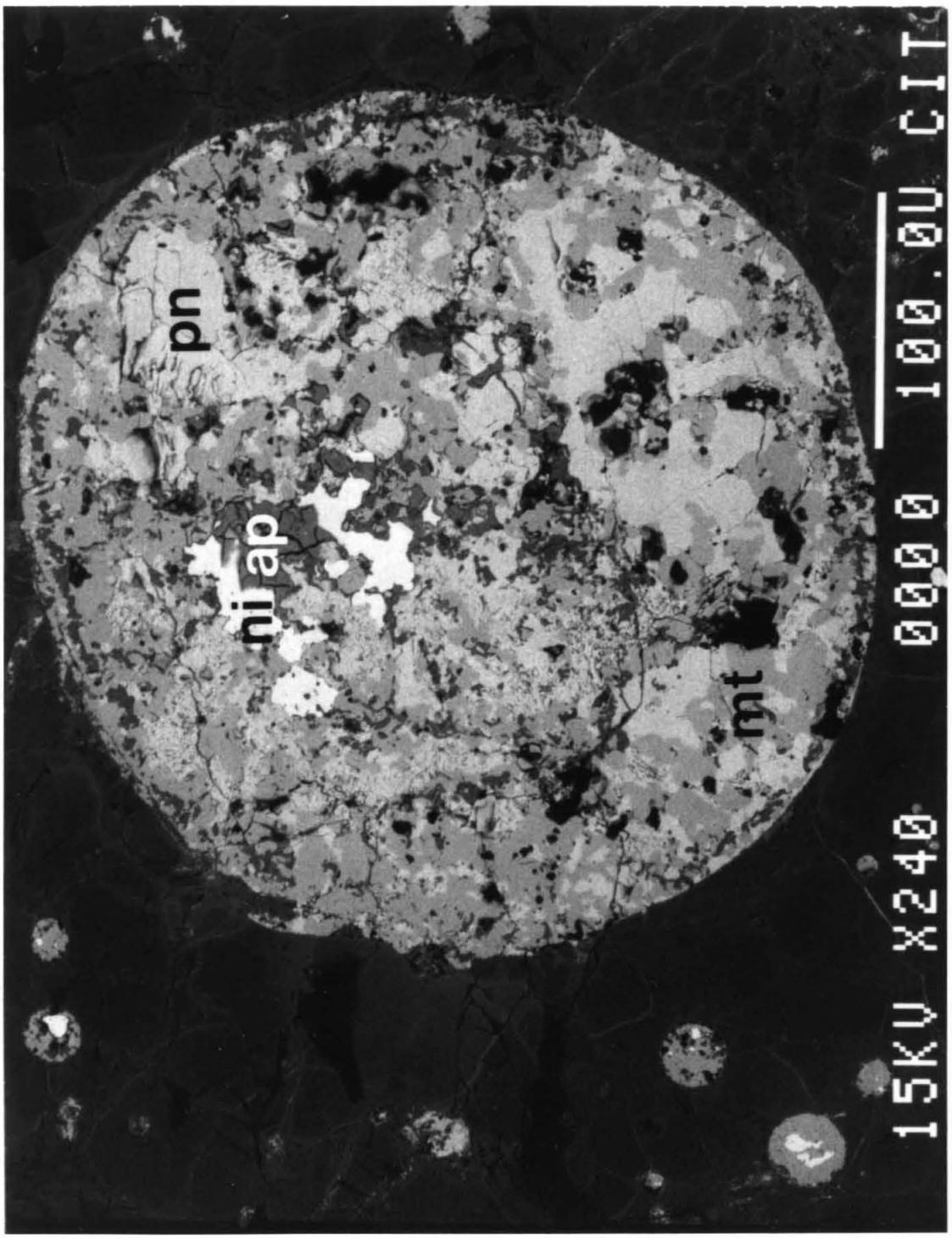
pn
ni ap
mt
15KV X240 0000 100.0U CIT

A secondary electron image of an opaque assemblage from an olivine chondrule is shown in Fig. 4.11. The only major difference is the lack of refractory siderophile-rich phases in opaque assemblages from olivine chondrules. Identical compositions of Ni-Fe metal, sulfides, oxides and apatite are observed (App. III). Therefore, the opaque assemblages in olivine chondrules record identical temperature, fS_2 and fO_2 equilibration conditions as those in CAI, suggesting that equilibration occurred after CAI and chondrules had accreted on planetesimal bodies. The conditions of prolonged heating ($\geq 10^3$ years) at 770K under oxidizing and sulfidizing conditions required to produce opaque assemblages are unlikely to have occurred in the solar nebula. They would instead be more plausible during metamorphism on a planetesimal body where trapped volatiles could produce the necessary fO_2 and fS_2. The *in situ* decay of ^{26}Al could have provided an ample heat source if opaque assemblage equilibration occurred during an early metamorphic event on a parent body. The interiors of bodies only a few km in radius could reach temperatures in excess of 770K if they had ^{26}Al abundances similar to the value of $(^{26}Al/^{27}Al)_o \approx 5\times10^{-5}$ measured in some CAI (*e.g.*, Lee *et al.*, 1977). Alternatively, very shallow burial in larger bodies could provide an adequate thermal environment for equilibration (*cf.* Mashamichi *et al.*, 1981).

4.5 COMPARISON WITH PREVIOUS MODELS

Previous studies of the chemical compositions, mineralogy and textural relationships of opaque assemblages have led most workers to concur that opaque assemblages formed before the host CAI, and to agree on the following scenario for their origin and evolution (*e.g.*, Armstrong *et al.*, 1985, 1987; Bischoff and Palme, 1987). 1) Condensation of μm-sized Ru,Os-rich grains at very high temperature in a supernova or in a hot part of the solar nebula. 2) Condensation of Ni-Fe metal followed by condensation of magnetite and Fe-Ni sulfides, or

reaction of Ni-Fe metal in the nebula to form magnetite and Fe-Ni sulfides. 3) Aggregation of these and other phases in the solar nebula to form opaque assemblages. 4) Mixture of opaque assemblages with proto-CAI silicates before (or during) a brief high-temperature ($\sim$1700K) event, during which the silicate portion of the CAI melted or partially melted, followed by rapid cooling.

The high-temperature CAI melting event was postulated to have been so brief, and cooling so rapid, that the delicate textures and mineral intergrowths in opaque assemblages were preserved as they existed before CAI melting. According to this model, the phase assemblages in opaque assemblages look through the CAI melting event and record highly sulfidizing and oxidizing conditions during condensation very early in the history of the solar nebula. Since some silicate minerals in the host CAI preserve evidence for crystallization under reducing conditions in the solar nebula (Beckett *et al.*, 1988), this view of opaque assemblage origin implies that the condensing nebula was heterogeneous, with local variations in temperature of hundreds of degrees and in fO_2 of many orders of magnitude. It further implies turbulence within the nebula capable of mixing the various phases formed under these conditions.

The new model proposed in this chapter and in App. II and III contrasts markedly with the previous model. The two models are compared in cartoon form in Fig. 4.12. The new model suggests that all of the siderophile elements condensed as alloys under reducing solar gas conditions in contrast to the previous idea that each phase condensing in its own microenvironment at variable fO_2 and fO_2 and then aggregating in the nebula to form opaque assemblages. After aggregation of alloys with proto-CAI silicates, the silicate melting event resulted in the formation of immiscible metallic liquid droplets which scavenged siderophile elements (*e.g.*, PGE, Re, W and Mo) from the silicate melt. The complex mineralogy that

Fig. 4.12 Cartoon depicting models for the multistage origin proposed for opaque assemblages by previous authors (*e.g.*, Armstrong *et al.*, 1985; Bischoff and Palme, 1987) contrasted with the new model proposed in this study. See text for discussion.

ORIGIN OF OPAQUE ASSEMBLAGES

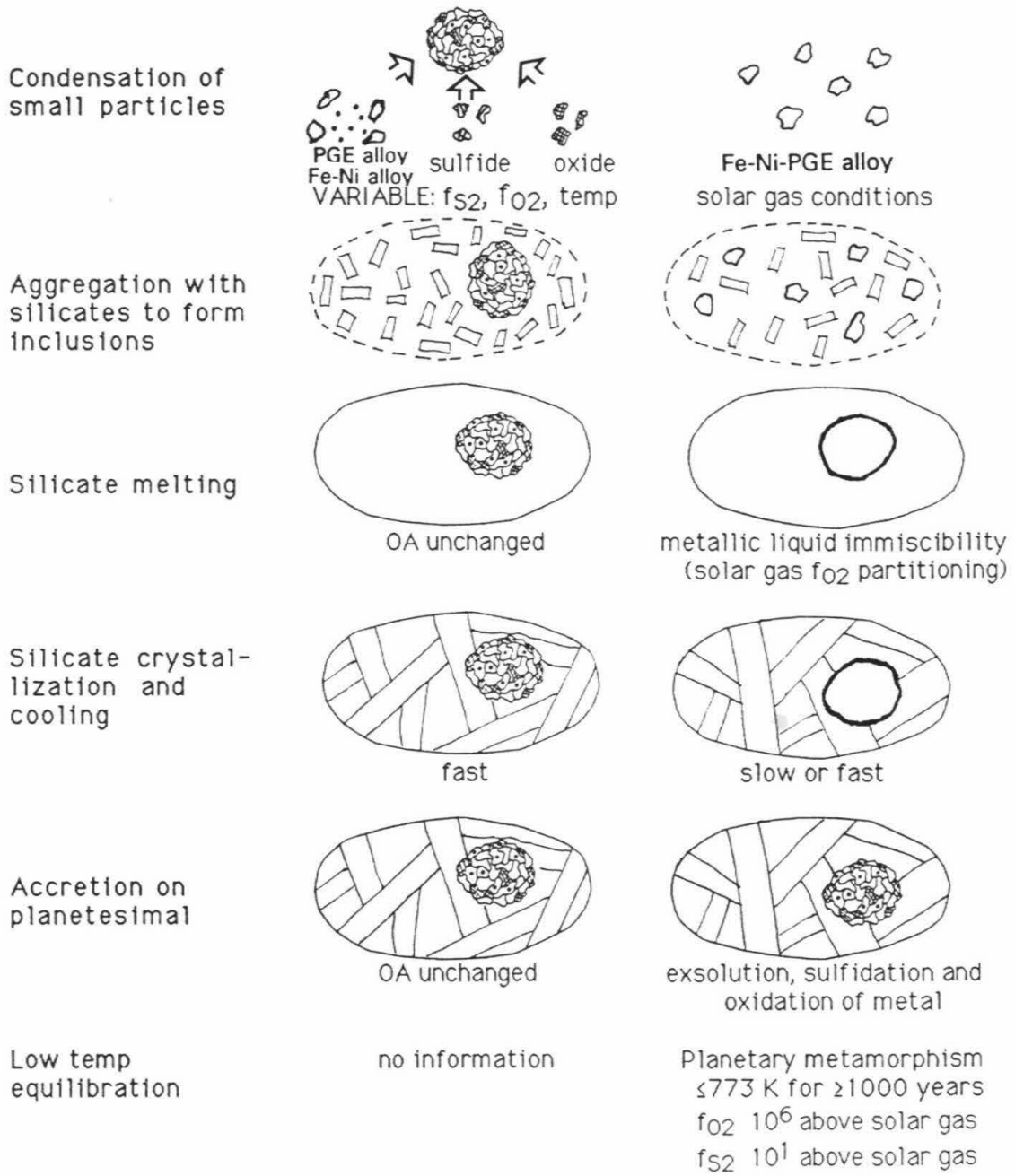

now characterizes opaque assemblages is believed to have formed from these proto-opaque assemblage alloy droplets by sulfidation, oxidation, and exsolution. This could have occurred during metamorphism for $\geq 10^3$ yr at 770K and at an fS_2 one log unit above, and an fO_2 six log units above, a solar gas composition. The two-stage evolution proposed in the new model, which includes homogeneous alloy formation at high temperature followed by reequilibration and redistribution of elements during metamorphic reactions at lower temperature, provides a general explanation of the approximately solar refractory siderophile element ratios in all CAI in spite of the highly fractionated compositions of individual opaque assemblages and the mineral phases found within them.

The alternative scenario for the origin of opaque assemblages, which suggests that they formed in the solar nebula before CAI melting and were subsequently captured in the CAI and rapidly cooled (Armstrong *et al.*, 1985, 1987; Bischoff and Palme, 1987), is considered by this author to be unlikely because the low temperature mineral assemblages could not have survived melting and subsequent cooling of the bulk CAI for any plausible cooling rates. The previous model also does not provide an explanation for the solar refractory siderophile element ratios in CAI.

The conditions that were estimated for the temperature, fS_2 and fO_2 of equilibration for opaque assemblages from both CAI and chondrules are very similar and suggest that these two components of C3V meteorites share a common, late low-temperature history, perhaps on a planetesimal body. Studies of opaque assemblages may therefore provide quantitative constraints on the post-accretionary equilibration conditions of C3V meteorites.

CHAPTER 5. TERRESTRIAL FRACTIONATION

The geochemical behavior of Pt-group elements is strongly influenced by the presence or absence of metallic iron. During planetary differentiation core-forming metallic iron liquid is believed to remove virtually all of the PGE in a planet to the planet's core. A small proportion of the PGE, however, remains in the silicate fraction of the planet where the geochemical behavior becomes much more complex and poorly understood. At the sulfur and oxygen fugacities prevalent in the earth's crust and upper mantle a metallic iron phase is absent, and sulfides and oxides become important in fractionating the PGE with respect to one another.

The general trends of terrestrial PGE fractionation were introduced in section 2.6. The average concentrations of PGE and Re in representative terrestrial materials were given in Table 2.4 and are plotted relative to C1 chondrite concentrations on Fig. 5.1. Ratios are plotted in order of decreasing melting temperature for the PGE, with Re following Pd. Fig. 5.1 includes ophiolitic peridotites and spinel lherzolite xenoliths as samples of suboceanic and subcontinental mantle respectively. The average patterns for these two rock-types are virtually flat at the 10^{-2} x chondritic level. The data for oceanic basalts and granitic rocks are included as samples of the differentiated oceanic and continental crust. These crustal patterns have steep positive slopes. Relative to the mantle samples, Os and Ru are depleted by a factor of ~ 100, Pt and Pd are depleted by a factor of ~ 10, and Re is enriched by a factor of ~ 2. Because of the low concentrations of PGE and Re in crustal rocks and the small mass of the crust relative to the mantle ($< 1\%$) crustal extraction from the mantle does not significantly effect mantle PGE contents. The data for ophiolitic chromitites are also included since these samples may represent a residuum of a high degree of mantle partial melting. The pattern has a steep negative slope which is complementary to the crustal samples. Ir and Ru

Fig. 5.1 Average concentrations of PGE and Re from Table 2.4 normalized to C1 chondrite concentrations in representative terrestrial materials. Data sources are given on Table 2.4. The PGE are plotted in order of decreasing melting temperature. Re is plotted after Pd because it behaves more similarly to Pd during terrestrial fractionation than any of the other PGE. Lines connecting the elements are dashed where data for a particular element are unavailable. Arrows (↓) connected to data points designate maximum values. See text for discussion.

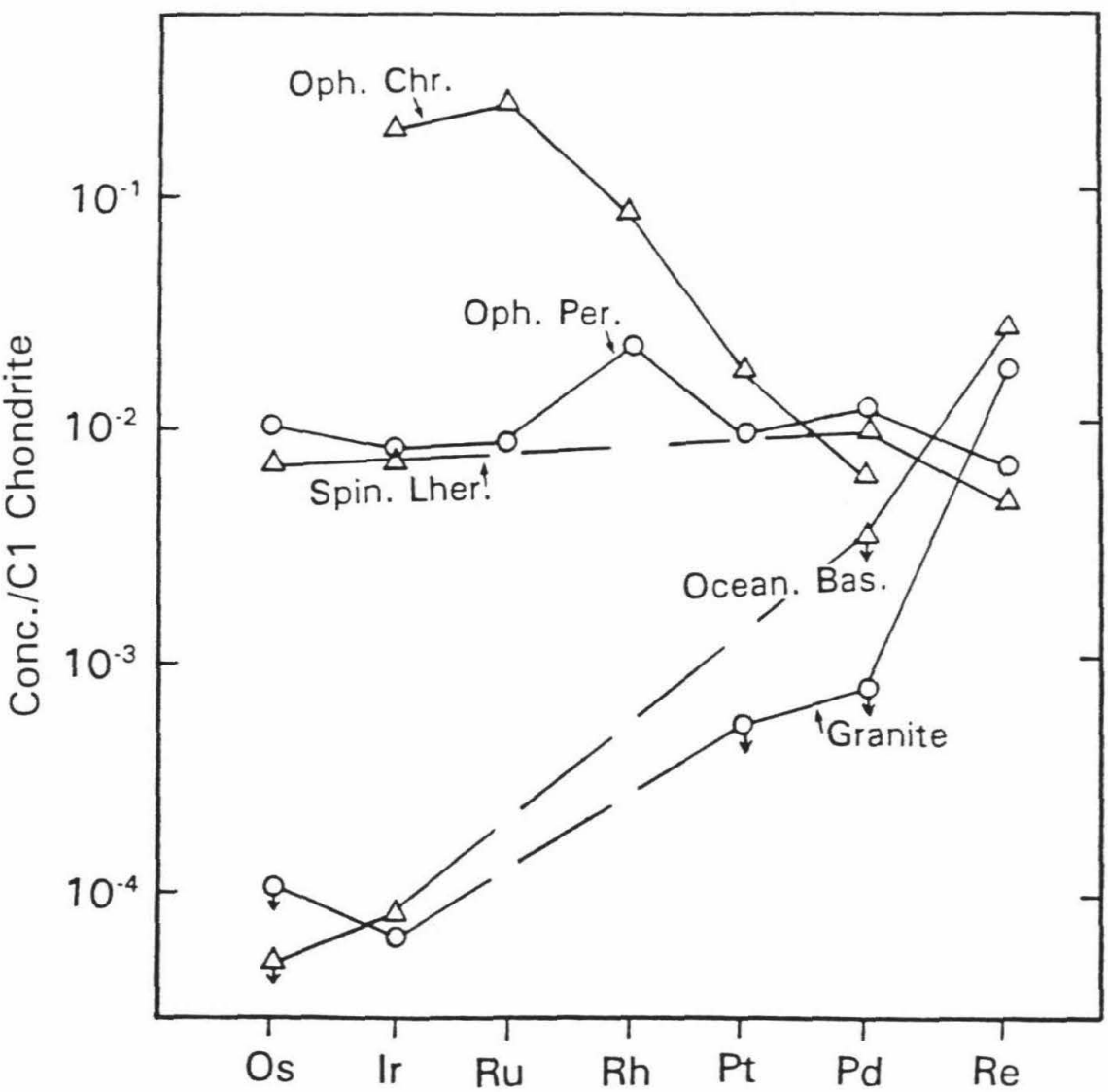
Oph. Chr.
Oph. Per.
Spin. Lher.
Ocean. Bas.
Granite
Conc./C1 Chondrite
10-1
10-2
10-3
10-4
Os
Ir
Ru
Rh
Pt
Pd
Re

are enriched relative to the mantle samples by a factor of 20, Rh is enriched by a factor of 10, and Pt and Pd are approximately equal to mantle values. Re concentrations have not been measured in ophiolitic chromitites.

It is well known that some of the PGE can become highly concentrated into trace phases in peridotites. However, the solubility of PGE in major silicate and oxide phases and the mechanisms by which they are concentrated into trace phases in the mantle and crust are not well understood. It is important to investigate the mechanisms which result in the tremendous fractionations of this chemically similar group of elements so that the PGE can be used as petrogenetic indicators and as a tool for mineral deposit exploration. A fundamental problem in PGE geochemistry is the role of Os-Ir-Ru alloys in the fractionation of PGE. These alloys occur as inclusions in chromite crystals in virtually all PGE-rich rocks. Although their origin has been widely debated, no previous experimental studies have been undertaken to clarify their origin.

In App. IV a preliminary experimental investigation designed to determine the origin of Os-Ir-Ru alloy inclusions in chromites and their role in PGE fractionation is presented. This chapter is largely a summary of the literature on terrestrial PGE fractionation with some discussion of the results of the experiments presented in App. IV. The geochemical behavior of the PGE are explored during the processes of core formation, mantle partial melting, and the magmatic differentiation of layered mafic-ultramafic intrusions. The final section of this chapter summarizes the application of the Re-Os geochronometer.

5.1 CORE FORMATION

The most direct evidence that we have for the behavior of PGE during core formation in planetary bodies comes from the study of iron meteorites. These samples are widely believed

to be the product of melting and gravitational segregation of metallic Fe in asteroid size bodies. Wasson and colleagues (*e.g.*, Scott and Wasson, 1975) have classified about 500 iron meteorites into 12 chemical groups (each believed to be from a separate parent body) based on their Ga, Ge, Ir and Ni contents. Chemical fractionations between groups are generally believed to have occurred in the solar nebula (Scott, 1972; Kelly and Larimer, 1977), whereas chemical variations within most groups reflect fractional crystallization of molten metal during the solidification of the cores of planetary bodies (Scott, 1972). PGE are enriched in early crystallizing Fe-Ni metal to ~ 100 x chondritic and the concentrations decrease by $\sim 10^4$ with decreasing Ni content in magmatic groups (Pernicka and Wasson, 1987). The PGE content of the parental metallic liquids from which each iron meteorite group crystallized can be roughly estimated using a fractional crystallization model and estimates of the liquid metal/solid metal partition coefficients for the PGE (Willis and Goldstein, 1982). For example, the PGE pattern for the estimated parental liquid from which the group IIIAB iron meteorites crystallized is plotted on Fig. 2.11 (Willis, 1980). The PGE occur in chondritic proportions at 1 to 2 x C1 chondrite values consistent with an origin by removal of virtually all of the PGE into cores of approximately chondritic composition parent bodies.

The partitioning of Ir and Re between iron metal containing 22% S and basaltic glass was measured at 1270°C and $\log fO_2 = -13$ by Jones and Drake (1986). The silicate/metal partition coefficients ($D_{S/M}$) for Ir and Re are $\sim 5 \times 10^{-5}$ and $\sim 5 \times 10^{-4}$ respectively. Under these conditions, equilibration between the mantle and core of a planet would result in nearly complete removal of Ir and Re (and presumably the rest of the PGE) to the core.

In most models for core formation in the earth it is assumed that the earth has a chondritic bulk composition. The earth's composition may have been established by 1) homogeneous accretion of chondritic material or 2) heterogeneous accretion of a mixture of refractory-rich

and refractory-poor material that condensed from the nebula at various temperatures. Recent accretionary models suggest that the earth accreted from km-sized planetesimals containing roughly chondritic abundances of the elements (*e.g.*, Stevenson, 1981).

If core formation in the earth was a simple equilibrium process, one would expect the earth's mantle to have concentrations of "highly siderophile" elements (PGE and Re) at the 10^{-4} to 10^{-5} x chondritic level based on the available partitioning data. Many workers have argued that the siderophile element content of the upper mantle is well represented by spinel lherzolite xenoliths (*e.g.*, Jagoutz *et al.*, 1979). Spinel lherzolite xenoliths have "highly siderophile" element contents of $\sim 10^{-2}$ x chondritic in conflict with much lower concentrations expected for mantle-core equilibration. As a result, many models have been developed to explain the high concentrations of "highly siderophile" elements in the mantle. The models must also explain the partitioning of the "moderately siderophile" elements (*e.g.*, Co, Ni and Mo) which, according to partitioning data (Jones and Drake, 1986), should be depleted by 10^{-3} to 10^{-4} x chondritic by equilibrium core formation but are instead 0.1 to 0.2 x chondritic in spinel lherzolite xenoliths (Jagoutz *et al.*, 1979).

The proposed models have been reviewed by Jones and Drake (1986) and can be classified into four categories 1) incomplete core formation leaving a small quantity of metal in the mantle to be subsequently oxidized (Jones and Drake, 1986), 2) equilibration between mantle silicates and an Fe-S-O metallic liquid (rather than Fe-S liquids as in the partitioning experiments) (Brett, 1984), 3) heterogeneous accretion involving a late 'veneer' of chondritic material that did not separate to the core (*e.g.* Kimura *et al.*, 1974; Chou, 1978) and 4) establishment of highly siderophile element concentrations by partitioning at megabar pressures, perhaps at the core-mantle boundary (*cf.* Ringwood, 1977). It must be emphasized that partitioning data are limited to only a narrow range of pressure, temperature, fO_2, and fS_2.

Considering the data that do exist, none of the first three models quantitatively predicts the "highly" and "moderately" siderophile element abundances inferred for the upper mantle (Jones and Drake, 1986). The fourth model is presently untestable because high pressure partition coefficients are entirely unknown. Recently Schmitt *et al.* (1989) suggested a model of late accretion of a volatile-rich chondritic 'veneer' followed by removal of a sulfide liquid to the core. They suggest that sulfide removal may be capable of depleting the highly siderophile elements but not the moderately siderophile elements. This is an interesting explanation of the observations, but more experimental data on the partitioning of siderophiles between metal, sulfide and silicate are needed to test the model.

Most investigators accept the idea that the relatively constant PGE content of spinel lherzolite xenoliths are representative of the bulk upper mantle, but this assumption may not be entirely valid. Garnet lherzolite PGE abundances are much more highly variable and appear to have been affected by introduction of S-bearing metasomatic fluids (Mitchell and Keays, 1981). Neutron activation studies of phases separated from garnet and spinel lherzolite xenoliths indicate that intergranular sulfides contain the bulk of the PGE in these rocks (Mitchell and Keays, 1981; Jagoutz *et al.*, 1979). Since these sulfides would be intergranular liquids under mantle conditions, the PGE may have considerable mobility. It is also possible that the intergranular sulfides could have originated by liquid immiscibility from sulfide-saturated basic magmas. Partial melts of undepleted mantle are probably sulfide-saturated as indicated by the ubiquitous presence of sulfides in mantle xenoliths. Since the solubility of S decreases with decreasing pressure (Wendlandt, 1982), melts migrating through the mantle could deposit intergranular sulfides genetically unrelated to the host lherzolites. This could conceivably lead to large-scale redistributions of PGE within the mantle during successive melting and metasomatic episodes and may be responsible for the highly variable

PGE contents in garnet lherzolites. Although spinel lherzolite xenoliths are presently our best estimate of the siderophile content of the upper mantle, much more work needs to be done to fully understand the mobility of mantle sulfides and their influence on PGE distributions in the mantle.

5.2 ORIGIN OF THE MOON

Determination of the PGE content of the lunar mantle is a more difficult exercise than for the earth's mantle because there are no lunar mantle samples available. Estimates of mantle abundances have been surmised from the study of volcanic rocks presumably derived from the moon's mantle. This is not a straightforward exercise in the case of PGE because of the vital importance of trace phases and fO_2 and fS_2 to their partitioning behavior. If one could estimate with some confidence the bulk PGE contents of the mantles of the earth and moon, then in principle one could gain insight into whether or not they formed from the same material. However, the difficulty in interpreting lunar mantle PGE abundances based on the study of lunar volcanic rocks has led to considerable controversy concerning the origin of the moon (*cf.* Delano and Ringwood, 1978; Anders, 1978).

Some workers have compared the low PGE content of volcanic rocks from the moon with the high PGE content of mantle xenoliths from the earth and concluded that the mantles of the moon and earth have highly contrasting abundances of PGE (Newsom and Taylor, 1989). This is a rather tenuous approach considering the complexities and magnitude of PGE partitioning during crustal genesis. Drake (1987) estimated the Ir and Re contents of the moon's mantle from Ir and Re concentrations in lunar basalts by attempting to correct for the fractionations observed between mantle xenoliths and basalts on earth. While this is a better approach than that of Newsom and Taylor (1989), it is still unreliable because the partitioning

of PGE during partial melting depends on intensive variables such as fO_2 and fS_2 and the presence or absence of certain phases in the residuum (discussed below) which are unlikely to be the same in the moon and earth.

In summary, the data are insufficient for a reliable estimation of the PGE contents in the bulk mantle of the moon. Therefore, tests of whether the moon originated from the earth's mantle, based on comparisons between terrestrial and lunar PGE contents, are premature. Even if the PGE contents of the mantles of the moon and earth were precisely known, the comparison would be inconclusive since the relative PGE contents could easily be changed by further core formation or further accretion of Sun-orbiting debris after the formation of the moon (Stevenson, 1987).

5.3 MANTLE PARTIAL MELTING

The representative analytical data for PGE in terrestrial mantle and crustal rocks presented in Table 2.4 and Fig. 5.1 suggest that Os, Ir and Ru behave as highly compatible elements whereas Rh, Pd, Pt and Re behave as only slightly compatible elements during mantle partial melting. While this idea has become generally accepted, the reason for this behavior and the phase(s) that accommodate these elements in the mantle are the subject of debate. Suggested host phases for Os, Ir and Ru include olivine, FeS, Os-Ir-Ru alloys and chromite. Brugmann *et al.* (1987), citing experimentally determined partition coefficients of Malvin *et al.* (1986), argued that olivine is the host phase for Os, Ir and Ru during fractionation of komatiites which do not contain sulfides or spinel. The compatibility of Os, Ir and Ru in olivine has been drawn into question by the work of Capobianco and Drake (1990), who showed the results of Malvin *et al.* (1986) to be invalid based on further analyses of the experimental run-products.

Unlike the komatiites studied by Brugmann *et al.* (1987), mantle peridotites contain spinel and sulfide, and these phases dominate the partitioning of PGE (Mitchell and Keays, 1981). Most workers have attributed the highly fractionated PGE patterns of mantle-derived melts to the presence of an Os-Ir-Ru-rich alloy in the mantle source region (Bird and Basset, 1980; Keays, 1982; Campbell and Barnes, 1984; Barnes *et al.*, 1985). Given this assumption, Keays (1982) suggested that mantle partial melts were saturated with Ir. The ubiquitous presence of Os-Ir-Ru-rich alloys in ophiolitic peridotites has been cited as evidence in favor of this hypothesis. A role for spinel in the fractionation of PGE has largely been discounted due to the lack of conclusive evidence that PGE are compatible in the spinel structure. However, the widespread occurrence of Os-Ir-Ru-rich alloys as inclusions in Cr-rich spinels from ophiolitic peridotites and layered intrusions suggests that chromite plays some role in the fractionation of PGE. The relationship between Or-Ir-Ru-rich alloys and chromites is unquestionably one of the least understood aspects of PGE geochemistry.

In several early studies it was proposed that Os, Ir and Ru could be accommodated in solid solution in the chromite lattice at magmatic temperatures (*e.g.*, Gijbels *et al.*, 1974; Morgan *et al.*, 1976; Naldrett and Cabri, 1976). More recently, petrographic studies have identified discrete 1 to 20 μm diameter inclusions of alloys and sulfides in chromite from nearly every major ophiolite and layered intrusion (*e.g.*, Talkington *et al.*, 1984; Auge, 1988). Alloy compositions range from $\sim$80% Ir to $\sim$80% Os with Ru contents up to $\sim$50% (Legendre and Auge, 1986; Talkington and Lipin, 1986). These compositions correspond to the minerals osmiridium, iridosmine and rutheniridosmine according to the nomenclature of Harris and Cabri, (1973). Sulfide compositions span the solid solution between laurite and erlichmanite $(Ru,Os)S_2$ with up to $\sim$20% Ir (Legendre and Auge, 1986; Talkington and Lipin, 1986). Several petrographic features of the inclusions have been used to argue that

they did not form by exsolution from chromite including: 1) euhedral and anhedral habits, 2) non-crystallographic orientation, and 3) compositional diversity. Based on these types of features, virtually every petrographic investigator has suggested that alloys and sulfides precipitate directly from magmatic liquids creating nucleation sites for chromite crystals, which crystallize around the small particles and mechanically remove them to chromitite layers (*e.g.*, Talkington *et al.*, 1984; Auge, 1988).

I have experimentally studied several aspects of the origin of Ir-rich alloys in chromite. The details of this preliminary investigation are presented in App. IV. In summary, the solubility of Ir in FeS liquid in equilibrium with Ir metal at 1250°C was determined to be $\sim 4\%$. The solubility of Ir in synthetic and natural chromites in equilibrium with Ir metal at 1450°C was investigated and found to be below the electron microprobe detection limit of ~ 80 ppm. It was, however, demonstrated that Ir is mobile in chromite at magmatic temperatures and probably diffuses though chromite at a rate similar to the diffusion of major cations (App. IV).

If Ir-rich alloys were stable in mantle peridotites, the high solubility of Ir in FeS indicates that Ir concentrations in coexisting FeS liquid should be $\sim 4\%$. The concentration of Ir in sulfides from spinel lherzolite xenoliths are many orders of magnitude lower at ≤ 10 ppm (Jagoutz *et al.*, 1979). Additionally, recent experimental data on the solubility of Ir in basaltic melt (Amosse *et al.*, 1990) indicates that melts saturated with Ir at fO_2's and fS_2's in the range estimated for mantle partial melting would have concentrations of ~ 100 ppb, which is over three orders of magnitude higher than observed in basalts (≤ 0.04 ppb; Table 2.4). The high Ir solubilities in FeS liquid and basalt suggest that Ir-rich alloys would not be stable in mantle peridotites which contain FeS liquid or have had a silicate liquid fraction removed by partial melting. Instead, one would predict that Ir resides in the mantle dissolved in FeS

liquid or another major phase. Mitchell and Keays (1981) analyzed mineral separates from mantle xenoliths for Ir and Pd and found that spinel was enriched in PGE relative to olivine, clinopyroxene and orthopyroxene but that 60 to 80% of the PGE of the xenoliths was contained in the minor intergranular FeS component. It is unclear how much of the 20 to 40% of the PGE that reside in the major phases is dissolved in them or is due to inclusions of sulfides or other trace phases in the major phases.

Silicate/sulfide partition coefficients for PGE have not been determined experimentally and estimates in the literature vary widely from 10^{-2} (Ross and Keays, 1979) to 10^{-5} (Campbell and Barnes, 1984). If the positively sloped PGE patterns for oceanic basalts (Fig. 5.1) were controlled by simple silicate/sulfide partitioning during mantle partial melting then Os, Ir and Ru would have to be much more compatible than Rh, Pt and Pd in FeS liquid. This is not consistent with the patterns that would be expected from the relative thermodynamic stabilities of PGE sulfides which decrease in the order Ru⇒Pt⇒Ir⇒Os (Fig. 2.10). This pattern is also not consistent with the more chalcophile nature of Rh, Pt and Pd compared to Os, Ir and Ru in layered intrusions such as the Stillwater Complex (see section 5.4). Instead, an additional residual phase in the mantle other than FeS, in which Os, Ir and Ru are more compatible than Rh, Pt and Pd seems to be indicated.

In spite of the textural arguments made in favor of Os-Ir-Ru alloy inclusions having formed as liquidus phases and having been trapped by crystallizing chromite, the limited experimental data summarized in App. IV suggest that these alloys would not be stable in the presence of either FeS or basaltic liquid at magmatic temperatures, even if trapped in chromite crystals. The stability of Os-Ir-Ru alloys in the presence of chromite at magmatic temperatures is still unknown, but the apparent mobility of Ir in chromite and the ability of Ir and Ru to substitute into compounds with the spinel structure under highly oxidizing

conditions (*e.g.*, Krutzsch and Kemmler-Sack, 1983; Capobianco and Drake, 1990) suggests that ppm level solubility of Os, Ir and Ru in the chromite structure at high temperatures is at least plausible. It has been suggested by several authors that Ir, Os and Ru substitute for Cr^{3+} in the spinel lattice (Agiorgitis and Wolf, 1978; Morgan *et al.*, 1976). The solubility of these elements in chromite is presently unknown but almost certainly decreases with temperature. Thus, it is possible that exsolution is responsible for forming Os-Ir-Ru alloys during cooling of magmatic chromite after it crystallized with ppm level concentrations of Os-Ir-Ru in solid solution. This would provide an explanation for the fractionation of Os-Ir-Ru from Rh-Pt-Pd during the process of mantle partial melting without having to resort to a metallic Os-Ir-Ru alloy phase in the mantle. The possible compatibility of Os, Ir and Ru in chromite suggests that the presence or absence of spinel (in addition to FeS) in the mantle of the earth and the moon could play a major role in determining the PGE abundances of crustal rocks formed by partial melting.

5.4 MAGMATIC CRYSTALLIZATION

The magmatic process that results in the concentration of PGE from parental magmas with < 100 ppb total PGE into ~ 1 m thick PGE-rich sulfide and chromite horizons with > 10 ppm total PGE is a remarkable feature of layered intrusions. The PGE-rich sulfide and chromite layers concentrate trace elements from very large volumes of magma. The mechanisms by which Rh, Pt and Pd are collected by immiscible iron-sulfide liquids has been extensively studied and was recently reviewed by Naldrett *et al.* (1987). The concentration mechanism for Os, Ir and Ru has not been given much attention, but there is clearly a link with the crystallization of chromite. As stated by Naldrett *et al.* (1987) "*these metals* [Os, Ir and Ru] *may well have been scavenged by chromite in an as yet not-understood way.*"

The Stillwater Complex in Montana provides a good example for discussion of the fractionation of PGE in layered mafic-ultramafic intrusions. The principles are the same in other intrusions such as the Bushveld Complex in South Africa, the Great Dyke in Zimbabwe and the Bird River Sill in Manitoba. Average PGE (and Re) abundances for several different rock-types from the Stillwater Complex are given in Table 5.1 (along with data sources) and plotted normalized to C1 chondrite values in Fig. 5.2. Basal norites are believed to be the best estimates of the parental magma composition of the Stillwater Complex. The PGE contents of the Stillwater basal norites are also virtually the same as the chilled margin rocks from the Bushveld complex (*cf.* Naldrett *et al.*, 1987). Comparison of Fig. 5.2 with Fig. 5.1 shows that the steep positively sloped PGE pattern for the basal norites is very similar to the patterns for basalts and granites, except that the norites are enriched in all of the PGE by a factor of ~ 10. The Re content of the basal norites is unknown, but based on the patterns for basalts and granites their chondrite normalized Re content is probably somewhat higher than the Pd content. Equilibration and settling of immiscible iron-sulfide into a ~ 2 m layer called the "J-M Reef" resulted in 10^1 to $> 10^2$ enrichments in PGE, while retaining the steep positive slope (Fig. 5.2). Crystallization and settling of chromitite layers that do not have high concentrations of accompanying iron-sulfide (chromitites B-K) resulted in $\sim 10^2$ enrichments of Os, Ir and Ru, but $\leq 10^1$ enrichments in Rh, Pt and Pd, resulting in an overall flat PGE pattern (Fig. 5.2). Re is not enriched in the J-M Reef sulfides or in the chromitites suggesting that it is more compatible with silicate liquid than with sulfide or chromite. The pattern for the A chromitite is more complex because it also contains considerable concentrations of iron-sulfide. Chromite has enriched this layer in Os, Ir and Ru, and iron-sulfide has enriched this layer in Rh, Pt and Pt. The resulting pattern is enriched in all of the PGE by $> 10^2$ compared to the basal norites (Fig. 5.2). In summary, all of the PGE appear

Table 5.1 Average PGE (and Re) concentrations in some representative rock-types from the Stillwater Complex, Montana, USA (in ppb).

Rock-type	**Ru**	**Rh**	**Pd**	**Os**	**Ir**	**Pt**	**Re**
Stillwater Complex							
Basal zone [1,2]	--	≤6.0	45	0.82	0.90	21	--
J-M Reef [3,4]	50	150	17300	22	19	5000	6.5
B-K Chromitites [1,2]	199	62	66	48	36	89	0.65
A Chromitites [1]	510	93	8130	--	303	4100	--

-- indicates no data available.
[1] Page *et al.* (1976); [2] Lambert *et al.* (1989); [3] Barnes *et al.* (1985); [4] Martin (1989).

Fig. 5.2 Average concentrations of PGE normalized to C1 chondrites from various layers of the Stillwater Complex, Montana, USA. Data sources are given on Table 5.1. Data are plotted in the same order as in Fig. 5.1. See text for discussion.

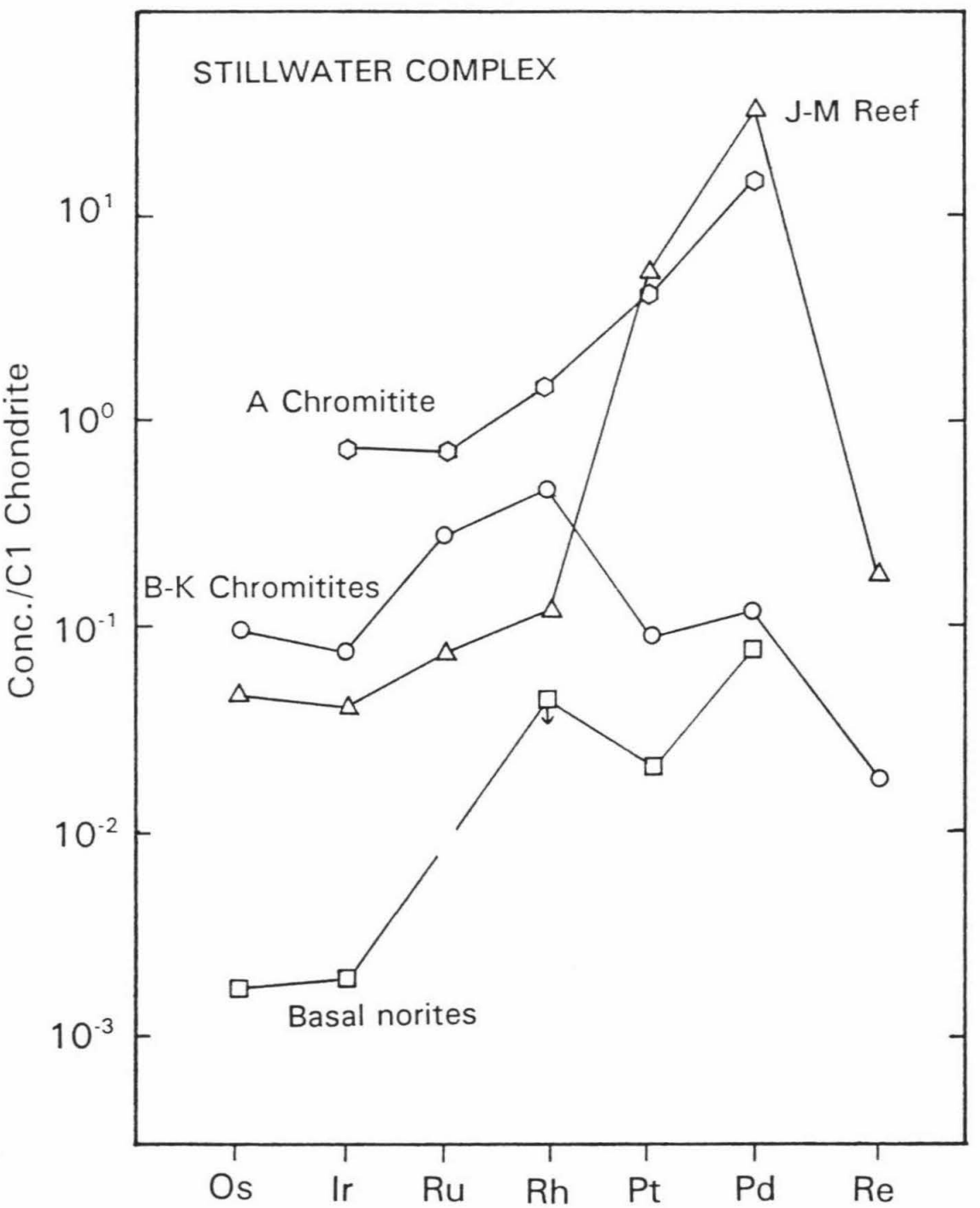
STILLWATER COMPLEX
J-M Reef
A Chromitite
B-K Chromitites
Basal norites
Conc./C1 Chondrite
10^{1}
10^{0}
10^{-1}
10^{-2}
10^{-3}
Os
Ir
Ru
Rh
Pt
Pd
Re

to be compatible in iron-sulfide, but Rh, Pt and Pd are more compatible than Os, Ir and Ru. In contrast, only Os, Ir and Ru appear to be compatible in chromite.

As in the case of ophiolitic peridotites, Os-Ir-Ru-rich alloy and sulfide phases are found included in chromite crystals from layered intrusions. The most common Os-Ir-Ru mineral found in layered intrusions is laurite-erlichmanite solid solution $(Ru,Os,Ir)S_2$ (*e.g.*, Talkington and Lipin, 1986), although Os-Ir-Ru alloys have also been observed (*e.g.*, Cabri and Laflamme, 1988). Extensive subsolidus exsolution and reequilibration of Rh, Pd and Pt-rich sulfides and alloys is known to have taken place in sulfide-rich horizons such as the J-M Reef. It is likely that preexisting Os-Ir-Ru alloys would have been sulfidized during cooling or metamorphism to form laurite at the high ambient fS_2's. Therefore, the origin of laurite inclusions in chromite from layered intrusions is basically the same problem as the origin of Os-Ir-Ru alloys in ophiolitic chromites that was discussed in section 5.3.

During the growth and settling of chromite crystals at magmatic temperatures, Cr and Os-Ir-Ru were efficiently scavenged from large volumes of magma. Most workers have concluded that laurite and Os-Ir-Ru alloys crystallized directly from the silicate magma providing nucleation sites for chromite crystals which grew around them and then settled into chromitite layers. However, as discussed in App. IV and section 5.3 this mechanism does not seem likely. Instead, it is possible that Os, Ir and Ru were accommodated in solid solution as oxides in the chromite lattice and later exsolved as Os-Ir-Ru alloys or laurite at subsolidus temperatures.

5.5 RE-OS GEOCHRONOMETER

^{187}Re decays to ^{187}Os by β^- emission with a halflife of ~ 40 Æ. The usefulness of this isotopic system as a geochronometer has long been recognized (*e.g.*, Herr *et al.*, 1961) but

due to the analytical difficulties in measuring Os isotope ratios it has not been widely utilized. Hirt *et al.* (1963) first determined the ^{187}Re halflife to be 43 $\pm$5 Æ by measuring ^{187}Os in molybdenites of known age which contain abundant Re but no common Os. A more accurate determination of the ^{187}Re halflife was determined by Luck and Allegre (1983) from analyses of iron meteorites. Fractionations of Re and Os are observed between iron meteorite groups; when ^{186}Os is used as a reference isotope and ^{187}Os/^{186}Os is plotted versus ^{187}Re/^{186}Os, a linear array is established. From the slope of this line and the age of chondritic and achondritic meteorites determined by the Rb-Sr and U-Pb isotopic systems a halflife of 45.6 $\pm$1.2 Æ was calculated (Luck and Allegre, 1983). A direct laboratory measurement of the ^{187}Re halflife suggests that it has a significantly lower value of 42.3 $\pm$1.3 Æ (Lindner *et al.*, 1989). This has caused considerable confusion because if the laboratory value is accepted, the age of iron meteorites based on the data of Luck and Allegre (1983) is 4.17 $\pm$0.16 Æ, suggesting that iron meteorites are 0.38 $\pm$0.16 Æ younger than chondrites. This conflicts with iron meteorite ages inferred from the ^{107}Ag-^{107}Pd system (Kaiser and Wasserburg, 1983; Chen and Wasserburg, 1990) that suggest a much shorter timescale between late nucleosynthesis and iron meteorite formation.

Under the reducing conditions of iron and chondritic meteorite genesis, both Re and Os behave as siderophile elements and partition strongly into the metallic phase. Magmatic crystallization of metallic liquids results in fractionations in the Re/Os ratio which range from 0.05 to 0.2 in both the IIAB and IIIAB iron meteorite groups (Pernicka and Wasson, 1987). Under the more oxidizing conditions of terrestrial magmatism Re behaves more like a lithophile element and Os more like a siderophile element, resulting in dramatic fractionations in the Re/Os ratio (Fig. 5.1). The Re/Os ratio of mantle peridotite xenoliths is a nearly chondritic value of $\sim$0.08, whereas the Re/Os ratio of basalts is $\sim$35 (Hertogen *et al.*,

1980). The fractionation arises because Re concentrations of basalts generated by partial melting are close to peridotite values (~1 ppb) but Os concentrations are lower than peridotites by more than a factor of 10^2 (~0.03 ppb) (Table 2.4).

The Re/Os fractionation results in enormous variations in the $^{187}Os/^{186}Os$ ratio between the mantle (~1.0) and average continental crust (~30) (Palmer and Turekian, 1986). Allegre and Luck (1980) measured the $^{187}Os/^{186}Os$ ratio of osmiridium alloys from alluvial deposits associated with ultramafic rocks of known age. They found that these data define a straight line when plotted against age, implying that the mantle source region for all of the osmiridiums has a present Re/Os ratio of 0.085 (the same ratio measured in peridotites) and has changed through time only as a result of the decay of ^{187}Re. The Os isotopic composition at the time of crystallization of the Stillwater intrusion is also consistent with the osmiridium mantle evolution trend (Martin, 1989; Lambert *et al.*, 1989). Some mantle peridotite xenoliths have lower than predicted $^{187}Os/^{186}Os$ suggesting that parts of the sub-continental mantle may have been depleted in Re relative to Os at least 2 Æ ago (Walker *et al.*, 1989). Future studies of Os isotopes from a variety of mantle-derived rocks will test whether there is mantle heterogeneity with respect to the time integrated Re/Os ratio due to processes such as 1) Re depletion from partial melt extraction, 2) radiogenic Os introduction from subduction of oceanic crust, and 3) heterogeneity remaining from incomplete core formation or meteoritic input to the mantle.

The Re-Os isotopic system may prove useful as a geochronometer in certain geological situations where other isotopic systems are inappropriate. For example, iron meteorites, Alaska-type ultramafics, chromitites and sulfides often lack sufficient concentrations or exhibit sufficient fractionations of Rb-Sr, Sm-Nd, K-Ar or U-Pb for dating. Each of these rock-types has high concentrations of Re and Os and is a potential candidate for dating using the Re-Os

system. Basic studies to determine the concentrations, fractionations and mobility of Re and Os in these types of rocks must be done to determine the feasibility of utilizing the Re-Os system. A recent study of Re-Os systematics in organic-rich black shales indicates that Re is concentrated in black shales by reduction from seawater, and that Re/Os ratios vary enough to allow isochron dating (Ravizza and Turekian, 1989). The data indicate that some mobility of Re and/or Os occurs during diagenesis but that the disturbance is less than that which affects the U-Th-Pb and Rb-Sr systems, and may be small enough to allow direct dating of depositional ages.

CHAPTER 6. RESONANCE IONIZATION OF SPUTTERED ATOMS

Geochemical studies of the distribution of Pt-group elements in rocks and minerals have been primarily limited to bulk chemical methods. Radiochemical neutron activation has played the dominant role in establishing the geochemical data base for PGE because it is the only method capable of measuring the sub-ppba (parts per billion atomic) concentrations of PGE that occur in most geological materials (Crockett and Cabri, 1981). The distribution of the PGE among the major rock-forming minerals and their influence on the fractionation of PGE during magmatic processes is virtually unknown and is an important analytical goal in geochemistry. Attempts to determine the concentrations of PGE in minerals using bulk analyses of mineral separates have been ambiguous because of the prevalence of PGE-rich sulfide inclusions and interstitial sulfides (Mitchell and Keays, 1981). Only in unusual cases, where PGE are highly concentrated into sulfides in ore deposits, have *in situ* analytical techniques such as electron microprobe x-ray analysis, synchrotron x-ray fluorescence or particle-induced x-ray emission of PGE been possible (Cabri, 1988). The measurement of the isotopic composition of small quantities of Os is also an important analytical goal in geochemistry because of the geochemical applications of the radioactive decay of ^{187}Re to ^{187}Os (section 5.5).

Resonance ionization mass spectrometry (RIMS) is a newly developing field in chemistry and physics (Hurst and Payne, 1988) that may provide the basis for a new method of ultrasensitive *in situ* geochemical analysis. RIMS has already been successfully utilized for isotopic analysis of Re, Os and Kr in geological materials following chemical separation (*e.g.*, Walker *et al.*, 1988; Thonnard *et al.*, 1987). Several research groups have coupled RIMS with primary ion beam sputtering for use as an *in situ* analytical technique. They have

achieved ultrasensitive detection of impurities such as Fe, In and Si in synthetic industrial materials (Pellin *et al.*, 1988; Parks *et al.*, 1988; Pappas *et al.*, 1989).

The purpose of this work was to investigate the potential application of resonance ionization coupled with ion sputtering (or *resonance ionization of sputtered atoms*) as a new tool in analytical geochemistry. This method holds great promise and should eventually allow the *in situ* measurement of extremely low concentrations of PGE in most minerals, and the measurement of Os isotope ratios on very small sample sizes. The experimental work was carried out at Argonne National Laboratory using a modified version of the SARISA (surface analysis by resonance ionization of atoms) apparatus developed by Pellin *et al.* (1988). A detailed description of the apparatus and the ionization schemes that were evaluated for Os and Re are given in App. V. The analytical procedures and capabilities of the technique for quantitative analyses of Os are given in App. VI. In this chapter a general introduction to resonance ionization of sputtered atoms is given, some highlights of the experimental results presented in Apps. V and VI are summarized, and the future applications of this technique for *in situ* PGE analysis and Os isotope ratio measurement are discussed.

6.1 TRADITIONAL IONIZATION TECHNIQUES

The mass spectrometric analysis of matter is a three step process of ionization, mass separation and ion detection. The methods of mass separation and detection are common to all elements and have been extensively developed. A recent review of mass spectrometry is provided by Duckworth *et al.* (1986). The limitation for elements that are presently difficult to analyze by mass spectrometry (such as the PGE) is in the ionization step. My work has emphasized the development of a new laser-based method for the ionization of PGE, which can be coupled with traditional mass separation and detection systems. The ionization of

solids is itself a two part process which involves vaporizing the species to be analyzed and then removing or adding an electron to produce a charged particle that can be manipulated by electromagnetic fields.

Most isotope ratio measurements of solids are done by thermal ionization, in which the sample is deposited onto a refractory metal filament and heated in the mass spectrometer producing a cloud of vaporized ions and neutrals. By loading samples onto filaments along with a variety of materials such as silica gel and graphite (*e.g.*, Cameron *et al.*, 1969), most elements can now be ionized efficiently by thermal ionization. Some elements, however, evaporate from the filament almost entirely as neutral species and thus cannot be analyzed by thermal ionization. Several of the PGE (including Os) fall into this category. Due to the failure of thermal ionization for Os analysis, a wide variety of alternate methods have been evaluated for Os ionization including electron bombardment of volatile OsO_4 molecules (Herr *et al.*, 1961), laser ablation (Simmons, 1983), inductively coupled plasma ionization (Russ *et al.*, 1987), accelerator mass spectrometry (Teng *et al.*, 1987) and secondary ionization (Luck and Allegre, 1983).

The most successful Os ionization method has been secondary ionization, in which a focused beam of energetic primary ions (usually O^-) is used to bombard the sample and sputter material from it as both ions and neutral atoms. The ratio of sputtered ions to neutrals is difficult to predict *a priori*, and is a complex function of the primary ion used for sputtering, the element being analyzed, the matrix or substrate from which the element is being sputtered, and surface properties such as the extent of oxygen coverage (*e.g.*, Benninghoven, 1975; Williams, 1983). Elements with low ionization energies generally form secondary ions with high efficiency, allowing the ultrasensitive *in situ* analyses for which secondary ionization mass spectrometry has been so successful. Some elements, particularly

those with high ionization energies (including PGE), are sputtered predominantly as neutrals thus precluding the use of secondary ionization for ultrasensitive analyses. Although the ionization efficiency for Os is quite low with secondary ionization ($\leq 10^{-4}$; App. V), this is still the most efficient of the available methods and has been used extensively to measure the isotopic composition of Os after chemical separation from geologic materials (*e.g.*, Luck and Allegre, 1983). The low ionization efficiency necessitates large sample sizes (>1 ng of Os) and limits the precision ($< \pm 1\%$) due to ion counting statistics. Due to the isobaric interference between ^{187}Os and ^{187}Re, lengthy chemical separation procedures are required to quantitatively separate Re from Os prior to analysis by secondary ionization.

6.2 LASER RESONANCE IONIZATION

Resonance ionization is a multistep photon absorption process in which the final state is the ionization continuum of the atom. The individual photons that are used generally do not have sufficient energy to ionize atoms. Instead, their wavelengths are tuned to excite electronic energy levels that are characteristic for each element. First a photon excites an atom from its ground state to a resonant energy level. Then additional photons excite the atom further to other energy levels or to the ionization continuum. Ionization schemes ranging from one to three stepwise resonances have been utilized for this process. In general, the greater the number of resonant steps that are involved in an ionization scheme, the greater the elemental selectivity. To demonstrate the wide applicability of resonance ionization, Hurst *et al.* (1979) compiled a list of the simplest resonance ionization scheme that could be utilized for each element using either one or two lasers. They assumed that the fundamental wavelength of tunable dye lasers, which have sufficient power to saturate photoionization, is 380-750 nm (5.25-1.65 eV). They further assumed that dye lasers can be frequency doubled over the

wavelength range of 217-360 nm (5.71-3.44 eV). The five ionization schemes that they considered are given in Fig. 6.1 and are numbered 1-5 in order of increasing complexity. Using tabulated values for the energy levels of each element they showed that 57 elements could be ionized with one laser, 44 elements could be resonantly ionized with two lasers and only two elements (He and Ne) could not be ionized by these simple schemes (Fig. 6.2).

In order to saturate the resonance ionization levels a high power density on the order of 10^8 Wcm^{-2} in the ultraviolet region is usually required (Hurst and Payne, 1988). Therefore, continuous wave lasers, which have maximum ultraviolet power densities of $\sim 10^2$ Wcm^{-2} in a 1 mm spot, cannot be used efficiently. Ionization must instead be achieved by pulsed lasers. Pulsed lasers can produce ≥ 1 Jcm^{-2} per ~ 10 nsec pulse resulting in a $\geq 10^8$ Wcm^{-2} power density in a 1 mm diameter spot. Modern pulsed lasers operate at maximum repetition rates of 30 Hz (Nd-YAG lasers) to 200 Hz (excimer lasers).

Walker and Fassett (1986) were the first to demonstrate that photons from a pulsed dye laser could be used to enhance the ionization of Os in a mass spectrometer. They thermally vaporized neutral Os atoms from a filament and resonantly ionized them by shining a laser through the atomic vapor cloud. Walker and Fassett used a 10 Hz Nd-YAG laser, which resulted in a 10^{-7} efficiency for the detection of Os atoms loaded onto the filament due to the large differences in the duty cycle of the laser *versus* the continuously heated filament. To help alleviate this problem they minimized the size of the filament and thermally pulsed it as quickly as possible in synchronization with the laser. Because thermal diffusion in the filament limited the narrowness of the vaporization pulse width, this approach only improved the ionization efficiency by a factor of 10^2. With the duty cycle mismatch reduced to 10^{-5} for the pulsed experiment, and a mass spectrometer transmission efficiency of $\sim 10^{-2}$, Walker and Fassett detected 1 out of each 10^7 Os atoms that were vaporized.

Fig. 6.1 Classification of resonance ionization schemes using either one or two tunable dye lasers from Hurst *et al.* (1979). The vertical scale is in arbitrary units of energy. The hachured region indicates the ionization continuum. Wide arrows indicate resonant transitions and narrow arrows indicate ionization to an arbitrary position in the ionization continuum. ω_1 and ω_2 designate the frequencies of the dye lasers; 2ω indicates that the dye laser fundamental is frequency doubled; and the two arrows in scheme 5 without a resonant transition between them indicates a two photon absorption process.

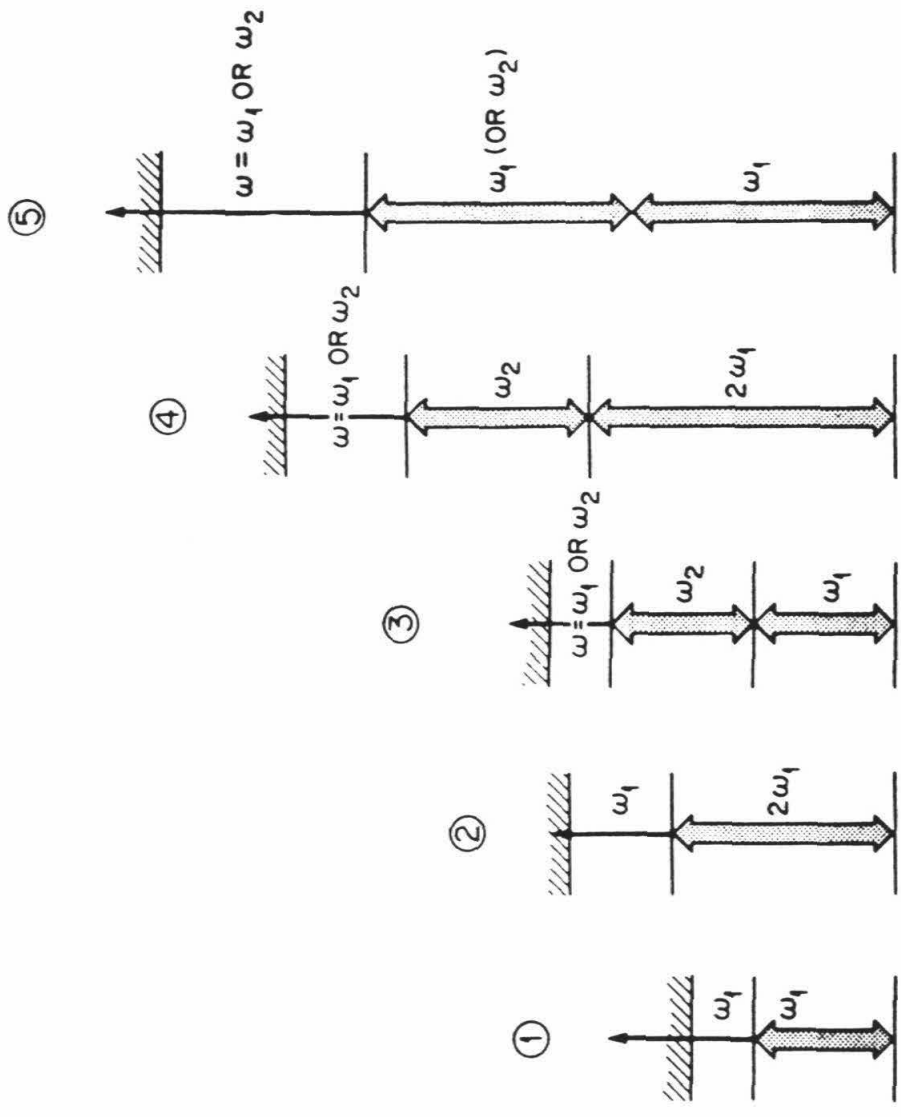
①
ω1
ω1
②
ω1
2ω1
③
ω = ω1 OR ω2
ω2
ω1
④
ω = ω1 OR ω2
ω2
2ω1
⑤
ω = ω1 OR ω2
ω1 (OR ω2)
ω1

Fig. 6.2 Periodic table of the elements indicating the simplest resonance ionization scheme possible using two dye lasers (from Hurst *et al.*, 1979). The definition of the ionization schemes (1-5) is given in Fig. 6.1. It was assumed that the fundamental wavelength of tunable dye lasers is 380-750 nm and the dye lasers can be frequency doubled over the wavelength range 217-360 nm (Hurst *et al.*, 1979).

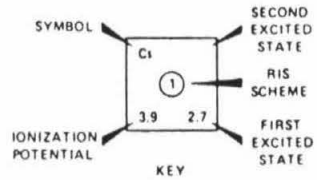

GROUP Ia		IIa		IIIb	IVb	Vb	VIb	VIIb	VIII			Ib	IIb	IIIa	IVa	Va	VIa	VIIa	
H (5) 13.6 10.2																			He (0) 24.6
Li (2) 5.4 3.8		Be 8.0 (4) 9.3 5.3												B 7.2 (4) 8.3 5.0	C (5) 11.3 8.6	N (5) 14.5 12.0	O (5) 13.6 11.0	F (5) 17.4 14.5	Ne (0) 21.6
Na (2) 5.1 3.8		Mg 5.1 (3) 7.6 2.7												Al (1) 6.0 3.1	Si 7.1 (4) 8.1 4.9	P (5) 10.6 8.3	S (5) 10.4 7.9	Cl (5) 13.0 10.3	Ar (5) 15.8 12.8
K (1) 4.3 3.1		Ca (2) 6.1 4.5		Sc (2) 6.6 4.7	Ti (2) 6.8 4.7	V (2) 6.7 4.5	Cr (2) 6.8 5.2	Mn (2) 7.4 5.7	Fe (2) 7.9 5.3	Co (2) 7.9 5.4	Ni (2) 7.6 5.4	Cu 6.2 (4) 7.7 3.8	Zn 6.9 (4) 9.4 4.0	Ga (1) 6.0 3.1	Ge 6.8 (4) 7.9 4.6	As (5) 9.8 7.5	Se (5) 9.8 7.3	Br (5) 11.8 9.3	Kr (5) 14.0 11.3
Rb (1) 4.2 3.0		Sr (2) 5.7 4.3		Y 5.0 (3) 6.4 3.0	Zr 4.6 (3) 6.8 1.9	Nb (2) 6.9 4.7	Mo (2) 7.1 4.8	Tc 5.5 (3) 7.3 2.9	Ru (2) 7.4 4.9	Rh (2) 7.5 5.0	Pd 7.2 (4) 8.3 5.0	Ag 6.0 (4) 7.6 3.8	Cd 6.6 (4) 9.0 3.8	In (1) 5.8 3.0	Sn (2) 7.3 5.4	Sb 7.2 (4) 8.6 5.4	Te 7.9 (4) 9.0 5.5	I (5) 10.5 8.0	Xe (5) 12.1 9.6
Cs (1) 3.9 2.7		Ba (2) 5.2 3.8		La (1) 5.6 3.0	Hf ? (3?) 7 3.1	Ta 5.3 (3) 7.9 2.7	W 5.6 (3) 8.0 3.2	Re (2) 7.9 5.3	Os 5.9 (3) 8.7 2.9	Ir 6.5 (3) 9 3.3	Pt 6.5 (4) 9.0 4.0	Au 7.7 (4) 9.2 4.6	Hg 7.9 (4) 10.4 4.9	Tl (1) 6.1 3.3	Pb 6.4 (4) 7.4 4.4	Bi 6.2 (4) 7.3 4.0	Po 7.4 (4) 8.4 4.8	At (5?) 9.5 ?	Rn (5) 10.7 8.2
Fr (1?) 4 ?		Ra (2) 5.3 3.9		Ac ? (3?) 6.9 2.8															

Ce (1) 5.5 2.9	Pr (1) 5.4 2.8	Nd (1) 5.5 2.8	Pm (1?) 5.6 ?	Sm (1) 5.6 2.8	Eu (2) 5.7 4.2	Gd (1) 6.2 3.1	Tb (1) 5.8 3.2	Dy (1) 5.9 3.1	Ho (1) 6.0 3.1	Er (1) 6.1 3.2	Tm (1) 6.2 3.2	Yb (2) 6.3 4.7	Lu (1) 5.4 3.0
Th (1?) 6.1	Pa (1?) 5.9	U (2) 6.2 4.2	Np (1) 6.3 3.2	Pu (1) 5.7 2.9	Am (2) 6.0 4.2	Cm (1) 6.2 3.1	Bk (1) 6.2 3.2	Cf (1?) 6.3	Es (2) 6.4 4.6	Fm (1?) 6.5	Md (1?) 6.6	No (1?) 6.6	Lw (1?)

6.3 RESONANCE IONIZATION COUPLED WITH SPUTTERING

The resonance ionization method that I have investigated, utilizes a primary ion beam to sputter neutral atoms instead of a filament to thermally vaporize them. In principle, this method should be capable of much higher efficiency than thermal vaporization. The major advantage is that by utilizing electrostatic deflection the ion beam can be precisely pulsed to more closely match the duty cycles of vaporization and ionization. The method has the added advantage that the element being analyzed does not have to be chemically separated from the geologic sample and loaded onto a filament for analysis. Instead, analyses can be made directly on sample specimens (*in situ*) or on chemically concentrated solid fractions.

A schematic diagram of the resonance ionization of sputtered atoms apparatus is shown in Fig. 6.3. It consists of three main subunits: a pulsed primary ion source, three tunable dye lasers pumped by a pulsed XeCl excimer laser and an energy- and angle- refocusing time-of-flight mass spectrometer. A 5 keV primary Ar^+ ion beam with an average current of 2.0 μA and a diameter of $\sim$70 μm is used for sputtering. During analyses, the primary ion beam is chopped into pulses of 200 nsec width by electrostatic deflection at a 40 to 200 Hz repetition rate. The sputtering rate in the 40 Hz pulsed mode is $\sim$10 minutes per monolayer of target. Sputtered species fill a volume above the target during and after the arrival of the primary Ar^+ ion pulse. Approximately 300 nsec after the end of each primary ion pulse, a XeCl excimer laser is fired producing a $\sim$10 nsec ultraviolet pulse which is used to pump the three tunable dye lasers to produce three beams of light. The three laser beams are spatially and temporally overlapped in a volume that extends from about 0.5 to 1.5 mm above the target surface and has a diameter of $\sim$1 mm (Fig. 6.4). Photoionization of sputtered neutral Os atoms occurs within this volume. The time delay between the end of the primary ion pulse and the laser firing is precisely adjusted to maximize the number of sputtered atoms in the

Fig. 6.3 Schematic diagram of the laser resonance ionization of sputtered atoms apparatus used in this study. The wavelength and energy per pulse are given for the XeCl excimer pump laser as is the partitioning of the energy to the three dye lasers for ionization scheme E. The type of dye used for each tunable dye laser in scheme E is given as well as the fundamental or frequency doubled energy produced by each dye laser. The components of the primary ion gun and time-of-flight mass spectrometer are labeled.

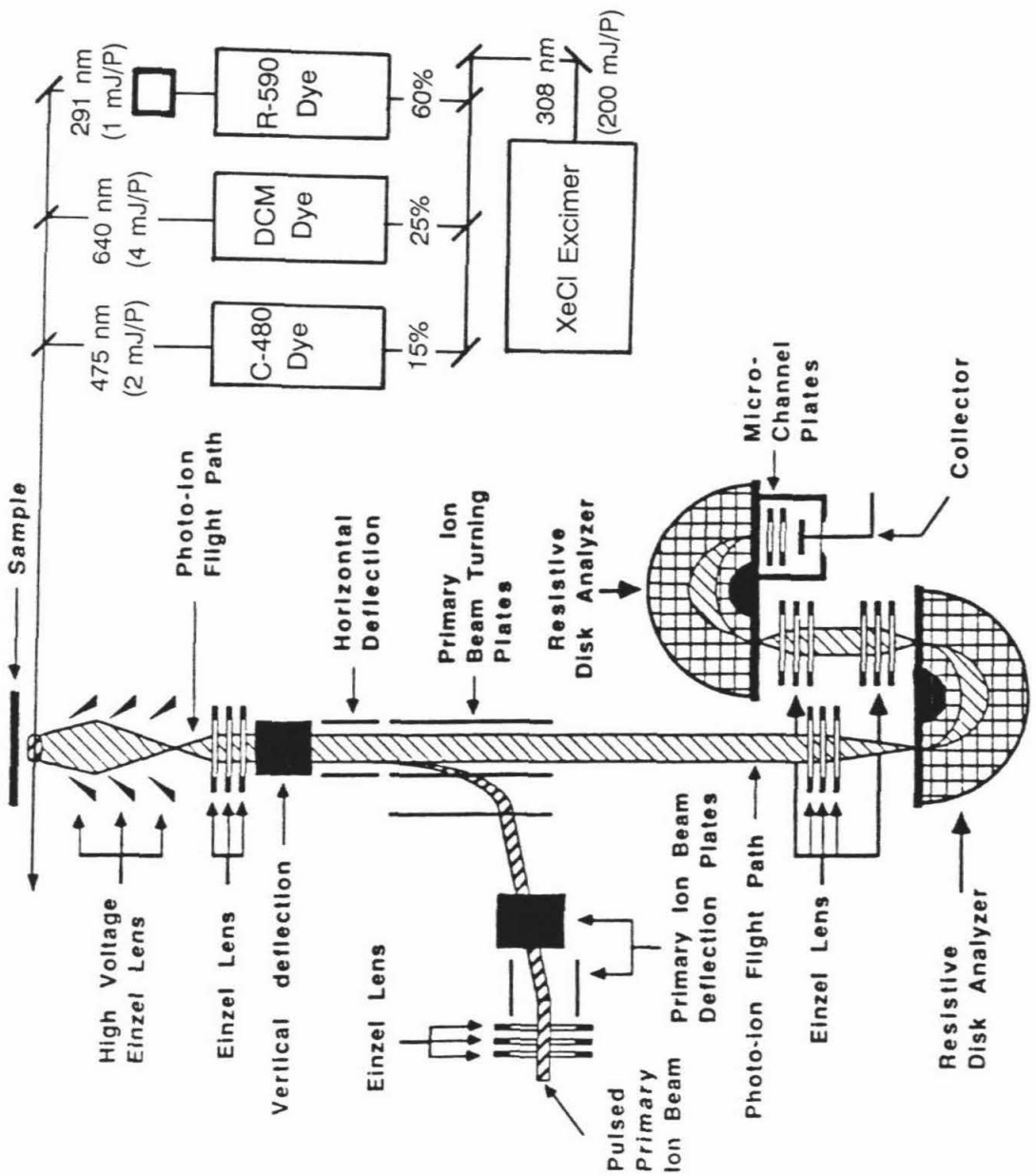
Sample
Photo-Ion Flight Path
Horizontal Deflection
Primary Ion Beam Turning Plates
Resistive Disk Analyzer
Micro-Channel Plates
Collector
High Voltage Einzel Lens
Einzel Lens
Vertical deflection
Einzel Lens
Pulsed Primary Ion Beam
Primary Ion Beam Deflection Plates
Photo-Ion Flight Path
Einzel Lens
Resistive Disk Analyzer
475 nm (2 mJ/P)
640 nm (4 mJ/P)
291 nm (1 mJ/P)
C-480 Dye
DCM Dye
R-590 Dye
15%
25%
60%
XeCl Excimer
308 nm
(200 mJ/P)

Fig. 6.4 Schematic diagram of the photoionization region in the apparatus used in this study. Neutral Os atoms are sputtered during the 200 nsec primary Ar^+ ion pulse. Approximately 300 nsec after the end of each primary ion pulse the lasers are fired producing Os^+ photoions in the region 0.5 to 1.5 mm from the sample. The ions are accelerated into the mass spectrometer for detection.

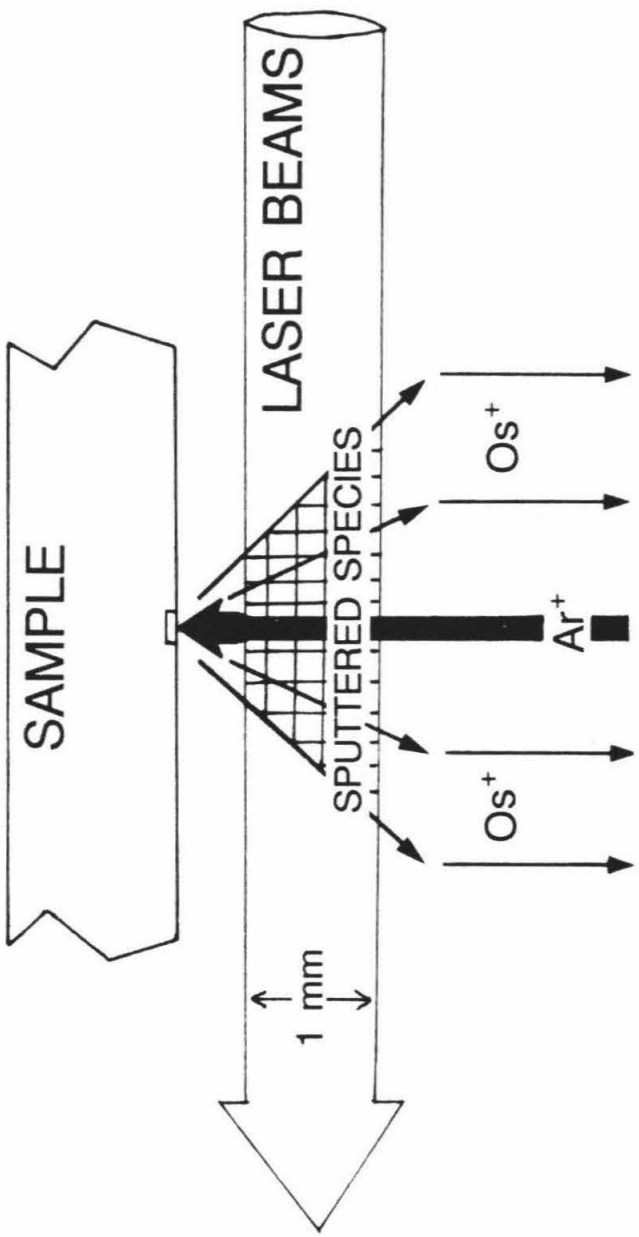
SAMPLE
LASER BEAMS
SPUTTERED SPECIES
Os+
Ar+
Os+
1 mm

ionization volume, which depends on the velocity distribution of the sputtered atoms of interest. Positively charged Os^+ photoions are accelerated away from the target and are focussed in the time-of-flight mass spectrometer by a series of einzel lenses, deflection plates, and two hemispherical resistive disk analyzers. Ions are detected with a chevron-type microchannel plate electron multiplier and arrival times are recorded in 5 nsec windows by a pulse-counting system at low signal levels or by a transient charge digitizer at higher signal levels.

6.4 MULTIPHOTON IONIZATION SCHEMES

One of the most powerful features of resonance ionization is that the ionization process can be elementally selective. In principle this should allow the *in situ* isotopic analysis of both parent and daughter isotopes (such as ^{187}Re and ^{187}Os) without chemical separation, and reduce isobaric and molecular interferences in trace element analyses to levels that will allow ultrasensitive measurements. Walker and Fassett (1986) demonstrated that they could load equal amounts of Re and Os onto a single filament and consecutively analyze Re and then Os with an ionization selectivity of 10^3 for each element with respect to the other. Re was first ionized with a single unfocused laser beam ($\sim$3 mm diameter) tuned to excite Re from the ground state to a single resonance level and then to the ionization continuum. The laser was then tuned to ionize Os from a thermally excited state (containing $\sim$8% of the Os atoms) to a single resonance and then to the ionization continuum. Fassett and Walker found that if the laser beam was tightly focused there was a broadening of resonant transitions and a large increase in nonresonance background, both of which degraded elemental selectivity.

In the experiments reported here, resonance ionization of sputtered atoms was used to analyze samples with equal amounts of Re and Os dissolved in the same Fe-Ni matrix. Since

Re and Os are vaporized simultaneously and with the same efficiency, it is possible to quantitatively evaluate the selectivity of various resonance ionization schemes. Five different classes of ionization schemes (designated A-E) were studied and are shown in Fig. 6.5. Scheme C is equivalent to scheme 1 on Fig. 6.1, scheme D is equivalent to scheme 4 on Fig. 6.1 and scheme E utilizes three lasers and is therefore more complex that any of the ionization schemes on Fig 6.1 from Hurst *et al.* (1979). Measurements of the selectivity of Os ionization relative to Re are reported on Fig. 6.6 for each of the ionization schemes (A-E) that I investigated. Under the experimental conditions reported in App. V the single-resonance two-photon Os ionization scheme (scheme C), which is similar to that used by Walker and Fassett (1986), was found to be ~ 30 x more selective for Os than for Re. Scheme D was ~ 100 x more selective for Os than for Re. By utilizing three resonance energy levels (scheme E) a maximum selectivity for Os relative to Re of $> 10^3$ was demonstrated. The final resonance energy level in this three level scheme (E) is at an energy higher than the ionization potential and is therefore autoionizing. The autoionizing energy level was found by scanning the ionizing laser energy from the ionization potential up in energy while monitoring the signal intensity. Utilization of this previously unknown autoionizing energy level enhanced the signal intensity 10 x relative to scheme C and 5 x relative to scheme D.

6.5 ANALYTICAL CAPABILITIES

To test the efficiency and quantitative capabilities of resonance ionization of sputtered atoms for PGE analyses, synthetic metal standards and metallic phases from iron meteorites that have known Os concentrations were analyzed. The analytical procedures and experimental results are given in App. VI. When the Os^+ signal intensity is plotted versus

Fig. 6.5 Generalized ionization schemes evaluated for Os. Asterisks denote broadband excimer radiation. I.P. indicates the ionization potential for Os.

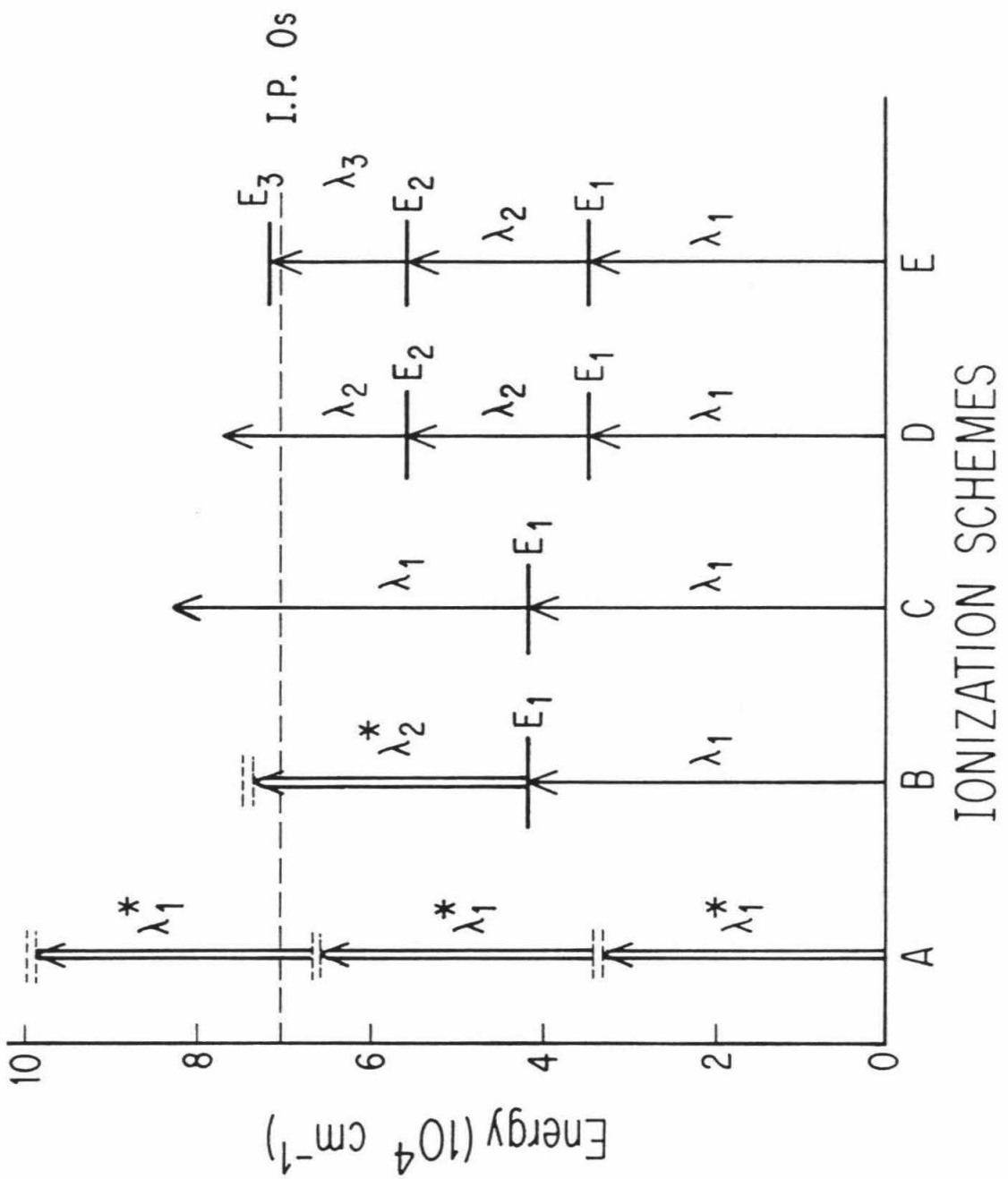
Energy (10^4 cm^{-1})
10
8
6
4
2
0
I.P. Os
E_3
E_2
E_1
λ_1
λ_2
λ_3
*
A
B
C
D
E
IONIZATION SCHEMES

Fig. 6.6 Relative selectivity for ionization of Os compared to Re measured as the logarithm of the ratio of the observed to the true $^{192}Os^{+}/^{185}Re^{+}$ ratio for ionization schemes A-E.

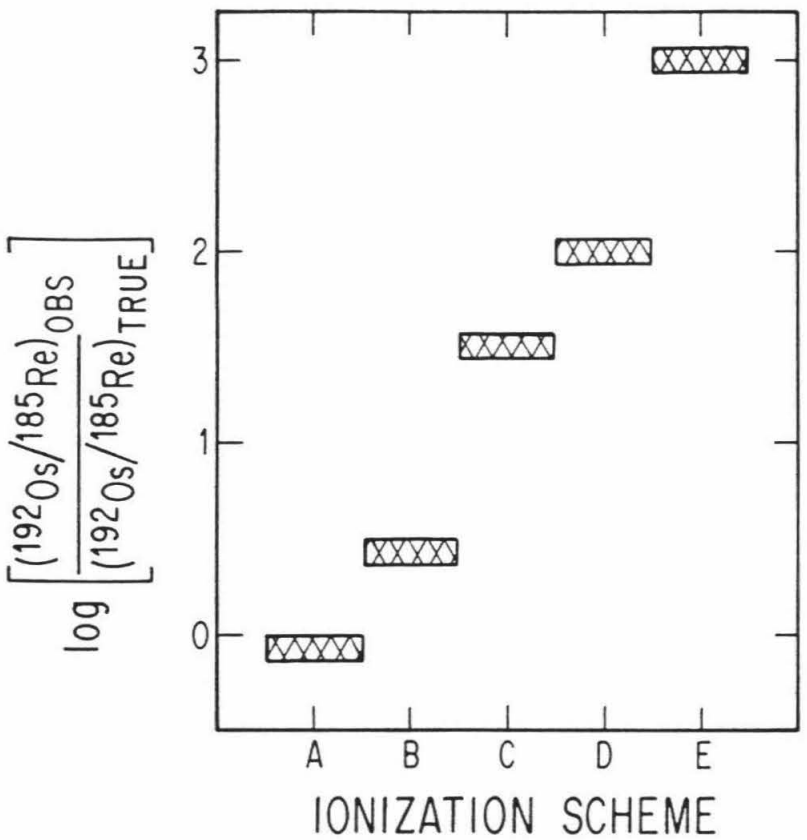
log [(192Os/185Re)OBS / (192Os/185Re)TRUE]
3
2
1
0
A
B
C
D
E
IONIZATION SCHEME

the known Os concentration of the samples, which range from 0.3 to 1000 ppma, the data form a linear array of slope one (Fig. 6.7). The accuracy is $\pm 10\%$ and is well represented by the reproducibilty of replicate analyses. The useful yield (defined here as the ratio of ions detected to atoms sputtered) and the detection limit are two parameters frequently used to characterize an analytical technique. The useful yield is determined from the ratio of Os^+ ions detected per laser shot to the number of Os atoms sputtered from the sample per primary ion pulse. When the number of Os counts per laser shot is divided by the number of atoms sputtered per primary ion pulse a useful yield of $\sim 1\%$ is calculated (App. VI). This useful yield is 10^5 higher than pulsed thermal vaporization resonance ionization (Walker and Fassett, 1986) and $\geq 10^2$ higher than secondary ion mass spectrometry (App. V).

The Os^+ ion yield and the average background count rate were used to calculate the detection limit for *in situ* chemical analysis of Os from Poisson statistics at the 95% confidence level (App. VI). Following the approximation derived by Ziebold (1967) the detection limit for Os for this experiment is 38 ppba for a 125 sec analysis and 7 ppba for a 3600 sec analysis. Utilization of a 200 Hz excimer laser (which are now commercially available) should lower the detection limit to ~ 2 ppba (App. VI). For comparison, the detection limit for PGE commonly quoted for electron microprobe x-ray analysis is ~ 100 ppma with a spatial resolution of $\sim 10\ \mu$m (Crocket and Cabri, 1981). Accelerator mass spectrometry has been used to measure Os, Ir and Pt concentrations in iron meteorites with a detection limit of < 1 to 6 ppba, but with spatial resolution of ≥ 1 mm which is inadequate for most *in situ* applications (Teng *et al.*, 1987; Rasmussen *et al.*, 1989). Particle-induced x-ray emission and synchrotron x-ray fluorescence have been used for analysis of Ru, Rh, Pd and Pt with detection limits in the range of 1-20 ppma and a spatial resolution of $< 10\ \mu$m (Cabri, 1988). Finally, secondary ion mass spectrometry has recently been applied to the

Fig. 6.7 Logarithmic plot of normalized Os^+ signal intensity in ppma *versus* Os concentration determined gravimetrically for synthetic samples or by radiochemical neutron activation for iron meteorite samples by Pernicka and Wasson (1987) and Davis (1977). Circles are synthetic metal standards and triangles and diamonds are iron meteorites. Signal intensities were normalized to the 1000 ppma standard. The minimum detection limit of 7 ppba is calculated for a 3600 sec analysis.

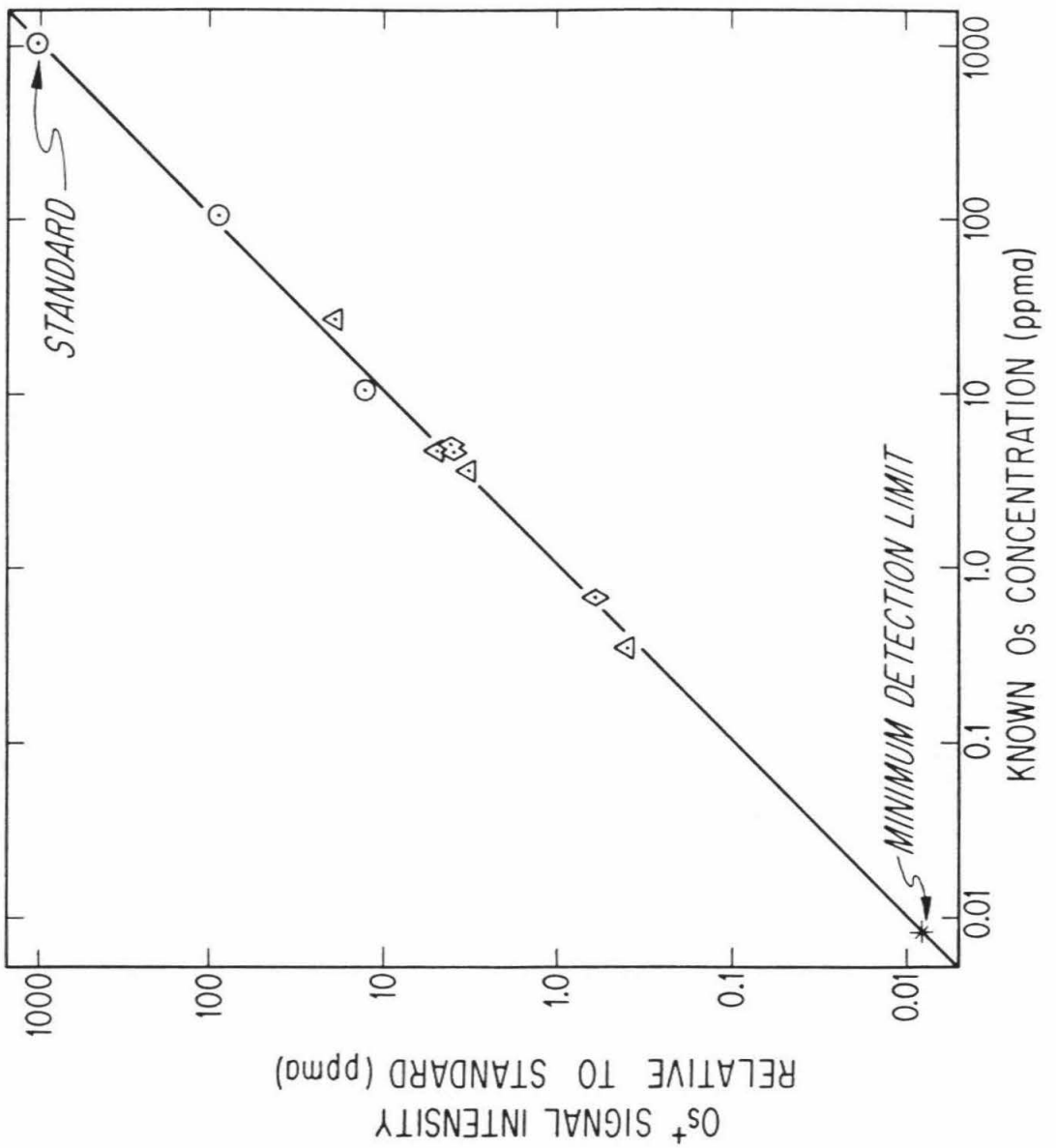
STANDARD
MINIMUM DETECTION LIMIT
1000
100
10
1.0
0.1
0.01
0.01
0.1
1.0
10
100
1000
KNOWN Os CONCENTRATION (ppma)
Os+ SIGNAL INTENSITY
RELATIVE TO STANDARD (ppma)

analysis of Pd, Rh, Ir and Pt with detection limits in the range of 30-200 ppba and a spatial resolution of 60 μm (Chryssoulis *et al.*, 1989).

Resonance ionization of sputtered atoms samples the large neutral fraction of atoms that are sputtered, rather than the much smaller secondary ion fraction sampled by secondary ion mass spectrometry. Matrix-dependent variations in sensitivity should be smaller for photoionization than for sputter-initiated secondary ionization because ionization occurs in the gas phase and is largely independent of the physical properties of the sample. Variations in relative ion yield of several orders of magnitude are common for secondary ion mass spectrometry (*e.g.* Williams, 1983) but appear to be much less than a factor of 10 for resonance ionization of sputtered atoms (Parks *et al.*, 1988). The yield of photoions using resonance ionization of sputtered atoms should depend only on 1) the sputtering rate of the sample, 2) the relative sputter yield of neutral atoms, ions and molecules, and 3) the extent of surface segregation and/or contamination during an analysis.

6.6 POTENTIAL APPLICATIONS

The high useful yield and elemental selectivity of resonance ionization of sputtered atoms allows chemical and isotopic analyses to be made on small numbers of Os (or other PGE) atoms without the need for chemical separation. As discussed in App. V, the time-of-flight mass spectrometer used in these experiments is adequate for concentration measurements but not appropriate for high precision ($< \pm 1\%$) isotope ratio measurements of Os due to its low mass resolution. Resonance ionization of sputtered atoms can, in principle, be coupled with a magnetic sector, quadrupole, or high resolution time-of-flight mass spectrometer for high precision isotope measurements. In this case, the precision of Os measurements would be limited primarily by ion counting statistics. Os occurs in geological materials dissolved at low

concentrations in sulfides, silicates, and spinels and as a major constituent in μm-sized PGE-rich sulfides and alloys. Os measurements of geochemical interest can be grouped into the following categories: 1) *in situ* chemical analyses of Os (and other PGE) at low (sub-ppma) concentrations, 2) *in situ* isotopic analyses of Os at low concentrations, 3) *in situ* isotopic analyses of Os in μm-sized PGE-rich sulfides and alloys, and 4) isotopic analyses of Os chemically concentrated from geological materials.

Simple counting statistics can be used to calculate the approximate precision of Os concentration and $^{187}Os/^{186}Os$ isotope ratio measurements that are potentially possible using this method. In App. VI a useful yield of 1% is demonstrated, which corresponds to 0.069 Os^+ counts per laser shot per ppma of Os in a sample. The experiments reported here were run at a 40 Hz repetition rate, but excimer lasers are available which operate at repetition rates of up to 200 Hz. For a 1 hour analysis at 200 Hz one can calculate that there would be $5x10^4$ Os^+ counts per ppma of Os in a sample. Based on the calculated count rates and counting statistics, it should be possible to measure Os concentrations *in situ* with a precision of $\pm 10\%$ down to 2 ppba, and with a precision of $\pm 1\%$ down to 200 ppba. These detection limits will allow the investigation of Os partitioning and solubilities in mineral phases from iron meteorites, terrestrial mafic and ultramafic rocks, and in phases synthesized in laboratory experiments.

Most geological applications of Os isotope studies require the measurement of $^{187}Os/^{186}Os$ ratios with $< \pm 1\%$ precision (Allegre and Luck, 1980). My calculations indicate that this should be possible for *in situ* measurements of samples with ≥ 15 ppma Os. This is a considerably higher concentration than needed for Os concentration measurements because ^{187}Os and ^{186}Os are minor isotopes ($\sim 1.6\%$ abundance) of Os. As a result, *in situ* Os isotope

investigations will be limited to materials that are enriched in Os such as iron meteorites and Ni-Fe sulfides in peridotites and mafic-ultramafic layered intrusions.

Os is a major constituent in PGE-rich alloys and sulfides that are commonly found as inclusions in spinels associated with ophiolites and layered mafic-ultramafic intrusions. These inclusions range in size from 1 to 20 μm in diameter and have Os concentrations of up to $\sim$20% (*e.g.*, Stockman and Hlava, 1984; Talkington *et al.*, 1984). Although the primary Ar^+ ion beam used in the resonance ionization of sputtered atoms apparatus has a $\sim$70 μm fwhm diameter, small inclusions can still be analyzed for $^{187}Os/^{186}Os$ with a precision of $< \pm 1\%$ if they have high Os concentrations. For example, a 1μm diameter inclusion with 5% Os or a 5μm diameter inclusion with 0.2% Os should be adequate for such an analysis. Thus, the Os isotope systematics of PGE-rich alloys and sulfides from most ophiolites and layered mafic-ultramafic intrusives should be amenable to *in situ* Os isotope studies.

Finally, resonance ionization of sputtered atoms can be used to measure the isotopic composition of extremely small samples of Os that have been chemically concentrated from geological materials. Following separation of Os from rocks by acid dissolution and distillation (*cf.* Luck and Allegre, 1983), samples with as little as 10^{-15} grams of Os could theoretically be used for $^{187}Os/^{186}Os$ ratio measurements with $< \pm 1\%$ precision if they were deposited as thin films onto a substrate for sputtering. Chemical separation of Os would allow Os isotope analyses of mg-size samples of virtually all rock-types including felsic crustal rocks which have Os concentrations as low as $\sim$0.01 ppba (Table 2.4). Os can quite easily be concentrated by a factor of $\sim$10 from bulk rocks into NiS or Ni metal by fire assay fusion (Hoffman *et al.*, 1978). Alternatively, Os can be concentrated by $\sim 10^4$ by NiS fire assay fusion followed by acid dissolution and filtration of acid insoluble residues (Teng *et al.*, 1987). These residues could then be sputtered directly or fused with NiS or Ni metal for

sputtering. Fire assay concentration of Os would allow Os isotopic analysis of ultramafic rocks which generally contain 1 to 10 ppba Os.

It has been shown that resonance ionization of sputtered atoms can be used for quantitative analysis of trace levels of Os in metallic phases with a spatial resolution of $\sim 70\ \mu m$. This technique can be adapted to trace analysis of most high ionization potential elements (including all of the PGE) in a wide variety of natural and synthetic materials by determining the appropriate ionization scheme for each element and tuning the dye laser wavelengths accordingly. To obtain multielement analyses in a single spot, dye laser wavelengths will have to be rapidly tuned to the ionization scheme for each element. The high useful yield and elemental selectivity of resonance ionization of sputtered atoms should eventually allow *in situ* measurement of PGE concentrations down to 2 ppba and the *in situ* measurement of Os isotope ratios down to concentrations of ~ 15 ppma without chemical separation.

REFERENCES

Agioritis G. and Wolf R. (1978) Aspects of osmium, ruthenium and iridium contents in some Greek chromites. *Chem. Geol.* 23, 267-272.

Allegre C.J. and Luck J.M. (1980) Osmium isotopes as petrogenetic and geologic tracers. *Earth and Planet. Sci. Lett.* 48, 148-154.

Alvarez L.W., Alvarez W., Asaro F., and Michel H.V. (1980) Extraterrestrial cause for the Cretaceous-Tertiary extinction. *Science* 108, 1095-1108.

Amossé J., Allibert M., Fischer W. and Peboule M. (1990) Experimental study of the solubility of platinum and iridium in basic silicate melts - Implications for the differentiation of platinum-group elements during magmatic processes. *Chem. Geol.* 81, 45-53.

Anders E. (1978) Procustean science: Indigenous siderophiles in the lunar highlands, according to Delano and Ringwood. *Pro. Lunar Planet. Sci. Conf. 9th*, 161-184.

Anders E. (1987) Local and exotic components of primitive meteorites, and their origin. *Phil. Trans. Royal Soc. Lond. [A]* 323, 287-304.

Anders E. and Grevesse N. (1989) Abundances of the elements: Meteoritic and solar. *Geochim. Cosmochim. Acta* 53, 197-214.

Armstrong J. T., El Goresy A. and Wasserburg G. J. (1985) Willy: A prize noble Ur-Fremdling - Its history and implications for the formation of Fremdlinge and CAI. *Geochim. Cosmochim. Acta* 49, 1001-1022.

Armstrong J. T., Hutcheon I. D. and Wasserburg G. J. (1987) Zelda and company: Petrogenesis of sulfide-rich Fremdlinge and constraints on solar nebular processes. *Geochim. Cosmochim. Acta* 51, 3155-3173.

Arrhenius G. and Raub C. J. (1978) Thermal history of primordial metal grains. *J. Less-common Metals* 62, 417-430.

Auge T. (1988) Platinum-group minerals in the Tiebaghi and Vourinos ophiolitic complexes: genetic implications. *Can. Mineral.* 26, 177-192.

Barnes S.J. and Naldrett A.J. (1985) Geochemistry of the J-M (Howland) reef of the Stillwater complex, Minneapolis adit area. I. Sulfide chemistry and sulfide-olivine equilibrium. *Econ. Geol.* 80, 627-645.

Barnes S.J., Naldrett A.J. and Gorton M.P. (1985) The origin of the fractionation of platinum-group elements in terrestrial magmas. *Chem. Geol.* 53, 303-323.

Barton P. B. and Skinner B. J. (1979) Sulfide mineral stabilities. In *Geochemistry of Hydrothermal Ore Deposits* (ed. H. L. Barnes), pp. 278-403. Wiley and Sons.

Beamish F.E. (1966) *The Analytical Chemistry of the Noble Metals*. Pergamon ,Oxford. 609 p.

Beamish F.E. and Van Loon J.C. (1972) *Recent Advances in the Analytical Chemistry of the Noble Metals*. Pergamon, Oxford. 511 p.

Beamish F.E. and Van Loon J.C. (1977) *Analysis of Noble Metals, Overview and Selected Methods*. Academic Press, New York. 327 p.

Beckett J. R., Live D., Tsay F., Grossman L. and Stolper E. M. (1988) Ti^{3+} in meteoritic and synthetic hibonite. *Geochim. Cosmochim. Acta* 52, 1479-1496.

Benninghoven A. (1975) Developments in secondary ion mass spectroscopy and applications to surface studies. *Surf. Sci.* 53, 596-625.

Bird J.M. and Bassett W.A. (1980) Evidence of a deep mantle history in terrestrial osmium-iridium-ruthenium alloys. *J. Geophys. Res.* 85, 5461-5470.

Bischoff A. and Palme H. (1987) Composition and mineralogy of refractory-metal-rich assemblages from a Ca,Al-rich inclusion in the Allende meteorite. *Geochim. Cosmochim. Acta* 51, 2733-2748.

Blander M., Fuchs L. H., Horowitz C. and Land R. (1980) Primordial refractory metal particles in the Allende meteorite. *Geochim. Cosmochim. Acta* 44, 217-223.

Blander M. and Katz J.L. (1967) Condensation of primordial dust. *Geochim. Cosmochim. Acta* 31, 1025-1034.

Brandstätter F. and Kurat G. (1983) All-Jim: A large Ca-Al-rich chondrule from Allende (C3). (abstr.) *Meteoritics* 18, 272.

Brett R. (1984) Chemical equilibration of the Earth's core and upper mantle. *Geochim. Cosmochim. Acta* 48, 1183-1188.

Brugmann G.E., Arndt N.T., Hofmann A.W. and Tobschall H.J. (1987) Noble metal abundances in komatiite suites from Alexo, Ontario, and Gorgona Island, Columbia. *Geochim. Cosmochim. Acta* 51, 2159-2169.

Cabri L.J. (1981) The platinum-group minerals. In *Platinum-group elements: Mineralogy, geology, recovery* (ed. Cabri, L.J.) Canad. Inst. Mining Metall. Spec. Vol. 23, pp. 83-150.

Cabri L.J. (1988) Applications of proton and nuclear microprobes in ore deposit mineralogy and metallurgy. *Nucl. Inst. and Meth. in Phys. Res.* B30, 459-465.

Cabri L.J., LaFlamme J.H.G., Stewart J.M., Turner K. and Skinner B.J. (1978) On cooperite, braggite and vysotskite. *Amer. Mineral.* 63, 832-839.

Cabri L.J. and Laflamme J.H.G. (1988) Mineralogical study of the Platinum-group element distribution and associated minerals from three stratigraphic layers, Bird River sill, Manitoba. *CANMET Report* CM88-1E, Canadian Govt. Publ. Center, 33 p.

Cameron A.E., Smith D.H. and Walker R.H. (1969) Mass spectrometry of nanogram-size samples of lead. *Anal. Chem.* 41, 525.

Cameron A.G.W. (1973) Abundances of the elements in the solar system *Space Sci. Rev.* 15, 121-146.

Cameron A.G.W. (1962) Formation of the Sun and Planets. *Icarus* 1, 13.

Campbell I.H. and Barnes S.J. (1984) A model for the geochemistry of the platinum-group elements in magmatic sulfide deposits. *Can. Mineral.* 22, 151-160.

Capobianco C.J. and Drake M.J. (1990) Partitioning of ruthenium, rhodium and palladium between spinel and silicate melt. *Geochim. Cosmochim. Acta* 54, 869-874.

Chase M.W.Jr., Davies C.A., Downey J.R.Jr., Frurip D.J., McDonald R.A. and Syverud A.N. (1985) JANAF thermochemical tables, 3rd ed. *J. Phys. Chem. Ref. Data* 14, Supp. 1.

Chen J.H. and Wasserburg G.J. (1990) The presence of ^{107}Pd in the early solar system *Lunar Planet. Sci. Conf. XXI*, 184-185.

Chou C.L. (1978) Fractionation of siderophile elements in the earth's upper mantle. *Proc. Lunar Planet. Sci. Conf. 9th*, 219-230.

Chryssoulis S.L., Alcock R.A., Sizgoric M.B. and Cabri L.J. (1989) Quantitative trace PGE analyses of phyrrhotite, pentlandite and millerite (abstr). *5th International Platinum Symposium, Geol. Soc. of Finland Bull.* 61, 56.

Clayton D.D. (1964) Cosmoradiogenic chronologies of nucleosynthesis. *Astrophys. J.* 137, 637-663.

Cotton F.A. and Wilkinson G. (1980) *Advanced inorganic chemistry*. Wiley and Sons, 1396 pp.

Crockett J.H. (1981) Geochemistry of the platinum-group elements. In *Platinum-group elements: Mineralogy, geology, recovery* (ed. Cabri, L.J.) Canad. Inst. Mining Metall. Spec. Vol. 23, pp. 47-64.

Crockett J.H., Keays R.R. and Hsieh S. (1967) Precious metal abundances in some carbonaceous and enstatite chondrites. *Geochim. Cosmochim. Acta* 31, 1615-1623.

Crockett J.H. and Cabri L.J. (1981) Analytical methods for the platinum-group elements. In *Platinum-Group Elements: Mineralogy, Geology, Recovery.* (ed. Cabri L.J.), pp 71-82. The Canad. Inst. of Mining and Metall.

Davis A.M. (1977) The cosmochemical history of the pallasites. *Ph.D. Dissertation, Yale University.*

Delano J.W. and Ringwood A.E. (1978) Siderophile lements in the lunar highlands: nature of indigenous component and implications for the origin of the moon. *Proc. Lunar Planet. Sci. Conf. 9th*, 111-159.

Drake M.J. (1987) Geochemical constraints on the origin of the moon. *Geochim. Cosmochim. Acta* 47, 1759-1767.

Duckworth H.E., Barber R.C. and Venkatasubramanian V.S. (1986) *Mass Spectrometry*, Cambridge University Press, 337 p.

El Goresy A., Nagel K. and Ramdohr P. (1978) Fremdlinge and their noble relatives. *Proc. Lunar Planet. Sci. Conf.* 9th, 1279-1303.

Elliott R.P. (1965) *Constitution of Binary Alloys, 1st Supplement*. McGraw Hill, New York, 877 p.

Fegley B. and Palme H. (1985) Evidence for oxidizing conditions in the solar nebula from Mo and W depletions in refractory inclusions in carbonaceous chondrites. *Earth and Planet. Sci. Lett.* 72, 311-326.

Fuchs L. H. and Blander M. (1977) Molybdenite in calcium-aluminum-rich inclusions in the Allende meteorite. *Geochim. Cosmochim. Acta* 41, 1170-1175.

Geiger T. and Bischoff A. (1989) Mineralogy of metamorphosed carbonaceous chondrites (abstr). *Meteoritics* 24, 269.

Geller S. (1962) The crystal structure of the superconductor $Rh_{17}S_{15}$. *Acta. Cryst.* 15, 1198-1201.

Gijbels R.H., Millard H.T., Desborough G.A. and Bartel A.J. (1974) Osmium, ruthenium, iridium and uranium in silicates and chromite from the eastern Bushveld Complex, South Africa. *Geochim. Cosmochim. Acta* 38, 319-337.

Goldberg E.D., Koide M., Yang J.S. and Bertine K.K. (1988) Comparative marine chemistries of platinum group metals and their periodic table neighbors. In *Metal speciation: Theory, analysis and applications.* (eds. J.R. Kramer and H.E. Allen), pp. 201-217, Lewis Publishers.

Greenwood N.N. (1968) *Ionic Crystals, Lattice Defects and Nonstoichiometry*. Butterworth & Co. Ltd.

Griffith W.P. (1967) *The Chemistry of the Rarer Platinum Metals (Os, Ru, Ir, and Rh).* Interscience, London. 491 p.

Grossman L. (1972) Condensation in the primitive solar nebula. *Geochim. Cosmochim. Acta* 36, 597-619.

Grossman L. (1973) Refractory trace elements in Ca-Al-rich inclusions in the Allende meteorite. *Geochim. Cosmochim. Acta* 37, 1119-1140.

Grossman L. (1980) Refractory inclusions in the Allende meteorite. *Ann. Rev. Earth Planet. Sci.* 8, 559-608.

Grossman L., Olsen E. and Lattimer J. M. (1979) Silicon in carbonaceous chondrite metal: Relic of high temperature condensation. *Science* 206, 449-451.

Grossman L. and Ganapathy R. (1976) Trace elements in the Allende meteorite--I. coarse-grained, Ca-rich inclusions. *Geochim. Cosmochim. Acta* 40, 331-344.

Grossman L., Davis A. M., Ekambaram V., Armstrong J. T., Hutcheon I. D. and Wasserburg G. J. (1986) Bulk chemical composition of a Fremdling from an Allende Type B inclusion. (abstr.) *Lunar Planet. Sci.* XVII, 295-296.

Hansen M. and Anderko K. (1958) *Constitution of Binary Alloys*. McGraw Hill, New York. 1305 p.

Harris D.C. and Cabri L.J. (1973) The nomenclature of the natural alloys of osmium, iridium and ruthenium based on new compositional data of alloys from world-wide occurences. *Can. Mineral.* 12, 280-284.

Hartley F.R. (1973) *Chemistry of Platinum and Palladium*. Wiley, New York. 544 p.

Hashimoto A., Kumazawa M. and Onuma N. (1979) Evaporation metamorphism of primitive dust material in the early solar system. *Earth Planet. Sci. Lett.* 43, 13-21.

Herr W., Hoffmeister W., Hirt B., Geiss J. and Houtermans F.G. (1961) Versuch zur datierung von eisenmeteoriten nach der rhenium-osmium-methode. *Z. Naturforsch.* 16a, 1053-1058.

Hertogen J., Janssens M.-J. and Palme H. (1980) Trace elements in ocean ridge basalt glasses: implications for fractionations during mantle evolution and petrogenesis. *Geochim. Cosmochim. Acta* 44, 2125-2143.

Hirt B., Tilton G.R., Herr W. and Hoffmeister W. (1963) The halflife of ^{187}Re. In *Earth Sciences and Meteoritics* (eds. J. Geiss and E.D. Goldberg), pp. 273-280. North Holland Publishing Co., Amsterdam.

Hoffman E.L., Naldrett A.J., Van Loon J.C., Hancock R.G.V. and Manson A. (1978) The determination of all of the platinum group elements and gold in rocks and ore by neutron activation analysis after preconcentration by a nickel sulfide fire-assay technique on large samples. *Analytica Chimica Acta* 102, 157-166.

Hsieh K., Chang Y. A. and Zhang T. (1982) The Fe-Ni-S system above 700 C. *Bull. Alloy Phase Equil.* 3, 165-172.

Hultgren R., Desai P.D., Hawkins D.T., Gleiser M., Kelley K.K. and Wagman D.D. (1973) *Selected Values of the Thermodynamic Properties of the Elements*. American Society for Metals, Metals Park, Ohio.

Hurst G.S., Payne M.G., Kramer S.D. and Young J.P. (1979) Resonance ionization spectroscopy and one-atom detection. *Rev. Mod. Phys.* 51, 767-819.

Hurst G.S. and Payne M.G. (1988) *Principles and applications of resonance ionization spectroscopy*. IOP Publishing Ltd, 417 p.

Hutcheon I.D., Armstrong J.T. and Wasserburg G.J. (1987) Isotopic studies of Mg, Fe,Mo,Ru and W in Fremdlinge from Allende refractory inclusions. *Geochim. Cosmochim. Acta* 51, 3175-3192.

Jagoutz E., Palme H., Baddenhausen H., Blum K., Cendales M., Dreibus G., Spettel V., Lorenz V. and Wanke H. (1979) The abundances of major, minor and trace elements in the earth's mantle as derived from primitive ultramafic nodules. *Proc. Lunar Planet. Sci. Conf. 10th* 2031-2050.

Jones J.H. and Drake M.J. (1986) Geochemical constraints on core formation in the Earth. *Nature* 322, 221-228.

Kaiser T. and Wasserburg G. J. (1983) The isotopic composition and concentration of Ag in iron meteorites and the origin of exotic silver. *Geochim. Cosmochim. Acta* 47, 43-58.

Keays R.R. (1982) Palladium and iridium in komatiites and associated rocks: Application to petrogenetic problems. In *Komatiites* (eds. N.T. Arndt and E.G. Nisbet) pp. 435-458, Allen Unwin, London.

Kelly W. R. and Larimer J. W. (1977) Chemical fractionations in meteorites--VIII. Iron meteorites and the cosmochemical history of the metal phase. *Geochim. Cosmochim. Acta* 41, 93-111.

Kimura K., Lewis R.S. and Anders E. (1974) Distribution of gold and rhenium between nickel-iron and silicate melts: implications for the abundances of siderophile elements on the earth and moon. *Geochim. Cosmochim. Acta* 38, 683-701.

King E.A. (1983) Reduction, partial evaporation, and spattering: Possible chemical and physical processes in fluid drop chondrule formation. *Pro. Lunar Planet. Sci. Conf. 14th*, 180-187.

Kracher A., Keil K., Kallemeyn G. W., Wasson J. T., Clayton R. N. and Huss G. I. (1985). The Leoville (CV3) accretionary breccia. *J. Geophys. Res.* 90, D123-D135.

Krutzch B. and Kemmler-Sack S. (1983) Sauerstoff-spinelle mit ruthenium und iridium. *Mat. Sci. Bull.* 18, 647-652.

Kurat G., Hoinkes G. and Fredriksson K. (1975) Zoned Ca-Al-rich chondrule in Bali: New evidence against the primordial condensation model. *Earth and Planet. Sci. Lett.* 26, 140-144.

Kyte F.T., Smit J. and Wasson J.T. (1985) Siderophile interelement variations in the Cretaceous-Tertiary boundary sediments from Caravaca, Spain. *Earth Planet. Sci. Lett.* 73, 183-195.

Lambert D.D., Morgan J.W., Walker R.J., Shirey S.B., Carlson R.W., Zientek M.L. and Koski M.S. (1989) Rhenium-osmium and samarium-neodymium isotopic systematics of the Stillwater complex. *Science* 244, 1169-1174.

Larimer J.W. (1967) Chemical fractionations in meteorites - I. Condensation of the elements. *Geochim. Cosmochim. Acta* 31, 1215-1238.

Larimer J.W. and Anders E. (1967) Chemical fractionations in meteorites-II. Abundance patterns and their interpretation. *Geochim. Cosmochim Acta.* 31, 1239-1270.

Lattimer J.M., Schramm D.N. and Grossman L. (1978) Condensation in supernova ejecta and isotopic anomalies in meteorites. *Astrophys. J.* 219, 230-249.

Lee T., Papanastassiou D.A. and Wasserburg G.J. (1977) Aluminum-26 in the early solar system: Fossil or fuel? *Astrophys. J.* 211, L107-L110.

Legendre O. and Auge T. (1986) Mineralogy of platinum-group-mineral inclusions in chromitites from different ophiolitic complexes. In *Metallogeny of Basic and Ultrabasic Rocks* (eds. Gallagher M.J., Ixer R.A., Neary C.R. and Prichard H.M.), pp 361-372. Inst. Mining Metall., London.

Leonard B.F., Desborough G.A. and Page N.J. (1969) Ore microscopy and chemical compositions of some laurites. *Amer. Mineral.* 54, 1330-1346.

Lindner M., Leich D.A., Russ G.P., Bazan J.M. and Borg R.J. (1989) Direct determination of the halflife of ^{187}Re. *Geochim. Cosmochim. Acta* 53, 1597-1606.

Loebenstein J.R. (1989) Platinum-group metals. *Minerals Yearbook, 1987.* U.S. Govt. Printing Office, 689-700.

Lord H.C. III (1965) Molecular equilibria and condensation in a soar nebula and cool stellar atmospheres. *Icarus* 4, 279-288.

Luck J.M. and Allegre C.J. (1983) ^{187}Re-^{187}Os systematics in meteorites and cosmochemical consequences. *Nature* 302, 130-132.

MacPherson G.J., Wark D.A. and Armstrong J.T. (1988) Primative material surviving in chondrites: Refractory inclusions. In *Meteorites and the early solar system.* (eds. Kerridge J.F. and Matthews M.S.), pp 746-807. Univ. of Arizona Press, Tucson.

Malvin D.J., Drake M.J., Benjamin T.M., Duffy C.J., Hollander M. and Rogers P.S.Z. (1986) Experimental partitioning studies of siderophile elements amongst lithophile phases: Preliminary results using PIXE microprobe analysis. *Pro. Lunar Planet. Sci. Conf. 17th*, 514-515.

Martin C.E. (1989) Re-Os isotopic investigation of the Stillwater complex, Montana. *Earth and Planet. Sci. Lett.* 93, 336-344.

Mashamichi M., Fujii N. and Takeda H. (1981) Ordinary chondrite parent body: An internal heating model. *Proc. Lunar Sci. Conf.* 12th, 1145-1152.

Mason B. and Taylor S.R. (1982) Inclusions in the Allende meteorite. *Smithsonian Contrib. Earth Sci.* 25, 1-30.

Massalski T. B. (1986) *Binary Alloy Phase Diagrams*. Amer. Soc. Metals. 2208p.

McLaughlin A.I.G. (1946) Toxic Manifestations of osmium tetroxide. *British Journal of Industrial Medicine* 3, 183-186.

McMahon B. M. and Haggerty S. E. (1980) Experimental studies bearing on the magnetite-alloy-sulfide association in the Allende meteorite: Constraints on the conditions of chondrule formation. *Proc. Lunar Planet. Sci. Conf.* 11th, 1003-1025.

McSween H. Y. Jr. (1977) Petrographic variations among carbonaceous chondrites of the Vigarano type. *Geochim. Cosmochim. Acta* 41, 1777-1790.

Meeker G. P., Wasserburg G. J. and Armstrong J. T. (1983) Replacement textures in CAI and implications regarding planetary metamorphism. *Geochim. Cosmochim. Acta* 47, 707-721.

Mills K.C. (1974) *Thermodynamic Data for Inorganic Sulfides, Tellurides, and Selenides.* Butterworths, London. 845 p.

Misra K. C. and Fleet M. E. (1973) The chemical compositions of synthetic and natural pentlandite assemblages. *Econ. Geol.* 68, 518-539.

Mitchell R.H. and Keays R.R. (1981) Abundance and distribution of Au,Pd, and Ir in some spinel and garnet lherzolites: Implication for the nature and origin of precious metal-rich intergranular components in the upper mantle. *Geochim. Cosmochim. Acta* 45, 2425-2442.

Moffatt W.G. (1979) *The Handbook of Binary Phase Diagrams*. General Electric, Schenectady.

Morgan J.W. (1986) Ultramafic xenoliths: clues to Earth's late accretionary history. *J. Geophys. Res.* 91, 12375-12387.

Morgan J.W. and Lovering J.F. (1967) Rhenium and Osmium abundances in chondritic meteorites. *Geochim. Cosmochim. Acta* 31, 1893-1909.

Morgan J.W. and Lovering J.F. (1967) Rhenium and Osmium abundances in some igneous and metamorphic rocks. *Earth and Planet. Sci. Lett.* 3, 219-224.

Morgan J.W., Ganapathy R., Higuchi H. and Krahenbuhl U. (1976) Volatile and siderophile trace elements in anorthositic rocks from Fiskenaesset, West Greenland: comparison with lunar and meteoritic analogues. *Geochim. Cosmochim. Acta* 40, 861-888.

Muller O. and Roy R. (1969) Synthesis and crystal structure of Mg_2PtO_4 and Zn_2PtO_4. *Mat. Res. Bull.* 4, 39-43.

Muller O. and Roy R. (1971) Synthesis and crystal structure of some new complex palladium oxides. In *Platinum Group Metals and Compounds* (ed. R.F. Gould). American Chemical Society.

Naldrett A.J. (1981) Platinum-group element deposits. In *Platinum-Group Elements: Mineralogy, Geology, Recovery.* (ed. Cabri L.J.), pp 197-232. The Canad. Inst. of Mining and Metall.

Naldrett A.J. and Cabri L.J. (1976) Ultramafic and related mafic rocks: Their classification and genesis with special reference to the concentration of nickel sulfides and platinum-group elements. *Econ. Geol.* 71, 1131-1158.

Naldrett A.J., Cameron G., von Gruenewaldt G. and Sharpe M.R. (1987) The formation of stratiform PGE deposits in layered intrusions. In *Origins of igneous layering*. Ed. I. Parsons, pp. 313-397, Reidel Publishing Company.

Newsom H.E. and Taylor S.R. (1989) Geochemical implications of the formation of the moon from a giant impact. *Nature* 338, 29-34.

Officer C.B. and Drake C.L. (1985) Terminal Cretaceous environmental events. *Science* 227, 1161-1167.

Page N.J., Rowe J.J. and Haffty J. (1976) Platinum metals in the Stillwater Complex, Montana. *Econ. Geol.* 71, 1352-1363.

Page N.J., Cassard D. and Haffty J. (1982) Pd, Pt, Rh, Ru and Ir in chromitites from the Massif du Sud and Tiebaghi Massif, New Caledonia. *Econ. Geol.* 77, 1571-1577.

Page N.J., Zientek M.L., Czamanske G.K. and Foose M.P. (1985) Sulfide mineralization in the Stillwater Complex and underlying rocks. In *Stillwater Complex.* Eds. G.K. Czamanske and M.L. Zientek, pp. 147-210, Montana Bureau of Mines and Geology Spec. Pub. 92.

Palme H. and Wlotzka F. (1976) A metal particle from a Ca,Al-rich inclusion from the meteorite Allende, and condensation of refractory siderophile elements. *Earth Planet. Sci. Lett.* 33, 45-60.

Palme H., Wlotzka F., Nagel K. and El Goresy A. (1982) An ultra-refractory inclusion from the Ornans carbonaceous chondrite. *Earth. Planet. Sci. Lett.* 61, 1-12.

Palmer M.R. and Turekian K.K. (1986) $^{187}Os/^{186}Os$ in marine manganese nodules and the constraints on the crustal geochemistries of rhenium and osmium. *Nature* 319, 216-220.

Pappas D.L., Hrubowchak D.M., Ervin M.H. and Winograd N. (1989) Atom counting at surfaces. *Science* 243, 64-66.

Parks J.E., Spaar M.T. and Cressman P.J. (1988) Analysis of high purity solids by resonance ionization spectroscopy. *J. Crystal Growth* 89, 4-15.

Pellin M.J., Young C.E., and Gruen D.M. (1988) Multiphoton ionization followed by time-of-flight mass spectroscopy of sputtered neutrals. *Scanning Microscopy* 2, 1353-1364.

Peng Z., Chang C. and Ximen L. (1978) Discussion of published articles in the research of new minerals of the platinum-group discoverd in China in recent years. *Acta. Geol. Sin.* 4, 326-336.

Pernicka E. and Wasson J.T. (1987) Ru, Re, Os, Pt and Au in iron meteorites. *Geochim. Cosmochim. Acta* 51, 1717-1726.

Poths H., Schmitt-Strecker S. and Begemann F. (1987) On the isotopic composition of ruthenium in the Allende and Leoville carbonaceous chondrites. *Geochim. Cosmochim. Acta* 51, 1143-1149.

Rasmussen K.L., Greenway T.J.L. and Gwozdz R. (1989) The composition of kamacite in iron meteorites investigated by accelerator mass spectrometry, neutron activation analysis and analytical electron microscopy. *Nucl. Instr. and Meth. in Phys. Res.* B36, 43-52.

Ravizza G. and Turekian K.K. (1989) Application of the ^{187}Re-^{187}Os system to black shale geochronometry. *Geochim. Cosmochim. Acta* 53, 3257-3262.

Ringwood A.E. (1977) Composition of the core and implications for the origin of the earth. *Geochim. J.* 11, 111-135.

Ross J.R. and Keays R.R. (1979) Precious metals in volcanic-type nickel sulfide deposits in Western Australia, I. Relationship with the composition of the ores and their host rocks. *Can. Mineral.* 17, 417-435.

Russ G.P., Bazan J.M. and Date A.R. (1987) Osmium isotopic ratio measurements by inductively coupled plasma source mass spectrometry. *Anal. Chem.* 59, 984-989.

Sax N.I. (1968) *Dangerous Properties of Industrial Materials*. Van Nostrand Reinhold, New York.

Schmitt W., Palme H. and Wanke H. (1989) Experimental determination of metal/silicate partition coefficients for P,Co,Ni,Cu,Ga,Ge,Mo, and W and some implications for the early evolution of the Earth. *Geochim. Cosmochim. Acta* 53, 173-185.

Scott E.R.D. (1972) Chemical fractionation in iron meteorites and its interpretation. *Geochim. Cosmochim. Acta* 36, 1205-1236.

Scott E.R.D. and Wasson J.T. (1975) Classification and properties of iron meteorites. *Rev. Geophys. Space Sci.* 13, 527-546.

Shunk F.A. (1969) *Constitution of Binary Alloys, 2nd Supplement*. McGraw-Hill, New York. 720 p.

Simmons D.S. (1983) Isotopic analysis with the laser microprobe mass analyzer. *Internat. Jour. Mass Spec. Ion Proc.* 55, 15-30.

Snetsinger K.G. (1971) Erlichmanite (OsS_2), a new mineral. *Amer. Mineral.* 56, 1501-1506.

Stevens G.T., Hatherly M. and Bowles J.S. (1978) The ordered phase fields of the iron-nickel-platinum equilibrium diagram. *J. Mater. Sci.* 13, 499-504.

Stevenson D.J. (1981) Models of the Earth's core. *Science* 214, 611-619.

Stevenson D.J. (1987) Origin of the moon - the collision hypothesis. *Ann. Rev. Earth. Planet. Sci.* 15, 271-315.

Stockman H.W. and Hlava P.F. (1984) Platinum-group minerals in alpine chromitites from southwestern Oregon. *Econ. Geol.* 79, 491-508.

Stolper E. M. (1982) Crystallization sequences of Ca,Al-rich inclusions from Allende: An experimental study. *Geochim. Cosmochim. Acta* 46, 2159-2180.

Stolper E. M. and Paque J. M. (1986) Crystallization sequences of Ca-Al-rich inclusions from Allende: The effects of cooling rate and maximum temperature. *Geochim. Cosmochim. Acta* 50, 1785-1806.

Svendsen S. R. (1979) High energy enthalphy and decomposition pressures of RuS_2. *Acta Chem. Scandinavica* A33, 601-607.

Symonds R.B., Rose W.I., Reed M.H., Lichte F.E. and Finnegan D.L. (1987) Volatilization, transport and sublimation of metallic and non-metallic elements in high temperature gases at Merapi Volcano, Indonesia. *Geochim. Cosmochim. Acta* 51, 2083-2101.

Talkington R.W. and Lipin B.R. (1986) Platinum-group minerals in chromite seams of the Stillwater complex, Montana. *Econ. Geol.* 81, 1179-1186.

Talkington R.W., Watkinson D.H., Whittaker P.J. and Jones P.C. (1984) Platinum-group minerals and other solid inclusions in chromite of ophiolitic complexes: occurrence and petrological significance. *TMPM Tschermaks Min. Petr. Mitt.* 32, 285-301.

Teng R.T.D., Fehn U., Elmore D., Hemmick T.K., Kubik P.W. and Gove H.E. (1987) Determination of Os isotopes and Re/Os ratios using AMS. *Nucl. Instr. and Meth. in Phys. Res.* B29, 281-285.

Thonnard N., Willis R.D., Wright M.C. and Davis W.A. (1987) Resonance ionization spectroscopy and the detection of ^{81}Kr. *Nucl. Instr. and Meth. in Phys. Res.* B29, 398-406.

Walker R.J. and Fassett J.D. (1986) Isotopic measurement of subnanogram quantities of rhenium and osmium by resonance ionization mass spectrometry. *Anal. Chem.* 58, 2923-2927.

Walker R.J., Shirey S.B. and Stecher O. (1988) Comparative Re-Os, Sm-Nd and Rb-Sr isotope and trace element systematics for Archean komatiite flows from Munro Township, Abitibi Belt, Ontario. *Earth and Planet. Sci. Lett.* 87, 1-12.

Walker R.J., Carlson R.W., Shirey S.B. and Boyd F.R. (1989) Os, Sr, Nd, and Pb isotope systematics of southern African peridotite xenoliths: Implications for the chemical evolution of subcontinental mantle. *Geochim. Cosmochim. Acta* 53, 1583-1595.

Wänke H., Baddenhausen H., Palme H. and Spettel B. (1974) On the chemistry of the Allende inclusions and their origin as high temperature condensates. *Earth Planet. Sci. Lett.* 23, 1-7.

Wark D. A. (1986) Evidence for successive episodes of condensation at high temperature in a part of the solar nebula. *Earth Planet. Sci. Lett.* 77, 129-148.

Watson E.B., Ben Othman D., Luck J.M. and Hofmann A.W. (1987) Partitioning of U, Pb, Cs, Yb, Hf, Re and Os between chromian diopside pyroxene and haplobasaltic liquid. *Chem. Geol.* 62, 191-208.

Wendlandt R.F. (1982) Sulphur saturation of basalt and andesite melts at high pressures and temperatures. *Am. Mineral.* 67, 877-885.

Williams P. (1983) Secondary ion mass spectrometry. In *Applied Atomic Collision Physics* 4 (ed. Datz S.), pp 327-377, Academic Press.

Willis J. (1980) The bulk composition of iron meteorite parent bodies. *Ph.D. Dissertation, Univ. of California, Los Angeles.*

Willis J. and Goldstein J.I. (1982) The effects of C, P, and S on trace element partitioning during solidification in Fe-Ni alloys. *J. Geophys. Res.* 87, A435-A445.

Yokai K., Takahashi K. and Arnould M. (1983) The ^{187}Re-^{187}Os chronology and chemical evolution of the galaxy. *Astronom. and Astrophys.* 117, 65-82.

Zeibold T.O. (1967) Precision and sensitivity in electron microprobe analysis. *Anal. Chem.* 39, 858-861.

Zoller W.H., Parrington J.R. and Phelan Kotra J.M. (1983) Iridium enrichment in airborne particles from Kilauea Volcano: January 1983. *Science* 222, 1118-1121.

Geochimica et Cosmochimica Acta Vol. 53, pp. 483–489

0016-7037/89/$3.00 + .00

Diffusion, phase equilibria and partitioning experiments in the Ni-Fe-Ru system

JOEL D. BLUM*, G. J. WASSERBURG*, I. D. HUTCHEON*, J. R. BECKETT and E. M. STOLPER
Division of Geological and Planetary Sciences, California Institute of Technology, Pasadena, CA 91125, U.S.A.

(*Received July* 27, 1988; *accepted in revised form November* 18, 1988)

Abstract—The diffusion coefficient for Ru in Ni (D^{Ru}_{Ni}) was determined by the thin-film diffusion method in the temperature range of 1073 to 1673 K and is given by the expression:

$$D^{Ru}_{Ni}\ (cm^2\ sec^{-1}) = 5.0\ (\pm 0.7) \cdot 10^{-3} \exp[-2.3\ (\pm 0.1) \cdot 10^{12}\ erg\ mole^{-1}/RT]$$

where R is the gas constant and T is the temperature in K. Phase boundaries and tie lines in a Ni-Fe-Ru-rich system were determined at 1273, 1073 and 873 K. A wide miscibility gap is present at each temperature, separating a close-packed hexagonal εRu-Fe phase from a face-centered cubic γNi-Fe phase. The partitioning behavior of Pt and Ir between phases in a Ni-Fe-Ru-rich system and V between phases in a Ni-Fe-O-rich system was determined at 873 K. Pt partitions preferentially into the γNi-Fe phase, whereas Ir prefers the εRu-Fe phase. V partitions strongly into Fe oxides relative to γNi-Fe. The experimental results have applications in the fields of meteoritics, ore-deposit geology and materials science.

INTRODUCTION

METALLIC PHASES CONTAINING high concentrations of the Pt-group elements (PGEs) Ru, Rh, Os, Ir and Pt occur associated with metallic Ni-Fe phases in refractory inclusions in C3V chondritic meteorites (*e.g.* PALME and WLOTZKA, 1976) and in terrestrial ultramafic rocks (LEGENDRE and AUGÉ, 1986; MOCHALOV *et al.*, 1985). Studies of PGE-rich alloys in meteorites have played an important role in the formulation of recent theories of the early condensation and chemical and thermal evolution of the solar nebula (ARMSTRONG *et al.*, 1985; BISCHOFF and PALME, 1987; BLUM *et al.*, 1988). In addition, the extent of interdiffusion between PGE-rich phases and Ni-Fe phases has been used to constrain the thermal histories of meteorites in which these phases occur (ARRHENIUS and RAUB, 1978; BLUM *et al.*, 1988). Studies of PGE-rich alloys in terrestrial ultramafic rocks have contributed to the understanding of the behavior of PGEs in silicate systems and to the thermal and chemical history of certain PGE-rich ore deposits (DISTLER *et al.*, 1986). The behavior of PGE-rich alloys is also of interest in the field of super-alloy development and coatings technology because the addition of PGEs to Ni-rich alloys reduces oxidation and corrosion at high temperatures without adversely affecting other mechanical properties (*cf.* CORTI *et al.*, 1980).

In this study, we describe a series of experiments designed primarily to constrain phase equilibria in Ni-Fe-Ru-rich systems at temperatures of 1273, 1073 and 873 K and to determine the rate of Ru diffusion in Ni as a function of temperature. We also investigated Pt and Ir partitioning between phases in a Ni-Fe-Ru-rich system and V partitioning between phases in a Ni-Fe-O-rich system at 873 K. Phase equilibria and partitioning was investigated by analyzing alloys within a macroscopic compositional gradient. This procedure assumes local equilibrium on a microscopic scale between coexisting phases. Provided that local equilibrium is achieved, large portions of compositional space can be investigated from a single experiment at each temperature. Diffusion studies were done by the thin-film method (*cf.* CRANK, 1975). The diffusion of Ru in Ni was chosen for study because it provides a good analogue for the more compositionally complex Ni-Fe-Ru-rich alloy system found in refractory inclusions in meteorites. In a companion paper (BLUM *et al.*, 1989), we present analyses of PGE-rich alloys in meteorites and utilize the experimental data presented here to constrain models for the origin of opaque assemblages in chondritic meteorites. The data presented here may also be of value in the study of PGE-rich alloys in terrestrial ultramafic rocks and in materials science research. Preliminary results have been published previously (BLUM *et al.*, 1988).

* *Also:* Lunatic Asylum of the Charles Arms Laboratory.

EXPERIMENTAL METHODS

Diffusion experiments

Thin-film diffusion experiments were conducted to determine the diffusion coefficient for Ru in Ni (D^{Ru}_{Ni}) as a function of temperature. A flat surface of a 5 mm thick disk of polycrystalline >99.6% purity Ni metal was polished with diamond paste. The sample was lightly etched electrolytically with a 30% HCl solution, and a ~1 μm layer of Ni was electroplated onto the surface to enhance the surface adhesion of Ru. A ⅓ μm layer of Ru was electroplated onto the surface from a sulfamate solution (WEISBURG, 1988) and the sample was then cut into several pieces. For the experiments at 1073 and 1273 K, samples were sealed into evacuated silica tubes with >99.999% purity graphite, and for the experiments at 1473 and 1673 K, samples were placed in alumina crucibles suspended by Pt wire. The sample containers were plunged into the hot regions of furnaces at 1073, 1273, 1473 and 1673 K, annealed for times indicated on Fig. 1 (ranging from 20 minutes to 5.7 days) and then quenched in water. The experiments at 1273 and 1073 K were carried out in a horizontal tube Lindberg SB furnace open to the ambient atmosphere; the graphite included in the silica tubes prevented the oxidation of the samples. The experiments at 1673 and 1473 K were carried out in a vertical tube Deltech VT-31 furnace. To prevent oxidation of the samples, the oxygen fugacity (f_{O_2}) was maintained 2 log units more reducing than the Fe-$Fe_{1-x}O$ buffer by a flowing CO-CO_2 gas mixture containing 6 volume% CO_2. Temperatures were monitored with a Pt/Pt10Rh thermocouple adjacent to the sample. The thermocouples were calibrated at the melting point of Au (1337 K) and found to be accurate within ±2 K. After quenching, each silica tube experiment was checked with a spark coil to ensure that it had remained under vacuum before the sample was removed from the silica tube. All samples were then cut in half, and each half was polished with diamond paste perpendicular to the original electroplated surface; one

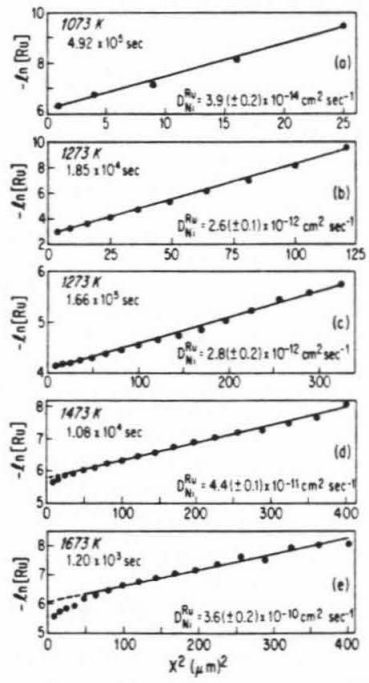

FIG. 1. Diffusion profiles for Ru-Ni thin-film experiments. The natural logarithm of the Ru concentration in atom% ([Ru]) is plotted against the square of the distance from the Ru-Ni diffusion interface. Analytical uncertainties are approximately equal to the symbol size. The temperature and duration of annealing are given for each experiment. The diffusion coefficients (D^{Ru}_{Ni}) and associated errors are calculated from the slope of the lines fitted to the data.

half was C-coated for Ru analysis and the other half was Pd-coated for C analysis.

Phase equilibria and partitioning experiments

Homogeneous alloys were synthesized from fine-grained metallic powders of Ni, Fe, Ru, Pt, Ir and V of >99.99% purity. For each composition, pure metals were weighed in appropriate ratios and homogenized by shaking in plastic containers with a SPEX vibrational mixer. The powders were then placed in alumina crucibles suspended by Pt wire, and plunged into a Deltech VT-31 furnace at 1823 K with the same gas mixture as in the diffusion experiments, to prevent the oxidation of the samples. The powders melted within a few minutes and were kept molten for at least two hours. The temperature was reduced to 1673 K (which is below the solidus for all of the alloys) for at least one hour to allow the alloys to crystallize, and they were then quenched in water. The crystalline alloys were annealed using the same gas mixture at 1673 K for at least an additional 24 hours to assure homogeneity, and they were again quenched in water. Starting materials for experiments were obtained by cutting each alloy into ~2 mm cubes using a diamond saw. The above procedure was used to synthesize the following alloy compositions given in atom percent: (1) $Ni_{46.4}Fe_{32.0}Ru_{20.0}Pt_{1.6}$; (2) $Ni_{44.1}Fe_{30.4}Ru_{19.0}Pt_{1.5}Ir_{5.0}$; and (3) $Ni_{61.3}Fe_{38.2}V_{0.5}$.

Homogeneous mixtures of Ni and NiO powder (Ni-NiO buffer) were placed in silica tubing with one end closed and the other end collapsed to ~1 mm. Pieces of each alloy were individually sealed into larger diameter evacuated silica tubes along with a Ni-NiO-bearing silica tube so that interaction between alloys and the buffer could take place only via the gas phase. Pieces of alloy (1) were also sealed into evacuated silica tubes with >99.999% purity graphite to prevent oxidation. The samples were annealed in a Lindberg SB furnace at 1273, 1073 and 873 K for 1, 40 and 105 days, respectively, and then quenched in water. Samples were prepared for analysis following the procedure outlined above for the diffusion experiments.

Quantitative analyses

Experimental starting materials and run products were investigated by secondary and back-scattered electron imaging using a JEOL JSM 35 analytical scanning electron microscope (SEM); quantitative analyses were made using a TN 5500 energy dispersive analyzer system (EDS) on the SEM and a wavelength dispersive system (WDS) on a JEOL 733 electron microprobe. All analyses were made at 15 keV accelerating voltage with a beam current of 75 pA on the SEM and 50 nA on the electron probe, except for C analyses which were made at 60 nA.

Peak deconvolution and background subtraction procedures were employed following SCHAMBER *et al.* (1980). Pure metals were used as standards and data were reduced using the ZAF correction procedure (*cf.* ARMSTRONG, 1984). The analytical accuracy was determined from analyses of secondary standards to be about ±5% of the values reported for EDS analyses and about ±3% of the values reported for WDS analyses. Detection limits were about 0.1 atom% for EDS analyses and about 0.01 atom% for WDS analyses, except for C analyses which had a detection limit of about 0.4 atom%. EDS analyses of low concentrations close to the detection limit (0.1 to 0.3%) have higher errors of up to ±25% of the values reported.

The size of the X-ray production region was calculated using the Monte Carlo simulation method of JOY (1984) as modified by ARMSTRONG (1988). The calculation was performed for average compositions of both the γNi-Fe phase and the εRu-Fe phase. The diameter of the region (which was nearly spherical) in which 99.9% of the X-rays were produced for EDS analyses on the SEM was found to vary from 0.5 to 0.7 μm for the elements Si, Fe, Co, Ni, Ru, Re, Os, Ir and Pt. The diameter of the X-ray production region for WDS analyses on the electron probe was approximately disk-shaped, with a diameter of about 2.5 to 2.7 μm and a depth of 0.5 to 0.7 μm because of the ~2 μm diameter electron beam.

Quantitative analyses of phase equilibria and partitioning experiment run products were made using the EDS on the SEM in order to take advantage of the small X-ray production region when analyzing small phases. Quantitative analyses of the diffusion experiments were made using the WDS on the electron probe because of the necessity of measuring Ru concentrations as low as ~0.01 atom%. Concentrations of Ru and Ni were measured at 1 μm intervals in a linear profile perpendicular to the diffusion interface by automatically stepping the stage. The individual analyses overlap since the X-ray production region was about 2.7 μm in diameter.

Homogeneity of starting materials for the diffusion and phase equilibria experiments was determined by backscattered electron imaging and by EDS-SEM analyses along profiles at 1 μm spacings. Starting materials and experimental run products were checked for the presence of impurities, including C, Si, Cr, Fe and Co. In all cases, concentrations were below the WDS-electron microprobe detection limits. Although these impurities were not present, the analytical total for WDS-electron microprobe analyses of the Ni substrate used in the diffusion experiments ranged from 96 to 98%, suggesting that the Ni contained 2 to 4% of an undetected impurity, which was probably oxygen.

EXPERIMENTAL RESULTS

Diffusion coefficients

Thin-film diffusion experiments were used to determine the value of D^{Ni}_{Ru} at each of the four annealing temperatures by plotting the natural logarithm of the Ru concentration *versus* the square of the distance from the Ru-Ni diffusion interface (Fig. 1a–e). These plots yield approximately linear arrays; the slopes of lines fitted to these data are equal to

$(4D^{Ru}_{Ni}t)^{-1}$, following the thin-film diffusion approximation (*cf.* CRANK, 1975). D^{Ru}_{Ni} increases with temperature from 3.9 $(\pm 0.2)\cdot 10^{-14}$ cm^2 sec^{-1} at 1073 K to 3.6 $(\pm 0.2)\cdot 10^{-10}$ cm^2 sec^{-1} at 1673 K (Fig. 1a–e). Two experiments were conducted at 1273 K with different annealing times ($1.66\cdot 10^5$ and $1.85\cdot 10^4$ seconds) as a test of the reproducibility of the method. The calculated value of D^{Ni}_{Ru} for the longer annealing time was 2.8 $(\pm 0.2)\cdot 10^{-12}$ cm^2 sec^{-1}, in close agreement with the value of 2.6 $(\pm 0.1)\cdot 10^{-12}$ cm^2 sec^{-1} obtained for the shorter annealing time (Fig. 1b, c).

The four analyses closest to the interface (from 3 to 6 microns) on the 1473 and 1673 K profiles (Fig. 1d, e) deviate from linearity and were excluded from the linear regressions. The deviation from linearity may be due to more rapid diffusion in a surface layer at the higher temperatures, resulting from high porosities or organic or oxide impurities typical of electroplated deposits. Alternatively, the nonlinearity could be caused by evaporation of Ni from the sample surface during annealing in the gas-mixing furnace. In either case, by excluding the data points near the interfaces for the 1473 and 1673 K experiments, we believe that we have avoided the problem and determined accurate values for D^{Ru}_{Ni}.

The experimentally determined values of $-\ln D^{Ru}_{Ni}$ are plotted *versus* $10^4/T$ in Fig. 2. The equation of the line fitted to these data yields D^{Ni}_{Ru} (cm^2 sec^{-1}) = 5.0 $(\pm 0.7)\cdot 10^{-3}$ $\exp(-2.3\cdot 10^{12}/RT)$, where R is the gas constant, T is the temperature in K, and the activation energy is 2.3 $(\pm 0.1)\cdot 10^{12}$ erg mole^{-1}. The activation energy determined here for Ru diffusion in Ni is similar to the activation energy for Pt diffusion in Ni ($1.8\cdot 10^{12}$ erg mole^{-1}; KUBASCHEWSKI and EBERT, 1944). The linearity of the data shown in Fig. 2 supports our procedure of excluding anomalous near-surface data points in the higher temperature experiments and suggests that a single diffusion mechanism dominates at each temperature. The diffusion mechanism is probably lattice diffusion, which has been shown to dominate over grain-boundary diffusion in alloys at temperatures above about 900 K (*cf.* SHEWMON, 1963).

Phase equilibria and partition coefficients

Phase equilibrium experiments were performed in two ways: Ni-Fe-Ru-Pt ± Ir alloys were annealed with graphite

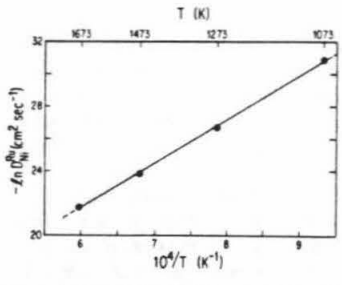

FIG. 2. The variation of the diffusion coefficient for Ru in Ni (D^{Ru}_{Ni}) with temperature (T) in K. The natural logarithm of D^{Ru}_{Ni} is plotted against $10^4/T$; uncertainties are smaller than the symbol size. An expression for D^{Ru}_{Ni} as a function of T was calculated from the equation for the line fitted to the data and is given in the text.

("graphite experiments") or with Ni-NiO ("Ni-NiO experiments"). Run products from graphite experiments either remained as homogeneous alloys or exsolved into two coexisting phases, depending on the annealing temperature. Run products from Ni-NiO experiments are more complicated because of partial oxidation of the initially homogeneous alloys under the oxidizing conditions imposed by the Ni-NiO buffer. In each of these samples, oxidation of the original alloys produced a rind of Fe-rich oxide surrounding a zone of Fe-rich oxide intergrown with Ni-Fe-Ru-Pt ± Ir alloys (Fig. 3). Near regions where the Fe-rich oxide formed, the alloys were enriched in Ni-Ru-Pt ± Ir because these elements are excluded from the oxide. A compositional gradient was thus established in the alloy from the zone of oxide-alloy intergrowths extending inward from this zone; where the composition became sufficiently enriched in Ni and Ru, a ϵRu-Fe and γNi-Fe phase exsolved. The α, ϵ and γ designations used in this paper for the metallic solid-solution fields in the Ni-Fe-Ru-rich system are based on compositional data rather than direct determination of crystal structure.

The graphite experiments provide information about phase equilibria based on the presence or absence of multiple phases and the compositions of coexisting phases in the run products. In addition, if the ϵRu-Fe phase produced in the Ni-NiO experiments is assumed to be in local equilibrium with the γNi-Fe phase with which it is in contact (within 2 to 3 μm), then the compositions of coexisting phases in the Ni-NiO experiments also constrain the phase diagram. Analyses of coexisting phases in both sets of experiments with alloy composition $Ni_{46.4}Fe_{32.0}Ru_{20.0}Pt_{1.6}$ are listed in Table 1. The data are projected from Pt onto the Ni-Fe-Ru plane and shown as isothermal sections at 1273, 1073 and 873 K in Fig. 4. At 1273 K (Fig. 4a), the alloy composition falls in a one-phase region, and, therefore, exsolution occurred only in the Ni-NiO experiment. At 1073 K (Fig. 4b) and 873 K (Fig. 4c), exsolution occurred in both types of experiments, and the results from the graphite and Ni-NiO experiments are in close agreement, supporting our assumption of local equilibrium on a 2 to 3 μm scale in each of the Ni-NiO experiments. The binary joins of the diagrams in Fig. 4a–d were taken from previously determined binary diagram compilations for Ni-Ru (NASH, 1986), Ru-Fe (SWARTZENDRUBER and SUNDMAN, 1983) and Ni-Fe (KUBASCHEWSKI, 1983). Also plotted on the 1273 K diagram (Fig. 4a) are results of experiments on 12 of the 25 alloy compositions in the Ni-Fe-Ru system studied by AKOPYAN *et al.* (1974). The exact compositions of exsolved phases were not determined in that study, but the presence or absence of exsolution in all of the alloy compositions throughout the diagram is generally consistent with our experiments.

The consistency of our data with the Ni-Ru binary system (NASH, 1986) at each temperature and with the ternary data of AKOPYAN *et al.* (1974) at 1273 K suggests that the presence of 1.6% Pt in our samples does not have a major effect on the phase relations. Moreover, when the exsolved phases from the Ir-bearing experiments described below are projected from Ir + Pt onto the Ni-Fe-Ru plane, phase boundaries and tie lines are nearly identical to those for the Ir-free experiments, showing that the addition of 5% Ir to the Ni-Fe-Ru system also does not significantly affect phase relations.

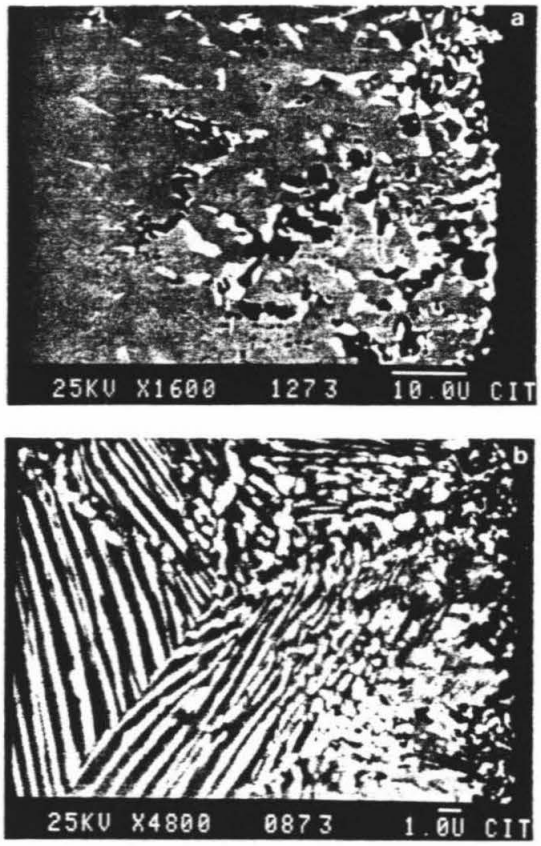

FIG. 3. SEM images of experimental run products used to determine phase equilibria in the Ni-Fe-Ru system at (a) 1273 K and (b) 873 K. White regions are the ϵRu-Fe phase, gray regions are the γNi-Fe phase and dark regions (including the right edge of each image) are Fe-rich oxide. Scale bars are 10 and 1 microns in (a) and (b) respectively.

At each temperature studied (Fig. 4a–c), the data define two solvi bounding a large miscibility gap that separates a close-packed hexagonal (cph) ϵRu-Fe phase (SWARTZENDRUBER and SUNDMAN, 1983) from a face-centered cubic (fcc) γNi-Fe phase (KUBASCHEWSKI, 1983). In the Fe-poor part of the system, tie lines are approximately parallel to the Ru-Ni edge of the triangle, and there is no significant change in their orientation with temperature. With decreasing temperature, the two-phase region expands, with the ϵRu-Fe and γNi-Fe phases moving closer to the binaries. An exception to this trend is the near overlap in compositions for a few of the analyses of the ϵRu-Fe phase at 1073 and 873 K. However, this is probably due to an analytical contribution to analyses of the ϵRu-Fe phase by the surrounding γNi-Fe phase in the 873 K experiments. Alloys annealed at 1273 and 1073 K developed lamellae and grains of ϵRu-Fe that were sufficiently large (1–5 μm) to easily analyze by SEM (Fig. 3a). The much slower diffusion rates at 873 K resulted in narrow ($\lesssim$0.8 μm) exsolution lamellae (Fig. 3b). Although care was taken to

Table 1. Analyses in atom percent of coexisting phases in phase equilibria and partitioning experiments.

		Fe	Ni	Ru	Pt	Ir
Starting Alloy		46.4	32.0	20.0	1.6	-
1273 K						
ϵRu-Fe	1a	3.49	12.89	83.71	0.32	-
	2a	2.74	13.10	83.85	0.31	-
	3a	13.06	18.18	68.33	0.44	-
	4a	14.43	21.54	63.62	0.42	-
	5a	13.74	18.32	67.64	0.30	-
	6a	15.84	21.39	62.36	0.41	-
	7a	5.63	15.44	78.68	0.25	-
	8a	12.11	16.74	70.83	0.32	-
γNi-Fe	1b	4.86	79.65	12.61	2.89	-
	2b	5.94	77.62	13.41	3.03	-
	3b	17.90	61.57	18.16	2.37	-
	4b	22.16	55.29	20.63	1.92	-
	5b	22.38	55.57	20.25	1.81	-
	6b	22.66	55.75	19.69	1.90	-
	7b	6.34	77.38	13.46	2.82	-
	8b	17.19	62.06	18.66	2.09	-
1073 K						
ϵRu-Fe	1a	2.80	7.13	89.93	0.14	-
	2a	7.67	9.98	82.25	0.11	-
	3a	19.70	14.01	66.02	0.27	-
	4b	22.15	14.16	63.50	0.18	-
	5a	15.63	13.54	70.62	0.22	-
	6a	9.24	9.77	80.80	0.19	-
	7a	2.77	9.88	87.27	0.10	-
	8a	5.17	8.44	86.25	0.15	-
	*9a	24.97	14.27	60.56	0.20	-
γNi-Fe	1b	6.57	84.65	6.17	2.62	-
	2b	14.25	72.77	10.73	2.25	-
	3b	27.46	57.85	12.81	1.88	-
	4b	30.11	54.63	13.40	1.86	-
	5b	23.21	62.67	12.15	1.97	-
	6b	16.21	70.39	11.08	2.32	-
	7b	4.75	85.71	6.60	2.94	-
	8b	4.56	85.55	6.92	2.97	-
	*9b	32.06	51.35	14.76	1.84	-
873 K						
ϵRu-Fe	1a	25.99	15.49	58.10	0.43	-
	2a	25.18	15.55	58.98	0.28	-
	3a	26.19	16.15	57.33	0.32	-
	4a	19.66	16.07	63.80	0.47	-
	5a	13.86	12.86	72.98	0.30	-
	6a	24.10	15.21	60.40	0.29	-
	7a	28.34	15.67	55.76	0.24	-
	8a	21.06	12.76	66.05	0.13	-
	9a	21.54	13.20	64.96	0.30	-
	10a	20.65	14.41	64.53	0.41	-
	11a	25.91	17.52	56.05	0.52	-
	*15a	31.43	17.59	50.33	0.64	-
	*16a	30.74	18.02	50.76	0.48	-
γNi-Fe	1b	25.72	66.55	5.65	2.09	-
	3b	29.28	63.25	6.23	2.12	-
	4b	26.62	66.60	4.59	2.19	-
	5b	25.99	66.99	4.85	2.16	-
	8b	27.96	65.28	4.61	2.15	-
	9b	27.20	66.26	4.40	2.15	-
	12b	24.28	67.89	5.78	2.05	-
	13b	16.87	77.03	3.43	2.68	-
	*14b	15.22	78.41	3.84	2.58	-
	*15b	29.36	64.17	4.48	1.99	-
	*16b	29.31	63.38	5.11	2.21	-
Starting Alloy		44.1	30.4	19.0	1.5	5.0
873 K						
ϵRu-Fe	2a	22.65	12.74	56.16	0.38	8.06
	3a	22.43	13.45	56.43	0.15	7.56
	4a	26.06	14.82	51.30	0.41	7.40
	6a	25.75	14.03	52.46	0.25	7.51
	7a	23.04	12.31	56.87	0.12	7.65
	8a	25.36	20.59	46.29	0.80	6.95
γNi-Fe	1b	24.90	63.43	4.44	2.31	4.92
	2b	26.73	60.33	5.66	2.26	5.02
	4b	29.75	56.53	6.79	2.33	4.60
	5b	26.59	62.35	4.57	2.41	4.08
	6b	30.25	54.76	8.22	1.97	4.79
	7b	28.02	59.91	5.37	2.12	4.57

Note: * indicates experiments annealed with graphite; all others annealed with Ni-NiO buffer. a and b represent analyses of adjacent phases in a single experiment. Analytical totals ranged from 96 to 104% and were normalized to 100%. - indicates below 0.1% detection limit. Analytical uncertainties are ±5% of the values reported.

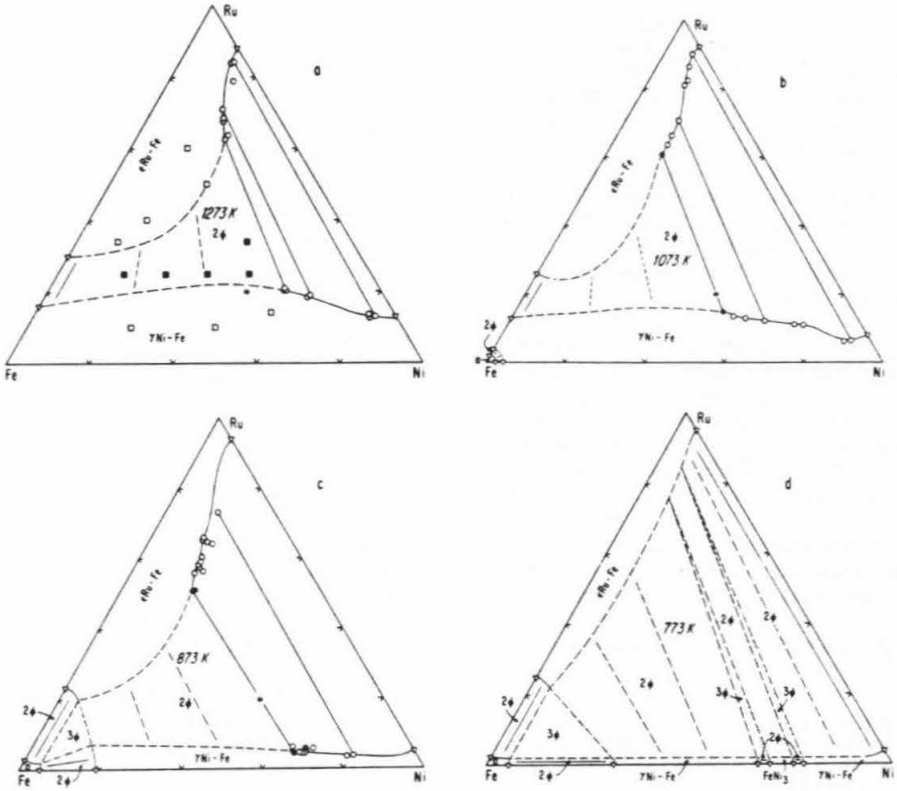

FIG. 4. Isothermal sections (in atom%) projected from Pt onto the Ni-Fe-Ru plane. Asterisks represent the starting alloy compositions used in the experiments. Circles are analyses of the experimental run products; open circles are experiments run with a Ni-NiO buffer and filled circles are experiments run with graphite. Solid tie lines connect analyses of adjacent phases (within 2–3 μm). Inverted triangles are phase boundaries from compilations of the Ni-Fe (KUBASCHEWSKI, 1983), Ru-Fe (SWARTZENDRUBER and SUNDMAN, 1983) and Ni-Ru (NASH, 1986) phase diagrams. Squares are alloy compositions studied by AKOPYAN *et al.* (1974) for which exsolution into two phases was either observed to occur (filled squares) or not occur (open squares). Phase boundaries and tie lines are solid near regions where there is experimental data; dashed phase boundaries and tie lines are estimated or schematic. The 773 K diagram is speculative and intended to be diagramatic only. Single-phase solid-solution regions include a fcc γNi-Fe phase, a cph ϵRu-Fe phase and a bcc αFe phase. Two-phase and three-phase regions are denoted by 2ϕ and 3ϕ respectively and three-phase regions are stippled.

analyze the centers of only the widest lamellae (~0.8 μm), we cannot rule out the possibility that these analyses contain an analytical contribution from the surrounding γNi-Fe, especially since the lamellae are almost certainly not perpendicular to the polished surface and the X-ray production region penetrated 0.5 to 0.7 μm into the sample. Analyses of γNi-Fe in the 873 K experiments are more reliable since lamellae are sometimes separated by $\gtrsim$1 μm, allowing analysis without analytical contribution from the adjacent ϵRu-Fe lamellae.

We studied the partitioning of Pt and Ir between coexisting ϵRu-Fe and γNi-Fe in the 873 K Ni-NiO experiments with alloy composition $Ni_{44.1}Fe_{30.4}Ru_{19.0}Pt_{1.5}Ir_{5.0}$. The compositions of ϵRu-Fe and γNi-Fe in this experiment are listed in Table 1. Pt concentrations are lower and Ir concentrations higher in ϵRu-Fe compared with γNi-Fe, and there are only small variations in Pt and Ir concentrations within each phase (Fig. 5). By taking the average Pt and Ir concentration for the ϵRu-Fe phase and the γNi-Fe phase, we calculate (ϵRu-Fe)/(γNi-Fe) partition coefficients for Pt (K^{Pt}) and Ir (K^{Ir}) between these two phases of 0.16 and 1.6, respectively. Although pure Pt and Ir both have fcc crystal structures, Pt is more compatible with fcc γNi-Fe, whereas Ir is more compatible with cph ϵRu-Fe.

Experiments with alloy composition $Ni_{61.3}Fe_{38.2}V_{0.5}$ annealed with Ni-NiO were used to constrain the partitioning of V between γNi-Fe and Fe-oxide at 873 K. The alloy was partially oxidized and developed Fe-V oxide rims and intergrowths similar to the Fe-rich oxides in the Ni-NiO experiments described above. Near regions where Fe-V oxide formed, the removal of Fe and V from the alloy resulted in Ni-enriched alloys that contained no detectable V ($\leq$0.1%).

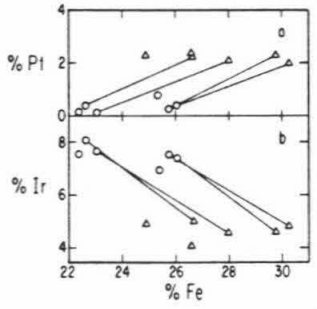

FIG. 5. The concentration of (a) Pt and (b) Ir plotted against Fe (in atom%) for the partitioning experiment at 873 K. Triangles are concentrations in the fcc γNi-Fe phase, and circles are concentrations in the cph εRu-Fe phase. Tie lines connect analyses of adjacent phases (within 2–3 μm).

INTERPRETATION OF THE Ni-Fe-Ru PHASE DIAGRAMS

Experimental data projected onto the Ni-Fe-Ru plane from Pt are plotted in Fig. 4 (a–c), along with phase boundaries in the three binary systems: Ni-Ru, Ni-Fe and Ru-Fe. The complete isothermal section at 1273 K (Fig. 4a) can reasonably be constructed using our data, the results of AKOPYAN *et al.* (1974) and available data in the literature for the bounding binary systems. Guided by the topology of the 1273 K diagram, we have constructed isothermal sections at 1073 and 873 K (Fig. 4b, c) by extrapolating our experimental data for these temperatures and data from the bounding binary systems into compositional space not yet investigated. The diagram at 773 K (Fig. 4d) is based on trends observed with decreasing temperature in our higher temperature experiments and on limited binary data, and, therefore, is only speculative. In each isothermal section, there is a large miscibility gap, where a cph εRu-Fe phase coexists with a fcc γNi-Fe phase. The miscibility gap expands with decreasing temperature as the εRu-Fe phase becomes poorer in Ni and the γNi-Fe phase becomes poorer in Ru. The Fe content of εRu-Fe and γNi-Fe phases connected by equilibrium tie lines is approximately equal for bulk compositions with ≲70% Fe. At 1273 and 1073 K, the two-phase region extends continuously from the Ru-Ni to the Ru-Fe binary. At ~920 K, there is an invariant point in the Ru-Fe binary; and below this temperature, a three-phase region develops in the Ni-Fe-Ru ternary, in which a body centered cubic (bcc) αFe phase, a fcc γNi-Fe phase and a cph εRu-Fe phase coexist. At ~790 K, $FeNi_3$ becomes stable in the Ni-Fe binary (KUBASCHEWSKI, 1983), and two narrow three-phase regions may develop, in which εRu-Fe, Ni_3Fe and γNi-Fe coexist.

CONCLUSIONS

D_{Ni}^{Ru} was determined by the thin-film diffusion method in the temperature range of 1073 to 1673 K and is given by the expression:

$$D_{Ni}^{Ru}\ (cm^2\ sec^{-1}) = 5.0\ (\pm 0.7) \cdot 10^{-3} \exp[-2.3\ (\pm 0.1) \cdot 10^{12}\ erg\ mole^{-1}/RT]$$

where R is the gas constant and T is the temperature in K. Phase boundaries and tie lines in a Ni-Fe-Ru-rich system were determined at 1273, 1073 and 873 K. A wide miscibility gap is present at each temperature, separating a cph εRu-Fe phase from a fcc γNi-Fe phase. The partitioning behavior of Pt and Ir between phases in a Ni-Fe-Ru-rich system and V between phases in a Ni-Fe-O-rich system was determined at 873 K. Pt partitions preferentially into the γNi-Fe phase, whereas Ir prefers the εRu-Fe phase. V partitions strongly into Fe oxides relative to γNi-Fe.

Whereas traditional methods of phase equilibria in Ni-Fe-PGE systems require the preparation and annealing of many different alloy compositions (*e.g.* STEVENS *et al.*, 1978), we were able to investigate a large portion of a Ni-Fe-Ru-rich system with a single experiment at each temperature by establishing a concentration gradient within which local equilibrium between coexisting phases was maintained. This method has similarities with the study of phase equilibria at disequilibrium planar interfaces (*e.g.* PINNEL and BENNETT, 1979), in that it makes a wide compositional field available for study within a single sample.

The experimental results presented here have direct applications to the origin and thermal history of PGE-rich alloys in meteorites and are utilized for this purpose in a companion paper (BLUM *et al.*, 1989). The data may also be useful in the study of certain PGE ore deposits and in materials science research.

Acknowledgements—We thank G. R. Rossman for allowing us to use his furnace and vacuum line, A. M. Weisberg of Technic Inc. for electroplating Ru onto Ni for use as starting materials in our diffusion experiments, D. A. Vanko for Russian translation, J. T. Armstrong and J. P. Poirier for helpful discussions and J. I. Goldstein, J. H. Jones and an anonymous referee for reviews. Funding was provided by NASA NAG 9-43 and NAG 9-105, NSF EAR 86-18526 and DOE DE-FG03-88ER13851. Division Contribution No. 4647 (604).

Editorial handling: H. Y. McSween, Jr.

REFERENCES

AKOPYAN A. S., RAEVSKAYA M. V., SOKOLOVA I. G. and SOKOLOVSKAYA E. M. (1974) The 1000°C isothermal cross section of the phase diagram of the Ru-Ni-Fe system. *Vestnik Moskovskogo Universiteta Khimiya* **29**, 467–471.

ARMSTRONG J. T. (1984) Quantitative analysis of silicate and oxide minerals: A re-evaluation of ZAF corrections and proposal for new Bence-Albee coefficients. In *Microprobe Analysis—1984* (eds. A. D. ROMIG, JR. and J. I. GOLDSTEIN), pp. 208–212. San Francisco Press.

ARMSTRONG J. T. (1988) Quantitative analysis of silicate and oxide minerals: Comparison of Monte Carlo, ZAF and $\phi(\rho z)$ procedures. In *Microbeam Analysis—1988* (ed. D. E. NEWBURY), pp. 237–246. San Francisco Press.

ARMSTRONG J. T., EL GORESY A. and WASSERBURG G. J. (1985) Willy: A prize noble Ur-Fremdling—Its history and implications for the formation of Fremdlinge and CAI. *Geochim. Cosmochim. Acta* **49**, 1001–1022.

ARRHENIUS G. and RAUB C. J. (1978) Thermal history of primordial metal grains. *J. Less-common Metals* **62**, 417–430.

BISCHOFF A. and PALME H. (1987) Composition and mineralogy of refractory-metal-rich assemblages from a Ca,Al-rich inclusion in the Allende meteorite. *Geochim. Cosmochim. Acta* **51**, 2733–2748.

BLUM J. D., WASSERBURG G. J., HUTCHEON I. D., BECKETT J. R. and STOLPER E. M. (1988) 'Domestic' origin of opaque assemblages in refractory inclusions in meteorites. *Nature* **331**, 405–409.

BLUM J. D., WASSERBURG G. J., HUTCHEON I. D., BECKETT J. R. and STOLPER E. M. (1989) Origin of opaque assemblages in C3V meteorites: Implications for nebular and planetary processes. *Geochim. Cosmochim. Acta* **53**, 545–558 (this issue).

CORTI C. W., COUPLAND D. R. and SELMAN G. L. (1980) Platinum-enriched superalloys. Enhanced oxidation and corrosion resistance for industrial and aerospace applications. *Platinum Metal Rev.* **24**, 2–11.

CRANK J. (1975) *The Mathematics of Diffusion*. Oxford Univ. Press. 414p.

DISTLER V. V., KRYACHKO V. V. and LAPUTINA I. P. (1986) Evolution of platinum-group parageneses in Alpine-type ultramafics. *Intl. Geol. Rev.* **28**, 1068–1085.

JOY D. C. (1984) Beam interactions, contrast and resolution in the SEM. *J. Microsc.* **136**, 241–258.

KUBASCHEWSKI O. (1983) *Iron-Binary Phase Diagrams*. Springer-Verlag, Berlin.

KUBASCHEWSKI O. and EBERT H. (1944) Diffusion measurements in gold and platinum alloys. *Z. Elektrochem.* **50**, 138–144.

LEGENDRE O. and AUGÉ T. (1986) Mineralogy of platinum-group mineral inclusions in chromitites from different ophiolitic complexes. In *Metallogeny of Basic and Ultrabasic Rocks* (eds. M. J. GALLAGHER, R. A. IXER, C. R. NEARY and H. M. PRICHARD), pp. 361–372. Inst. of Mining and Metallurgy.

MOCHALOV A. G., DMITRENKO G. G., ZHERNOVSKII I. V. and RUDASHEVSKII N. S. (1985) New iridium-osmium-ruthenium type (solid solutions of rare platinum-group elements with iron) of platinum-group mineralization in chromium spinel-group minerals in alpine-type ultramafic rocks of the Koryak Highland. *Zapiski Vses. Mineral. Obshch.* **114**, 544–554 (in Russian).

NASH P. (1986) The Ni-Ru (nickel-ruthenium) system. *Bull. Alloy Phase Diagrams* **7**, 130–133.

PALME H. and WLOTZKA F. (1976) A metal particle from a Ca,Al-rich inclusion from the meteorite Allende, and condensation of refractory siderophile elements. *Earth Planet. Sci. Lett.* **33**, 45–60.

PINNEL M. R. and BENNETT J. E. (1979) On the formation of the ordered phases CuAu and Cu_3Au at a copper/gold planar interface. *Metallurg. Trans.* **10A**, 741–747.

SCHAMBER F. H., WODKE N. F. and MCCARTHY J. J. (1980) Least squares fit with digital filter: The method and its application to EDS spectra. In *Proc. 8th Intl. Conf. on X-ray Optics and X-ray Microanal.* (ed. D. R. BEAMAN, R. E. OGILVIE and D. B. WITTRY), pp. 124–132. Pendell Publ. Co.

SHEWMON P. G. (1963) *Diffusion in Solids*. McGraw-Hill. 203p.

STEVENS G. T., HATHERLY M. and BOWLES J. S. (1978) The ordered phase fields of the iron-nickel-platinum equilibria diagram. *J. Materials Sci.* **13**, 499–504.

SWARTZENDRUBER L. J. and SUNDMAN B. (1983) The Fe-Ru (iron-ruthenium) system. *Bull. Alloy Phase Diagrams* **4**, 155–160.

WEISBURG A. M. (1988) Ruthenium plating. In *Metal Finishing* (ed. M. MURPHY), p. 286. Metals and Plastics Publ., Inc.

Reprinted from Nature, Vol. 331, No. 6155, pp. 405-409, 4 February 1988

'Domestic' origin of opaque assemblages in refractory inclusions in meteorites

Joel D. Blum, G. J. Wasserburg, Ian D. Hutcheon, John R. Beckett & Edward M. Stolper

Division of Geological and Planetary Sciences, California Institute of Technology, Pasadena, California 91125, USA

Experimental studies indicate that opaque assemblages rich in refractory siderophile elements were formed within host calcium- and aluminium-rich inclusions (CAIs) by exsolution, oxidation and sulphidization of homogeneous alloys, rather than by aggregation of materials in the solar nebula before the formation of CAIs. These opaque assemblages are thus not the oldest known solid materials, as was once thought, and they do not constrain processes in the early solar nebula before CAI formation. Instead, the assemblages record the changing oxygen fugacity experienced by CAIs during slow cooling in nebular and/or planetary environments.

CALCIUM- and aluminium-rich inclusions (CAIs) in C2 and C3 chondritic meteorites are generally believed to be representative of the earliest solids formed in the primitive solar nebula[1,2]. They are enriched relative to cosmic proportions in the elements that are most refractory in a gas of solar composition. Reflecting this trend is an enrichment (~20×C1 chondrite) in the refractory siderophile elements (Ru, Os, Re, Pt, Ir, W and Mo)[3-5], which are concentrated in multi-phase opaque assemblages[6-8]. The bulk chemistry of these assemblages has strong affinities with the calculated earliest condensates from a hot portion of the solar nebula[5,6,13]. Extensive investigations have shown that many of the assemblages are composed of discrete micrometre-sized refractory siderophile metal nuggets surrounded by Ni-Fe metal, V-rich magnetite and Fe-Ni sulphides with associated molybdenite, molybdate, tungstate and phosphate[9-13]. The opaque assemblages are typically spheroidal and 1-1,000 μm in diameter. They occur as inclusions in all of the major silicate phases of CAIs, are sometimes found in embayments in spinel, and are often rimmed by a thin (≤20 μm) rind of V-rich fassaite[9,11,12] (see Fig. 1). In addition to the opaque assemblages described above, there exist other small (0.5-3.0 μm) refractory siderophile metal nuggets not associated with Ni-Fe metal, magnetite or sulphide[7,10,13,37]. The net refractory siderophile element content of CAIs is controlled by the combination of these smaller objects and the opaque assemblages described here. We will focus here on the origin of the opaque assemblages.

Owing in part to the presumption that refractory siderophile metal nuggets formed either as condensates in expanding supernova envelopes (outside the Solar System) or as the earliest high-temperature nebular condensates, early workers postulated that the opaque assemblages were exotic and formed before CAIs[7-9]. As a result, the opaque assemblages are often referred to by the genetic name "Fremdlinge"[8,9], which is German for strangers or foreigners. We prefer to refer to the objects, previously called "Fremdlinge", by the simple descriptive name "opaque assemblages".

Recent studies of the chemical compositions, mineralogy and textural relationships of opaque assemblages have led most workers to concur that opaque assemblages formed before the host CAIs, and to agree on the following scenario for their origin and evolution[11-13]: (1) condensation of Ru,Os-rich nuggets at very high temperature (~1,500-2,000 K) in a supernova envelope or in a hot part of the solar nebula; (2) condensation of Ni-Fe metal followed either by oxidation of Fe and reaction with V in a nebular gas to produce V-rich magnetite or by direct condensation of V-rich magnetite; (3) aggregation of Ru,Os-rich nuggets, Ni-Fe metal, V-rich magnetite and associated phases in the nebula at low temperature (~870 K) to form opaque assemblages; and (4) mixture of opaque assemblages with proto-CAI material before (or during) a brief high-temperature (~1,700 K) event, during which the silicate portion of the host CAI melted or partially melted, followed by rapid cooling. The high-temperature CAI melting event was postulated to have been so brief, and cooling so rapid, that the delicate textures and mineral intergrowths in opaque assemblages were preserved as they existed before CAI melting. Thus, opaque assemblages have been inferred to record conditions in the solar nebula before CAI crystallization, providing important constraints on the temperature, composition and degree of mixing in the early nebula[9,11-13,15].

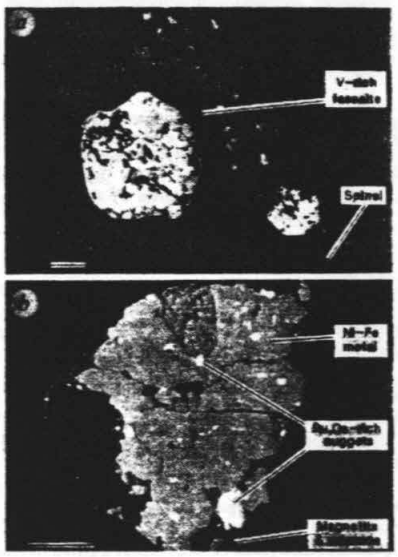

Fig. 1 Backscattered-electron images of opaque assemblages from CAIs. *a*, Two opaque assemblages (round bright objects) which occur in embayments in a spinel crystal in Allende sample USNM 5241. The surrounding silicate is melilite and the rim around the larger opaque assemblage is V-rich fassaite. *b*, An opaque assemblage in Allende JIM analysed in this study, which includes Ru,Os-rich nuggets, Ni-Fe metal, V-rich magnetite and sulphides. Scale bars, 10 μm.

To test experimentally models for the formation of opaque

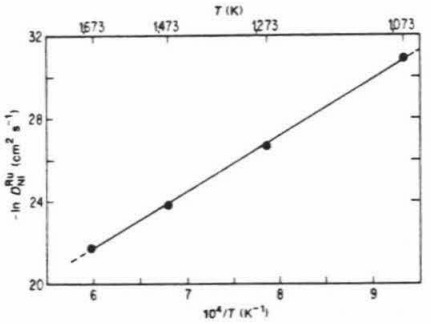

Fig. 2 Summary of the results of Ru-Ni thin-film diffusion experiments at four different temperatures, yielding a reliable estimate of the diffusion coefficient (D_{Ni}^{Ru}) as a function of temperature (T), based on the fitted line. The equation of the line is $D_{Ni}^{Ru} = 0.005 \exp(-2.3 \times 10^{12}/RT)$; the activation energy thus determined is $(2.3 \pm 0.1) \times 10^{12}$ erg mol^{-1}, and R is the gas constant in c.g.s. units.

assemblages, we have determined the diffusion coefficient for Ru in Ni (D_{Ni}^{Ru}) as a function of temperature, studied phase equilibria in the system Ni-Fe-Ru-O, and studied the partitioning of minor amounts of Pt, Ir and V between coexisting phases in systems dominated by Ni, Fe, Ru and O. Based on our experiments, we propose a new model for the origin of opaque assemblages that is in sharp contrast with the prevailing scenario[11-13]. We suggest that opaque assemblages originated as homogeneous metallic droplets in CAI silicate liquids and that, after crystallization and subsequent cooling to a temperature of $\lesssim 870$ K, these once homogeneous alloys exsolved into immiscible metallic phases as they were partially oxidized and sulphidized to form the multi-phase opaque assemblages now observed in CAIs. The possibility that some refractory siderophile metal nuggets in opaque assemblages might have formed by exsolution was suggested previously[6,10,14], but this view was subsequently rejected by most workers in favour of the formation of these nuggets as primary condensates[9,11-13,15], and has therefore received little serious attention until now. The implications of our model are that opaque assemblages do not constrain the high-temperature thermal histories of CAIs or conditions in the solar nebula before CAI melting, as suggested previously. Instead, they provide important constraints on the low-temperature thermal histories of CAIs and on the changing oxygen fugacity (f_{O_2}) in cooling nebular and/or planetary environments.

Experiments and analyses

Thin-film diffusion experiments were conducted by electroplating a 0.3-μm film of Ru onto a slab of polycrystalline Ni. Pieces of this material were annealed at 1,673, 1,473, 1,273 and 1,073 K in evacuated silica tubes with graphite for times ranging from 0.3 to 137 h. The samples were sectioned and Ru concentration ([Ru]) profiles measured at 1-μm intervals perpendicular to the interface, using a JEOL 733 electron microprobe following procedures given in ref. 11. The value of D_{Ni}^{Ru} was determined at each temperature (T) from the approximately linear slope of $-\ln[Ru]$ versus the square of the distance, following the thin-film approximation[16]. The values of D_{Ni}^{Ru} determined in this way are shown plotted against $1/T$ in Fig. 2 and yield the expression for $D_{Ni}^{Ru}(T)$ given in the Fig. 2 legend.

To study Ni-Fe-Ru-O phase equilibria and Pt and Ir partitioning, we first produced a powdered metal mixture with the composition $Ni_{58}Fe_{40}Pt_2$ (in atomic proportions). To aliquots of this mixture, we added 10% Ru, 20% Ru, 10% Ru+5% Ir, and 20% Ru+5% Ir. The powders were melted and homogenized. Pieces of this material were then sealed in evacuated silica

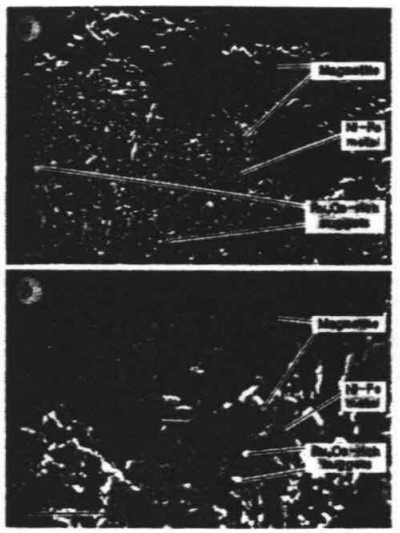

Fig. 3 Secondary-electron images comparing a typical experimental run product (*a*) and a portion of the opaque assemblage "Willy"[11] from Allende USNM 5241 (*b*). Note the textural and chemical similarities, which include: (1) a magnetite rim and intergrowths; (2) Ni-Fe metal with dissolved Pt and Ir; and (3) Ru ± (Os, Ir)-rich nuggets. Scale bars, 10 μm.

tubes with a Ni-NiO buffer and annealed at 1,273 and 1,073 K for 1 and 9 days respectively. Reaction of oxygen with each of the synthetic alloys produced an outer rind of magnetite and a zone of magnetite (or in some instances wüstite) intergrown with Ni-Fe-Pt-Ru(± Ir) alloys just inside the rind (Fig. 3). The removal of Fe from metal to form magnetite produced metal enriched in Ni, Pt, Ru, ±Ir near regions where magnetite had formed, because these metals have very low solubilities in magnetite. A compositional gradient was thus established, and where the metal composition became sufficiently enriched in Ni and Ru, a Ru-rich metallic phase (nuggets) exsolved. Coexisting Ru-rich nuggets and Ni-Fe-rich metals in synthetic samples were analysed using a JEOL JSM 35 analytical scanning electron microscope (ASEM) following procedures given in ref. 11. Only exsolved nuggets larger than the ~0.8-μm X-ray interaction volume were analysed, to minimize interference from surrounding phases. Pt was concentrated in the Ni-Fe metal, whereas Ir partitioned into both the Ni-Fe metal and the exsolved Ru-rich nuggets. The positions of phase boundaries and tie-lines at 1,273 and 1,073 K in the Ni-Fe-Ru phase diagram were determined by analysing the compositions of coexisting Ru-rich nuggets and Ni-Fe metals and assuming local equilibrium on a 2-3-μm scale. The experimentally determined 1,273- and 1,073-K phase diagrams, and the 873-K diagram inferred from the three binary systems, are shown projected from the Pt apex in Fig. 4.

To study V partitioning between Ni-Fe metal and magnetite, we dissolved V into Ni-Fe under f_{O_2} conditions one log unit more oxidizing than the solar gas curve (Fig. 5) to form a $Ni_{38}Fe_{61}V_1$ alloy. We annealed this alloy under the same experimental conditions as the Ni-Fe-Pt-Ru(±Ir) alloys. Essentially all of the V initially in the metal alloy partitioned into the magnetite rim and intergrowths, resulting in V-free (< 0.1%) Ni-Fe metal and V-rich magnetite.

To compare the experimental run products with naturally occurring opaque assemblages in CAIs, three opaque assemblages from Allende sample JIM[17] (Fig. 1*b*), Allende USNM

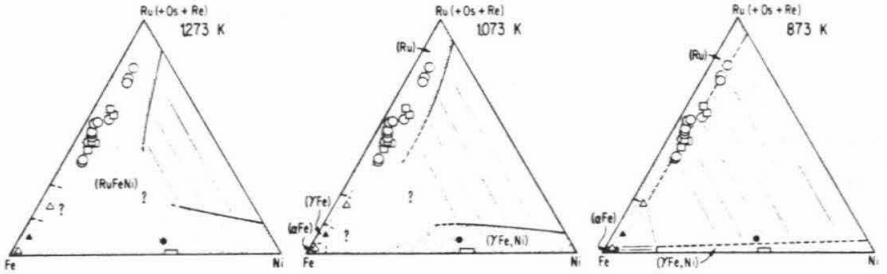

Fig. 4 Isothermal sections for the sub-solidus phase diagram in the Ni-Fe-Ru system (projected from Pt). Experimentally determined phase boundaries (including data from the three binary systems[19,39,40]) are shown as dark solid lines; dark dashed lines are phase boundaries extrapolated into compositional regions not yet investigated. Phase diagrams are incomplete (denoted by "?") in the Fe-rich region at 1,273 and 1,073 K, where several constructions are possible. Single-phase regions are shaded. Tie-lines are shown in two-phase regions as light solid lines; they were determined experimentally where they connect solid phase boundaries and were estimated where they connect dashed phase boundaries. For comparison, analyses of metal phases (open symbols) from three opaque assemblages in CAIs (Allende JIM (○), Allende USNM 5241 "Willy"[11] (□) and Leoville UNM 575 (△) are shown. The rectangular region near the Ni-Fe edge of the triangle encloses 42 analyses of Ni-Fe metal from both Allende opaque assemblages. The approximate bulk metal composition of the two Allende opaque assemblages (●) and the Leoville opaque assemblage (▲) are also shown.

5241 ("Willy")[11] (Fig. 3*b*) and Leoville UNM 575[18] were studied. Each comprises mostly Ni-Fe metal, V-rich magnetite and Ru,Os-rich nuggets. The opaque assemblage from Leoville UNM 575 has a 2×10-μm Ru,Os-rich lamella rather than discrete nuggets. Most Ru,Os-rich nuggets in the two Allende opaque assemblages are 0.1-1 μm in diameter, allowing no more than a single analysis of the largest nuggets. One unusually large 3×5-μm Ru,Os-rich nugget was found in the opaque assemblage from Allende JIM and four non-overlapping analyses were made on this nugget. Compositions of Ru,Os-rich nuggets and the lamella, and adjacent Ni-Fe metal, were measured by ASEM and bulk opaque-assemblage metal compositions were calculated from point-counts. Pt occurs only in the Ni-Fe metal; Ru,Os and Re occur almost entirely in the Ru,Os-rich nuggets; and Ir occurs in both Ni-Fe metal and Ru,Os-rich nuggets. We have represented the sum of the three chemically similar hexagonal-close-packed noble metals (Ru + Os + Re) as the Ru apex in Fig. 4, so that the compositions of Ru,Os-rich nuggets from opaque assemblages can be compared with the Ni-Fe-Ru phase diagrams. The compositions of Ru,Os-rich nuggets from the two Allende opaque assemblages (open circles and squares) spread along a linear trend of constant Ni concentration with variable proportions of Ru and Fe, whereas the Ni-Fe metal (open rectangle) has a fairly constant $Ni_{67}Fe_{33}$ composition. The Ru,Os-rich nugget compositions are lower in Ni than the composition that would be predicted to be in equilibrium with Ni-Fe metal at 1,073 K based on our experimentally determined phase boundaries in the 1,073-K diagram (Fig. 4). However, inspection of the 1,273- and 1,073-K diagrams shows that equilibrium nugget compositions contain progressively less Ni with decreasing temperature. Based on this trend and the inferred 873-K diagram, we suggest that Ru,Os-rich nuggets equilibrated with Ni-Fe metal at ≤873 K. The nearly constant Ni-Fe metal composition could not have been in equilibrium with most of the Ru,Os-rich nugget compositions. We attribute this to homogenization of Ni-Fe metal after equilibration with Ru,Os-rich nuggets, as discussed below.

A good test of the applicability of the inferred phase diagram is the composition of the two coexisting metals in the opaque assemblage from the Leoville CAI, because the bulk metal composition is extremely Ni-poor and lies close to the previously determined Fe-Ru binary system[19]. If the two metal phases were once in equilibrium, their compositions should plot at the ends of a tie-line crossing the bulk metal composition at a particular temperature. As can be seen in Fig. 4, the Leoville opaque assemblage metal compositions (open triangles) agree closely with equilibrium at 873 K.

Diffusion constraints

Arrhenius and Raub[20] first pointed out that the existence of sharp contacts between Ru,Os-rich or Pt-rich nuggets and Ni-Fe metal in opaque assemblages provides an important constraint on the cooling history of opaque assemblages and host CAIs. This argument was largely ignored, however, because D^{Ru}_{Ni} was not known[20] and although D^{Pt}_{Ni} was known, the existence of primary contacts between Pt-rich nuggets and Ni-Fe metal has never been confirmed[11]. The expression for $D^{Ru}_{Ni}(T)$ determined here now permits a calculation of the initial cooling rate (r_0) required to preserve contacts between Ru,Os-rich nuggets and Ni-Fe metal. Using the maximum Ru concentrations in Ni-Fe metal measured 0.5 and 1.0 μm from Ru,Os-rich nuggets, and the equation for diffusion from a 1-μm-diameter sphere[16], we first calculated the value for the time integral of $D^{Ru}_{Ni}(T)$ (or $\tau(\infty)$) that would produce the observed gradients[21]. Equating this to the approximation for $\tau(\infty)$ given by Kaiser and Wasserburg[22] ($\tau(\infty) \approx D(T_0)RT_0^2/Er_0$, where R is the gas constant and E is the activation energy), and assuming that the maximum temperature of melting (T_0) was ~1,700 K, we calculate $r_0 \geq 10^5$ K h^{-1}. Although this r_0 is possible for CAIs in a radiative environment[23], it is unreasonably rapid in light of experimental studies of textures and phase chemistries of the silicate portion of CAIs, which imply much slower cooling ($r_0 \approx 0.5$-20 K h^{-1}; refs 23-27). On the other hand, we calculate from $D^{Ru}_{Ni}(T)$ that the diffusion of Ru in Ni is sufficiently rapid for exsolution of typical 1-μm Ru,Os-rich nuggets (at 10-μm spacings) to occur on a reasonable timescale of about 10 days or 10 years, depending on whether exsolution began at 1,073 or 873 K.

Origin of opaque assemblages

In our phase equilibrium and partitioning experiments, we began with homogeneous Ni-Fe-V alloys and produced V-rich magnetite as rims and intergrowths within V-poor Ni-Fe metal. We also began with Ni-Fe-Pt-Ru(±Ir) alloys and produced magnetite as rims and intergrowths within Ni-Fe metal enriched in Ni and Ru. Ru-rich nuggets were produced by exsolution, and we observed that most Pt remained in the Ni-Fe phase, whereas Ir partitioned into both phases. The textures and mineral chemistries that we produced in the laboratory show a remarkable resemblance to natural opaque assemblages (Fig. 3), and lead us to suggest a new model for their origin. Following previous

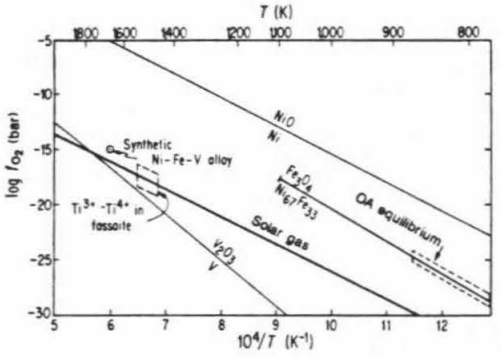

Fig. 5 Plot of $\log f_{O_2}$ versus $1/T$ with relevant equilibrium curves. The conditions of equilibrium for opaque assemblages (OA) are from ref. 11 and this work; the solar gas curve is at $P = 10^{-3}$ bar[41]; the V/V_2O_3 curve is calculated from thermodynamic data[42]; the $Ni_{67}Fe_{33}/Fe_3O_4$ curve is from ref. 30; the fassaite crystallization conditions are based on $Ti^{3+} - Ti^{4+}$ (ref. 36); the open circle gives the experimental conditions for synthesis of the Ni-Fe-V alloy used as starting material in our V partitioning experiments.

workers, we assume that proto-CAIs are refractory, early nebular condensates or evaporative residues. We propose that when the silicate portions of CAIs melted, refractory siderophile elements which had previously condensed as refractory metal alloys[5,6,13] partitioned into homogeneous metallic droplets. At the temperature of CAI melting ($\sim 1{,}700$ K), Ni-Fe metal would occur as molten droplets, consistent with the spheroidal shapes of many opaque assemblages. At this temperature, the only solid phase in most CAIs would be spinel[24]. Subsequent crystallization of spinel could result in the occurrence of opaque assemblages in embayments in spinel crystals (Fig. 1*a*). As CAIs cooled from $\sim 1{,}700$ to $\sim 1{,}500$ K, the metallic droplets crystallized as homogeneous alloys and silicate minerals crystallized around them. At the still lower sub-solidus temperature of ≤ 870 K, the homogeneous alloys exsolved into immiscible metallic phases (such as Ru,Os-rich nuggets and Ni-Fe metal) as they were partially oxidized and sulphidized to form magnetite and associated phases, completing the formation of opaque assemblages.

An important requirement of this model is that there must be a substantial change in f_{O_2} during the formation of the opaque assemblages within the host CAIs. This change is required to explain several basic features of the opaque assemblages, including the oxidation of Ni-Fe metal to magnetite and the initial partitioning of substantial amounts of V into the metal phase at high temperature, followed by subsequent oxidation and diffusion into magnetite. In the remaining discussion, we address the origin of some of the detailed characteristics of opaque assemblages in the context of this model.

Ru,Os-rich nuggets

Ru,Os-rich nuggets from individual opaque assemblages show a large variability in (Ru + Os + Re)/Fe ratios. The compositions spread along the inferred 873-K phase boundary in the Ni-Fe-Ru diagram (Fig. 4). This behaviour is consistent with the exsolution of the Ru,Os-rich nuggets in stages during the removal of Fe from Ni-Fe metal to form magnetite and Fe sulphide, so that a variety of nugget compositions formed as the bulk metal composition became more Ni-rich. If the Ru,Os-rich nuggets were the product of simple equilibrium exsolution, there would be a single nugget composition falling on a common tie-line crossing the bulk metal composition. Only one Ru,Os-rich nugget was large enough to permit multiple analyses; analyses of four separate areas indicate that this nugget is heterogeneous in composition[21]. It is possible that all nuggets are somewhat zoned, and we expect that the edges of each nugget have a constant composition in equilibrium with adjacent $Ni_{67}Fe_{33}$.

Ni–Fe metal

The Ni-Fe metal compositions of opaque assemblages in most Allende CAIs are fairly constant ($Ni_{67}Fe_{33}$), in contrast to the variable compositions of Ru,Os-rich nuggets. We consider $Ni_{67}Fe_{33}$ to reflect the Ni-Fe metal composition in equilibrium with magnetite at the f_{O_2} of the local CAI environment, and thus to be the endpoint of the oxidation process. We suggest that the Ni-Fe metal homogenized during oxidation and exsolution, whereas the isolated Ru,Os-rich nuggets were kinetically inhibited from re-equilibrating with each other. This is consistent with the lower value of D^{Ru}_{Ni} at 873 K determined here ($\sim 2\times10^{-16}$ cm^2 s^{-1}), compared to the value of $D^{Ni}_{Ni\text{-}Fe}$ at 873 K determined by Hirano *et al.*[28] ($\sim 3\times10^{-15}$ cm^2 s^{-1}). We note that $Ni_{67}Fe_{33}$ alloy also coexists with magnetite and sulphide in opaque spheroids in olivine-rich chondrules from Allende[29,30], suggesting that both chondrules and CAIs in this meteorite were exposed to the same ambient f_{O_2} and that the opaque assemblages in the chondrules also represent an oxidation endpoint.

There is a substantial discrepancy between the predictions of equilibrium condensation from a cooling gas of solar composition and the composition of Ni-Fe metal observed in Allende, as models predict a maximum Ni content of about $Ni_{20}Fe_{80}$, whereas $Ni_{67}Fe_{33}$ is observed[31,32]. This discrepancy can be partly accounted for by the enrichment of opaque-assemblage metal in Ni caused by the removal of Fe during oxidation. But adding the Fe contribution from magnetite and Fe sulphide in Allende opaque assemblages back into the bulk metal composition only brings the composition back to a minimum Ni content of about $Ni_{33}Fe_{67}$, which is still somewhat more Ni-rich than the $Ni_{20}Fe_{80}$ condensate composition. If metal condensation occurred under conditions more oxidizing than a solar gas, condensation of more Ni-rich metal is theoretically possible[13].

V-rich phases

The V-rich fassaite rims that frequently surround opaque assemblages can also be understood in the context of our model. We suggest that metallic V was present in molten Ni-Fe alloy droplets at high temperature, in contrast to previous models that assume that V was always present as V_2O_3, which is the oxidized form of V known to occur in silicate and oxide phases[11,12]. In our view, metallic V condensed from the solar nebula either as a metal, or as an oxide which was subsequently reduced during the melting of CAIs. Consider a plot of $\log f_{O_2}$ versus $1/T$ that includes both the solar gas curve (at $P = 10^{-3}$ bar) and the equilibrium curve for the reaction $2V + \frac{3}{2}O_2 = V_2O_3$ (Fig. 5). The two curves cross at $T \approx 1{,}770$ K and $\log f_{O_2} \approx -15$, so that for $T \geq 1{,}770$ K metallic V is stable at the f_{O_2} of a solar gas. A detailed calculation of the $\log f_{O_2}$ versus $1/T$ curve along which an opaque-assemblage alloy with metallic V would be in equilibrium with a CAI silicate liquid containing oxidized V, indicates that this curve would be displaced somewhat to the right of the V/V_2O_3 curve. The shift would lower the temperature at which V would be stable in a Ni-Fe metal droplet immersed in CAI silicate liquid at the f_{O_2} of a solar gas to $\sim 1{,}670$ K. This calculation uses available estimates of V activities in metal[33] and silicate[34], V concentrations in opaque assemblages and bulk

CAIs[11], and an estimate of the fraction of atoms in CAIs once contained in opaque assemblages[11]. As CAIs cooled along the solar gas curve, V in refractory siderophile alloys would be expected to oxidize progressively and diffuse out of the metal because of the difference in the slopes of the solar gas and V/V_2O_3 curves (Fig. 5). The oxidized V could have diffused into surrounding fassaite, resulting in the V-rich fassaite rims. The oxidized V in the silicates may have been present as VO rather than V_2O_3 at high temperatures. But as the V/VO curve is only ~1 log unit more reducing than the V/V_2O_3 curve, the change in speciation would not significantly affect the above argument.

All of these phases in opaque assemblages cannot be produced simply by cooling of a solar gas, because the $Ni_{67}Fe_{33}$ metal and V-rich magnetite must have equilibrated at an f_{O_2} that is ~6 log units more oxidizing than the solar gas curve at a temperature of ≤870 K (Fig. 5). The deviation from the solar gas curve that led to the formation of V-rich magnetite at ~870 K could also have influenced the oxidation of V at intermediate temperatures. Nevertheless, in the context of our model for the origin and evolution of opaque assemblages, the f_{O_2} of the early high-temperature solar nebula must have been at least as reducing as the solar gas curve during CAI melting because of the necessity for V to occur in the alloy. This f_{O_2} is consistent with estimates of the f_{O_2} during CAI crystallization based on Ti^{3+}–Ti^{4+} in fassaites[35,36] (Fig. 5). In these reducing conditions, the siderophile elements Mo, W and P would also have been in a reduced state in the opaque-assemblage alloy. By the time CAIs cooled to ~870 K, however, the f_{O_2} must have deviated from the solar gas curve and increased dramatically to form the V-rich magnetite and possibly the molybdate, tungstate and phosphate found in opaque assemblages.

Other phases

In addition to the coexistence of Ru,Os-rich nuggets and Ni-Fe metal, there are other intergrown phases in opaque assemblages that indicate equilibrium at ≤870 K (for example, $Ni_{67}Fe_{33}$-Fe_3O_4-FeNiS, Fe-FeS-MoS_2 and Fe-Fe_3O_4-$FeAl_2O_4$)[11]. Although we have not explored diffusion within these phases experimentally, we consider it unlikely that intergrowths of these phases could have survived CAI melting and slow cooling. Instead, we also interpret these assemblages as the products of low-temperature re-equilibration.

Our model for opaque assemblages predicts that the refractory siderophiles that are soluble in Ni-Fe metal at low temperature (such as Pt and Ir) should occur dissolved in Ni-Fe metal in opaque assemblages. This is generally the case, but occasionally Pt,Ir-rich nuggets are observed in sulphide-rich opaque assemblages. It has been shown[11,12] that these nuggets formed during low-temperature sulphidization of Ni-Fe-Pt-Ir metal.

The occurrences of small (0.5–3 μm) refractory siderophile metal nuggets in silicate or oxide phases in CAIs with no associated Ni-Fe metal, magnetite or sulphide[7,10,13,37] are not specifically addressed by our model. These nuggets may be either primary condensate grains that did not come in contact with Ni-Fe metal droplets, remnants of digested opaque assemblages, or metals precipitated directly from the CAI silicate liquid.

Finally, it should be noted that isotopic studies of opaque assemblages and isolated refractory siderophile metal nuggets have found no evidence of large isotopic anomalies in any of the elements studied (Mg, Fe, Ru, Mo, W)[38]. These results suggest that opaque assemblages, including Ru,Os-rich nuggets, were most probably formed within the solar nebula rather than outside the Solar System.

Conclusion

We have reproduced the basic assemblage of Ru,Os-rich nuggets, Ni-Fe metal and V-rich magnetite, characteristic of opaque assemblages, by oxidation of a homogeneous alloy at low temperature in the laboratory. We infer that opaque assemblages originated in CAI silicate liquid as homogeneous, probably molten, metal alloy droplets which included the elements Ru, Os, Re, Pt, Ir, W, Mo, P and V in the reduced state. The proto-CAI material most plausibly represents refractory early nebular condensates or evaporative residues. We propose that the complex mineralogy that now characterizes opaque assemblages formed from the alloy droplets by exsolution during progressive oxidation and sulphidization. This process probably occurred during the slow cooling of CAIs at a temperature of ≤870 K. The alternative scenario, that opaque assemblages formed in the solar nebula before CAI melting and were subsequently captured in the CAIs[9,11–13,15], is not tenable because the low-temperature mineral assemblages could not have survived the CAI melting event for any plausible cooling rate. In our view, opaque assemblages do not contain much information on the high-temperature thermal histories of CAIs or record an independent history before CAI formation; they are not 'foreigners' to CAIs in the sense implied by the name "Fremdlinge". Instead, they are 'domestic' and provide equally important constraints on the lower-temperature thermal histories of CAIs and on the changing oxygen fugacity in cooling nebular and/or planetary environments.

We acknowledge the careful analytical and petrographic studies of "Fremdlinge" by J. T. Armstrong and A. El Goresy which set the framework for this study. We thank G. R. Rossman for making his laboratory available to us and H. Palme, K. Keil and the U.S. Museum of Natural History for loaning us the meteorite specimens used in this study, and H. Palme for a careful review. Funding was provided by grants from NASA and NSF, and by Caltech's Caroline Dobbins Fellowship to J.D.B. J.D.B., G.J.W. and I.D.H. are at the Lunatic Asylum of the Charles Arms Laboratory (No. 4537/591).

Received 19 October; accepted 24 December 1987.

1. Grossman, L. *A. Rev. Earth planet. Sci.* **8**, 559–608 (1980).
2. Wasserburg, G. J. & Papanastassiou, D. A. in *Essays in Nuclear Astrophysics* (eds Barnes, C. A., Clayton, D. D. & Schramm, D. N.) 77–140 (Cambridge University Press, New York, 1982).
3. Grossman, L. *Geochim. cosmochim. Acta* **37**, 1119–1140 (1973).
4. Wänke, H., Baddenhausen, H., Palme, H. & Spettel, B. *Earth planet. Sci. Lett.* **23**, 1–7 (1974).
5. Fegley, B. & Kornacki, A. S. *Earth planet. Sci. Lett.* **68**, 181–197 (1984).
6. Palme, H. & Wlotzka, F. *Earth planet. Sci. Lett.* **33**, 45–60 (1976).
7. Wark, D. A. & Lovering, J. F. *Lunar Sci.* **7**, 912–914 (1976).
8. El Goresy, A., Nagel, K., Dominik, B. & Ramdohr, P. *Meteoritics* **12**, 215–216 (1977).
9. El Goresy, A., Nagel, K. & Ramdohr, P. *Proc. Lunar planet. Sci. Conf.* **9**, 1279–1303 (1978).
10. Wark, D. A. & Lovering, J. F. *Lunar Sci.* **9**, 1214–1217 (1978).
11. Armstrong, J. T., El Goresy, A. & Wasserburg, G. J. *Geochim. cosmochim. Acta* **49**, 1001–1022 (1985).
12. Armstrong, J. T., Hutcheon, I. D. & Wasserburg, G. J. *Geochim. cosmochim. Acta* (in the press).
13. Bischoff, A. & Palme, H. *Geochim. cosmochim. Acta* **51**, 2733–2748 (1987).
14. Fuchs, L. H. & Blander, M. *Proc. Lunar planet. Sci. Conf* **11**, 929–944 (1980).
15. Palme, H., Wlotzka, K., Nagel, K. & El Goresy, A. *Earth planet. Sci. Lett.* **61**, 1–12 (1982).
16. Crank, J. *The Mathematics of Diffusion* (Oxford University Press, New York, 1975).
17. Brandstätter, F. & Kurat, G. *Meteoritics* **18**, 272 (1983).
18. Kracher, A. *et al Proc. Lunar planet. Sci. Conf.* **16**, D123–D135 (1985).
19. Swartzendruber, L. J. & Sundman, B. *Bull. Alloy Phase Diagrams* **4**, 155–160 (1983).
20. Arrhenius, G. & Raub, C. J. *J. less-common Metals* **62**, 417–430 (1978).
21. Blum, J. D., Armstrong, J. T., Hutcheon, I. D. & Wasserburg, G. J. *Lunar planet. Sci.* **18**, 97–98 (1987).
22. Kaiser, T. & Wasserburg, G. J. *Geochim. cosmochim. Acta* **47**, 43–58 (1983).
23. MacPherson, G. J., Paque, J. M., Stolper, E. M. & Grossman, L. *J. Geol.* **92**, 289–305 (1984).
24. Stolper, E. M. & Paque, J. M. *Geochim. cosmochim. Acta* **50**, 1785–1806 (1986).
25. Wark, D. A. & Lovering, J. F. *Geochim. cosmochim. Acta* **46**, 2581–2594 (1982).
26. Beckett, J. R. & Grossman, L. *Lunar planet. Sci.* **13**, 31–32 (1982).
27. Barber, D. J., Martin, P. M. & Hutcheon, I. D. *Geochim. cosmochim. Acta* **48**, 769–783 (1984).
28. Hirano, K., Cohen, M. & Averback, B. L. *Acta Metall.* **9**, 440–445 (1961).
29. Haggerty, S. E. & McMahon, B. M. *Proc. Lunar planet. Sci. Conf.* **10**, 851–870 (1979).
30. McMahon, B. M. & Haggerty, S. E. *Proc. Lunar planet. Sci. Conf* **11**, 1003–1025 (1980).
31. Kelly, W. R. & Larimer, J. W. *Geochim. cosmochim. Acta* **41**, 93–111 (1977).
32. Grossman, L., Olsen, E. & Lattimer, J. M. *Science* **206**, 449–451 (1979).
33. Chipman, J. & Dastur, M. N. *J. Metals, N. Y.* **191**, 111–115 (1951).
34. Palme, H. & Schmitt, W. *Lunar planet. Sci. Conf.* **17**, 623–624 (1986).
35. Stolper, E. M., Paque, J. M. & Rossman, G. R. *Lunar planet. Sci.* **13**, 772–773 (1982).
36. Beckett, J. R. & Grossman, L. *Lunar planet. Sci.* **17**, 36–37 (1986).
37. Wark, D. A. *Earth planet. Sci. Lett.* **77**, 129–148 (1986).
38. Hutcheon, I. D., Armstrong, J. T. & Wasserburg, G. J. *Geochim. cosmochim. Acta* **51**, 3175–3192 (1987).
39. Nash, P. *Bull. Alloy Phase Diagrams* **7**, 130–133 (1986).
40. Kubaschewski, O. *Iron-Binary Phase Diagrams* (Springer, New York, 1983).
41. Grossman, L. *Geochim. cosmochim. Acta* **36**, 597–619 (1972).
42. Chase, M. W. Jr *et al J. phys. chem. Ref. Data* **14**, Suppl. 1 (1985).

Geochimica et Cosmochimica Acta Vol. 53, pp. 543–556
Copyright © 1989 Pergamon Press plc. Printed in U.S.A.

0016-7037/89/$3.00 + .00

Origin of opaque assemblages in C3V meteorites: Implications for nebular and planetary processes

JOEL D. BLUM*, G. J. WASSERBURG*, I. D. HUTCHEON*, J. R. BECKETT and E. M. STOLPER
Division of Geological and Planetary Sciences, California Institute of Technology, Pasadena, CA 91125, U.S.A.

(*Received July* 27, 1988; *accepted in revised form November* 18, 1988)

Abstract—Mineral phases from opaque assemblages (OAs) in Ca, Al-rich refractory inclusions (CAIs), chondrules and matrix in C3V meteorites were chemically analyzed and compared with experimentally determined phase equilibria and partitioning data in the Ni-Fe-Ru, Ni-Fe-S and Ni-Fe-O systems to estimate the temperature, sulfur fugacity (f_{S_2}) and oxygen fugacity (f_{O_2}) of OA formation. The kinetics of dissolution and exsolution of metallic phases in the Ni-Fe-Ru system were used to constrain the thermal history of OAs that occur in CAIs. Based on this work, we suggest that OAs formed after the crystallization of host CAIs by exsolution, sulfidation and oxidation of precursor alloys at low temperatures (~770 K) and higher than solar gas f_{S_2} and f_{O_2}. Our model contrasts with previous models that call upon the formation of CAI OAs by aggregation of previously formed phases in the solar nebula prior to the crystallization of CAIs. Opaque assemblages in CAIs and chondrules probably originated as homogeneous alloys during melting of the silicate portions of CAIs and chondrules. The compositions of these precursor alloys reflect high-temperature and low-f_{O_2} conditions in the early solar nebula. The similarities in the temperature, f_{S_2} and f_{O_2} of equilibration for OAs that occur in CAIs, chondrules and matrix suggest that these three components of C3V meteorites share a common, late low-temperature history. The mineral phases in OAs do not preserve an independent history prior to CAI and chondrule melting and crystallization, but instead provide important information on the post-accretionary history of C3V meteorites and allow us to quantify the temperature, f_{S_2} and f_{O_2} of cooling planetary environments.

INTRODUCTION

C3V CHONDRITIC METEORITES consist predominantly of refractory Ca,Al-rich inclusions (CAIs) and olivine-pyroxene chondrules (and mineral fragments), embedded in a fine-grained silicate matrix. CAIs are particularly important to our understanding of nebular processes because they are widely believed to be representative of refractory materials formed by condensation early in the history of the primitive solar nebula (*cf.* GROSSMAN, 1980). Olivine-pyroxene chondrules are less refractory than CAIs and are believed to be mixtures of materials condensed from the nebula (RUBIN and WASSON, 1987). The origin of the matrix is uncertain, but compositional similarities with chondrules suggest an origin involving nebular condensation (RUBIN and WASSON, 1987) and/or alteration of preexisting chondrules (HOUSLEY and CIRLIN, 1983). Although CAIs, chondrules and matrix in C3V chondrites are quite different in bulk composition, they all contain similar multiphase assemblages of alloys, sulfides and oxides that we term *opaque assemblages* (OAs).

Opaque assemblages in CAIs and chondrules are generally spheroidal, 10 to 1000 μm in diameter and consist primarily of γNi-Fe, magnetite (Fe_3O_4), pentlandite [$(Fe,Ni)_9S_8$], pyrrhotite ($Fe_{1-x}S$) and Ca-phosphate [$Ca_3(PO_4)_2$ or $Ca_5(PO_4)_3(F,OH,Cl)$] (Figs. 1–4). CAI OAs (previously called "Fremdlinge"; *e.g.* EL GORESY *et al.*, 1978) additionally contain phases rich in refractory siderophile elements (Figs. 1–3), including Pt-group element-rich metallic phases (most commonly εRu-Fe), molybdenite (MoS_2) and scheelite-powellite solid solution [Ca(W,Mo)O_4], reflecting the large bulk-chemical enrichments in refractory elements in CAIs compared to chondrules. Matrix OAs are generally irregular in shape, 5 to 25 μm across and consist mainly of γNi-Fe and pentlandite with minor pyrrhotite, magnetite and Ca-phosphate (Fig. 5).

The major mineral phases and textural relationships in OAs from CAIs, chondrules and matrix have many similarities, suggesting that they could have formed by similar processes. However, several diverse scenarios have been proposed in the literature for the formation of these three types of OAs:

Opaque assemblages in CAIs have been hypothesized by most recent workers to have formed by the nebular condensation of Pt-group element-rich metallic phases, Ni-Fe alloys, sulfides and oxides that were mechanically mixed at low temperature (<1000 K) in the solar nebula. Subsequently, OAs are believed to have been incorporated into proto-CAI material before (or during) a brief high temperature (~1700 K) event, during which the silicate portion of the host CAIs partially melted and crystallized (ARMSTRONG *et al.*, 1985a, 1987; BISCHOFF and PALME, 1987). According to this model, the phase assemblages in CAI OAs look through the CAI melting event and record highly sulfidizing and oxidizing conditions during condensation very early in the history of the solar nebula. Since some silicate minerals in the host CAIs preserve evidence for crystallization under reducing conditions in the solar nebula (BECKETT *et al.*, 1988), this view of CAI OA origin implies that the condensing nebula was heterogeneous, with local variations in temperature of hundreds of degrees and in oxygen fugacity (f_{O_2}) of many orders of magnitude. It further implies turbulence within the nebula capable of mixing the various phases formed under these conditions. An alternative hypothesis is that the phase assemblages within CAI OAs are not relicts of nebular condensation and instead evolved during a low temperature re-equilibration event(s) after CAI crystallization (BLUM *et al.*, 1988).

Opaque assemblages in chondrules have been proposed to have formed either by sulfidation and oxidation of Ni-Fe alloys in chondrules (HAGGERTY and MCMAHON, 1979) or

* *Also:* Lunatic Asylum of the Charles Arms Laboratory.

by crystallization from metallic-sulfide-oxide liquids that formed immiscible droplets in crystallizing chondrule melts (HAGGERTY and MCMAHON, 1979; MCMAHON and HAGGERTY, 1980). MCMAHON and HAGGERTY (1980) suggested that during chondrule crystallization the nebula either had much higher than solar gas f_{S_2} and f_{O_2} levels, or that chondrules were somehow isolated from the nebular gas, allowing the stabilization of immiscible metallic-sulfide-oxide liquids.

Opaque assemblages in matrix have been proposed to have formed by alteration of alloys that formed by direct condensation from the nebula (RUBIN and GROSSMAN, 1985) or by alteration of alloys from preexisting chondrules (HOUSLEY and CIRLIN, 1983). It has been suggested that this alteration process included the exsolution of $(Fe,Ni)_3P$ from Ni-Fe-P alloys during cooling, which reacted with Ca and O_2 to form Ca-phosphate, while the remaining Ni-Fe alloy was sulfidized to form pentlandite (RAMBALDI and RAJAN, 1982; RUBIN and GROSSMAN, 1985).

To provide a basis for testing models for the formation of OAs in CAIs, chondrules and matrix, we report in a companion paper (BLUM *et al.*, 1989) the results of experiments on phase equilibria, minor element partitioning and diffusion in Ni-Fe-Ru-rich systems, chosen as simplified analogues for some of the assemblages observed in CAI OAs. In this paper, we present analyses of meteoritic OAs, which are used in conjunction with phase equilibria and diffusion data of our own (BLUM *et al.*, 1989) and from the literature to further develop the hypothesis for the origin of OAs in CAIs recently proposed by BLUM *et al.* (1988). We extend our model to OAs in chondrules and matrix and place quantitative constraints on the conditions recorded by the observed phase assemblages and on the thermal histories of OAs. We will make the case that OAs in CAIs, chondrules and matrix could all have formed from homogeneous alloys of different original compositions that initially experienced high temperature reducing conditions and subsequently reequilibrated under conditions of much lower temperature and much higher f_{S_2} and f_{O_2}.

DESCRIPTION OF OPAQUE ASSEMBLAGES STUDIED

Five OAs from Type B CAIs (GROSSMAN, 1980) in C3V chondrites were chosen for study. They are from Allende samples JIM (BRANDSTÄTTER and KURAT, 1983), USNM 5241 ("WILLY" and "F3"; ARMSTRONG *et al.*, 1985a) and EGG3 (MEEKER *et al.*, 1983), and from Leoville sample UNM 575 (KRACHER *et al.*, 1985). We will refer to the individual OAs from CAIs as "JIM-OA1," "WILLY," "F3," "EGG3-OA1" and "LE0575-OA1", respectively. The Allende meteorite belongs to the "oxidized subgroup" of C3V meteorites, which generally contains Ni-rich Ni-Fe alloys, whereas the Leoville meteorite belongs to the "reduced subgroup," which generally contains Fe-rich Ni-Fe alloys (MCSWEEN, 1977). The α, ϵ and γ designations used in this paper for the metallic solid-solution fields in the Ni-Fe-Ru-rich system are based on compositional data rather than direct determination of crystal structure.

JIM-OA1 has a cross-sectional diameter of ~ 30 μm and consists of the phases γNi-Fe, pyrrhotite, ϵRu-Fe, Ca-phosphate, molybdenite and magnetite in order of decreasing abundance (Fig. 1). The ϵRu-Fe phase occurs within γNi-Fe, pyrrhotite and magnetite, but not within Ca-phosphate or molybdenite. Typically, ϵRu-Fe grains within γNi-Fe range in size from 0.3 to 1.0 μm, whereas those within pyrrhotite range from 0.1 to 0.3 μm. One unusually large ($3 \cdot 5$ μm) ϵRu-Fe grain occurs in JIM-OA1 adjacent to γNi-Fe, pyrrhotite and magnetite (Fig. 1). Detailed descriptions of WILLY and F3 can be found in ARMSTRONG *et al.* (1985a). EGG3-OA1 has an irregular shape

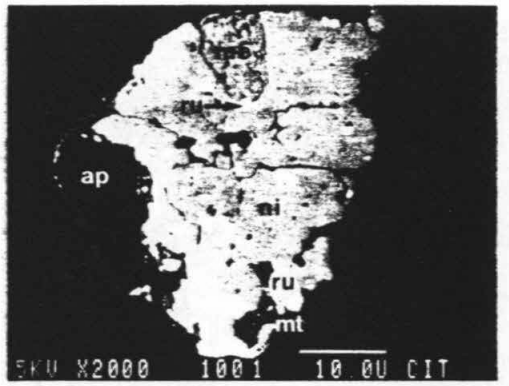

FIG. 1. SEM image of CAI OA JIM-OA1: ru = ϵRu-Fe, ni = γNi-Fe, po = pyrrhotite, mo = molybdenite, ap = apatite and mt = magnetite. Scale bar is 10 microns.

and is $5 \cdot 15$ μm in cross-section. The mineralogy of EGG3-OA1 is typical of OAs in EGG3 (ARMSTRONG *et al.*, 1985b) and consists of very Ni-rich γNi-Fe, heazlewoodite (Ni_3S_2), Ca-phosphate, molybdenite and ϵRu-Fe. LE0575-OA1 has a cross-sectional diameter of about 15 μm and consists of the phases V-rich magnetite, αFe (kamacite), ϵRu-Fe and γNi-Fe (taenite) (Fig. 3). The ϵRu-Fe and γNi-Fe phases occur as ~ 1 μm wide lamellae in the αFe phase, and V-rich magnetite occurs as a partial rim around all of the metallic phases.

We have studied OAs from olivine-pyroxene chondrules and interstitial matrix in many Allende samples. The chondrule OAs that we studied are spheroidal, range in size from 10 to 300 μm and consist of a variety of combinations of γNi-Fe, magnetite, pentlandite, pyrrhotite and Ca-phosphate. The largest chondrule OA that we encountered is shown in Fig. 4. It contains γNi-Fe, magnetite, pentlandite and Ca-phosphate, and is surrounded by much smaller OAs that contain either γNi-Fe and magnetite or γNi-Fe, magnetite and pentlandite (Fig. 4). Descriptions of many Allende chondrule OAs can be found in HAGGERTY and MCMAHON (1979), who studied OAs from over 1000 Allende chondrules, and in HOUSLEY and CIRLIN (1983). Allende matrix OAs that we studied occur as irregular grains and veins 5 to 25 μm across and consist primarily of γNi-Fe and pentlandite (Fig. 5) or pentlandite only. Occasionally, we encountered small (<1 μm) regions of Ca-phosphate or magnetite associated with the matrix OAs. RUBIN and GROSSMAN (1985) reported 5 to 10 μm grains of Ca-phosphate occurring as rims on pentlandite and PECK (1983) reported magnetite grains adhering to olivine in Allende matrix.

ANALYSES OF OPAQUE ASSEMBLAGES

We analyzed metallic and sulfide phases from CAIs, chondrules and matrix OAs described above by analytical scanning electron microscope (SEM), following procedures given in BLUM *et al.* (1989). Analyses are given in Tables 1 and 2 and are reported in atom% throughout this paper unless noted otherwise.

CAI OAs

We mainly concentrated on analyzing metallic phases in CAI OAs (Table 1). Sulfide compositions have been given by ARMSTRONG *et al.* (1985a, 1987) for several of the OAs that we studied; analyses of sulfides in OAs that have not been previously studied are given in Table 2. Our analyses of magnetite from each OA indicate that Ni contents are

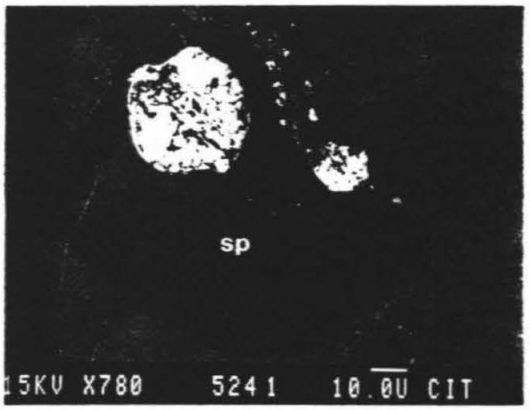

FIG. 2. SEM image of CAI OA F3 (large, round object), surrounded by V-rich fassaite (vfs) and occurring in an embayment in a spinel (sp) crystal. The surrounding host phase is melilite. Scale bar is 10 microns.

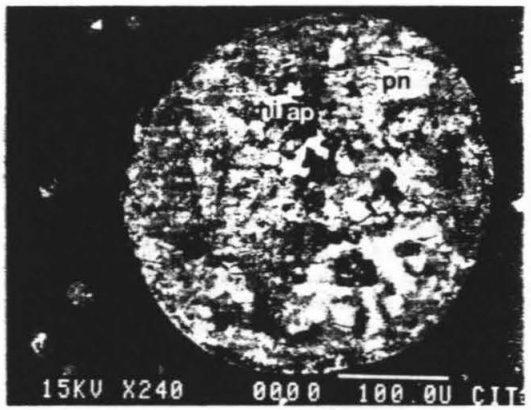

FIG. 4. SEM image of an Allende chondrule OA: pn = pentlandite; other abbreviations as in Fig. 1. Scale bar is 100 microns.

≤0.5% and V contents range from 0.1 to ~12%, consistent with the data of ARMSTRONG *et al.* (1985a).

The γNi-Fe and εRu-Fe phases contain concentrations measurable by SEM (≳0.1%) of the elements Ni, Fe, Co, Ru, Os, Re, Ir and Pt. We measured Ru, Os and Re concentrations in γNi-Fe 0.5 and 1.0 μm from εRu-Fe grains in each OA to determine whether these metallic phase boundaries were compositionally sharp within the resolution of our analyses, which has been calculated to be 0.5 to 0.7 μm (BLUM *et al.*, 1989). Ru, Os and Re concentrations do not increase toward the boundaries and show the same degree of variability as concentrations measured far from boundaries, indicating that they are sharp within the analytical resolution. Most εRu-Fe grains are so small that they can only be analyzed at their center. The large εRu-Fe grain in JIM-OA1 was analyzed in nine nonoverlapping regions and is compositionally heterogeneous (Table 1, analyses 11a–i). The large εRu-Fe lamella in LE0575-OA1 was analyzed in six nonoverlapping regions and is homogeneous (Table 1, analyses 1–6).

Compositional data for metallic phases in CAI OAs are shown in Fig. 6a, where analyses for Ni, Fe and Ru are normalized to 100% and plotted in the Ni-Fe-Ru plane. This representation is used to depict the compositions of metallic phases in CAI OAs because Ni, Fe and Ru comprise ≳95% of the composition of γNi-Fe and αFe, and ~65 to 90% of the composition of εRu-Fe, and because the phase equilibria of compositions near this plane have been studied experimentally (BLUM *et al.*, 1989). An alternative approach, which attempts to account for the influence on phase relations of those components not in the Ni-Fe-Ru system, is to group elements that are chemically similar; *i.e.* Ni and Co are combined at the Ni apex, and Ru, Re and Os are combined at the Ru apex (Fig. 6b). This approach groups elements that have the same crystal structures, form complete solid solutions, have similar melting temperatures, and partition sim-

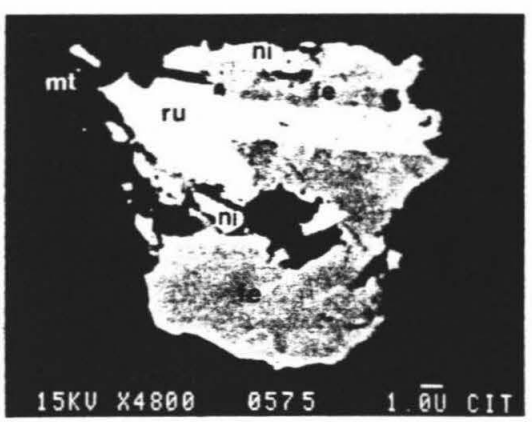

FIG. 3. SEM image of CAI OA LE0575-OA1: fe = αFe; other abbreviations as in Fig. 1. Scale bar is 1 micron.

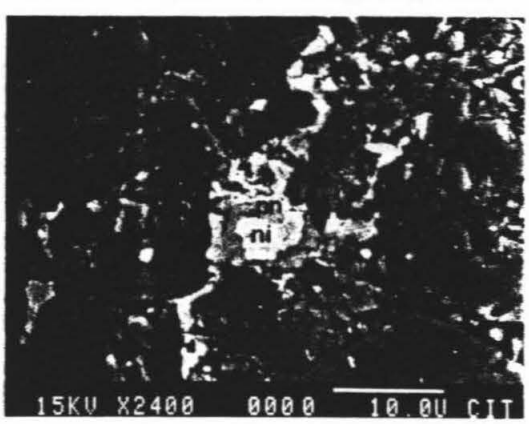

FIG. 5. SEM image of an Allende matrix OA. Abbreviations as in Fig. 1. Scale bar is 10 microns.

Table 1. Analyses in atom percent of coexisting metallic phases in opaque assemblages from CAIs.

		Fe	Co	Ni	Ru	Re	Os	Ir	Pt
JIM-OA1	1	37.46	0.40	5.49	45.77	-	8.19	2.68	-
εRu-Fe	2	41.52	0.67	4.81	43.88	-	6.18	2.96	-
	3	14.40	0.83	6.59	41.33	5.97	30.23	0.66	-
	4	10.44	0.37	4.53	51.17	3.53	28.48	1.47	-
	5	14.64	0.80	5.81	49.50	2.34	26.92	-	-
	6	18.27	-	4.45	47.34	1.32	28.62	-	-
	7	9.71	-	7.62	53.48	2.35	24.58	2.26	-
	8	22.11	-	5.21	49.51	1.18	20.33	1.66	-
	9	33.03	0.43	6.25	48.10	-	10.14	2.06	-
	10	17.52	-	7.23	43.78	2.63	27.43	1.41	-
†	11a	42.06	0.62	3.86	46.05	-	4.02	3.42	-
	b	40.29	0.49	4.24	47.12	-	4.83	3.04	-
	c	38.43	0.37	4.08	48.87	-	5.06	3.19	-
	d	41.38	0.70	4.27	46.42	-	3.73	3.50	-
	e	47.48	0.57	6.27	39.26	-	1.60	4.83	-
	f	49.13	0.58	7.18	37.55	-	1.93	3.63	-
	g	51.30	1.83	6.34	32.84	-	1.93	5.75	-
	h	46.30	1.50	5.60	40.55	-	1.67	4.39	-
	i	41.91	1.18	4.63	44.30	0.34	4.61	3.03	-
JIM-OA1	1	38.20	0.88	57.40	1.45	-	-	1.09	0.99
γNi-Fe	2	38.11	1.32	57.09	1.45	-	-	1.09	0.95
	3	36.52	1.52	59.03	0.71	0.19	-	1.19	0.85
	4	35.91	1.57	58.64	0.71	0.71	-	1.28	1.18
	5	34.90	1.50	60.80	0.41	0.16	-	1.08	1.16
	6	36.83	1.29	58.68	0.96	0.12	-	1.04	1.09
	7	37.14	1.62	57.74	1.43	-	-	1.23	0.95
	8	37.43	1.33	57.07	1.67	-	0.35	1.05	1.11
	9	37.98	1.33	56.78	1.47	-	0.27	1.07	1.11
	10	36.56	1.49	58.46	1.00	0.19	-	1.14	1.15
	11	38.16	0.98	56.96	1.25	0.36	-	1.19	1.10
	12	36.39	1.52	58.94	0.61	0.32	-	1.10	1.11
	13	37.20	1.26	58.20	1.12	0.12	-	1.10	1.01
WILLY	1	30.00	1.19	6.51	35.47	5.29	20.84	0.69	-
εRu-Fe	2	43.55	1.12	6.39	32.38	0.73	13.77	2.09	-
	3	42.66	0.84	7.90	31.59	1.00	14.08	1.95	-
	4	45.29	1.78	6.67	32.39	-	11.86	2.20	-
WILLY	1	35.62	2.16	61.23	0.33	0.20	-	0.31	0.13
γNi-Fe	2	36.14	1.87	61.34	0.21	0.10	-	0.24	0.10
	3	35.97	1.98	61.37	0.18	0.12	0.28	-	0.11
	4	36.61	2.48	60.62	-	-	-	0.12	0.17
	5	35.32	2.36	61.96	-	-	-	0.21	0.15
	6	35.76	2.27	61.47	0.28	-	0.10	0.14	-
	7	35.39	2.40	61.08	0.42	0.16	0.15	0.18	0.23
	8	35.27	1.96	62.16	0.37	-	-	0.24	-
	9	36.32	2.45	60.39	0.33	-	0.15	0.12	0.24
	10	35.33	2.21	61.92	-	0.14	-	0.24	0.16
	11	36.39	2.21	60.45	0.26	0.28	-	0.40	-
	12	35.32	2.21	62.26	-	-	-	0.21	-
	13	35.03	1.98	62.44	0.33	-	-	0.22	-
F3	1	40.19	0.47	7.14	28.81	-	20.64	2.75	-
εRu-Fe	2	34.41	0.87	6.47	26.41	1.88	28.20	1.76	-
F3	1	35.53	1.87	61.05	0.60	-	-	0.80	0.16
γNi-Fe	2	35.67	2.38	60.43	0.61	-	-	0.78	0.12
	3	35.64	1.96	60.82	0.72	-	-	0.86	-
EGG3-OA1	1	1.83	0.38	4.07	60.17	2.56	28.62	2.37	-
εRu-Fe	*2	3.66	.79	4.72	60.82	2.63	27.38	-	-
EGG3-OA1	1	14.21	1.45	83.02	0.36	-	-	0.51	0.45
γNi-Fe	2	14.42	1.93	82.98	-	-	-	-	0.53
	3	14.01	1.88	82.99	-	-	-	0.49	0.31
	4	13.90	1.63	82.38	0.48	0.15	-	0.46	0.35
LE0575	1	69.29	-	4.54	18.27	0.23	4.97	2.70	-
-OA1	2	71.47	-	4.22	16.75	-	4.76	2.80	-
εRu-Fe	3	72.08	-	4.13	15.51	0.32	5.10	2.47	0.39
	4	70.82	-	4.54	16.12	0.20	5.20	2.42	0.70
	5	71.49	-	4.14	15.85	0.29	5.74	2.09	0.40
	6	68.74	-	5.00	18.16	0.55	4.48	3.07	-
LE0575	1	72.50	0.28	10.40	8.53	0.88	1.76	3.61	2.06
-OA1	2	72.90	-	12.63	7.67	0.32	1.76	2.25	2.48
γNi-Fe	3	73.80	-	10.46	8.53	0.48	2.33	2.83	1.57
	4	75.61	-	10.02	7.04	0.39	1.85	2.91	2.19
LE0575	1	92.47	0.29	2.96	1.26	-	0.47	0.75	1.80
-OA1	2	92.01	0.56	2.77	1.11	0.25	-	1.72	1.58
αFe	3	93.04	0.52	2.57	1.06	-	-	1.21	1.60
	4	91.44	0.64	3.35	1.41	-	-	1.59	1.57
	5	92.44	0.45	2.69	0.84	0.19	-	1.71	1.69
	6	92.05	0.41	3.03	1.27	-	-	1.69	1.54

Note: - indicates below 0.1% detection limit. V, Si, P, S, Ti, Cr, Rh and Mo were analyzed but were below detection limits. Analytical totals ranged from 96 to 104 percent and were normalized to 100%. * indicates that composition was normalized to exclude partial analysis of surrounding γNi-Fe. † Analyses 11a-i represent non-overlapping analysis of one large grain of εRu-Fe. Analytical uncertainties are about ±5% of the values reported.

ilarly between phases in OAs. Greater than 95% of the composition of each major metallic phase is accounted for on the (Ni + Co)-Fe-(Ru + Re + Os) diagram (Fig. 6b). Pt and Ir are excluded by both treatments, but these are minor constituents in the metallic phases, do not mimic the behavior of any of the major elements in the metallic phases, and, in any case, appear to have little influence on phase equilibria in the Ni-Fe-Ru system at the concentrations found in OAs (BLUM *et al.*, 1989). The resulting compositional regions in Figs. 6a and b are very similar; for convenience, Fig. 6a will be used for comparison with the Ni-Fe-Ru phase diagram in the following section.

To evaluate the relationship between the concentrations of Ru, Os and Ir and the Fe content of εRu-Fe grains and lamellae, we have plotted them *versus* Fe for JIM-OA1 and LE0575-OA1 (Fig. 7). Ru concentrations in εRu-Fe grains in JIM-OA1 (Fig. 7, open circles) are relatively insensitive to variations in Fe, whereas Os displays a negative, and Ir a positive, correlation with Fe. The γNi-Fe phase in JIM-OA1 (Fig. 7, asterisk) has a restricted compositional range. Each of the three phases from LE0575-OA1 (Fig. 7, filled circles) have distinct concentrations of Ru and Os.

The partitioning of Pt and Ir between εRu-Fe and γNi-Fe can be evaluated for the CAI OAs that we analyzed. Pt and Ir concentrations of γNi-Fe are nearly constant for each OA studied; Ir concentrations are somewhat variable in εRu-Fe from each OA (Table 1). The (εRu-Fe)/(γNi-Fe) partition coefficients (K^i for element i) were calculated for Pt and Ir in each CAI OA using the average Pt and Ir concentrations, except for the Pt content of εRu-Fe, which was below the 0.1% detection limit, allowing us only to calculate an upper limit for K^{Pt}: JIM-OA1 ($K^{Pt} \leq 0.1$, $K^{Ir} = 2.4$); WILLY ($K^{Pt} \leq 0.7$, $K^{Ir} = 2.2$); F3 ($K^{Pt} \leq 0.2$, $K^{Ir} = 2.5$); EGG3-OA1 ($K^{Pt} \leq 0.1$, $K^{Ir} = 2.4$); and LE0575-OA1 ($K^{Pt} \leq 0.1$, $K^{Ir} = 0.9$). These K^{Pt} and K^{Ir} values are similar to those determined experimentally at 873 K by BLUM *et al.* (1989) ($K^{Pt} = 0.16$ and $K^{Ir} = 1.6$). In both the OAs and the experiments of BLUM *et al.* (1989), Pt partitions preferentially into face-centered cubic (fcc) γNi-Fe, whereas Ir partitions preferentially into close-packed hexagonal (cph) εRu-Fe.

Chondrule OAs

Our analyses of metallic phases and sulfides from Allende chondrule OAs are given in Table 2 to augment the extensive analytical data of HAGGERTY and MCMAHON (1979). Chondrule OAs are texturally similar to CAI OAs and are comprised of the same major mineral phases. The compositions of γNi-Fe, pyrrhotite and pentlandite are similar in most chondrule and CAI OAs (Tables 1 and 2; HAGGERTY and MCMAHON, 1979; ARMSTRONG *et al.*, 1985a, 1987). Refractory siderophile element-rich phases, which are common in CAI OAs, have never been reported in chondrule OAs. Refractory siderophile and V abundances in γNi-Fe, sulfides and oxides from chondrule OAs are ≤0.1%. The refractory siderophile contents of bulk OAs from chondrules have not been determined, but the refractory siderophile contents of whole chondrules are approximately chondritic (RUBIN and WASSON, 1987).

Matrix OAs

We analyzed γNi-Fe + pentlandite assemblages in matrix OAs, and give analyses in Table 2; major element analyses of phases in matrix OAs have not previously been published.

Table 2. Analyses in atom percent of coexisting γNi-Fe and sulfides in opaque assemblages.

		S	Fe	Co	Ni
Matrix OAs					
γNi-Fe	1a	-	32.22	1.71	66.07
	2a	-	31.93	1.77	66.30
	3a	0.17	31.57	1.44	66.82
	4a	-	31.97	1.58	66.45
Pentlandite	1b	47.53	36.42	0.49	15.56
	2b	45.03	37.72	0.65	16.60
	3b	45.63	34.82	0.68	18.87
	4b	49.44	34.79	0.55	15.23
Chondrule OAs					
γNi-Fe	1a	-	28.07	1.09	70.84
	2a	-	31.53	1.61	66.86
Pentlandite	1b	45.86	32.27	1.14	20.73
	2b	47.15	36.51	0.60	15.74
Pyrrhotite	2c	51.75	48.25	-	-
	3	50.57	46.82	-	-
JIM-OA1					
Pyrrhotite	1	51.86	48.14	-	-
	2	50.17	46.63	-	0.35
	3	49.78	47.47	-	0.20
γNi-Fe		(see Table 1)			
EGG3-OA1					
Heazlewoodite	1	41.92	0.66	-	57.42
	2	41.25	0.30	0.18	57.52
	3	39.09	0.92	0.31	59.32
γNi-Fe		(see Table 1)			

Note: a and b represent analyses of adjacent phases within a single OA. - indicates below 0.1% detection limit. Analytical totals ranged from 96 to 104% and were normalized to 100%. Analytical uncertainties are about ±5% of the values reported.

Concentrations of refractory siderophile elements in all matrix OA phases that we analyzed are ≲0.1%, and we did not observe any discrete refractory siderophile element-rich phases. As in the case of chondrules, the bulk matrix refractory siderophile contents are approximately chondritic (RUBIN and WASSON, 1987).

CONDITIONS OF OPAQUE ASSEMBLAGE FORMATION AS INDICATED BY PHASE EQUILIBRIA

Ni-Fe-Ru system

Phase boundaries and equilibrium tie lines in Ni-Fe-Ru-rich systems at 1073, 873 and 773 K were estimated based on experimental data by BLUM *et al.* (1989) and are plotted in Fig. 8 along with compositional regions for metallic phases from CAI OAs from the data in Fig. 6a; similar compositional regions result if Fig. 6b is used to represent the CAI OA data. In each of the CAI OAs studied, γNi-Fe compositions fall in narrow ranges (Fig. 8). Based on the phase diagram, we would expect the composition of εRu-Fe in equilibrium with the γNi-Fe to fall in a similarly narrow compositional range joined by tie lines to the γNi-Fe. This is observed for the Ni-poor αFe and εRu-Fe that coexist in LE0575-OA1 and the Fe-poor γNi-Fe and εRu-Fe that coexist in EGG3-OA1, which can be approximated by tie lines at ~870 K in the Fe-Ru binary and at ~770 K in the Ni-Ru binary, respectively (Fig. 8b, c). In contrast, the narrow compositional range of γNi-Fe in JIM-OA1, WILLY and F3 is in contact with εRu-Fe that spans a broad range roughly parallel to the Ru-Fe side of the ternary diagram at ~5 to 10% Ni (Fig. 8). These εRu-Fe compositions cannot represent equilibrium, but the orientation of the compositional trend parallel to the edge of the two-phase region at ~770 K suggests that their compositions were controlled by equilibration with γNi-Fe at this temperature (Fig. 8c).

In the experiments of BLUM *et al.* (1989), initially homogeneous Ni-Fe-Ru-rich alloys were annealed at high f_{O_2}; Ni enrichment was observed in alloys at the outer edges of experimental charges where they were exposed to O_2, due to depletion of the alloys in Fe as Fe-rich oxides formed. This process resulted in the exsolution of εRu-Fe grains that span a compositional range similar to that of εRu-Fe grains in natural CAI OAs. In general, Fe oxidation or sulfidation will result in bulk alloy compositions that lie along a trend radial to the Fe apex. If exsolution accompanies Fe depletion, each stage of exsolution will produce coexisting εRu-Fe and γNi-

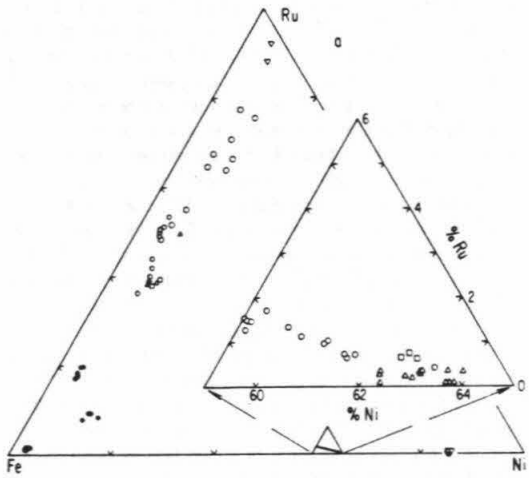

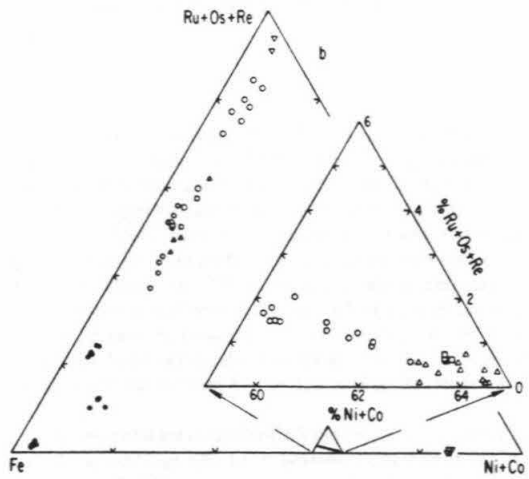

FIG. 6. Chemical compositions of metallic phases in the five CAI OAs studied, normalized and plotted on the a) Ni-Fe-Ru triangle and b) on the (Ni + Co)-Fe-(Ru + Os + Re) triangle. Open circles are from JIM-OA1, filled circles are from LE0575-OA1, triangles are from WILLY, squares are from F3 and inverted triangles are from EGG3-OA1. Insets show enlargements of the γNi-Fe field for JIM-OA1, WILLY and F3.

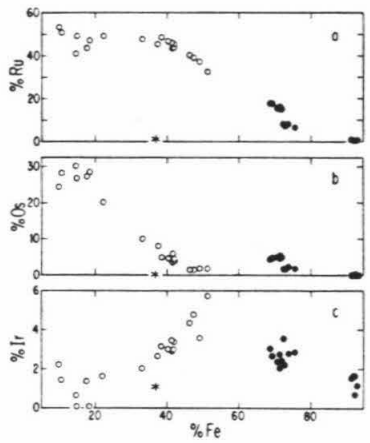

FIG. 7. Concentration of a) Ru, b) Os and c) Ir plotted against Fe for metallic phases in the two CAI OAs studied for which there is a large variation in Fe content. Open circles represent concentrations in ϵRu-Fe from JIM-OA1, asterisks represent the average concentrations of γNi-Fe from JIM-OA1, and filled circles represent concentrations in the three metallic phases from LE0575-OA1.

Fe phases that are progressively lower in Fe (a schematic path for an initially Fe-rich alloy is depicted with an arrow in Fig. 8c). If the process goes to completion, the final, homogeneous γNi-Fe and ϵRu-Fe phases will be those in equilibrium with magnetite at the f_{O_2} of the environment in which the oxidation occurred (and/or in equilibrium with Ni-Fe sulfide at the f_{S_2} of this environment). If, as in the experiments of BLUM *et al.* (1989), the process does not go to completion, a gradient in ϵRu-Fe and γNi-Fe compositions, reflecting a gradient in f_{O_2} (and/or f_{S_2}) from the outside to the center of the alloy, is expected. To generate the widest range of ϵRu-Fe compositions observed in CAI OAs by this kind of process, their exsolution must have begun from a bulk alloy composition at least as Fe-rich as $Ni_{40}Fe_{60}$.

The wide range of ϵRu-Fe compositions in natural CAI OAs could have evolved by exsolution during oxidation (or sulfidation) as in the experiments of BLUM *et al.* (1989). However, if this were the case, we would also expect a wide range of complementary γNi-Fe phase compositions (ranging from $Ni_{40}Fe_{60}$ to $Ni_{67}Fe_{33}$ in the case of JIM-OA1), but this is not observed. Instead, as pointed out earlier, γNi-Fe in contact with ϵRu-Fe covering the full range of observed compositions display a very restricted compositional range around $Ni_{67}Fe_{33}$. One possibility is that the γNi-Fe was homogenized subsequent to exsolution, whereas the ϵRu-Fe grains were kinetically inhibited from reequilibrating with surrounding γNi-Fe. This would require that interdiffusion in fcc γNi-Fe is much faster than in cph ϵRu-Fe. In order to account for the homogenization of the γNi-Fe over the ~ 10 μm radius of JIM-OA1, while retaining non-equilibrium ϵRu-Fe compositions over the ~ 1 μm radius of ϵRu-Fe grains, the ratio of interdiffusion constants ($\tilde{D}_\gamma/\tilde{D}_\epsilon$) must be 10^2 or higher. The determination of $\tilde{D}_\gamma/\tilde{D}_\epsilon$ at 773 K could, therefore, provide an important test of our model. Although the appropriate diffusion data are not available for this test, diffusion in the Ni-Fe system has been studied at low temperatures and may be somewhat analogous. DEAN and GOLDSTEIN (1986) studied interdiffusion in fcc γNi-Fe and body-centered cubic (bcc) αNi-Fe and found that at 773 K, $\tilde{D}_\gamma/\tilde{D}_\alpha \approx 5 \cdot 10^2$, suggesting that differences in crystal structure can account for large differences in $\tilde{D}$ at low temperature. In addition, both the possible presence of low concentrations of P in CAI OA Ni-Fe alloys and the importance of grain-boundary diffusion at lower temperatures (DEAN and GOLDSTEIN, 1986) may have enhanced the rate of homogenization of γNi-Fe compared to ϵRu-Fe.

The bulk compositions of alloys in the five CAI OAs that we studied were estimated by point-counting (Fig. 8). The bulk compositions enter two-phase (or three-phase) regions in the Ni-Fe-Ru diagram at $\lesssim$870 K (Fig. 8b). The compositional range of ϵRu-Fe grains from JIM-OA1, WILLY and F3 fall in a linear trend with constant Ni content along an estimated two-phase boundary at $\sim$770 K (Fig. 8c). The γNi-Fe phase from JIM-OA1, WILLY and F3 (Figs. 6a and 8c) also lies near a two-phase boundary estimated for $\sim$770 K. A lower temperature limit of 740 K can be inferred because the γNi-Fe compositions in these OAs would be expected to exsolve into two phases (γNi-Fe and $FeNi_3$) below 740 K according to a recent compilation of the Fe-Ni binary system (KUBASCHEWSKI, 1983), suggesting that equilibration occurred at >740 K. The coexisting ϵRu-Fe and γNi-Fe in EGG3-OA1 are close in composition to the Ni-Ru binary and indicate equilibration at $\sim$770 K (Fig. 8c).

LE0575-OA1 contains three distinct metallic phases (Fig. 8). The αFe and ϵRu-Fe compositions fall very close to the Ru-Fe binary and indicate equilibration temperatures of $\sim$870 K. The coexisting γNi-Fe is more difficult to interpret because the composition does not lie near one of the binaries, but we have inferred from binary data that a three-phase region exists in that region at temperatures of $\lesssim$870 K, and the γNi-Fe phase along with the αFe and ϵRu-Fe phases may define a three-phase triangle at $\sim$870 K (BLUM *et al.*, 1989; Fig. 8b).

Ni-Fe-S system

A schematic representation of the S-poor portion of the Ni-Fe-S phase diagram at 773 K is given in Fig. 9a based on the data of MISRA and FLEET (1973) and KUBASCHEWSKI (1983); the approximate positions of the pentlandite + pyrrhotite + γNi-Fe three-phase region at 773 and 558 K are given in Fig. 9b. Pentlandite is a stable phase only below 883 K (MISRA and FLEET, 1973). With decreasing temperature, the compositions of pentlandite and γNi-Fe coexisting with pyrrhotite become progressively lower in Ni, varying from 20 to 14% Ni in pentlandite and 64 to 27% Ni in γNi-Fe as temperature varies from 873 to 558 K (Fig. 9b; MISRA and FLEET, 1973).

Four assemblages in the Ni-Fe-S system occur in OAs (Fig. 9a): the assemblage γNi-Fe + heazlewoodite occurs in CAI OAs from EGG3; the assemblages pyrrhotite + γNi-Fe and pyrrhotite + pentlandite + γNi-Fe are common in both CAI and chondrule OAs; and the assemblage pentlandite + γNi-Fe is sometimes found in CAI and chondrule OAs and is the exclusive assemblage in matrix OAs. For any given assem-

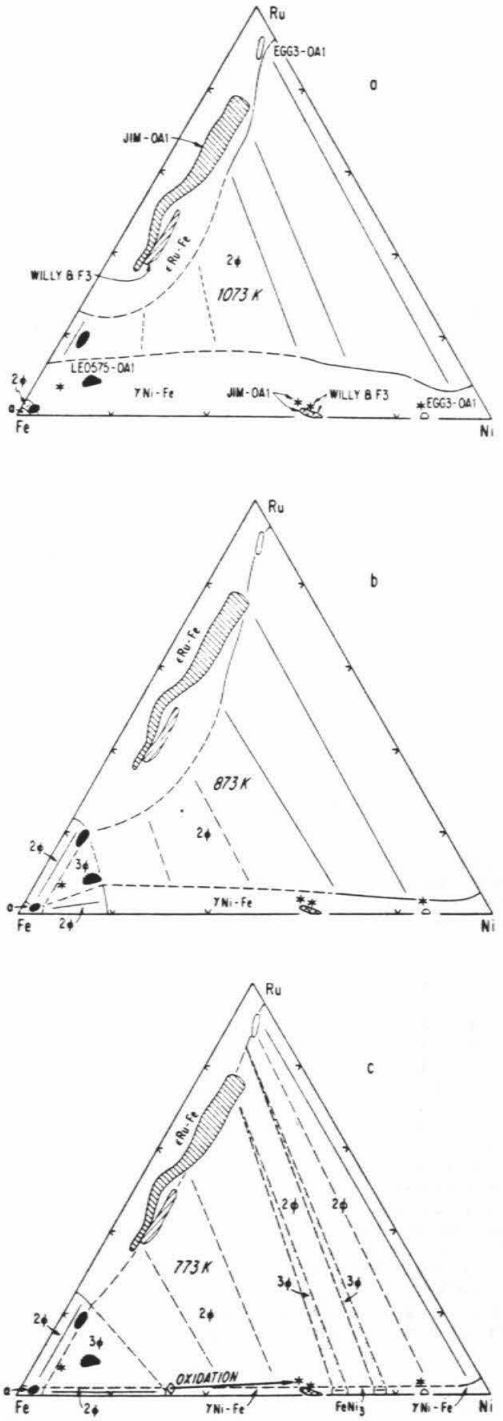

FIG. 8. Compositional regions of metallic phases in CAI OAs from Fig. 6a plotted on isothermal sections of the Ni-Fe-Ru plane along with phase equilibria from BLUM *et al.* (1989) at a) 1073 K, b) 873 K and c) 773 K. Phase boundaries and tie-lines are solid near regions where there is experimental data; dashed phase boundaries and tie lines are estimated or schematic. The 773 K diagram is speculative and is intended to be diagramatic only. Two- and three-phase regions are denoted by 2ϕ and 3ϕ respectively and three-phase regions are also stippled. Single-phase solid-solution regions include fcc γNi-Fe, cph εRu-Fe and bcc αFe. Asterisks represent bulk alloy compositions for each OA estimated from point-counting. The oxidation arrow in (c) connects the approximate total bulk compositions (including alloys, sulfides and oxides) of JIM-OA1, WILLY and F3 (diamond) with the approximate bulk alloy compositions.

blage, the compositions of individual phases in all OAs studied from CAIs, chondrules and matrix are similar (Fig. 9b). The γNi-Fe and pentlandite compositions vary systematically depending on the assemblage, consistent with general trends of tie lines on the Ni-Fe-S phase diagram (Fig. 9a). The composition of γNi-Fe coexisting with pentlandite and pyrrhotite suggests equilibration at ~770 K, but the composition of pentlandite in this assemblage suggests equilibrium at ~560 K (MISRA and FLEET, 1973). One possibility is that the closure temperature for γNi-Fe equilibration with pentlandite and pyrrhotite was ~770 K in the OAs, but pentlandite and pyrrhotite continued to react and reequilibrate upon cooling to ~560 K.

The variety of sulfide phases present in OAs gives an indication of the f_{S_2} during equilibration. Stability curves for Mo, Fe, Ni-Fe, Ru and Pt sulfides are shown in Fig. 10, as is the equilibrium solar gas curve. The curve labeled Ni-Fe alloy/Ni-Fe sulfide shows the conditions under which OA sulfide and alloys could coexist; it is calculated from the reaction $Fe + \frac{1}{2}S_2 \rightarrow FeS$, assuming ideal solution in the alloy and sulfide and an alloy composition of $Ni_{67}Fe_{33}$. The conditions of equilibration between $Ni_{85}Fe_{15}$ and Ni_3S_2, calculated from the reaction $3Ni + S_2 \rightarrow Ni_3S_2$, falls within 0.2 log units of the curve shown. Thus the f_{S_2} of equilibrium for the assemblage $Ni_{67}Fe_{33}$-FeS (found in most CAI and chondrule OAs) and the assemblage $Ni_{85}Fe_{15}$-Ni_3S_2 (found in CAI OA EGG3-OA1) are nearly identical. The f_{S_2} and temperature constraints (discussed above) are combined and shown as region I in Fig. 10. The position of region I with respect to the Mo/MoS, Ru/RuS_2 and Pt/PtS curves is consistent with the observation that Mo in CAI OAs occurs as MoS_2, whereas Ru and Pt occur in metallic phases but not as sulfides. The f_{S_2} of equilibration is higher than the f_{S_2} of a solar gas at temperatures above about 700 K.

Ni-Fe-O system

The conditions of f_{O_2} and temperature at which Ni-Fe alloys are in equilibrium with Ni-poor magnetite for several alloy compositions relevant to OAs are shown in Fig. 11, based on MCMAHON and HAGGERTY (1980). Curve (a) shows the conditions of equilibrium for αFe metal and Fe_3O_4, and curves (b) and (c) show the conditions of equilibrium for $Ni_{67}Fe_{33}$ and $Ni_{85}Fe_{15}$ alloy with Fe_3O_4.

Magnetites from CAI OAs (ARMSTRONG *et al.*, 1985a, 1987) and chondrule OAs (HAGGERTY and MCMAHON, 1979) contain ≤0.5% Ni, and those that are low in V (≤0.1%) are therefore close in composition to Fe_3O_4. From Fig. 11, we see that the $Ni_{67}Fe_{33}$ alloy that occurs in most CAI OAs,

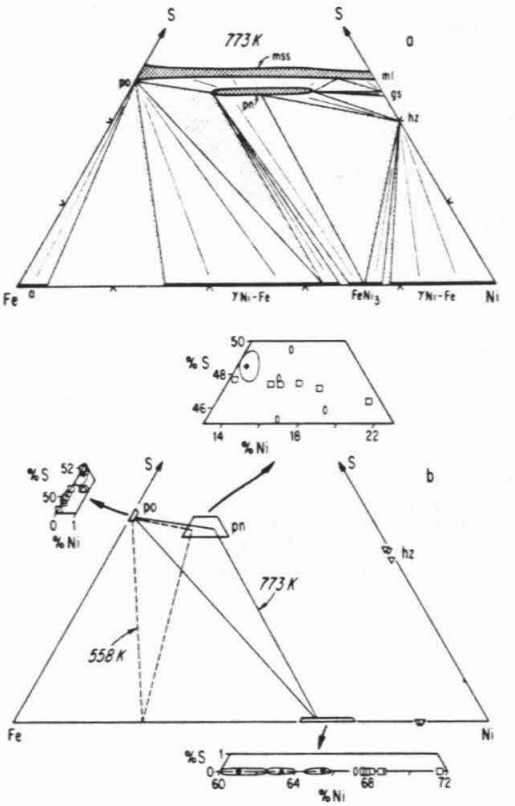

FIG. 9. a) A schematic representation of the sulfur-poor portion of the Ni-Fe-S phase diagram at 773 K and b) the position of the pentlandite + pyrrhotite + γNi-Fe three-phase region at two temperatures from our interpretation of the data of MISRA and FLEET (1973) and KUBASCHEWSKI (1983). The intersections of phase fields within the Ni-Fe binary contrast somewhat with those of MISRA and FLEET (1973) because these authors assumed the Ni-Fe binary phase relations of OWEN and LIU (1949) that have been shown to be incomplete (see compilation by KUBASCHEWSKI, 1983). mss = monosulfide solid solution, po = pyrrhotite, pn = pentlandite, ml = millerite, gs = godlevskite and hz = heazlewoodite. In (a), dark lines on the Ni-Fe binary indicate ranges of Ni-Fe solid solutions, dark stippled regions indicate ranges of monosulfide and pentlandite solid solution and tie lines are shown in two-phase regions. The compositions of sulfides and γNi-Fe from OAs were normalized to exclude Co and are shown in (b) for comparison; ovals are from matrix OAs (Table 2), squares are from chondrule OAs (Table 2; HAGGERTY and MCMAHON, 1979), circles are from CAI OA JIM-OA1 (Tables 1 and 2), inverted triangles are from CAI OA EGG3-OA1 (Tables 1 and 2), triangles are from CAI OA WILLY (ARMSTRONG *et al.*, 1985a; Table 1), and diamonds are from CAI OA ZELDA (ARMSTRONG *et al.*, 1987). Open symbols are individual analyses, and filled symbols within elliptical regions represent the mean and range of multiple analyses. Insets show enlargements of the γNi-Fe, pentlandite and pyrrhotite fields.

and in all chondrule and matrix OAs in Allende, would be in equilibrium with Fe_3O_4 only along curve (b) (at temperatures below ~1100 K). The αFe alloy in CAI LE0575-OA1 (≲3% Ni) equilibrates with Fe_3O_4 along curve (a) (tempera-

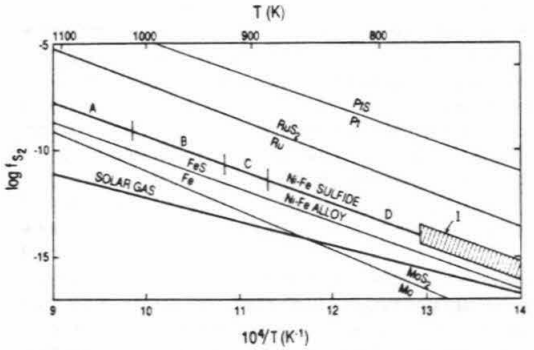

FIG. 10. Plot of the logarithm of f_{S_2} *versus* T for equilibria relevant to OA origin. Solar gas curve is from FUCHS and BLANDER (1977). Buffer curves are calculated from thermodynamic data compiled by BARTON and SKINNER (1979) except for the Ru/RuS_2 curve, which is from SVENDSEN (1979). The curve labeled Ni-Fe alloy/Ni-Fe sulfide is broken into four segments (A–D) based on Ni-Fe-S phase equilibria from the compilation of HSIEH *et al.* (1982) at $T \geq 973$ K and from MISRA and FLEET (1973) at $T \leq 873$ K. For each line segment, a different assemblage of sulfides may be in equilibrium with Ni-Fe alloy: A: FeS, Ni-S melt; B: FeS, Ni_3S_2, Ni-S melt; C: FeS, Ni_3S_2; and D: FeS, Ni_3S_2, $(Fe,Ni)_9S_8$. The position of the Ni-Fe alloy/Ni-Fe sulfide curve is calculated from the reactions $Fe + \frac{1}{2}S_2 \rightarrow FeS$ and $3Ni + S_2 \rightarrow Ni_3S_2$ (see text). Region I is the $f_{O_2} - T$ space for equilibration of CAI, chondrule and matrix OAs determined in this study; the region brackets the Ni-Fe alloy/Ni-Fe sulfide curve to display the approximate uncertainties due to non-ideal solution, compositional variability of phases and thermodynamic parameters.

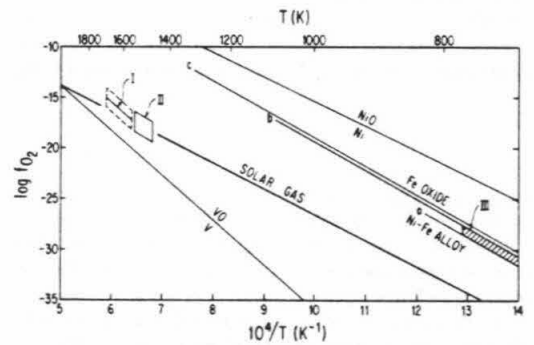

FIG. 11. Plot of the logarithm of f_{O_2} *versus* T for equilibria relevant to OA origin. The solar gas curve is at $P = 10^{-3}$ bar (GROSSMAN, 1972) and the V/VO and Ni/NiO curves are calculated from thermodynamic data (CHASE *et al.*, 1985). Curve (a) is Fe/Fe_3O_4, curve (b) is $Ni_{67}Fe_{33}/Fe_3O_4$, and curve (c) is $Ni_{85}Fe_{15}/Fe_3O_4$ (MCMAHON and HAGGERTY, 1980). Lines a, b and c end at the highest temperatures at which the alloys are stable with magnetite (MCMAHON and HAGGERTY, 1980). Region I is the $f_{O_2} - T$ space for partitioning of V between alloy and silicate liquids as calculated in the text. Region II is the $f_{O_2} - T$ space for crystallization of fassaite in CAIs based on reactions involving Ti^{3+}/Ti^{4+} ratios in fassaites (BECKETT and GROSSMAN, 1986). Region III is the $f_{O_2} - T$ space determined in this study for equilibration of CAI, chondrule and matrix OAs. The sizes of regions I, II and III display the approximate uncertainties due to non-ideal solution, compositional variability of phases and thermodynamic parameters.

tures below ~870 K), and the $Ni_{85}Fe_{15}$ alloy in CAI EGG3-OA1 equilibrates with Fe_3O_4 along curve (c) (temperatures below ~1330 K). If Fe-rich Ni-Fe alloys are exposed to an f_{O_2} more oxidizing than the Fe-Fe_3O_4 buffer at ≲870 K [curve (a)], magnetite will form, enriching the remaining alloy in Ni as demonstrated by BRETT (1967) and MCMAHON and HAGGERTY (1980). If log f_{O_2} were ~1 unit more oxidizing than the Fe-Fe_3O_4 buffer [*i.e.* on curve (b)], magnetite formation would proceed until the alloy was enriched in Ni to the $Ni_{67}Fe_{33}$ alloy composition. If log f_{O_2} were ~1.5 units more oxidizing than the Fe-Fe_3O_4 buffer [curve (c)], oxidation would proceed until the $Ni_{85}Fe_{15}$ alloy composition was reached. It is clear that oxidation of an initially Fe-rich alloy within a small range of oxygen fugacity near the Fe-Fe_3O_4 buffer can result in large variation in Ni-Fe alloy compositions.

Magnetites from CAI OAs sometimes contain up to 12% V as V_2O_3 (ARMSTRONG *et al.*, 1987) which coexists with Ni-Fe alloys that contain ≲0.1% V. This can be explained by the experiments of BLUM *et al.* (1989) which showed that, while 0.5% V can dissolve in Ni-Fe alloys at f_{O_2}'s slightly lower than the Fe-FeO buffer, when these alloys are exposed to f_{O_2}'s above the Fe-FeO buffer, V will oxidize from the alloy and partition strongly into magnetite rims as they form.

ALLOY DIFFUSION IN CAI OPAQUE ASSEMBLAGES

Preservation of sharp phase boundaries

ARRHENIUS and RAUB (1978) showed that the reported existence of sharp boundaries between Pt-rich metallic phases and Ni-Fe-rich metallic phases (EL GORESY *et al.*, 1978) in CAI OAs could provide important constraints on the cooling history of these OAs and their host CAIs if Pt-rich phases were early nebular condensates that aggregated with Ni-Fe-rich phases before the melting of CAIs, as suggested by EL GORESY *et al.* (1978). Using the diffusion coefficient (D) for Pt in Ni, ARRHENIUS and RAUB (1978) calculated that the sharp phase boundaries could not have existed at CAI liquidus or condensation temperatures (1600–1700 K) for more than a fraction of a second or at 900 K for more than one day without developing measurable diffusion gradients due to the dissolution of Pt in the Ni-Fe phase. They concluded that CAIs must have formed during extremely short thermal pulses.

Recent studies of CAI OAs (ARMSTRONG *et al.*, 1985a, 1987) have not confirmed the original report (EL GORESY *et al.*, 1978) of Pt-rich metallic phases in contact with Ni-Fe-rich metallic phases (as a rule, Pt-rich metallic phases are surrounded by sulfide); however, the approach taken by ARRHENIUS and RAUB (1978) is potentially powerful and can be used to interpret the commonly observed boundaries between εRu-Fe and γNi-Fe in CAI OAs that we have described above. Using the recent determination by BLUM *et al.* (1989) of the diffusion coefficient for Ru in γNi as a function of temperature [$D^{Ru}_{Ni}(T)$] as a simplified analog for the diffusion of Ru in γNi-Fe in CAI OAs, we have calculated isothermal survival times for sharp boundaries between εRu-Fe grains and surrounding γNi-Fe. Using the equation for radial diffusion from a sphere (*cf.* CRANK, 1975), we first calculated the maximum Ru gradient in γNi-Fe that could be hidden within the ~0.7 μm resolution of our analyses. This gradient corresponds to a Ru concentration of ~0.5% at a distance of 0.5 μm from a typical 1.0 μm diameter εRu-Fe grain and a value of $Dt = 2.5 \times 10^{-10}$ cm^2. Using $D^{Ru}_{Ni}(T)$ and the radial diffusion equation, we calculate that Ru(+Os + Re) gradients would be detectable in our analyses if 1 μm εRu-Fe spheres were suddenly juxtaposed against Ni and held isothermally for ≳4 seconds at 1673 K, ≳28 seconds at 1473 K or ≳2 weeks at 873 K; a result similar to that of ARRHENIUS and RAUB (1978).

Another approach to this problem is to calculate the cooling rate (r_0) required to form Ru(+Os + Re) gradients that would be detectable in our analyses, rather than calculating the isothermal diffusion times. In this calculation, we replace Dt with $\int_0^\infty D(t)dt \approx D(T_0)RT_0^2/Er_0$, where R is the gas constant, E is the activation energy, T_0 is the maximum temperature and r_0 is the cooling rate (KAISER and WASSERBURG, 1983). For the identical Ru(+Os + Re) gradient used in the isothermal case, the integral is equal to 2.5×10^{-10} cm^2, and we can calculate r_0 for any given T_0. During CAI melting, the value of T_0 reached was probably ~1700 K (STOLPER, 1982), for which we calculate $r_0 \gtrsim 10^5$ K hr^{-1}. For a T_0 of 1550 K (which is a reasonable lower limit), we calculate $r_0 \gtrsim 10^4$ K hr^{-1}. Although these cooling rates are possible for CAIs in a radiative environment (*cf.* MACPHERSON *et al.*, 1984), they are at odds with inferences based on experimental studies of the silicate portion of Type B CAIs, which imply much slower cooling at $r_0 \approx 0.5$–20 K hr^{-1} (STOLPER and PAQUE, 1986). Even the lowest T_0 (1550 K) and highest r_0 (200 K hr^{-1}) values considered plausible by STOLPER and PAQUE (1986) for Type B CAIs would produce nearly complete homogenization of 1 μm εRu-Fe grains in γNi-Fe. We therefore consider it unlikely that sharp boundaries between εRu-Fe and γNi-Fe could have survived the crystallization of CAIs.

Exsolution of εRu-Fe grains

Although sharp boundaries between εRu-Fe and γNi-Fe in CAIs would be difficult to preserve during CAI melting, they could instead have formed by exsolution of εRu-Fe from Ni-Fe-Ru alloys during cooling of CAIs below the solidus, as suggested by BLUM *et al.* (1988). Using the diffusion coefficient for lattice diffusion of Ru in Ni (D^{Ru}_{Ni}) from BLUM *et al.* (1989), we can estimate the time scale necessary for exsolution of εRu-Fe from a homogeneous Ni-Fe-Ru(+Os+Re) alloy at various temperatures. We have applied the treatment of diffusion-limited exsolution given by HAM (1958) for this purpose. We assume that at $t = 0$, εRu-Fe nuclei capable of growth were present in Ni-Fe-Ru alloy and that the nuclei were separated by a constant spacing of $2A$, where A is the radius of influence of each nucleus. We further assume growth of spherical grains by diffusion of Ru(+Os + Re), thus decreasing the average concentration ($\bar{c}$) of Ru(+Os + Re) in the surrounding γNi-Fe with time. The initial concentration of Ru(+Os + Re) in the Ni-Fe-Ru alloy is c_0, the Ru(+Os + Re) concentration in γNi-Fe in equilibrium with exsolved εRu-Fe is c', and the Ru(+Os + Re) concentration in exsolved

ϵRu-Fe is c_p. The exsolved fraction at any given time is defined as $Y(t) = (c_0 - \bar{c})/(c_0 - c')$. HAM (1958) showed that for $Y(t) > \frac{1}{2}$:

$$Y(t) \approx 1 - 2\exp\left(\frac{-t}{\epsilon}\right); \quad \text{where} \quad \epsilon = \frac{c_p^{1/3}A^2}{3D(c_0 - c')^{1/3}}.$$

We calculated the time necessary for diffusion-limited exsolution of ϵRu-Fe grains in CAI OAs, using the value for $D^{Ru}_{Ni}(T)$ and estimating A, $\bar{c}$, c_0, c' and c_p. We use the maximum value of $A = 4$ μm from the spacings between ϵRu-Fe grains in JIM-OA1, WILLY and F3. The other parameter values are estimated from our analyses of metallic phases and estimates of bulk alloy compositions for JIM-OA1, WILLY and F3, and are given in Table 3. The calculated exsolution times are given in Table 4. It was shown above that exsolution was initiated below 870 K and probably occurred at ~770 K. According to our calculation, exsolution would require $\gtrsim 10^3$ years at 773 K.

We also calculated the cooling rate (r_0) if the diffusion-limited exsolution process described above occurred during continuous cooling rather than isothermally. We have calculated r_0 for the CAI OAs JIM-OA1, WILLY and F3 using data given in Table 3. We use the equations given by HAM (1958), replacing Dt with the approximation for $\int_0^\infty D(t)dt$ from KAISER and WASSERBURG (1983) given above. Values for r_0 were calculated at temperatures for the onset of exsolution (T_0) equal to 873, 773 and 673 K (see Table 4). If exsolution began at 773 K, a cooling rate of $\lesssim 10^{-6}$ K hr^{-1} is required. The formation of ϵRu-Fe grains by exsolution (controlled by lattice diffusion) is thus kinetically feasible with thermal metamorphism at constant temperature (~770 K) for at least 10^3 years or during slow cooling at rates less than 10^{-6} K hr^{-1} through the 770 K temperature range. If the grain size of γNi-Fe was very small relative to the spacing of ϵRu-Fe nuclei, grain-boundary diffusion could have played an important role in the diffusion-limited exsolution process below about 900 K (SHEWMON, 1963). We consider this unlikely, but if it were the case, the thermal metamorphism time scale could have been shorter and/or cooling rates faster than the values we have calculated based on lattice diffusion rates.

ORIGIN OF OPAQUE ASSEMBLAGES

We showed above that phase assemblages in all Allende OAs, whether from CAIs, chondrules or matrix, appear to have equilibrated at temperatures of ~770 K or lower, and at similar, relatively high levels of f_{S_2} and f_{O_2} (Figs. 8–11). We also showed that it is unlikely that CAI OAs are preserved aggregates of phases formed before the crystallization of their host CAIs and chondrules. Based on these observations, we propose the following model for the origin of OAs. Following previous workers, we assume that proto-CAI, proto-chondrule and proto-matrix material formed as condensates (or evaporative residues) in the solar nebula. When the silicate portions of CAIs and chondrules melted or partially melted under highly reducing conditions, siderophile elements that had previously condensed as alloys and/or oxides partitioned into molten, proto-OA alloy droplets. As CAIs and chondrules cooled, the alloy droplets crystallized to homogeneous solids which were included in the major silicate minerals (+ spinel) as they crystallized. At still lower temperatures of ~770 K, the homogeneous, proto-OA alloys exsolved into immiscible metallic phases as Fe was removed from them by partial oxidation and sulfidation, thus completing the formation of CAI and chondrule OAs. Uncertainty concerning the origin of the silicate portion of the matrix material prevents us from proposing a detailed model for matrix OAs, but we note that the common assemblage of pentlandite surrounding γNi-Fe in matrix OAs is consistent with the reequilibration of γNi-Fe at conditions of temperature, f_{S_2} and f_{O_2} similar to those experienced by CAI and chondrule OAs.

Table 3. Ru(+Os+Re) concentrations in atom percent used in diffusion-limited exsolution calculation. See text for explanation.

	$\bar{c}$	c_0	c'	c_p	Y
JIM-OA1	1.30	4.4	0.3	59	0.76
WILLY	0.49	1.7	0.3	50	0.86
F3	0.65	3.3	0.3	53	0.88

Table 4. Isothermal diffusion times (t) and cooling rates (r_0) calculated based on diffusion-limited exsolution model. See text for explanation.

		t (yr)			r_0 (K hr^{-1})		
	Dt(cm^2)	T_0 = 873 K	T_0 = 773 K	T_0 = 673 K	T_0 = 873 K	T_0 = 773 K	T_0 = 673 K
JIM-OA1	2×10^{-8}	4	5×10^2	3×10^4	9×10^{-4}	5×10^{-6}	6×10^{-8}
WILLY	8×10^{-8}	10	20×10^2	10×10^4	3×10^{-4}	1×10^{-6}	2×10^{-8}
F3	4×10^{-8}	7	9×10^2	5×10^4	5×10^{-4}	3×10^{-6}	4×10^{-8}

Nebular condensation

Our model contrasts with the suggestions of many previous workers that the metallic phases in CAI OAs are the direct products of equilibrium condensation from a gas of solar composition (*e.g.* PALME and WLOTZKA, 1976; BLANDER *et al.*, 1980; ARMSTRONG *et al.*, 1985a). Neither the compositions of individual ϵRu-Fe grains and γNi-Fe nor the bulk alloy compositions of CAI OAs that we studied are close to calculated condensates. Alloys condensed between 1700 and 1500 K are predicted to have about 1 to 10% of each refractory siderophile element and relatively low Ni (0.1–3%) and Fe (0.3–20%) concentrations (PALME and WLOTZKA, 1976). The ratio of Ni/(Ni + Fe) could only reach a maximum of 0.20 in these very high-temperature condensates (PALME and WLOTZKA, 1976; KELLY and LARIMER, 1977; GROSSMAN *et al.*, 1979), far lower than the value of 0.67 in alloys in most CAI, chondrule and matrix OAs. Below about 1460 K, refractory siderophile concentrations are predicted to drop rapidly to the 10 ppm level, and Ni/(Ni + Fe) is predicted to rapidly approach the cosmic value of ~0.06 (GROSSMAN, 1972; PALME and WLOTZKA, 1976). To condense alloys with refractory siderophile contents close to those of CAI OA bulk alloy compositions, PALME and WLOTZKA (1976) argued that the temperature interval for the condensation of these grains would have to be in the very narrow range of 1462 to 1466 K, but even these condensates would be far too poor in Ni to match observed OA alloy compositions. BISCHOFF and PALME (1987) suggested that γNi-Fe in CAI OAs condensed along with magnetite directly from the nebula at an f_{O_2} far higher than a solar gas to account for the high values of Ni/

(Ni + Fe) observed; although alloys with high Ni/(Ni + Fe) could condense under these conditions, we deem it unlikely that magnetite (or Fe sulfide) could have survived CAI melting without being converted to metallic Fe under the very reducing solar gas conditions of CAI melting.

The model proposed here for OAs suggests that all of the Ni and Fe currently in alloys, oxides and sulfides in each OA was originally in a homogeneous, proto-OA alloy. According to this view, it is the Ni and Fe contents of the bulk OA (rather than the present bulk alloy composition) that give us an estimate of the proto-OA alloy compositions. Our model does not require that proto-OA alloy compositions were controlled by condensation processes, but it is interesting to consider whether this could be the case. The majority of CAI, chondrule and matrix OAs [Ni/(Ni + Fe) $\approx$ 0.25 to 0.50] could have originated as condensate alloys [Ni/(Ni + Fe) $\lesssim$ 0.20] that were oxidized and/or sulfidized, provided that some Fe was lost from the bulk OAs to neighboring spinel and silicates. Even EGG3-OA1 [Ni/(Ni + Fe) $\approx$ 0.90] could have formed in this way if a large enough amount of Fe was lost to the surroundings. We have found petrographic evidence for the loss of Fe from OAs in both CAIs and chondrules. As shown by ARMSTRONG *et al.* (1987), most spinels are enriched in Fe within $\sim$100 μm of CAI OAs with Fe concentration gradients increasing toward OAs, and as shown by HUA *et al.* (1988), olivine is sometimes enriched in Fe adjacent to OAs in chondrules.

LE0575-OA1 [Ni/(Ni + Fe) $\approx$ 0.05 to 0.06] and other OAs from meteorites of the C3V "reduced subgroup" cannot have formed from alloys whose compositions approximate a nebular condensate by the simple scenario of oxidation and/or sulfidation with subsequent loss of Fe. The bulk Ni/(Ni + Fe) ratio of LE0575-OA1 could match lower temperature condensates (<1400 K), but such condensates would contain <100 ppm total refractory siderophiles (PALME and WLOTZKA, 1976), whereas LE0575-OA1 has a total refractory siderophile content of about 10%. Possibly, the LE0575-OA1 bulk composition represents a mixture of alloys formed during two intervals of condensation; *i.e.* a mixture of a high-temperature condensate (high refractory siderophiles) and a lower-temperature condensate [low Ni/(Ni + Fe)].

Constraints on f_{O_2} during CAI and chondrule melting and crystallization

CAIs and chondrules are widely believed to have melted and recrystallized in the nebula subsequent to condensation. The composition of the cooling solar gas defines nearly a straight line on a plot of $\log f_{O_2}$ *versus* $1/T$ ("solar gas" curve, Fig. 11). Studies of Ti^{3+}/Ti^{4+} in fassaites in CAIs (STOLPER *et al.*, 1982; BECKETT and GROSSMAN, 1986) indicate that fassaites in most CAIs crystallized in a narrow range of log f_{O_2} within about one unit of the solar gas curve (see Fig. 11). Fassaites are believed to preserve a record of the f_{O_2} during CAI crystallization, whereas the compositions of other phases such as magnetite, hibonite and melilite have been reset by highly oxidized subsolidus conditions (BECKETT *et al.*, 1988).

JOHNSON (1986) studied chondrules from C2 and unequilibrated ordinary chondrites and suggested that the lowest Fe content of the cores of olivines and pyroxenes could be used to calculate limiting f_{O_2} values for chondrule crystallization. Following the arguments given by JOHNSON (1986), we calculate that the low Fe contents of the cores of some olivines and pyroxenes from Allende chondrules ($\lesssim$1% fayalite, $\lesssim$1% ferrosilite; RUBIN and WASSON, 1987) could indicate original crystallization at an f_{O_2} within $\sim$2 orders of magnitude of the solar gas curve, with subsequent sub-solidus addition of Fe to the rims under more oxidizing conditions.

Melting of the silicate portions of CAIs and chondrules at a solar gas f_{O_2} would result in the partitioning of siderophile elements, originally condensed as either alloys or oxides, into immiscible alloy liquids. The estimated maximum temperature experienced during CAI melting is 1700 to 1800 K; the only major phase expected not to have completely melted is spinel (STOLPER, 1982). At temperatures of 1700 to 1725 K, most Ni-Fe alloys would melt (KUBASCHEWSKI, 1983) and the presence of dissolved P (MASSALSKI, 1986) or other elements could cause them to melt at even lower temperatures. During cooling, Ni-Fe alloy droplets and spinel would be the first phases to crystallize. The common occurrence of CAI OAs in embayments in spinel (Fig. 2) suggests that some spinel crystallized after the formation of proto-OA alloys. Many Type B CAIs have coarse-grained melilite rims that have very few inclusions of spinel and OAs. If crystallization proceeded from the outside of CAIs inward, advancing melilite crystal faces might have pushed early crystallized spinel and proto-OAs toward the center of the inclusion where melilite, fassaite and anorthite subsequently crystallized around them, resulting in textures observed in many CAIs. Chondrules are believed to have crystallized from maximum temperatures of 1670 to 1870 K (HEWINS, 1983), indicating that olivine and pyroxene in chondrules probably crystallized before or simultaneously with chondrule proto-OA alloy liquids.

During the stage when CAIs and chondrules were partially molten, Fe and Ni, if present, would form the major constituents of molten alloys. All other elements that are siderophile at the very reducing ambient f_{O_2} would be expected to partition strongly into the alloy liquid. As expected, common siderophiles, such as Co and P, are abundant in OAs from both CAIs and chondrules. Refractory siderophiles such as Mo, W, Re, Ru, Os, Pt and Ir occur in much higher concentrations in CAI OAs than in OAs from chondrules or matrix, reflecting the large enrichment of refractory siderophiles in the parental material for CAIs compared to the parental material for chondrules and matrix. Although it is expected that each individual proto-OA alloy droplet was homogeneous, compositional differences between alloy droplets within a given CAI or chondrule, inherited from alloys present in the initial unmelted proto-CAI and proto-chondrule aggregates, were probably preserved.

The partitioning of V between proto-OA alloys and silicate melt may be particularly sensitive to f_{O_2} for values of f_{O_2} near those of a solar gas because the V-VO buffer curve crosses the solar gas curve at a temperature near the range of CAI and chondrule melting (Fig. 11). If OAs originated as molten alloy droplets in silicate liquid, then we can estimate the f_{O_2} required to explain the observed partitioning of V between OAs and enclosing silicates. Since we require an estimate of the V content of the proposed precursor OA alloy droplets, we restrict our attention to CAI OAs due to insufficient data

on V contents of chondrule or matrix OAs. Most V is currently present in CAI OAs as V_2O_3 in magnetite in concentrations ranging up to 12% V (ARMSTRONG *et al.*, 1987). Two CAI OAs have been analyzed by SEM in detail to determine total V concentrations (ARMSTRONG *et al.*, 1987), and one bulk CAI OA has been analyzed by neutron activation (GROSSMAN *et al.*, 1986). If these three OAs originated as alloys, the initial V content would have been 1.1, 2.6 and 5.5 wt%, respectively; we will use the average of 3.1 wt% in our calculations. The V content of the host CAI silicate minerals (and spinel) has not been determined, but the average bulk CAI V content is ~620 ppm (WÄNKE *et al.*, 1974). We can estimate the V content of the host silicates (and spinel) by difference using the estimate of ARMSTRONG *et al.* (1985a), which suggests that OAs originally comprised about 0.1 wt% of CAIs. In this case, the average silicate (and spinel) host concentration of V would be about 590 ppm (note that most of the V in CAIs is in the silicate + spinel fraction). Partitioning between alloy and silicate at conditions of CAI melting would be determined by the reactions $V + {}^1/_2O_2 \rightarrow VO$ and $2V + {}^3/_2O_2 \rightarrow V_2O_3$. Although our calculation is based on VO, the presence of dissolved V_2O_3 would not greatly affect the following discussion. The equilibrium constant (K) can be calculated for the V/VO reaction from thermodynamic data (CHASE *et al.*, 1985), yielding:

$$K(T) = \frac{\gamma_{VO}^{sil} X_{VO}^{CAI}}{\gamma_{V}^{alloy} X_{V}^{CAI} f_{O_2}^{1/2}} = \exp(50995\ T^{-1} - 9.72)$$

where γ_i^j is the activity coefficient (of i in j), X_i^j is the mole fraction (of i in j) and T is the temperature in K. Lacking data on activity coefficients, we assume that their ratio is unity. We further assume that the fraction of the total V in CAIs that is now associated with OAs (X_V^{CAI}) was once in a proto-OA alloy in the metallic state and that the remaining V in CAIs (X_{VO}^{CAI}) was in the coexisting silicate melt. For any measured partitioning behavior, the equation can be solved for f_{O_2}, yielding an equilibration line on a plot of $\log f_{O_2}$ *versus* $1/T$. The line defined by the estimated average value of $X_{VO}^{CAI}/X_V^{CAI} = 0.05$ is plotted in Fig. 11 bounded by dashed curves calculated for X_{VO}^{CAI}/X_V^{CAI} greater and smaller than the average value by a factor of 3, which is a reasonable estimate of the accuracy of the value chosen for the ratio of V in OAs *versus* the silicate + spinel fraction of CAIs. The line for the average X_{VO}^{CAI}/X_V^{CAI} value is displaced 3 $\log f_{O_2}$ units above the pure V-VO buffer, which is shown for reference. In the temperature range of 1550 to 1700 K, the inferred $\log f_{O_2}$ from V partitioning lies within one unit of the solar gas curve. This result is consistent with a proto-OA alloy in equilibrium with a silicate melt and a gas of solar composition at the temperature of CAI partial melting and with f_{O_2} estimates of BECKETT and GROSSMAN (1986) from Ti^{3+}/Ti^{4+} in CAI fassaite (Fig. 11). If CAIs cooled along the solar gas curve (Fig. 11), V would oxidize progressively and diffuse out of the alloy into surrounding silicate (or spinel). This process may explain the observations of ARMSTRONG *et al.* (1985a, 1987) that many CAI OAs have rims (≲20 μm) of V-rich fassaite (Fig. 2) and that V is often highly enriched in spinels in the vicinity of OAs.

Opaque assemblage equilibration

According to our model, the final equilibration of OAs in CAIs, chondrules and matrix occurred during metamorphism or slow cooling under sulfidizing/oxidizing conditions. In an earlier section, we quantified the temperature, f_{S_2} and f_{O_2} for the formation of OA phase assemblages by comparison with experimentally determined phase equilibria. In general, equilibration conditions for OAs from CAIs, chondrules and matrix are similar even though relative modal abundances of alloy, sulfide and oxide sometimes vary widely in adjacent OAs within single CAIs or chondrules. One possible explanation for this is that sulfidizing and oxidizing gases gained access to proto-OA alloys selectively *via* cracks. In the remainder of this section, we speculate upon the origin of Ca-phosphate (present in most CAI, chondrule and matrix OAs) and scheelite-powellite [$Ca(W,Mo)O_4$; present in some CAI OAs] within the context of our model, and then discuss the possible environment for OA equilibration.

At the f_{O_2} and f_{S_2} of a solar gas, P, W and Mo are highly siderophile and would partition into a Ni-Fe alloy liquid if it was present. These elements are soluble in solid γNi-Fe at high temperatures, but at lower temperatures (≲1000 K) and high enough concentrations, they would probably exsolve into phases such as $(Fe,Ni)_3P$, Fe_2W and Fe_2Mo (*cf.* MASSALSKI, 1986). This type of concentration by exsolution would facilitate reaction of P, W and Mo with O_2 and a volatile species of Ca (HASHIMOTO and WOOD, 1986) to form Ca-phosphate and scheelite-powellite under oxidizing conditions at low temperature. This view contrasts with that of BISCHOFF and PALME (1987), who suggested that scheelite-powellite condensed under extremely oxidizing conditions ($f_{O_2} > 4$ log units above a solar gas) and from a gas with high nonsolar partial pressures of Ca and/or W and Mo in the solar nebula at temperatures of >1672 K before the formation of OAs or CAIs.

C3V meteorites are generally believed to have been brought together as accretionary breccias that were buried within planetesimal bodies (*cf.* KRACHER *et al.*, 1985). Since OAs in CAIs, chondrules and matrix from C3V meteorites all equilibrated at similar temperature, f_{S_2} and f_{O_2}, one possibility is that the equilibration occurred after these three major components had accreted into a common parent body. The slow cooling rates of $\lesssim 10^{-6}$ K hr^{-1} required to account for observed alloy exsolution in CAI OAs are consistent with such an environment, as are the sulfidizing and oxidizing conditions that we infer (HOUSLEY and CIRLIN, 1983). The *in situ* decay of ^{26}Al provides an ample heat source if OA equilibration occurred during an early metamorphic event on a parent body. The interiors of bodies only a few km in radius could reach temperatures in excess of 770 K for $(^{26}Al/^{27}Al)_0 \approx 5 \cdot 10^{-5}$, or, alternatively, very shallow burial in larger bodies could provide an adequate thermal environment for equilibration (*cf.* MASHAMICHI *et al.*, 1981).

Distribution of refractory siderophiles in CAIs

The refractory siderophile elements Ru, Os, Re, Ir and Pt are, in general, uniformly enriched to ~20× chondritic in bulk coarse-grained CAIs, whereas W and Mo are also enriched but sometimes not to this extent (GROSSMAN, 1973;

FEGLEY and PALME, 1985). The major host of the refractory siderophile elements in CAIs are OAs and in some cases refractory metal nuggets (RMNs; WARK, 1986). Refractory metal nuggets are small (0.5–5 μm) alloy grains which are distinguishable from the larger multiphase OAs. They usually occur in CAIs that do not contain OAs (WARK, 1986), but they are also occasionally found in OA-bearing CAIs (EL GORESY *et al.*, 1978; BISCHOFF and PALME, 1987). The composition of some RMNs could plausibly have been produced by direct nebular condensation (PALME and WLOTZKA, 1976; WARK, 1986). The preservation of condensate RMN compositions in some CAIs could reflect (1) the fact that some CAIs were never melted; (2) that some CAI melting events were of sufficiently short duration that RMNs did not have time to dissolve in proto-OA alloy droplets; or (3) that the host CAIs contained so little Ni + Fe that molten alloy droplets did not form during CAI melting. RMNs that are relicts of condensation might be expected to display a range of concentration of refractory siderophile elements due to the different volatilities of these elements; such a correlation appears to have been observed in the CAI studied by WARK (1986). Alternatively, RMNs could be remnants of OAs from which sulfide and oxide phases were removed by secondary processes.

The relative proportions of refractory siderophile elements in bulk coarse-grained CAIs suggest a role for nebular condensation (PALME and WLOTZKA, 1976; FEGLEY and PALME, 1985), yet the relative proportions of these elements in individual OAs and RMNs from single CAIs are sometimes highly variable (BISCHOFF and PALME, 1987). We prefer to explain these variations by processes that occurred during melting and equilibration of the CAIs rather than by a process that sampled diverse grains formed under variable conditions in the nebula, and averaged them to approximately chondritic ratios for each CAI.

CONCLUSIONS

We have shown by comparison of OA phase compositions with experimentally determined phase equilibria and partitioning behavior that alloy, sulfide and oxide assemblages in OAs from CAIs, chondrules and matrix could have been produced by the exposure of homogeneous alloys to high values of f_{S_2} and f_{O_2} at low temperature. We infer that CAI and chondrule OAs originated at low f_{O_2} in CAI and chondrule silicate liquids as homogeneous Ni-Fe alloy droplets that contained other siderophile elements (*e.g.* P, Co, V, W, Mo, Re, Ru, Os, Pt and Ir) in the reduced state. The complex mineralogy that now characterizes OAs formed from these proto-OA alloy droplets by sulfidation, oxidation, and exsolution. This occurred during slow cooling ($\lesssim 10^{-6}$ K hr^{-1}) or metamorphism for $\gtrsim 10^3$ yr at ~770 K and at an f_{S_2} one log unit above, and an f_{O_2} six log units above, a solar gas composition. The two-stage evolution proposed here, which includes homogeneous alloy formation at high temperature followed by reequilibration at lower temperature, provides a general explanation of the approximately solar refractory element ratios in bulk CAIs, chondrules and matrix, as well as the complex compositions of individual phases now observed in OAs.

We consider alternative scenarios for the origin of CAI OAs, which suggest that they formed in the solar nebula before CAI melting and were subsequently captured in the CAIs and rapidly cooled (ARMSTRONG *et al.*, 1985a, 1987; BISCHOFF and PALME, 1987), to be unlikely because the low temperature mineral assemblages could not have survived melting and subsequent cooling of the bulk CAI for any plausible cooling rates. The scenario for the origin of OAs in chondrules that suggests they formed by crystallization of metallic-oxide-sulfide liquid droplets (HAGGERTY and MCMAHON, 1979; MCMAHON and HAGGERTY, 1980) is not likely because sulfur would probably have been vaporized and Fe oxide reduced to metallic Fe under the relatively reducing conditions of chondrule melting in the nebula. On the other hand, the scenario of origin by oxidation of preexisting alloys (HAGGERTY and MCMAHON, 1979) is consistent with our findings. Similarly, a scenario proposed for the origin of OAs in matrix involving alteration of alloys (HOUSLEY and CIRLIN, 1983; RUBIN and GROSSMAN, 1985) is supported by our findings.

The conditions that we estimate for the temperature, f_{S_2} and f_{O_2} of equilibration for CAI, chondrule and matrix OAs are very similar and suggest that these three components of C3V meteorites share a common, late low-temperature history, perhaps on a planetesimal body. Studies of OAs may therefore provide quantitative constraints on the post-accretionary equilibration conditions of C3V meteorites.

Acknowledgements—We thank H. Palme and J. T. Armstrong for helpful discussions, S. E. Haggerty, K. C. Misra and an anonymous referee for reviews, and H. Palme, K. Keil and the U.S. Museum of Natural History for loaning us the meteorite specimens used in this study. Funding was provided by NASA Grants NAG 9-43 and NAG 9-105 and NSF Grant EAR 86-18526. Division Contribution No. 4664 (631).

Editorial handling: H. Y. McSween, Jr.

REFERENCES

ARMSTRONG J. T., EL GORESY A. and WASSERBURG G. J. (1985a) Willy: A prize noble Ur-Fremdling—Its history and implications for the formation of Fremdlinge and CAI. *Geochim. Cosmochim. Acta* **49**, 1001–1022.

ARMSTRONG J. T., HUTCHEON I. D. and WASSERBURG G. J. (1985b) Ni-Pt-Ge-rich Fremdlinge: Indicators of a turbulent early solar nebula (abstr.). *Meteoritics* **20**, 603–604.

ARMSTRONG J. T., HUTCHEON I. D. and WASSERBURG G. J. (1987) Zelda and company: Petrogenesis of sulfide-rich Fremdlinge and constraints on solar nebular processes. *Geochim. Cosmochim. Acta* **51**, 3155–3173.

ARRHENIUS G. and RAUB C. J. (1978) Thermal history of primordial metal grains. *J. Less-common Metals* **62**, 417–430.

BARTON P. B. and SKINNER B. J. (1979) Sulfide mineral stabilities. In *Geochemistry of Hydrothermal Ore Deposits* (ed. H. L. BARNES), pp. 278–403. J. Wiley & Sons.

BECKETT J. R. and GROSSMAN L. (1986) Oxygen fugacities in the solar nebula during crystallization of fassaite in Allende inclusions (abstr.). *Lunar Planet. Sci. Conf. XVII*, 36–37.

BECKETT J. R., LIVE D., TSAY F., GROSSMAN L. and STOLPER E. M. (1988) Ti^{3+} in meteoritic and synthetic hibonite. *Geochim. Cosmochim. Acta* **52**, 1479–1496.

BISCHOFF A. and PALME H. (1987) Composition and mineralogy of refractory-metal-rich assemblages from a Ca,Al-rich inclusion in the Allende meteorite. *Geochim. Cosmochim. Acta* **51**, 2733–2748.

BLANDER M., FUCHS L. H., HOROWITZ C. and LAND R. (1980) Primordial refractory metal particles in the Allende meteorite. *Geochim. Cosmochim. Acta* **44**, 217–223.

BLUM J. D., WASSERBURG G. J., HUTCHEON I. D., BECKETT J. R. and STOLPER E. M. (1988) "Domestic" origin of opaque assemblages in refractory inclusions in meteorites. *Nature* **331**, 405–409.

BLUM J. D., WASSERBURG G. J., HUTCHEON I. D., BECKETT J. R. and STOLPER E. M. (1989) Diffusion, phase equilibria and partitioning experiments in the Ni-Fe-Ru system. *Geochim. Cosmochim. Acta* **53**, 485–491 (this issue).

BRANDSTÄTTER F. and KURAT G. (1983) All-Jim: A large Ca-Al-rich chondrule from Allende (C3) (abstr.). *Meteoritics* **18**, 272.

BRETT R. (1967) Metallic spherules in impactite and tektite glasses. *Amer. Mineral.* **52**, 721–733.

CHASE M. W. JR., DAVIES C. A., DOWNEY J. R. JR., FRURIP D. J., MCDONALD R. A. and SYVERUD A. N. (1985) JANAF thermochemical tables, 3rd edn. *J. Phys. Chem. Ref. Data* **14**, Supp. 1.

CRANK J. (1975) *The Mathematics of Diffusion*. Oxford Univ. Press. 414p.

DEAN D. C. and GOLDSTEIN J. I. (1986) Determination of interdiffusion coefficients in the Fe-Ni and Fe-Ni-P systems below 900°C. *Met. Trans.* **17A**, 1131–1138.

EL GORESY A., NAGEL K. and RAMDOHR P. (1978) Fremdlinge and their noble relatives. *Proc. Lunar Planet. Sci. Conf. 9th*, 1279–1303.

FEGLEY B. JR. and PALME H. (1985) Evidence for oxidizing conditions in the solar nebula from Mo and W depletions in refractory inclusions in carbonaceous chondrites. *Earth Planet. Sci. Lett.* **72**, 311–326.

FUCHS L. H. and BLANDER M. (1977) Molybdenite in calcium-aluminum-rich inclusions in the Allende meteorite. *Geochim. Cosmochim. Acta* **41**, 1170–1175.

GROSSMAN L. (1972) Condensation in the primitive solar nebula. *Geochim. Cosmochim. Acta* **36**, 597–619.

GROSSMAN L. (1973) Refractory trace elements in Ca-Al-rich inclusions in the Allende meteorite. *Geochim. Cosmochim. Acta* **37**, 1119–1140.

GROSSMAN L. (1980) Refractory inclusions in the Allende meteorite. *Ann. Rev. Earth Planet. Sci.* **8**, 559–608.

GROSSMAN L., OLSEN E. and LATTIMER J. M. (1979) Silicon in carbonaceous chondrite metal: Relic of high temperature condensation. *Science* **206**, 449–451.

GROSSMAN L., DAVIS A. M., EKAMBARAM V., ARMSTRONG J. T., HUTCHEON I. D. and WASSERBURG G. J. (1986) Bulk chemical composition of a Fremdling from an Allende Type B inclusion (abstr.). *Lunar Planet. Sci. XVII*, 295–296.

HAGGERTY S. E. and MCMAHON B. M. (1979) Magnetite-sulfide-metal complexes in the Allende meteorite. *Proc. Lunar Planet. Sci. 10th*, 851–870.

HAM F. S. (1958) Theory of diffusion-limited precipitation. *J. Phys. Chem. Solids* **6**, 335–351.

HASHIMOTO A. and WOOD J. A. (1986) Enhanced volatility of CaO in H_2O-rich gas environments as a factor in the alteration of Ca,Al-rich inclusions (abstr.). *Meteoritics* **21**, 391–392.

HEWINS R. H. (1983) Dynamic crystallization experiments as constraints on chondrule genesis. In *Chondrules and Their Origins* (ed. E. A. KING), pp. 122–133. Lunar and Planetary Inst.

HOUSLEY R. M. and CIRLIN E. H. (1983) On the alteration of Allende chondrules and the formation of matrix. In *Chondrules and Their Origins* (ed. E. A. KING), pp. 145–161. Lunar and Planetary Inst.

HSIEH K., CHANG Y. A. and ZHANG T. (1982) The Fe-Ni-S system above 700°C. *Bull. Alloy Phase Equil.* **3**, 165–172.

HUA X., ADAM J., PALME H. and EL GORESY A. (1988) Fayalite-rich rims, veins, and halos around and in forsteritic olivines in CAIs and chondrules in carbonaceous chondrites: Types, compositional profiles and constraints on their formation. *Geochim. Cosmochim. Acta* **51**, 1389–1408.

JOHNSON M. C. (1986) The solar nebula redox state as recorded by the most reduced chondrules of five primitive chondrites. *Geochim. Cosmochim. Acta* **50**, 1497–1502.

KAISER T. and WASSERBURG G. J. (1983) The isotopic composition and concentration of Ag in iron meteorites and the origin of exotic silver. *Geochim. Cosmochim. Acta* **47**, 43–58.

KELLY W. R. and LARIMER J. W. (1977) Chemical fractionations in meteorites—VIII. Iron meteorites and the cosmochemical history of the metal phase. *Geochim. Cosmochim. Acta* **41**, 93–111.

KRACHER A., KEIL K., KALLEMEYN G. W., WASSON J. T., CLAYTON R. N. and HUSS G. I. (1985). The Leoville (CV3) accretionary breccia. *J. Geophys. Res.* **90**, D123–D135.

KUBASCHEWSKI O. (1983) *Iron-Binary Phase Diagrams*. Springer-Verlag, Berlin.

MACPHERSON G. J., PAQUE J. M., STOLPER E. M. and GROSSMAN L. (1984) The origin and significance of reverse zoning in melilite from Allende Type B inclusions. *J. Geol.* **92**, 289–305.

MASHAMICHI M., FUJII N. and TAKEDA H. (1981) Ordinary chondrite parent body: An internal heating model. *Proc. Lunar Sci. Conf. 12th*, 1145–1152.

MASSALSKI T. B. (1986) *Binary Alloy Phase Diagrams*. Amer. Soc. Metals. 2208p.

MCMAHON B. M. and HAGGERTY S. E. (1980) Experimental studies bearing on the magnetite-alloy-sulfide association in the Allende meteorite: Constraints on the conditions of chondrule formation. *Proc. Lunar Planet. Sci. Conf. 11th*, 1003–1025.

MCSWEEN H. Y. JR. (1977) Petrographic variations among carbonaceous chondrites of the Vigarano type. *Geochim. Cosmochim. Acta* **41**, 1777–1790.

MEEKER G. P., WASSERBURG G. J. and ARMSTRONG J. T. (1983) Replacement textures in CAI and implications regarding planetary metamorphism. *Geochim. Cosmochim. Acta* **47**, 707–721.

MISRA K. C. and FLEET M. E. (1973) The chemical compositions of synthetic and natural pentlandite assemblages. *Econ. Geol.* **68**, 518–539.

OWEN E. A. and LIU Y. H. (1949) Further X-ray study of the equilibrium diagram of the iron-nickel system. *Iron and Steel Inst. J.* **163**, 132–137.

PALME H. and WLOTZKA F. (1976) A metal particle from a Ca,Al-rich inclusion from the meteorite Allende, and condensation of refractory siderophile elements. *Earth Planet. Sci. Lett.* **33**, 45–60.

PECK J. A. (1983) An SEM petrographic study of C3(V) meteorite matrix (abstr.). *Lunar Planet. Sci. Conf. XIV*, 598–599.

RAMBALDI E. R. and RAJAN R. S. (1982) Evidence for primitive phosphates in highly unequilibrated chondrites (abstr.). *Meteoritics* **17**, 271–272.

RUBIN A. E. and GROSSMAN J. N. (1985) Phosphate-sulfide assemblages and Al/Ca ratios in type-3 chondrites. *Meteoritics* **20**, 479–489.

RUBIN A. E. and WASSON J. T. (1987) Chondrules, matrix and coarse-grained chondrule rims in the Allende meteorite: Origin, interrelationships and possible precursor components. *Geochim. Cosmochim. Acta* **51**, 1923–1937.

SHEWMON P. G. (1963) *Diffusion in Solids*. McGraw-Hill. 203p.

STOLPER E. M. (1982) Crystallization sequences of Ca,Al-rich inclusions from Allende: An experimental study. *Geochim. Cosmochim. Acta* **46**, 2159–2180.

STOLPER E. M. and PAQUE J. M. (1986) Crystallization sequences of Ca-Al-rich inclusions from Allende: The effects of cooling rate and maximum temperature. *Geochim. Cosmochim. Acta* **50**, 1785–1806.

STOLPER E. M., PAQUE J. M. and ROSSMAN G. R. (1982) The influence of oxygen fugacity and cooling rate on the crystallization of Ca-Al-rich inclusions from Allende (abstr.). *Lunar Planet. Sci. Conf. XIII*, 772–773.

SVENDSEN S. R. (1979) Free energy, enthalpy and decomposition pressures of RuS_2. *Acta Chem. Scandinavica* **A33**, 601–607.

WÄNKE H., BADDENHAUSEN H., PALME H. and SPETTEL B. (1974) On the chemistry of the Allende inclusions and their origin as high temperature condensates. *Earth Planet. Sci. Lett.* **23**, 1–7.

WARK D. A. (1986) Evidence for successive episodes of condensation at high temperature in a part of the solar nebula. *Earth Planet. Sci. Lett.* **77**, 129–148.

APPENDIX IV. PRELIMINARY EXPERIMENTAL INVESTIGATION OF THE ORIGIN OF IR-RICH ALLOYS IN CHROMITE

INTRODUCTION

Chromite-rich rocks worldwide share the common feature of high concentrations of three of the PGE (Ir, Os and Ru) whether they occur in ophiolitic sequences or in layered intrusions. While it has been well documented that Ir, Os and Ru are strongly concentrated by the mineral chromite in most ultramafic occurrences (*e.g.*, Crocket, 1981), the reason for this association has not been well established. Interest in the origin of Ir, Os and Ru in chromite has increased as chromitites have become PGE mineral exploration targets (*e.g.*, Constantinides *et al.*, 1980; Page *et al.*, 1986; Naldrett and von Gruenewaldt, 1989).

In several early studies it was proposed that Ir, Os and Ru could be accommodated in solid solution in the chromite lattice at magmatic temperatures (*e.g.*, Gijbels *et al.*, 1974; Morgan *et al.*, 1976; Naldrett and Cabri, 1976). More recently petrographic studies have identified discrete 1 to 20 μm diameter inclusions of Ir-Os-Ru alloys and sulfides in chromite from nearly every major ophiolite and layered intrusion (*e.g.*, Talkington *et al.*, 1984; Auge, 1988). Alloy compositions range from $\sim$80% Ir to $\sim$80% Os with Ru contents up to $\sim$50% (Legendre and Auge, 1986; Talkington and Lipin, 1986) (all concentrations given in this Appendix are in weight fractions). These compositions correspond to the minerals osmiridium, iridosmine and rutheniridosmine according to the nomenclature of Harris and Cabri, (1973). Sulfide compositions span the solid solution between laurite and erlichmanite $(Ru,Os)S_2$ with up to $\sim$20% Ir (Legendre and Auge, 1986; Talkington and Lipin, 1986).

If the high Os, Ir and Ru contents of chromites were established by partitioning of PGE between chromite and silicate liquid, then the Os-Ir-Ru alloy and sulfide inclusions must have

formed by exsolution from originally homogeneous chromite crystals. However, several petrographic features of these inclusions have been used to argue against exsolution from chromite including: 1) euhedral and anhedral habits, 2) non-crystallographic orientation, and 3) compositional diversity. Based on these types of features, virtually every petrographic investigator has suggested that Ir-Os-Ru alloys and sulfides precipitate directly from magmatic liquids creating nucleation sites for chromite crystals, which crystallize around the small particles and mechanically remove them to chromitite layers (*e.g.*, Talkington *et al.*, 1984, 1986; Auge, 1988). Although Ir-Os-Ru-rich inclusions are observed as both alloys and sulfides, the discussion in this Appendix will concentrate on the relationship between alloys and chromite because most ophiolites and layered intrusions have cooled slowly, allowing the subsolidus reequilibration of alloys to sulfides or vice versa, depending on the ambient fS_2 (Stockman and Hlava, 1984; Legendre and Johan, 1981).

The origin of Ir-Os-Ru-rich inclusions in chromite is important to the understanding of PGE fractionation during mantle partial melting and crustal magmatic differentiation. Experimental data reported herein and in the literature will be used to discuss the plausibility of the two competing hypotheses for the origin of the inclusions, *i.e.*, 1) solid solution of Ir-Os-Ru in chromite followed by exsolution of alloys or 2) crystallization of Ir-Os-Ru alloys from silicate liquid followed by chromite nucleation and growth. It will be argued that the available data suggest that the first alternative is more plausible than the second. However, interpretation of the experiments reported here are somewhat ambiguous and a conclusive test of these hypotheses must await further experimentation.

EXPERIMENTAL METHODS

PGE-FeS liquid

Synthetic pyrrhotite ($Fe_{1-X}S$) was prepared by weighing pieces of pure Fe rod and S powder and sealing them in an evacuated silica glass tube. The tube was heated to 600°C for 24 hours to react the S and Fe. The FeS was then melted at 1250°C for 5 minutes and annealed at 1000°C for 24 hours to homogenize the sample. The sample tube was quenched in water and the sample was ground in an agate mortar under ethyl alcohol. A 50:50 mixture of $Fe_{1-X}S$ with Ir wire and a 50:50 mixture of $Fe_{1-X}S$ with Pt wire were sealed in evacuated silica tubes. The samples were melted in a vertical quench furnace at 1300°C for 1 hour and quenched into liquid nitrogen. They were then cut with a diamond saw, mounted in epoxy, polished with diamond paste, and carbon coated for electron beam analysis.

PGE-chromite

Synthetic chromite ($FeCr_2O_4$) was prepared by weighing and grinding pure FeO and Cr_2O_3 powder in an agate mortar under ethyl alcohol. The powdered mixture was pressed into a 10 mm diameter pellet using polyvinyl alcohol as a binding agent and hung by a 100 μm diameter Pt wire at 1500°C in a vertical quench gas-mixing furnace. The fO_2 was maintained midway between the iron-wüstite and wüstite-magnetite buffers using a flowing gas mixture of CO and CO_2. The pellet was quenched in distilled water and dried in an oven at 100°C. The grinding and annealing process were then repeated to increase homogeneity. Natural chromite $(Fe,Mg)(Cr,Al,Fe)_2O_4$ from the G-zone chromitite of the Stillwater Complex, Montana (for compositional data see Talkington *et al.*, 1986), was prepared by crushing the chromitite, handpicking chromite grains with minimum adhering silicate, and then grinding the chromite in an agate mortar under ethyl alcohol.

Pure Ir and Pt powders were weighed and added to splits of the synthetic and natural

chromite powders at the 1% level. The grain size of both the Ir and Pt was 0.3 to 2 μm. The samples were ground in an agate mortar under ethyl alcohol for 1 hour to evenly disperse the PGE and they were then split, diluted with pure chromite and reground to produce samples that contained 100, 500 and 1000 ppm of both Ir and Pt. These will be referred to as the "100 ppm," "500 ppm," and "1000 ppm" samples. Doped and undoped powders were pressed into pellets with a 3 mm diameter and 1 mm thickness. The pellets were hung with 25 μm diameter Pt wire in a vertical quench furnace at an fO_2 midway between the iron-wüstite and wüstite-magnetite buffers and annealed for 2 weeks at 1450°C. The fO_2 was chosen because it corresponds to the intrinsic fO_2 measured for chromitite samples from the Stillwater and Bushveld Complexes by Elliot *et al.* (1982). The pellets and Pt hanging wires were quenched, dried, cut into sections with a diamond saw, mounted in epoxy, polished with diamond paste and carbon coated for electron beam analysis.

Electron beam analysis

Quantitative analyses were made with an energy dispersive detector on a Camscan electron microscope (SEM) and wavelength dispersive detectors on a JEOL electron microprobe (EMP). Pure metals were used for standards, except for $Fe_{1-x}S$ which was used as the standard for S. All analyses were made at an accelerating voltage of 20 KeV with counting times of 100 sec. A beam current of 0.1 nAmp was used for energy dispersive analyses and a beam current of 500 nAmp was used for wavelength dispersive analyses. X-ray lines used for analyses were L_α for Pt and Ir, and K_α for Fe, Cr and S. The ZAF correction procedure was used for quantification of X-ray intensities.

EXPERIMENTAL RESULTS

PGE-FeS

SEM analyses of the PGE-FeS experiments indicate that both Ir and Pt are soluble in saturated FeS melt at the percent level but that in each case an interstitial metallic phase exsolves at grain boundaries upon quenching. In the Ir-FeS experiment, analyses of rastered areas (which included both FeS and the interstitial metallic grains that exsolved upon quenching) indicate that 3.9% Ir dissolved in the FeS liquid. The bulk of the Ir remained in the adjacent Ir wire. The quenched FeS retained 3.6% Ir and the intergranular metal grains, which range in size from 0.1 to 0.5 μm, are 88% Ir and 12% Fe.

In the Pt-FeS experiment, analyses of rastered areas (which included both FeS and the interstitial metallic grains that exsolved upon quenching) indicate that 14.9% Pt dissolved in the FeS liquid. As in the case of Ir, the bulk of the Pt remained in the attached Pt wire. The quenched FeS in this experiment retained only 0.3% Pt and the intergranular Pt metal grains were much larger, ranging in size from 1 to 5 μm. The composition of the exsolved metallic phase was 87% Pt and 13% Fe.

PGE-Chromite

The PGE-chromite experiments were designed to test whether the solubility of Ir in chromite was above or below the minimum detection limit for EMP analysis. Thus, the first problem was to determine the minimum detection limit for Ir and Pt in a chromite matrix. Synthetic and natural chromite samples that were not annealed were analyzed for Ir and Pt in 15 individual spots. The mean count rates correspond to concentrations of 105 $\pm$53 ppm Ir and 66 $\pm$51 ppm Pt (all uncertainties are given as $\pm 1\sigma$). These values are considered background intensities for a chromite with no Ir or Pt and were subtracted from all chromite analyses. The typical uncertainty of the individual analyses due to counting statistics is $\pm$45

ppm. Analyses of a secondary standard which contains 325 ppm Ir and 325 ppm Pt in a Ni matrix were used to calculate the detection limit from Poisson statistics at the 95% confidence level following the approximation of Ziebold (1967). The detection limit calculated for Ir is 81 ppm and for Pt is 110 ppm.

The three synthetic and three natural chromites that were annealed with Pt and Ir powder dispersed within them were next analyzed by EMP. The analyzed spots were verified not to contain metal grains using the backscattered electron detector on the EMP. The mean concentrations for 21 analyses from the six samples (after background and ZAF corrections) are 18 $\pm$42 ppm Ir and 17 $\pm$47 ppm Pt. These mean values are well below the minimum detection limits. Each of the six samples were also analyzed in two to four separate areas (in the interiors of the pellets) in a 400x400 μm raster pattern which included both chromite and the dispersed Ir and Pt grains. The mean of seven analyses of the two "100 ppm" samples are 114 $\pm$38 ppm Ir and 132 $\pm$77 ppm Pt [(Ir/(Pt+Ir)= 0.46]; the mean of five analyses of the two "500 ppm" samples are 236 $\pm$45 ppm Ir and 297 $\pm$125 ppm Pt [(Ir/(Pt+Ir)= 0.44]; and the mean of five analyses of the two "1000 ppm" samples are 642 $\pm$106 ppm Ir and 764 $\pm$68 ppm Pt [(Ir/(Pt+Ir)= 0.46].

The concentrations of Ir and Pt in the "500 and 1000 ppm" samples are lower than expected indicating that either the homogenization and dilution procedure was not quantitative or that Ir and Pt were lost from the samples during annealing either by diffusion into the Pt hanging wires or by volatilization. The Pt hanging wires were analyzed to see if they had gained Ir during annealing. Unfortunately, the sample pellets fell out of the Pt wire loops during quenching making it impossible to match the wires with individual samples. Two pieces of Pt wire that had not been annealed and eleven random pieces of Pt hanging wire from the experimental runs were analyzed. Both unannealed Pt wires analyzed contain

0.786% Fe and 0.070% Ir. The mean concentrations of the Pt hanging wire are 15.3 ±2.2% Fe and 0.248 ±0.071% Ir. The mass of Pt hanging wire used for each sample was ~1 mg and the mass of each sample was ~25 mg. Thus, the mean Ir added to the Pt hanging wire corresponds to an average of 70 ppm Ir from each of the 10 samples annealed. If most of the Ir was contributed by the four "500 and 1000 ppm" samples, as much as 175 ppm Ir could have been lost from each of these samples. This could at least partially explain the 200 to 350 ppm apparent loss of Ir from the "500 and 1000 ppm" samples. However, there were nearly equal losses of Ir *and Pt* which suggests that Pt was also lost from the sample to the hanging wire or both metals were volatilized during annealing.

The SEM was used to determine the Ir/(Ir+Pt) content of the individual metal grains in the samples after annealing. Each of the Ir and Pt alloy grains gained ~10% Fe from the surrounding chromite. Many of the grains were smaller than the ~1 μm x-ray interaction volume and thus also contain Fe and Cr in the analyses from the surrounding chromite. However, this does not effect the determination of the Ir/(Ir+Pt) ratio in the alloys. The natural chromite samples recrystallized during annealing (perhaps due to the presence of ~2% interstitial silicate glass that may have acted as a flux) and formed dense pellets which formed smooth surfaces when polished. The synthetic chromite samples remained porous after annealing and these samples (plus all of the unannealed samples) formed pitted surfaces when polished with only 10-20 μm diameter islands of well polished material.

The Ir and Pt grains were evenly dispersed throughout the chromite in the unannealed starting materials and no metal grains were observed adhering to one another. The sizes of 30 Ir grains that were measured with the SEM in unannealed samples ranged from 0.3 to 2.0 μm and averaged 0.8 μm, and the sizes of 25 Pt grains ranged from 0.3 to 1.5 μm and averaged 0.7 μm. The average spacings of Ir and Pt grains were calculated assuming a

0.75 μm grain size and are 130, 42 and 35 μm in the "100 ppm," "500 ppm" and "1000 ppm" samples respectively. Ir and Pt form a complete solid solution at 1450°C and thus the expected equilibrium condition would be a single metallic phase with a Ir/(Ir+Pt) ratio of ~0.5.

The Ir/(Ir+Pt) ratio of the metal grains after annealing yields information about the mobility of Ir and/or Pt in chromite at elevated temperatures. The Ir/(Ir+Pt) ratios for each grain analysis determined by SEM and the raster analyses determined by EMP are plotted of Fig. 1. The mean Ir/(Ir+Pt) ratios (X_n, n=number of analyses) of metal grains in the "100, 500 and 1000 ppm" Stillwater chromite samples are X_{30}=0.38 ±0.23, X_{17}=0.42 ±0.16, and X_{14}= 0.43 ±0.09, respectively. The mean Ir/(Ir+Pt) ratios of metal grains in the "100, 500 and 1000 ppm" synthetic chromite are X_{18}=0.10 ±0.06, X_{15}=0.40 ±0.17, and X_{20}= 0.45 ±0.11, respectively. With the exception of the "100 ppm synthetic sample," a definite pattern emerges. The mean Ir/(Ir+Pt) ratios are close to the bulk ratios determined from the raster analyses, and the standard deviations decrease systematically with increasing Ir and Pt concentration (and thus the decrease in distance between metal grains). This pattern is consistent with a process whereby Ir and/or Pt diffused through the chromite causing Pt grains to gain Ir, and/or Ir grains to gain Pt. It is not clear whether the diffusion mechanism is dominantly grain boundary or lattice diffusion.

A very rough approximation of the diffusion coefficient (D) for Ir (and/or Pt) in chromite can be calculated from the data. Ir and Pt grains in the "500 ppm" and "1000 ppm" samples in which grains were on average 42 and 35 μm apart have Ir/(Ir+Pt) close to 0.5 and thus have almost completely equilibrated. All of the Pt grains in the "100 ppm" samples have gained some Ir, but some have gained only a few percent. This suggests that the diffusion distance is greater than the 130 μm average distance between grains in the "100 ppm" samples

Fig. 1 Ir/(Ir+Pt) ratio from SEM spot analyses of alloy grains (open circles) and EMP raster analyses (400x400 μm) of chromite with included alloy grains (solid bars) in chromite samples annealed with Ir and Pt powder. "100 ppm, 500 ppm and 1000 ppm" indicate the concentration of Ir and Pt powder mixed into the chromite starting material. The dashed line indicates Ir=Pt which is the expected equilibrium condition. Raster analyses indicate that roughly equal concentrations of Ir and Pt are present in all of the bulk materials. The scatter in the 100 ppm raster analyses is probably due to poor counting statistics since the $\sim$100 ppm measured concentrations are only slightly higher than the 80 ppm detection limit. Note that in the Stillwater chromite the higher the concentration of metal grains (and thus the closer their spacings) the closer the alloy compositions are to Ir=Pt. The reason for the lack of Ir-rich alloys in the "100 ppm" synthetic sample is uncertain. See text for further discussion.

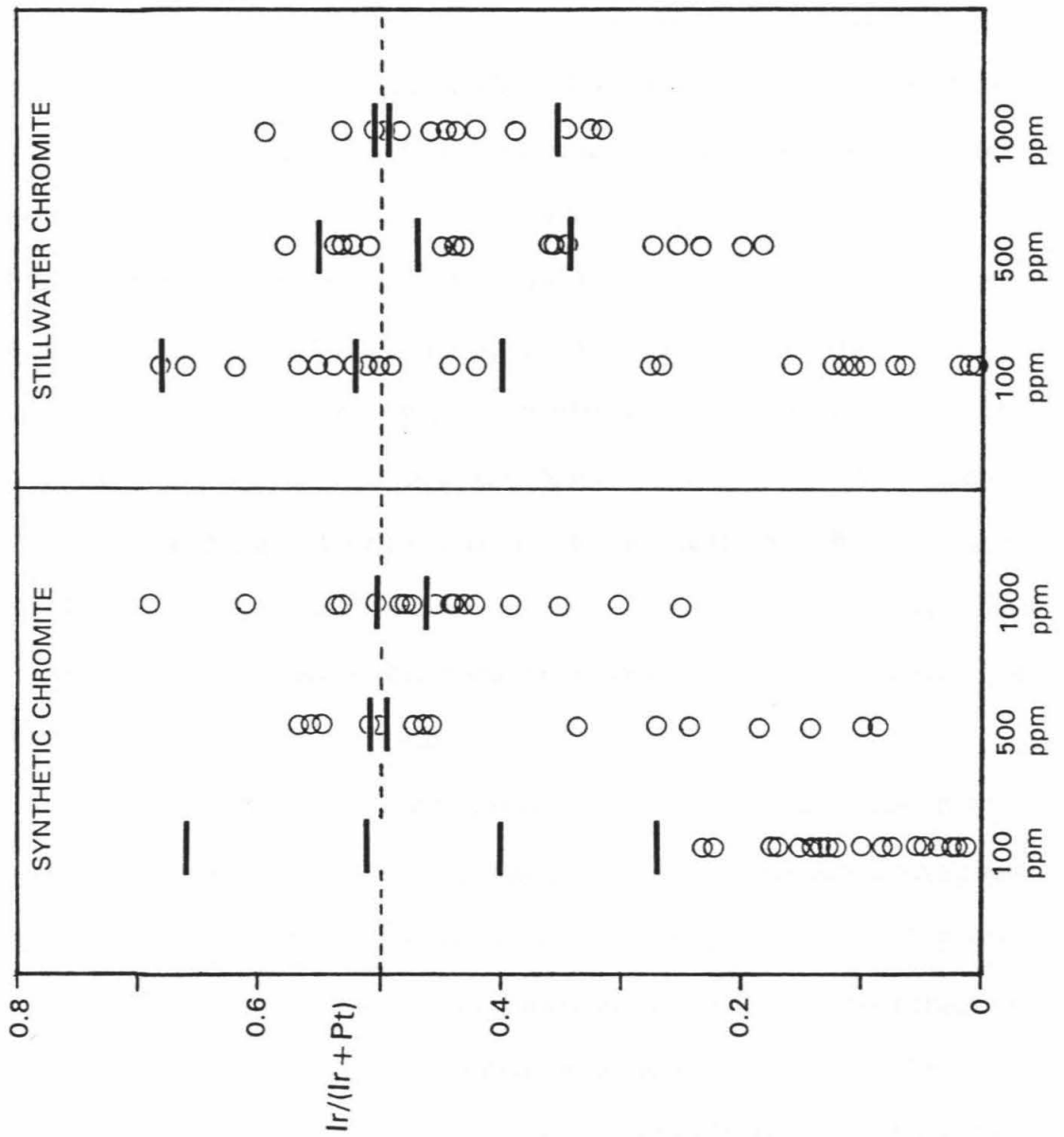
SYNTHETIC CHROMITE
STILLWATER CHROMITE
Ir/(Ir + Pt)
0.8
0.6
0.4
0.2
0
100 ppm
500 ppm
1000 ppm

and approximately equal to the maximum spacings between grains. A reasonable guess at this maximum distance based on observations of the unannealed samples is twice the average grain spacing, which is $\sim 260\ \mu m$. Following a rough approximation that the characteristic diffusion distance (X) is equal to $\sqrt{(Dt)}$, a value of $D \approx 6 \times 10^{-10}$ cm^2/sec is calculated for Ir and/or Pt diffusion in chromite at 1450°C. This calculation is intended only as an order of magnitude estimate. As indicated above, the diffusion mechanism is unknown.

Freer and O'Reilly (1980) studied Fe-Mg interdiffusion in pressed spinel powders between 800 and 1034°C in $FeAl_2O_4$-$MgAl_2O_4$ and Fe_2GeO_4-Mg_2GeO_4 couples as a function of composition. When their data are extrapolated to 1450°C, the interdiffusion rates in each system vary by several orders of magnitude depending on composition. With a Fe content of $\sim 25\%$, the Fe-Mg interdiffusion rates in both couples are equal to the diffusion rate for Ir (and/or Pt) in $FeCr_2O_4$ that was estimated above. This comparison is intended only to point out that Ir (and/or Pt) mobility in sintered spinel is within the range of values measured for major cation diffusion in sintered spinels.

The lack of identifiable metal grains rich in Ir in the "100 ppm" synthetic sample is difficult to understand. Three possible explanations are 1) the Ir grains (which have greater hardness than Pt) are plucked from the polished surface during polishing, 2) the Ir grains are smaller than $\sim 0.1\ \mu m$ and were thus not identifiable with the SEM, or 3) the Ir grains have dissolved in the chromite at a concentration level below the ~ 80 ppm detection limit of the EMP. The first explanation seems unlikely because the Ir/(Ir+Pt) ratio was 0.3 to 0.7 in the raster analyses, and because the lack of Ir grains is not observed in any of the unannealed samples, or in the annealed "500 ppm" or "1000 ppm" samples. The second explanation also seems unlikely because the Ir grains in the starting materials were all larger than 0.3 μm and easily identifiable with the SEM. Annealing should have the opposite effect of increasing

grain sizes in order to lower the surface free energy of the system. Thus, the third explanation which calls upon the dissolution of Ir in chromite at the < 80 ppm level seems to be the most likely. If this is the case, the solubility of Ir in the Stillwater chromite is probably lower than in the synthetic chromite. Additional experiments will clearly be necessary to draw firm conclusions concerning the solubility of Ir in chromite.

DISCUSSION

From the limited experimental data available we can gain some insight into the question of whether Ir-Os-Ru alloys in chromites originated by 1) exsolution from chromite or 2) crystallization from silicate liquids followed by chromite nucleation and growth. In the following discussion the stability of Ir-Os-Ru metallic phases coexisting with FeS liquid, chromite and silicate liquid will be considered.

PGE-sulfide

During magmatic crystallization of layered intrusions and the partial melting of mantle peridotite there is abundant evidence for sulfur oversaturation and the formation of immiscible FeS liquids (*e.g.*, Naldrett *et al.*, 1979; Mitchell and Keays, 1981). The high affinity of three of the PGE (Pd, Pt and Rh) for sulfides results in their strong partitioning into sulfide liquids and removal from the silicate fraction of a magma. This results in the formation of Pd, Pt and Rh-rich sulfide layers (commonly known as reefs) in layered intrusions such as the Bushveld and Stillwater Complexes. Similarly, Pd, Pt and Rh-rich sulfides are found in some mantle peridotite xenoliths and discrete Pd and Pt sulfides have even been observed (Mitchell and Keays, 1981). The other three PGE (Ir, Os and Ru) also have high affinities for sulfur relative to silicate liquid, but are concentrated both in sulfide and in chromite in layered intrusions and in peridotites (*e.g.*, Mitchell and Keays, 1981; Page and Talkington, 1984;

Naldrett *et al.*, 1987).

The presence of an immiscible FeS liquid phase has a strong effect on the partitioning of PGE. All of the PGE, including Ir, Os and Ru, have strong chalcophile affinities and dissolve in FeS in the presence of PGE alloys. The solubility of Ir in FeS liquid was determined in this study to be 3.9%. The solubility of Ru in solid FeS at 900°C has been determined to be 3.6 wt% in the presence of either RuS_2 or Ru metal (Makovicky *et al.*, 1986). Therefore, if Ir-Os-Ru alloys or sulfides coexisted with the FeS sulfides in peridotites or layered intrusions, the equilibrium concentration of these elements in the sulfides would be expected to be $\sim$4%, several orders of magnitude higher than the $\sim$10 ppm total PGE concentrations observed in magmatic sulfides from peridotite xenoliths and layered intrusions. This strongly suggests that Ir-Os-Ru-rich alloys were not present in the mantle during partial melting and were also not present in layered intrusions during magmatic crystallization.

PGE-chromite

If Ir partitions into chromite during chromite crystallization, then the solubility of Ir in chromite at magmatic temperatures must be at least as high as the bulk concentration of Ir in chromites which contain Ir-Os-Ru alloy and sulfide inclusions. Estimates of the Ir content of chromitites that contain Ir-Os-Ru alloys indicate that the total Ir content of chromite crystals and their inclusions do not exceed $\sim$1 ppm. This has been determined in two ways: 1) from the composition, size and frequency of occurrence of inclusions (*e.g.*, Cocherie *et al.*, 1989) and 2) from the bulk Ir content of chromite crystals plus inclusions (*e.g.*, Stockman and Hlava, 1984; Page *et al.*, 1986). Experiments reported above suggest that the Ir solubility in chromite at magmatic temperatures is below $\sim$80 ppm but that Ir can diffuse through chromite either by grain boundary or lattice diffusion. This result does not provide the necessary test of whether the solubility of Ir in chromite is $\geq$1 ppm. It does, however,

suggest that if Ir-Os-Ru alloys were trapped within chromite crystals as has been suggested, they might be able to diffuse into surrounding interstitial FeS liquid at magmatic temperatures. For example, using the diffusion coefficient for Ir in chromite estimated above, it would take only ~½ year for Ir to diffuse out of a typical 1 mm chromite grain, or ~50 years to diffuse out of a 1 cm grain. The mobility of Ir in chromite also suggests that if chromite were supersaturated with Ir at magmatic temperatures, Ir-Os-Ru alloys might be able to form by a diffusive exsolution mechanism at subsolidus temperatures. However, if the Ir diffusion mechanism is strictly grain boundary diffusion, one could argue that Ir-Os-Ru alloy inclusions in single chromite crystals might be isolated from surrounding phases.

PGE-silicate melts

Another test of the two hypotheses for the origin of Ir-Os-Ru alloy inclusions in chromite could come from a knowledge of the solubility of these elements in saturated silicate liquids. If Ir-Os-Ru alloys precipitate directly from silicate liquids as has been proposed, they must be saturated with Ir-Os-Ru. Investigations of the bulk composition of chilled margins from the Bushveld Complex and basal norites from the and Stillwater Complex give an indication of the PGE content of layered intrusion parental magmas. Estimates of Ir contents range from 0.1 to 0.4 ppb, while Ru contents range from 1 to 6 ppb (Davies and Tredoux, 1985; Page *et al.*, 1976). For comparison, the Ir and Os contents of basalts and granites that have been analyzed for PGE range from 0.001 to 0.4 ppb (Crockett, 1981; Morgan and Lovering, 1967; Hertogen *et al.*, 1980).

Amossè *et al.* (1990) measured the solubility of Ir in a basaltic liquid at 1430°C as a function of fO_2 and fS_2 and report that the solubility is ~100 ppb within the range of reasonable fO_2 and fS_2 conditions for mantle partial melting and the crystallization of layered intrusions. Although the data available on Ir-Os-Ru concentrations and solubilities in silicate

magmas is very limited and the nature of the dissolved PGE species is unknown, the low concentrations of Ir (by two orders of magnitude) relative to the apparent saturation level make it appear unlikely that silicate liquids became oversaturated with Ir (or Os and Ru) and precipitated Ir-Os-Ru alloys as liquidus phases.

Origin of Ir-rich alloys in chromite

In spite of textural arguments made in favor of Ir-Os-Ru alloys having formed as liquidus phases and having been trapped by crystallizing chromite, the limited experimental data summarized above suggest that these alloys would not be stable in the presence of either FeS or basaltic liquid at magmatic temperatures, perhaps even if trapped in chromite crystals. The stability of Ir-Os-Ru in the presence of chromite at magmatic temperatures and fO_2's is still unknown, but the apparent mobility of Ir in chromite and the ability of Ir and Ru to form compounds with the spinel structure under highly oxidizing conditions (*e.g.*, Krutzch and Kemmler-Sack, 1983; Capobianco and Drake, 1990) suggests that sub-ppm level solubility of Ir-Os-Ru in the chromite structure at high temperatures is at least plausible. It has been suggested by several authors that Ir, Os and Ru substitute for Cr^{3+} in the spinel lattice (Agiorgitis and Wolf, 1978; Morgan *et al.*, 1976). The solubility of these elements in chromite is presently unknown but almost certainly decreases with temperature. Thus, it is possible that exsolution is responsible for forming Ir-Os-Ru alloys during cooling of magmatic chromite after it crystallized with sub-ppm concentrations of Ir-Os-Ru in solid solution. Alteration and metamorphism of most peridotites and layered intrusions is indicative of slow cooling and may allow time for diffusion controlled exsolution. The textural features of Ir-Os-Ru alloy and sulfide inclusions in chromite that have been used by many authors to argue against the origin of these inclusions by exsolution are inherently inconclusive, particularly since it is likely that extensive subsolidus reequilibration has taken place.

REFERENCES

Agioritis G. and Wolf R. (1978) Aspects of osmium, ruthenium and iridium contents in some Greek chromites. *Chem. Geol.* 23, 267-272.

Amossé J., Allibert M., Fischer W. and Peboule M. (1990) Experimental study of the solubility of platinum and iridium in basic silicate melts - Implications for the differentiation of platinum-group elements during magmatic processes. *Chem. Geol.* 81, 45-53.

Auge T. (1988) Platinum-group minerals in the Tiebaghi and Vourinos ophiolitic complexes: genetic implications. *Can. Mineral.* 26, 177-192.

Capobianco C.J. and Drake M.J. (1990) Partitioning of ruthenium, rhodium and palladium between spinel and silicate melt. *Geochim. Cosmochim. Acta* 54, 869-874.

Cocherie A., Auge T. and Meyer G. (1989) Geochemistry of the platinum-group elements in various types of spinels from the Vourinos ophiolitic complex, Greece. *Chem. Geol.* 77, 27-39.

Constantinides C.C., Kingston G.A. and Fisher P.C. (1980) The occurrence of platinum group minerals in the chromitites of the Kokkinorotsos chrome mine, Cyprus. In *Proc. Int. Ophiolite Symp. Cyprus* (ed. Panayiotou A.), pp 93-101. Geol. Surv. Dep., Nicosia.

Crockett J.H. (1981) Geochemistry of the platinum-group elements. In *Platinum-group elements: Mineralogy, geology, recovery* (ed. Cabri, L.J.) Canad. Inst. Mining Metall. Spec. Vol. 23, pp. 47-64.

Davies G. and Tredoux M. (1985) The platinum group element and gold contents of the marginal rocks and sills of the Bushveld Complex. *Econ. Geol.* 80, 838-848.

Elliott W.C., Grandstaff D.E., Ulmer G.C., Buntin T. and Gold D.P. (1982) An intrinsic oxygen fugacity study of platinum-carbon associations in layered intrusions. *Econ. Geol.* 77, 1493-1510.

Freer R. and O'Reilly W. (1980) The diffusion of Fe^{2+} ions in spinels with relevance to the process of maghemitization. *Mineral. Mag.* 43, 889-899.

Gijbels R.H., Millard H.T., Desborough G.A. and Bartel A.J. (1974) Osmium, ruthenium, iridium and uranium in silicates and chromite from the eastern Bushveld Complex, South Africa. *Geochim. Cosmochim. Acta* 38, 319-337.

Harris D.C. and Cabri L.J. (1973) The nomenclature of the natural alloys of osmium, iridium and ruthenium based on new compositional data of alloys from world-wide occurrences. *Can. Mineral.* 12, 104-112.

Hertogen J., Janssens M.-J. and Palme H. (1980) Trace elements in ocean ridge basalt glasses: implications for fractionations during mantle evolution and petrogenesis. *Geochim. Cosmochim. Acta* 44, 2125-2143.

Krutzch B. and Kemmler-Sack S. (1983) Sauerstoff-spinelle mit ruthenium und iridium. *Mat. Sci. Bull.* 18, 647-652.

Legendre O. and Auge T. (1986) Mineralogy of platinum-group-mineral inclusions in chromitites from different ophiolitic complexes. In *Metallogeny of Basic and Ultrabasic Rocks* (eds. Gallagher M.J., Ixer R.A., Neary C.R. and Prichard H.M.), pp 361-372. Inst. Mining Metall., London.

Legendre O. and Johan Z. (1981) Mineralogie des platinoides dans les chromites massives de series ophiolitiques. *France, Centre National Recherche Scientifique, Rap. Ann. d'Activite, Juillet 1981*, 32-33.

Makovicky M., Makovicky E. and Rose-Hansen J. (1986) Experimental studies on the solubility and distribution of platinum group elements in base-metal sulphides in platinum deposits. In *Metallogeny of basic and ultrabasic rocks*. (eds. Gallagher M.J., Ixer R.A., Neary C.R. and Prichard H.M.), pp 415-425. Inst. Mining Metall., London.

Mitchell R.H. and Keays R.R. (1981) Abundance and distribution of Au,Pd, and Ir in some spinel and garnet lherzolites: Implication for the nature and origin of precious metal-rich intergranular components in the upper mantle. *Geochim. Cosmochim. Acta* 45, 2425-2442.

Morgan J.W., Ganapathy R., Higuchi H. and Krahenbuhl U. (1976) Volatile and siderophile trace elements in anorthositic rocks from Fiskenaesset, West Greenland: comparison with lunar and meteoritic analogues. *Geochim. Cosmochim. Acta* 40, 861-888.

Morgan J.W. and Lovering J.F. (1967) Rhenium and Osmium abundances in some igneous and metamorphic rocks. *Earth Planet. Sci. Lett.* 3, 219-224.

Naldrett A.J. and Cabri L.J. (1976) Ultramafic and related mafic rocks: Their classification and genesis with special reference to the concentration of nickel sulfides and platinum-group elements. *Econ. Geol.* 71, 1131-1158.

Naldrett A.J., Cameron G., von Gruenewaldt G. and Sharpe M.R. (1987) The formation of stratiform PGE deposits in layered intrusions. In *Origins of igneous layering*. (ed. Parsons I.), pp. 313-397, Reidel Publishing Company.

Naldrett A.J., Hoffman E.L., Green A.H., Chou C.L. and Naldrett S.R. (1979) The composition of Ni-sulfide ores, with particular reference to their content of PGE and Au. *Can. Mineral.* 17, 403-415.

Naldrett A.J. and von Gruenewaldt G. (1989) Association of platinum-group elements with

chromite in layered intrusions and ophiolite complexes. *Econ. Geol.* 84, 180-187.

Page N.J., Rowe J.J. and Haffty J. (1976) Platinum metals in the Stillwater Complex, Montana. *Econ. Geol.* 71, 1352-1263.

Page N.J., Singer D.A., Moring B.C., Carlson C.A., McDade J.M. and Wilson S.A. (1986) Platinum-group element resources in podiform chromitites from California and Oregon. *Econ. Geol.* 81, 1261-1271.

Page N.J. and Talkington R.W. (1984) Palladium, platinum, ruthenium and iridium in peridotites and chromitites from ophiolite complexes in Newfoundland. *Can. Mineral.* 22, 137-149.

Stockman H.W. and Hlava P.F. (1984) Platinum-group minerals in alpine chromitites from southwestern Oregon. *Econ. Geol.* 79, 491-508.

Talkington R.W. and Lipin B.R. (1986) Platinum-group minerals in chromite seams of the Stillwater complex, Montana. *Econ. Geol.* 81, 1179-1186.

Talkington R.W., Watkinson D.H., Whittaker P.J. and Jones P.C. (1984) Platinum-group minerals and other solid inclusions in chromite of ophiolitic complexes: occurrence and petrological significance. *TMPM Tschermaks Min. Petr. Mitt.* 32, 285-301.

Talkington R.W., Watkinson D.H., Whittaker P.J. and Jones P.C. (1986) Platinum-group element bearing minerals and other solid inclusions in chromite of mafic and ultramafic complexes: Chemical compositions and comparisons. In *Metallogeny of basic and ultrabasic rocks (regional presentations)* (eds. Carter B., Chowdhury M.K.R., Jankovic S., Marakushev A.A., Morten L., Onikhimovsky V.V., Raade G., Rocci G. and Augustithis S.S.), pp 223-249. Theophrastus Publishing, Athens.

Zeibold T.O. (1967) Precision and sensitivity in electron microprobe analysis. *Anal. Chem.* 39, 858-861.

Reprinted from Analytical Chemistry, 1990, 62, 209.

Resonance Ionization Mass Spectrometry of Sputtered Osmium and Rhenium Atoms

Joel D. Blum,*[1] M. J. Pellin, W. F. Calaway, C. E. Young, and D. M. Gruen

Materials Science, Chemistry, and Chemical Technology Divisions, Argonne National Laboratory, Argonne, Illinois 60439

I. D. Hutcheon and G. J. Wasserburg

Lunatic Asylum of the Charles Arms Laboratory, Division of Geological and Planetary Sciences, California Institute of Technology, Pasadena, California 91125

The mass spectrometric analysis of Os and Re was investigated by use of a pulsed primary Ar^+ ion beam to provide sputtered atoms for resonance ionization mass spectrometry. A useful yield of 10^{-2} and a detection limit of 8 ppb were demonstrated for Os concentration measurement. In situ measurements of Os concentration are obtainable by this method at the sub-part-per-million level in conducting and semiconducting materials with a full width at half maximum beam diameter of ~ 70 μm. An ionization scheme for Os that utilizes three resonant energy levels (including an autoionizing energy level) was investigated and found to have superior sensitivity and selectivity compared to nonresonant and one and two energy level resonant ionization schemes. An elemental selectivity for Os over Re of $\geq 10^3$ was demonstrated. It was found that detuning the ionizing laser from the autoionizing energy level to an arbitrary region in the ionization continuum resulted in a 5-fold decrease in signal intensity and a 10-fold decrease in elemental selectivity.

INTRODUCTION

The mass spectrometric analysis of small quantities of Os and Re is an important analytical goal in geochemistry with two main applications: (1) the in situ measurement of Os and Re concentrations at very low levels in geologic materials and in phases synthesized in laboratory experiments; (2) the measurement of Os isotope ratios both in situ and on small samples of Os chemically separated from geologic materials. In both instances the number of Os and Re atoms available for measurement is quite low. Therefore, it is of interest to develop a mass spectrometric measurement technique with a high ratio of ions detected to atoms present in the ion source (useful yield). The technique must also be able to discriminate against molecular interferences in the case of concentration measurements and discriminate between ^{187}Os and ^{187}Re atoms in the case of Os isotope ratio measurements.

At Argonne National Laboratory we have developed a resonance ionization mass spectrometer for ultrasensitive surface analysis of semiconductors with monolayer depth resolution. Surface analysis by resonance ionization of sputtered atoms (SARISA) has a high useful yield ($\geq 10^{-2}$) and a demonstrated sensitivity at the parts-per-billion (ppb) level for Fe concentration measurements in a Si matrix (*1–3*). It employs a pulsed primary ion beam to create a cloud of sputtered neutrals that efficiently fill the ionizing volume of pulsed lasers and an energy and angular refocusing time-of-flight mass spectrometer to maximize photoion detection. SARISA appears to be well suited for in situ determinations of Os and Re concentrations.

A major obstacle that must be addressed in order to demonstrate the utility of resonance ionization of sputtered atoms for Os and Re analyses is the identification of suitable ionization schemes for these elements. To this end, we have investigated a series of multiphoton ionization schemes for Os and Re with the goal of maximizing the Os photoion yield and minimizing the isobaric interference between Os and Re at mass 187. In this study we have evaluated the useful yield, detection limit, and selectivity of SARISA for the measurement of Os concentrations. This information is also important in evaluating the potential of the SARISA photoion source as a prototype of an elementally selective and highly efficient ion source for an isotope ratio mass spectrometer.

EXPERIMENTAL SECTION

Apparatus. The experiments were performed by use of the SARISA apparatus, described in detail by Pellin et al. (*2*). The instrument consists of three main subunits: a pulsed primary ion source, three pulsed tunable lasers, and an energy and angular refocusing time-of-flight mass spectrometer (Figure 1).

A mass analyzed 5 keV Ar^+ sputtering beam with a current of 2.0 μA and a full width at half maximum (fwhm) diameter of ~ 70 μm is produced by a Colutron ion gun. During analyses, the primary ion beam is chopped into pulses of 200 ns width by electrostatic deflection and is synchronized with the lasers operating at a 40-Hz repetition rate. The Ar^+ ion pulses strike the target in a chamber pumped to the low 10^{-9} Torr pressure range. The sputtering rate in the pulsed mode is ~ 10 min per monolayer of target. Sputtered species fill a volume above the target during and after the arrival of the primary ion pulse. During sputtering, the target is held at a 1.5-kV potential; incoming Ar^+ ions are decelerated to 3.5 keV and positive secondary ions produced by sputtering are accelerated to 1.5 keV. The secondary ions are not transmitted through the mass spectrometer which is designed to accept ions with 1.0 ± 0.1 keV energy.

Three hundred nanoseconds after the end of each ion pulse a XeCl excimer laser is fired producing a ~10-ns, 250-mJ UV pulse with a bandwidth of 0.3 to 0.5 nm centered about 307.9 nm. The excimer output is split into three beams which either are used to pump tunable dye lasers (loaded with Rhodamine, Coumarin, or DCM dye) or, for some experiments, are focused directly into the ionization region. When necessary, the visible fundamental dye laser output is frequency doubled in a nonlinear crystal to produce UV pulses. The laser beams are spatially and temporally overlapped in a volume that extends from about 0.5 to 1.5 mm above the target surface and has a diameter of ~1 mm. Photoionization of sputtered neutrals occurs within this volume and the photoions are accelerated away from the target and into the mass spectrometer. The target potential is lowered at the beginning of each laser shot, so that ions produced by photoionization are transmitted through the mass spectrometer, and is then

* Author to whom correspondence should be addressed.
[1] Present address: Division of Geological and Planetary Science, California Institute of Technology, Pasadena, CA 91125.

0003-2700/90/0362-0209$02.50/0

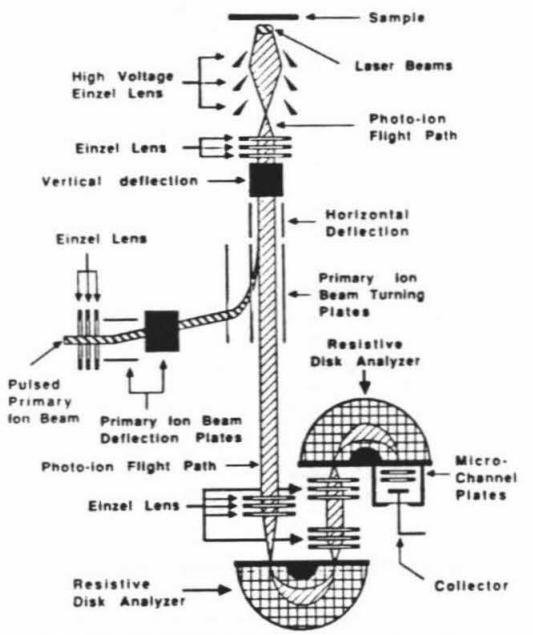

Figure 1. Schematic diagram of the SARISA experimental apparatus from Pellin et al. (*2*).

switched back to 1.5 kV before the arrival of the next primary ion pulse to again suppress the detection of sputtered secondary ions.

The photoion beam is focussed and shaped in the time-of-flight mass spectrometer by a series of einzel lenses, deflection plates, and two hemispherical energy analyzers, after which it strikes a chevron-type microchannel plate electron multiplier (Figure 1). The resulting electron pulse is measured by a transient charge digitizer at high signal levels or by a pulse-counting system at lower signal levels. The maximum ion transmission of the mass spectrometer is ~70% (*3*).

Samples. Four samples of metallic solid solutions were used as targets in this study. Two samples were synthesized from pure metals (*4*) and two samples are from meteorites. Synthetic sample 1 contains 95.2% Ni, 2.5% Os, and 2.3% Re. Synthetic sample 2 contains 99.8% Ni, 0.1% Os, and 0.1% Re. The meteorites are the Negrillos and Coahuila type IIAB hexahedrite iron meteorites, which are essentially comprised of a homogeneous mixture of 94.2% Fe, 5.4% Ni, and 0.4% Co with many other metals including Os, Re, Ir, Pt, and Au as parts-per-million level trace impurities. Radiochemical neutron activation analyses by Pernicka and Wasson (*5*) indicate that the Negrillos meteorite contains 25 ppm Os and 1.4 ppm Re (±12%) and that the Coahuila meteorite contains 3.4 ppm Os and 0.4 ppm Re (±12%). All concentrations are given in atomic proportions.

Ionization Schemes. Osmium was ionized by five different schemes to evaluate their relative sensitivities and selectivities. Rhenium was ionized by only the two simplest schemes. The ionization schemes all originate from the ground electronic state and can be grouped into five general types designated A through E (Figure 2). We report wavelengths as nanometers in air and energy levels as inverse centimeters in vacuum. Scheme A is nonresonant and requires the simultaneous absorption of two (in the case of Re) or three (in the case of Os) photons from the broad-band 307.9-nm excimer laser to reach the ionization continuum. Scheme B uses one ~240- or ~300-nm UV photon from a dye laser (λ_1) to raise Os or Re atoms to a resonant energy level (E_1) and one 307.9-nm excimer photon to ionize the atoms. Scheme C uses one ~240- or ~300-nm UV photon from a dye laser (λ_1) to raise atoms to a resonant energy level (E_1) and one additional photon (when ~240-nm photons are used) or two additional photons (when ~300-nm photons are used) of the same energy to ionize them. Scheme D uses one ~240- or ~300-nm UV photon (λ_1) from a dye laser to raise atoms to a first resonant energy level (E_1), one ~480- or ~600-nm visible photon (λ_2) from a second dye laser to raise atoms to a second resonant energy level (E_2), and a second visible photon (λ_2) from the second dye laser to produce photoions. In schemes A through D atoms are raised to an arbitrary energy above the ionization continuum by the ionizing photon. Scheme E is the same as scheme D except that the ionizing photon (λ_3) is generated from a dye laser tuned to reach an autoionizing resonant energy level (E_3) above the ionization potential (IP). The specific energy levels evaluated for each scheme are given in Table I.

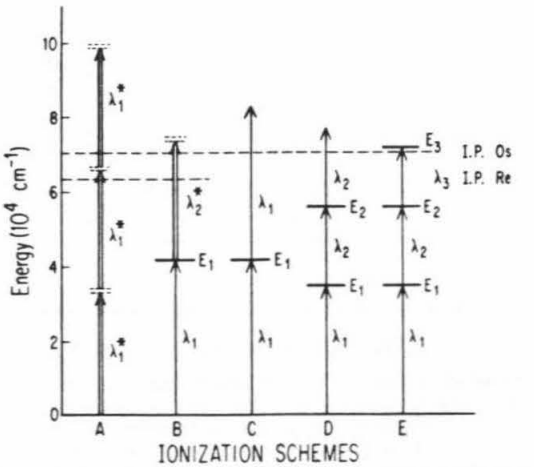

Figure 2. Generalized ionization schemes evaluated for Os (A–E) and Re (A–B). Asterisks denote broad-band excimer radiation.

Table I. Resonant Energy Levels Evaluated in this Study[a]

ionization scheme	energy level, cm^{-1} E_1	E_2	E_3
B_{Re}	41 557		
	41 313		
B_{Os}	41 876		
	41 726		
	41 232		
	41 225		
	40 362		
	34 365		
C	*b*		
D	41 726	58 175	
	41 232	56 729	
	40 362	56 222	
	34 365	55 402	
E	34 365	55 402	71 032

[a] E_1 and E_2 levels are from ref 18. [b] Same as B_{Os}.

Scheme E was found to be most favorable for Os ionization (following criteria discussed below) and will therefore be described in more detail (Figure 3). UV photons from the first dye laser are tuned to 290.906 nm to populate the E_1 level [E_1 = 34 365 cm^{-1}; angular momentum quantum number (J) = 5] from the ground state (J = 4). Visible photons at 475.216 nm then pump atoms from E_1 to the E_2 level (E_2 = 55 402 cm^{-1}; J = 5). Finally, the third dye laser is tuned to pump atoms from E_2 over the IP (≥69 000 cm^{-1}) to the most favorable autoionizing E_3 energy level (E_3 = 71 032 cm^{-1}) that could be accessed by scanning the third dye laser across the 635- to 665-nm region.

The energy needed per pulse to saturate each of the three levels was investigated by monitoring the Os^+ signal in the mass spectrometer while sequentially placing a series of partially transmitting filters into each of the laser beams separately. The important parameter for saturation is the energy density, which can be controlled by the size, shape, and position of the laser

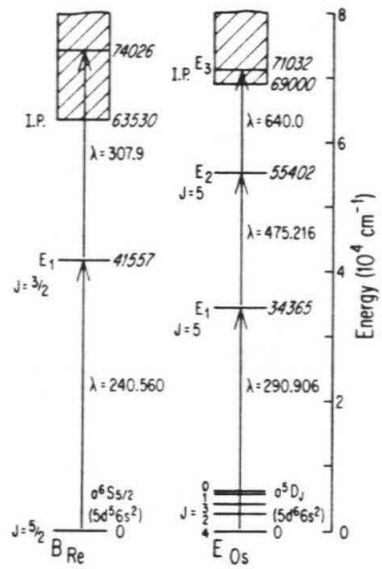

Figure 3. Specific ionization schemes used for Re and Os analyses.

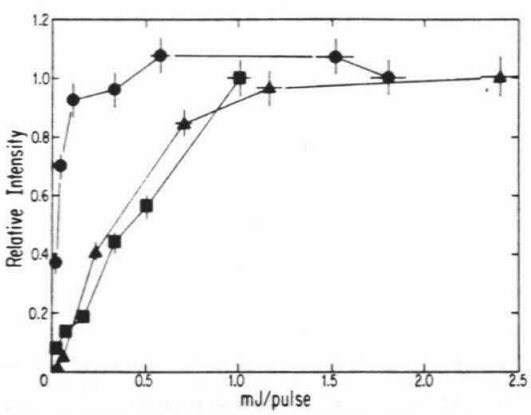

Figure 4. Relative Os signal intensity as a function of laser energy per pulse for ionization scheme E as each of the three laser beams was attenuated separately, while the other two beams were held at full energy. Error bars are included where estimated uncertainty exceeds symbol size. Saturation was not reached for λ_1 at a maximum energy of ~1 mJ/pulse (squares) but was reached for λ_2 at ~0.5 mJ/pulse (circles) and λ_3 at ~1.5 mJ/pulse (triangles).

beams as well as by the amount of incoming energy. By tightly focusing the laser beams, we were able to saturate each of the three energy levels, but in this configuration only a small portion of the cloud of sputtered atoms was ionized. Under normal operating conditions, we defocused the lasers to a diameter of ~1 mm in order to access a large portion of the cloud of sputtered atoms. With two of the three laser beams kept at full energy and one beam attenuated, E_1 was found not to be completely saturated with a maximum energy of ~1 mJ/pulse for λ_1, E_2 was saturated at an energy of ~0.5 mJ/pulse for λ_2, and E_3 was saturated at an energy of ~1.5 mJ/pulse for λ_3 (Figure 4). Subsequent experiments were run with an energy of ~1 mJ/pulse, ~2 mJ/pulse, and ~4 mJ/pulse at λ_1, λ_2, and λ_3, respectively.

Rhenium atoms were ionized by schemes A and B only (Figure 2). In scheme B (Figure 3), UV photons at 240.560 nm populated the E_1 level (E_1 = 41 557 cm^{-1}; $J = {}^3/_2$) from the ground state ($J = {}^5/_2$). The broad-band 307.9-nm excimer photons then raised the atoms from the excited energy level to the IP (≥63 530 cm^{-1}).

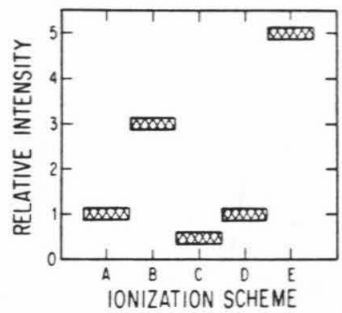

Figure 5. Relative signal intensities for Os ionization schemes.

RESULTS AND DISCUSSION

Sensitivity and Selectivity of Ionization Schemes. Synthetic sample 1 was used to investigate the relative sensitivity and selectivity of the ionization schemes for Os. We will use the Os^+ signal intensity for nonresonant ionization by scheme A as a reference value and discuss the Os^+ signal levels for the resonant schemes relative to this value (Figure 5). Ionization by scheme B was ~3 times more efficient than scheme A, showing the enhancement of ionization probability from the addition of a resonant step to the broad-band 307.9-nm laser beam. The ionization energy in scheme A significantly overshoots the IP, whereas the ionization energy in scheme B places the atom only slightly above the IP (Figure 2). The increased ionization of scheme B over A suggests that the broad-band laser in scheme B overlaps an autoionizing resonance or that the ionization cross section in the continuum decreases at energies much higher than the IP.

Ionization by scheme C was ~50% less efficient than by scheme A. This probably arises because the ~1 mJ/pulse UV dye laser does not have enough energy to saturate the ionization process. In scheme D the addition of a second resonance level allows the ionization step to be pumped by the visible dye laser fundamentals which have higher energy (~2 mJ/pulse) than the frequency doubled UV pulses. The increase in energy more nearly saturates the ionization step and results in a ~50% higher efficiency than by scheme C (about the same efficiency as scheme A). Scheme E is identical with scheme D except that the visible ionizing photons are tuned to match an autoionizing energy level, producing a signal enhancement of a factor of ~5 over scheme D and suggesting that the ionization step is only saturated at the autoionizing resonance. Similar ionization enhancements have been observed for Gd (*6*) and U (*7*) when dye lasers were tuned to match autoionizing energy levels.

The in situ measurement of the isotopic composition of Os in samples that also contain Re would require that the ^{187}Re peak (62.6% abundance isotope) be suppressed to eliminate isobaric interference with the ^{187}Os peak (~1.6% abundance isotope). As a measure of the selectivity of each Os^+ ionization scheme, we measured the $^{192}Os^+/^{185}Re^+$ ratio without correction for instrumental fractionation (to an accuracy of ~10%) for each scheme and normalized it to the true ratio of these stable isotopes in the synthetic sample calculated from the Os and Re concentrations and natural isotopic abundances. Since there was some variability in the $^{192}Os^+/^{185}Re^+$ ratio for different energy levels following a given ionization scheme, we have plotted in Figure 6 the $^{192}Os^+/^{185}Re^+$ ratio for the energy levels with the maximum selectivity for each scheme. Nonresonant ionization by 307.9-nm photons (scheme A) was slightly more efficient for Re than for Os and showed a ~30% Re enhancement. The addition of an Os resonant step to the excimer photons (scheme B) enhanced Os ionization by as much as 3-fold. For resonance ionization using narrow band

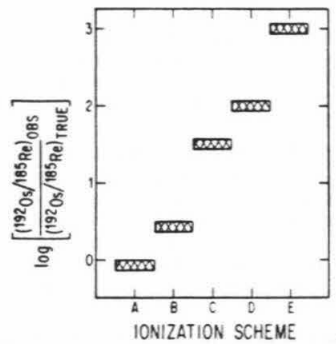

Figure 6. Relative selectivity for Os over Re measured as the log of the ratio of the observed to the true $^{192}Os^+/^{185}Re^+$ ratio for the Os ionization schemes.

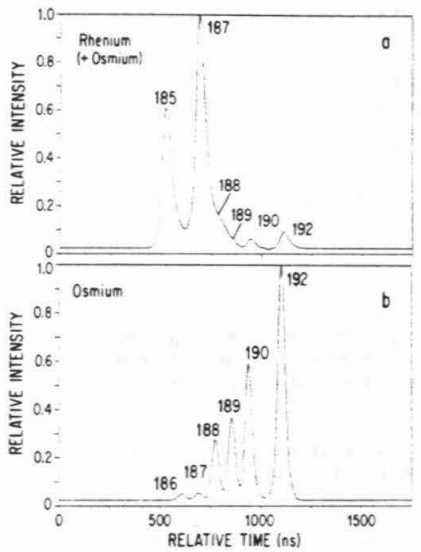

Figure 7. (a) Re spectrum (scheme B) taken at low mass resolution (~250) and (b) Os spectrum (scheme E) taken at higher mass resolution (~400) in the same synthetic sample (2.3% Re; 2.5% Os). Labels indicate the masses of the Re (185 and 187) and Os (186 to 190 and 192) isotope peaks. Note that scheme B for Re has low selectivity and scheme E for Os has high selectivity.

dye lasers only, Os was enhanced relative to Re by as much as 33 for single resonance (scheme C), 10^2 for double resonance (scheme D), and $\geq 10^3$ for triple resonance (scheme E). A signal intensity versus time-of-flight spectrum is shown in Figure 7a for resonance ionization of Re (mass 185 and 187) using ionization scheme B. The low selectivity of scheme B for Re is illustrated by the presence of nonresonantly ionized Os which is visible at masses 188 to 192. A similar spectrum is shown in Figure 7b for resonance ionization of Os from the same sample by ionization scheme E. The extremely high selectivity of scheme E for Os is illustrated by the complete absence of Re at mass 185 and 187. An Os selectivity similar to that of scheme E was reported for thermal vaporization RIMS using a two-photon single resonance scheme similar to scheme C, except that the transition originated from the ~8% populated thermally excited a^5D_3 state (Figure 3) rather than the ground state (*8*).

Os Concentration Measurement. Synthetic sample 2 and the two iron meteorite specimens were used to investigate the ability to measure Os concentrations quantitatively. Time-

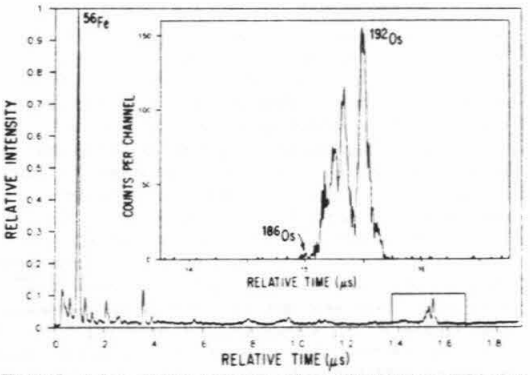

Figure 8. A time-of-flight spectrum collected with charge digitization for an Os analysis of the Negrillos iron meteorite using ionization scheme E. The peaks at 0–10 μs are due to nonresonant ionization of the major constituents in the sample (Fe, Ni, Co, and their oxides) and the peaks beginning at ~15 μs are due to resonant ionization of the 25 ppm Os. Inset shows counts per 5-ns channels across the Os peaks for a 125-s pulse-counting experiment in which only $^1/_5$ of a monolayer of material was removed from a 100-μm spot.

Table II. Pulse Counting Data for 125-s Os Analyses of Samples

sample	Os conc, ppm	Os^+ counts	counts per ppm
synth 2	1000	346 000	346
Negrillos	25	6 480	259
Coahuila	3.4	1 120	329
mean			311± 53 ($2\sigma_m$)

of-flight spectra were collected for 125 s (5000 laser shots) with a fwhm mass resolution at mass 187 ($M/\Delta M$) of ~250, which adequately resolved the peaks for the purpose of concentration measurement. Mass resolution can be increased to ~400 using an aperture positioned in the photoion path, but only at the cost of a loss in signal intensity by a factor of ~10.

A time-of-flight spectrum of the Negrillos meteorite collected with charge digitization is shown as an example in Figure 8. The peaks at 0 to 10 μs are due to nonresonant ionization of the major constituents in the sample (Fe, Ni, Co, and their oxides), and the peaks beginning at ~15 μs are due to resonant ionization of the 25 ppm Os. Because of the low concentration of Os a pulse counting system was also used to measure the Os peaks. The ion signal is recorded by dividing arrival times into 5-ns channels. The Os mass spectrum is shown as an inset in Figure 8 in which counts per 5-ns channels for a 125-s analysis are plotted. The small peak at 15 μs is ^{186}Os which is present at 0.40 ppm.

A background of 16 counts per 125 s across masses 186 to 192 was determined by detuning the UV laser 12 cm^{-1} from the center of the E_1 resonance level and repeating the experiment. The absence of interferences resonant with the UV laser frequency was verified by measuring a background of 18 counts per 125 s across these masses on stainless steel (Fe, Ni, Cr alloy) with the lasers tuned for Os analysis. This background intensity is assumed to represent the instrumental background for a sample containing no Os and was subtracted from the total counts measured for each sample to determine the net Os^+ counts.

The Os^+ counts summed over the major isotopes (masses 186 to 192) are given in Table II for three samples which have Os concentrations known to ±12% (*5*). The data demonstate that for Os concentrations between ~3 and 1000 ppm the measured Os^+ intensity is linearly proportional to the Os concentration in each sample. The ratio of Os^+ intensity to

Os concentration (relative ion yield) is constant to within ~20% for all three samples and the data define a linear calibration curve whose slope, 311 ± 53 ($2\sigma_m$) Os^+ counts per ppm Os, can be used to determine Os concentrations in samples of similar bulk composition.

The mean relative ion yield and background count rate were used to calculate the minimum detection limit for Os in metallic Ni–Fe phases. Following the treatment of Ziebold (*9*) we calculate from Poisson statistics that the detection limit for Os at the 95% confidence level is 41 ppb for a 125-s analysis and 7.7 ppb for a 3600-s analysis. We note that a 3600-s analysis would consume only ca. six monolayers of the sample.

Variations in the relative ion yield due to matrix effects should depend primarily on the sputtering rate of the sample as long as the dominant sputtered species are neutral atoms. Therefore, sputtering rates must be determined for each target material analyzed. Considerable data exist for pure elements which indicate variations of up to a factor of ~3 (*10*). Sputtering rates of most multielement matrix materials are unknown and will have to be measured. If large populations of ions or molecules are produced during sputtering, the population of sputtered neutral atoms available for photoionization will be diminished and will cause shifts in the relative ion yield.

Useful Yield. The useful yield is defined as the ratio of ions detected to atoms present in the ion source. The useful yield is determined from the ratio of Os^+ ions detected per laser shot to the number of Os atoms sputtered from the sample per primary ion pulse. The mean relative Os^+ ion yield corresponds to 0.062 count per ppm per laser shot. The amount of target material sputtered per primary ion pulse can be estimated from the sputter yield of pure Fe and Os under bombardment by 3.5-keV Ar^+ ions, which for both Fe and Os is 2.5 atoms per Ar^+ ion (*10*). With a primary ion current of ~2.0 μA and a pulse width of 0.20 μs, 2.5×10^6 ions strike the target per pulse and, therefore, approximately 6.3×10^6 Fe atoms are sputtered per pulse. Assuming that trace levels of Os are sputtered at the same rate as the Fe matrix, 6.3 Os atoms will be sputtered during each pulse per ppm of Os in the sample. Dividing the mean Os^+ counts per laser shot by the number of sputtered Os atoms per primary ion pulse gives a useful yield of 10^{-2}. The Os mass spectrum for the 25 ppm Os sample shown in Figure 8 was collected during 5000 primary ion pulses (125 s) by sputtering 7.8×10^5 Os atoms ($^1/_5$ of a monolayer in a 100-μm spot) and detecting 6.5×10^3 Os^+ ions.

The useful yield of the experiment described here appears to be considerably higher than that reported for other mass spectrometric techniques for Os analysis. However, in making such a comparison one must consider that the typical operating conditions (for instance, the mass resolution and the required sample preparation) of the various techniques differ markedly. The useful yield for resonance ionization mass spectrometry of chemically separated Os vaporized from a thermally pulsed filament has been reported at $\sim 10^{-7}$ (*8*) and the useful yield of inductively coupled plasma mass spectrometry of chemically separated Os has been reported at 10^{-5} to 10^{-6} (*11*). We have determined the useful yield for Os analysis by secondary ion mass spectrometry to be $\sim 10^{-4}$ using the Caltech Cameca IMS 3-F ionprobe with a O^- primary ion beam and a metallic Os target. Osmium analyses have also previously been made by thermal ionization of oxide species (*12*, *13*), secondary ion mass spectrometry (*14*, *15*), accelerator mass spectrometry (*16*), and laser ablation mass spectrometry (*17*), but useful yields have been been reported.

Applications. In situ Os and Re concentrations can now be measured at the sub-part-per-million level in conducting and semiconducting materials with a fwhm beam diameter of ~70 μm using SARISA. The linear dependence of the Os^+ signal on Os concentration allows the use of synthetic and well-characterized natural standards for quantitative analysis. Minor changes in the experimental configuration should allow analyses of most high IP elements including all of the Pt-group elements. These measurements may be applied to geochemical studies related to chemical fractionation and diffusion in metallic and sulfide phases in meteorites and terrestrial rocks and ore deposits as well as in phases synthesized in laboratory experiments.

The SARISA apparatus used in this study uses a low-resolution mass spectrometer (see mass spectra in Figures 7 and 8) and is therefore not appropriate for Os isotope ratio measurement. However, the high useful yield and selectivity for Os demonstrated here suggest that the SARISA photoion source may be superior to thermal vaporization as the ion source for Os isotope ratio measurements by resonance ionization. An important issue that remains to be resolved is whether the pulsed photoion source described here can be coupled with a mass spectrometer with sufficient mass resolution and abundance sensitivity for the measurement of Os isotopic ratios with ≤1% precision. If this can be accomplished, it will be possible to measure the isotopic composition of Os using much smaller sample sizes than needed for thermal vaporization resonance ionization. If measurements can be precisely calibrated by using standards, in situ isotopic analyses may eventually be possible.

ACKNOWLEDGMENT

We thank three anonymous reviewers, J. Whitten for technical assistance, J. Wasson for providing meteorite specimens, J. Blake for comments, and E. Stolper and G. Rossman for the use of furnaces.

Registry No. Os, 7440-04-2; Rh, 7440-15-5.

LITERATURE CITED

(1) Pellin, M. J.; Young, C. E.; Calaway, W. F.; Burnett, J. W.; Jorgensen, B.; Schweitzer, E. L.; Gruen, D. M. *Nucl. Instrum. Method* **1987**, *B18*, 446–451.
(2) Pellin, M. J.; Young, C. E.; Gruen, D. M. *Scanning Microsc.* **1988**, *2*, 1353–1364.
(3) Pellin, M. J.; Husinsky, W.; Calaway, W. F.; Burnett, J. W.; Schweitzer, E. L.; Young, C. E.; Jorgensen, B.; Gruen, D. M. *J. Vac. Sci. Technol.* **1987**, *B5*, 1477–1481.
(4) Blum, J. D.; Wasserburg, G. J.; Hutcheon, I. D.; Beckett, J. R.; Stolper, E. M. *Geochim. Cosmochim. Acta* **1989**, *53*, 483–489.
(5) Pernicka, E.; Wasson, J. T. *Geochim. Cosmochim. Acta* **1987**, *51*, 1717–1726.
(6) Rimke, H.; Peuser, P.; Sattelberger, P.; Trautmann, N.; Herrmann, G.; Ruster, W.; Ames, F.; Kluge, H. J.; Otten, E. W. In *Resonance Ionization Spectroscopy*; Hurst, G. S., Morgan, C. G., Eds.; Institute of Physics Conference Series No. 84; Institute of Physics: Bristol, 1987; pp 235–238.
(7) Janes, G. S.; Irving, I.; Pike, C. T.; Levy, R. H.; Levin, L. *IEEE J. Quantum Electron.* **1976**, *QE-12*, 111–120.
(8) Walker, R. J.; Fassett, J. D.; Travis, J. C. In *Resonance Ionization Spectroscopy*; Lucatorto, T. B., Parks, J. E., Eds.; Institute of Physics Conference Series No. 94; Institute of Physics: Bristol, 1989; pp 337–342.
(9) Ziebold, T. O. *Anal. Chem.* **1967**, *39*, 858–861.
(10) Matsunami, N.; Yamamura, Y.; Itikawa, Y.; Itoh, N.; Kazumata, Y.; Miyagawa, S.; Morita, K.; Shimizu, R.; Tawara, H. *Energy Dependence of the Yields of Ion-Induced Sputtering of Monatomic Solids*; Institute of Plasma Physics: Nagoya, Japan, 1983.
(11) Russ, G. P.; Bazan, J. M. *Anal. Chem.* **1987**, *59*, 984–989.
(12) Hirt, B.; Tilton, G.; Herr, W.; Hoffmeister, W. In *Earth Science and Meteoritics*; Geiss, J., Goldberg, E., Eds.; North Holland: Amsterdam, 1963; pp 273–280.
(13) Herr, W.; Wolfle, R.; Eberhardt, P.; Kopp, E. In *Radioactive Dating and Methods of Low-Level Counting*; IAEA: Vienna, 1967; pp 499–508.
(14) Luck, J. M.; Allegre, C. J. *Nature* **1983**, *302*, 130–132.
(15) Luck, J. M.; Allegre, C. J. *EOS* **1986**, *67*, 393.
(16) Teng, R. T. D.; Fehn, U.; Elmore, D.; Hemmick, T. K.; Kubik, P. W.; Gove, H. E. *Nuclear Instrum. Methods, Phys. Res.* **1987**, *B29*, 281–285.
(17) Simons, D. S. *Int. J. Mass Spetrom. Ion Processes* **1983**, *55*, 15–30.
(18) Meggers, W. F.; Corliss, C. H.; Scribner, B. F. *Tables of NBS Spectral Line Intensities Part I*, 2nd ed. U.S. Department of Commerce, Na-

tional Bureau of Standards Mongraph 145; U.S. Government Printing Office: Washington, DC, 1975.

RECEIVED for review May 9, 1989. Accepted October 24, 1989. This study was performed as part of a doctoral dissertation by the senior author at the California Institute of Technology (Caltech). Work was supported by the U.S. Department of Energy through BES-Material Sciences Contract W-31-109-ENG-38 to Argonne National Laboratory and BES-Engineering and Geosciences Grant DE-FG03-88ER13851 to Caltech. Caltech Division of Geological and Planetary Sciences Contribution Number 4759 (675).

Geochimica et Cosmochimica Acta Vol. 54, pp. 875–881

0016-7037/90/$3.00 + .00

LETTER

In situ measurement of osmium concentrations in iron meteorites by resonance ionization of sputtered atoms

JOEL D. BLUM,[1,2,*] M. J. PELLIN,[1] W. F. CALAWAY,[1] C. E. YOUNG,[1]
D. M. GRUEN,[1] I. D. HUTCHEON,[2] and G. J. WASSERBURG[2]

[1]Materials Science, Chemistry, and Chemical Technology Divisions, Argonne National Laboratory, Argonne, IL 60439, USA
[2]Lunatic Asylum of the Charles Arms Laboratory, Division of Geological and Planetary Sciences, California Institute of Technology, Pasadena, CA 91125, USA

(*Received December* 1, 1989; *accepted in revised form February* 2, 1990)

Abstract—Resonance ionization of sputtered atoms followed by time-of-flight mass spectrometry was used for *in situ* quantitative measurement of Os with a spatial resolution of ~70 μm. Osmium concentrations in synthetic metals and iron meteorites were measured to demonstrate the analytical capabilities of the technique. A linear correlation between Os^+ signal intensity and the known Os concentration was observed over a range of nearly 10^4 in Os concentration with an accuracy of ~ ±10%, a minimum detection limit of 7 parts per billion atomic, and a useful yield of 1%. Resonance ionization of sputtered atoms samples the dominant neutral-fraction of sputtered atoms and utilizes multiphoton resonance ionization to achieve high sensitivity and to eliminate atomic and molecular interferences. Matrix effects should be small compared to secondary ion mass spectrometry because ionization occurs in the gas phase and is largely independent of the physical properties of the matrix material. Resonance ionization of sputtered atoms can be applied to *in situ* chemical analysis of most high ionization-potential elements (including all of the Pt-group elements) in a wide range of natural and synthetic materials. The high useful yield and elemental selectivity of this method should eventually allow the *in situ* measurement of Os isotope ratios in some natural samples and in sample extracts enriched in Pt-group elements by fire assay fusion.

INTRODUCTION

ADVANCES IN THE understanding of trace element geochemistry are often limited by the sensitivity and spatial resolution of available analytical techniques. Resonance ionization mass spectrometry (RIMS) is developing as an analytical method with important applications in isotope geochemistry (e.g., WALKER et al., 1988; THONNARD et al., 1987) and may provide the basis for a new method of *in situ* trace element and isotopic analysis. We have recently established a RIMS technique that takes advantage of the high efficiency and elemental selectivity of multiphoton ionization, allowing *in situ* detection of sub-part per million atomic (ppma) concentrations of Os (BLUM et al., 1990). The experiments, which couple RIMS with ion sputtering, were carried out using the SARISA (surface analysis by resonance ionization of sputtered atoms) apparatus developed at Argonne National Laboratory (PELLIN et al., 1988). Several other groups have used a similar approach to achieve ultrasensitive detection of impurities in synthetic materials (PARKS et al., 1988; PAPPAS et al., 1989).

Geochemical studies of the platinum group elements (PGE: Ru, Rh, Pd, Os, Ir, Pt), which are present in most rocks and minerals at the sub-ppma level, have been mostly limited to bulk chemical methods such as radiochemical neutron activation analysis or isotope dilution. Electron microprobe X-ray analysis is the most widely used *in situ* analytical technique in geochemistry, but the detection limits for PGE (~100 ppma; CROCKET and CABRI, 1981) are not low enough for most applications. Interest in the distribution of PGE at low concentrations in sulfide ore minerals and in meteorite phases has led to the recent evaluation of several new techniques for *in situ* measurement of these precious metals. Accelerator mass spectrometry has been used to measure Os, Ir, and Pt concentrations in iron meteorites with a detection limit of <1 to 6 ppba, but with a spatial resolution of only ~1 mm (TENG et al., 1987; RASMUSSEN et al., 1989). Particle-induced X-ray emission and synchroton X-ray fluorescence have been used for analysis of Ru, Rh, Pd, and Pt with detection limits in the range of 1–20 ppma and a spatial resolution of <10 μm (CABRI et al., 1988). Finally, secondary ion mass spectrometry has recently been applied to the analysis of Pd, Rh, Ir, and Pt with detection limits in the range of 20–300 ppba (CHRYSSOULIS et al., 1990).

The measurement of the isotopic composition of small quantities of Os has long been recognized as an important analytical goal in geochemistry because of the geochemical applications of the radioactive decay of ^{187}Re to ^{187}Os (halflife = 4.2×10^{10} a; LINDNER et al., 1989). The high ionization potential (IP) of Os (8.6 eV; 69,000 cm^{-1}) precludes the use of conventional thermal ionization mass spectrometry. Osmium isotope ratios have been measured by electron impact ionization mass spectrometry of the volatile OsO_4 species using "large" μg samples of Os (HERR et al., 1967). Secondary

* *Present address:* Lunatic Asylum of the Charles Arms Laboratory, Division of Geological and Planetary Sciences, California Institute of Technology, Pasadena, CA 91125, USA.

ion mass spectrometry (SIMS) has been used successfully to measure Os and Re isotopic ratios to a precision of ~1% after chemical separation of ≥1 ng of Os (LUCK and ALLÈGRE, 1983). Several other methods including accelerator mass spectrometry (TENG et al., 1987), laser ablation mass spectrometry (SIMMONS, 1983), and inductively coupled plasma mass spectrometry (RUSS et al., 1987) have been explored for Os isotopic measurements but presently either require larger sample sizes or have inferior precision of SIMS.

Resonance ionization mass spectrometry following pulsed thermal vaporization has recently been shown to have similar capabilities as SIMS with respect to sample size and precision for Os and Re isotope ratio measurements (WALKER and FASSETT, 1986). This technique, however, is limited by the low Os ionization efficiency due to the large mismatch between the duration of the ionizing laser pulse and the thermal vaporization pulse. By closely matching the duty cycle between a pulsed primary ion beam and ionizing lasers, resonance ionization of sputtered atoms has the potential for an $\sim 10^5$ increase in ionization efficiency compared to thermal vaporization RIMS and an $\sim 10^2$ increase compared to SIMS (BLUM et al., 1990).

In this study we report our progress toward examining the capabilities of resonance ionization of sputtered atoms for quantitative geochemical analysis of one of the PGE (Os) in natural materials. Synthetic metals were used to establish a calibration curve for Os, and a suite of iron meteorites with known bulk Os concentrations were analyzed to test the linearity of the Os^+ signal with concentration. We will exhibit data which show that resonance ionization of sputtered atoms can be easily calibrated and may be used for *in situ* chemical analyses of PGE in a wide range of natural and synthetic materials. We also discuss the potential of this technique for the high efficiency measurement of Os isotope ratios.

EXPERIMENTAL METHODS

Samples

Synthetic and meteoritic samples of metallic solid solutions were analyzed. The synthetic samples consist of Os and Re dissolved in a Ni matrix. They were produced by weighing metallic powders and then melting, crystallizing, and annealing the metals in alumina crucibles in a vertical-quench controlled-atmosphere furnace (BLUM et al., 1989). The synthetic samples were not originally intended for use as analytical standards, and some have weighing uncertainties introduced during sample preparation that could readily be reduced. The synthetic sample used as a standard in this study contains 1000 ppma Os and Re (±4%). Two other synthetic samples that were analyzed contain Os and Re at the 100 ppma (±25%) and 10 ppma (±35%) levels. The meteoritic samples are the metallic Fe-Ni kamacite phase from three type IIAB iron meteorites which contain kamacite as the only metallic phase, one type IAB and one type IIIAB iron meteorite, both of which contain two Fe-Ni metallic phases (kamacite and taenite), and one pallasite which also contains kamacite and taenite. Samples were cut into wafers, polished with diamond paste and mounted onto stainless steel stubs with conducting epoxy. The bulk

Table 1. Analytical data for Os analyses of synthetic and meteoritic samples.

Sample	[1]Os conc. grav. ppma	[2]Os conc. RNAA ppma	[3]Os conc. ID ppma	[4]SARISA Os conc. ppma	[5]Net Os^+ counts (±2σ)
SYNTHETICS (session 1)					
Ni-Os-Re	1000	–	–	1000	2.04×10^5 (±0.04)
Ni-Os-Re	100	–	–	87.3	1.78×10^4 (±0.18)
Ni-Os-Re	10	–	–	12.5	2.56×10^3 (±0.28)
METEORITES (session 2)					
Ni-Os-Re	1000	–	–	1000	3.46×10^5 (±0.24)
Negrillos	–	25.3	14.8	18.7	6.48×10^3 (±0.20)
Eagle Station	–	4.50	–	4.85	1.68×10^3 (±0.26)
Coahuila	–	3.41	–	3.19	1.11×10^3 (±0.04)
North Chile	–	0.34	0.38	0.40	1.40×10^2 (±0.26)
METEORITES (session 3)					
Ni-Os-Re	1000	–	–	1000	1.46×10^5 (±0.12)
Henbury	–	4.88	3.90	4.00	5.82×10^2 (±0.92)
Eagle Station	–	4.50	–	4.01	5.86×10^2 (±0.58)
Canyon Diablo	–	0.65	0.61	0.60	8.85×10^1 (±1.70)

[1]Concentration determined gravimetrically during sample synthesis.
[2]Concentration determined by RNAA (Pernicka and Wasson, 1987; Davis, 1977).
[3]Concentration determined by isotope dilution (Herr *et al.*, 1961).
[4]SARISA Os concentration normalized to 1000 ppma standard.
[5]Mean of net Os^+ counts per 125 sec analyses for either 2 or 4 analyses (background subtracted).

concentration of Os in the meteoritic samples has been previously determined by radiochemical neutron activation analysis (RNAA) with a reported precision of ±12% for the iron meteorites (PERNICKA and WASSON, 1987) and ±14% for the pallasite (DAVIS, 1977). Comparison of these RNAA data with previous RNAA and isotope dilution (ID) determinations indicates general agreement within ~ ±20% (PERNIKA and WASSON, 1987, and references therein). The only significant discrepancy is for NEGRILLOS where the ID value of HERR et al. (1961) is ~40% lower than the RNAA value of PERNICKA and WASSON (1987). The names of each of the samples analyzed and the Os concentrations in ppma determined by RNAA and ID are given in Table 1.

Apparatus

The experiments were performed using the SARISA apparatus (PELLIN et al., 1988; BLUM et al., 1990) which consists of three main subunits: a pulsed primary ion source, three pulsed tunable lasers, and an energy and angular refocusing time-of-flight mass spectrometer. A mass analyzed 5 keV Ar^+ sputtering beam with an average current of 2.0 μA and a full width at half maximum (fwhm) diameter of ~70 μm is produced by a Colutron ion gun. During analyses, the primary ion beam is chopped into pulses of 200 nsec width by electrostatic deflection at a 40 Hz repetition rate. The Ar^+ ions strike the target in an ultra-high vacuum chamber pumped to a base pressure of 5×10^{-10} torr and operated at a pressure of $\sim 1 \times 10^{-9}$ torr during analyses. The sputtering rate in the 40 Hz pulsed mode is ~10 min per monolayer of target. Sputtered species fill a volume above the target during and after the arrival of the primary ion pulse. During sputtering, the target is held at a 1.5 kV potential; incoming Ar^+ ions are decelerated to 3.5 keV and positive secondary ions produced by sputtering are accelerated to 1.5 keV. The unwanted secondary ions are not transmitted through the mass spectrometer, which is designed to accept ions with 1.0 ± 0.1 keV energy.

Approximately 300 nsec after the end of each primary ion pulse a XeCl excimer laser is fired producing an ~10 nsec, 200 mJ ultraviolet (UV) pulse with a bandwidth of 0.3 to 0.5 nm centered about 307.9 nm. The excimer output is split into three beams which are used to pump three tunable dye lasers (loaded with Rhodamine 590, Coumarin 480, and DCM dyes, respectively) to produce three beams of visible light. The Rhodamine dye laser's visible light output is frequency doubled in a non-linear crystal to produce UV pulses. The three laser beams are spatially and temporally overlapped in a volume that extends from about 0.5 to 1.5 mm above the target surface and has a diameter of ~1 mm. Photoionization of sputtered neutral Os atoms occurs within this volume following a three energy level resonance ionization scheme which utilizes resonant energy levels for Os at 34365 and 55402 cm^{-1} and an autoionizing resonance energy level at 71032 cm^{-1} (Fig. 1). This ionization scheme has an elemental selectivity for Os relative to Re and other PGE of $>10^3$ (BLUM et al., 1990). The time delay between the end of the primary ion pulse and the laser firing is precisely adjusted to maximize the number of sputtered atoms in the ionization volume, which depends on the velocity distribution of the sputtered atoms of interest. Positively charged Os^+ photoions are accelerated away from the target and are focussed in the time-of-flight mass spectrometer by a series of einzel lenses, deflection plates, and two hemispherical energy analyzers. Ions are detected with a chevron-type microchannel plate electron multiplier, and arrival times are recorded in 5 nsec windows by a pulse-counting system at low signal levels (≤10 counts per laser shot) or by a transient charge digitizer at higher signal levels (>10 counts per laser shot).

Analytical procedure

Prior to each analysis a 2.0 μA direct current Ar^+ beam was rastered across the sample for 2 min in a 2.5 × 2.5 mm pattern to remove ~40 monolayers of the target and expose a clean surface for analysis. Each analysis consisted of summing the counts in each 5 nsec channel for a period of 125 sec at a repetition rate of 40 Hz (5000 pulses). The 1000 ppma sample gave a Os^+ count rate high enough to saturate the pulse-counting system for the most abundant Os isotopes. Therefore, this sample was analyzed using both transient charge digitization and pulse-counting. It was first analyzed by charge digitization with a normal primary ion pulse width of 200 nsec and was then analyzed with a shorter pulse width of 20 nsec. The integrated Os^+ signals

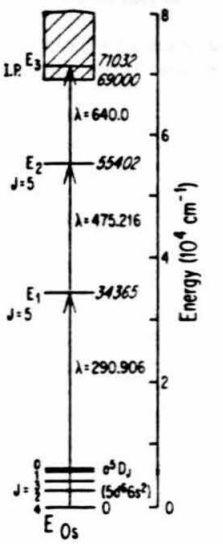

FIG. 1. Energy level diagram for Os resonance ionization scheme. Resonant energy levels (E_1, E_2, E_3) and the ionization potential (I.P.) are given as cm^{-1} in vacuum, and laser wavelengths are given as nm in air. Electronic configuration and angular momentum quantum numbers (J) are also given.

were used to calculate a conversion factor for the reduction in pulse width. The 1000 ppma sample was then analyzed with the pulse-counting system and a 20 nsec primary ion pulse, and the count rate was multiplied by the conversion factor to give the equivalent count rate with a 200 nsec primary ion pulse width. All other samples were analyzed with the pulse-counting system and a 200 nsec primary ion pulse width.

For Os isotopes, unit mass resolution corresponded to a difference in photoion arrival time of approximately 120 nsec (24 channels). Since the mass spectrometer was operated at low mass resolving power ($M/\Delta M$ ~ 250, at fwhm), neighboring Os isotopes were not fully resolved and the total ion signal was measured by summing the total number of counts in the channels between masses 185.5 and 192.5. The net Os^+ intensity for each sample was calculated by subtracting the average background intensity from the total. Each sample was analyzed at least twice and the total number of counts were averaged. The background was determined by collecting analyses in several ways: 1) the UV dye laser was detuned 12 cm^{-1} from the center of the first resonant energy level and an average of 16 counts per 125 sec were measured; 2) the UV dye laser beam was blocked and an average of 15 counts per 125 sec were measured; and 3) all three of the laser beams were blocked and an average of 4 counts per 125 sec were measured. The absence of interferences resonant with the UV frequency was verified by analyzing stainless steel for Os and recording only 18 counts per 125 sec. The background data indicate that contributions to the background signal are from two sources: 1) electronic noise and/or secondary ions which contribute ~4 counts per 125 sec, and 2) photoions produced by nonresonant ionization and/or laser ablation from the visible dye laser beams which contribute ~12 counts per 125 sec. For the experiments reported here, the average background of 16 counts per 125 sec is assumed to represent instrumental background for a sample containing no Os. The background correction is only significant for analyses of samples containing sub-ppma Os concentrations.

EXPERIMENTAL RESULTS

Analytical data

The analytical data for synthetic and meteoritic samples are given in Table 1, divided into three groups which represent

separate analysis sessions. The net Os^+ intensity (counts per 5000 laser pulses) for each sample is also given in Table 1. The number of ions detected per ppma of Os varied by about a factor of 2 between the three analysis sessions as indicated by the variation in the Os^+ intensity per 5000 pulses for the 1000 ppma Os standard (Table 1). This was probably due to the fact that the first resonant transition was not saturated with respect to laser power (BLUM et al., 1990) and therefore the photoion production was sensitive to variations in the laser power caused by dye degradation and by variations in laser beam alignment. To compensate for these variations in degree of ionization the 1000 ppma synthetic Os sample was analyzed at the start of each analysis session and used as an internal standard.

The calibration curve shown in Fig. 2 is a line of slope 1 determined from the measured Os^+ intensity for the 1000 ppma standard. The relative Os^+ intensities for the three synthetic samples are plotted versus the Os concentrations determined during sample synthesis (Fig. 2). It is evident that the three data points fall along the line of slope 1, indicating that the measured Os^+ intensity is proportional to the Os concentrations of the synthetic metals. Errors due to counting statistics are small for all three synthetic samples ($< \pm 2\%$ 2σ), and the best indicator of the analytical precision is provided by the reproducibility of replicate analyses. The variation in the net Os^+ intensity for replicate analyses of the synthetic metals suggests a measurement precision of $\sim \pm 10\%$ (2σ) for Os concentrations between 10 and 1000 ppma. The accuracy of the SARISA measurements is more difficult to assess since we have no independent determination of the Os concentration or homogeneity in the synthetic metals. The data for the 100 ppma and 10 ppma samples lie $\sim 2\sigma$ below and $\sim 4\sigma$ above the calibration curve, respectively, but

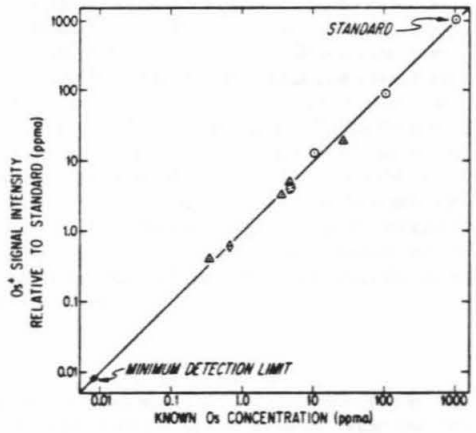

FIG. 2. Logarithmic plot of normalized Os^+ signal intensity in ppma versus Os concentration determined gravimetrically for synthetic samples or by RNAA for meteorite samples (PERNICKA and WASSON, 1987; DAVIS, 1977). Circles are synthetic metals analyzed during analysis session 1; triangles are meteorites analyzed during session 2; and diamonds are meteorites analyzed during session 3. Signal intensities for each analysis session were normalized to the 1000 ppma synthetic standard. The minimum detection limit of 7 ppba is calculated for a 3600 sec analysis.

within the weighing uncertainties introduced during sample preparation.

The capability of SARISA for quantitative elemental analysis of natural materials was investigated by measuring the Os abundances in Fe-Ni metal from five iron meteorites and one pallasite. The net Os^+ intensity and calculated Os abundances in ppma (normalized to the standard) are given in Table 1, and the data are plotted versus the RNAA Os abundances of PERNICKA and WASSON (1987) and DAVIS (1977) in Fig. 2. Except for NEGRILLOS, none of the data lie more than 2σ away from the slope 1 calibration curve, indicating excellent agreement between the Os concentrations measured here and those determined by RNAA. The close agreement between the SARISA analyses and the RNAA data suggests that 1) the linear relationship between measured Os^+ intensity and Os content extends to concentrations at least as low as 0.3 ppma, and 2) the accuracy is well represented by the reproducibility of replicate analyses and is $\sim \pm 10\%$ for Os concentrations between 0.3 and 1000 ppma. The Os concentration in NEGRILLOS determined with SARISA is $\sim 20\%$ lower than the value reported by PERNICKA and WASSON (1987) and $\sim 20\%$ higher than a previous determination by HERR et al. (1961). The variation between the three analytical methods may be due to the heterogeneous distribution of Os in NEGRILLOS metal rather than to major errors in the measurements.

In three of the meteorites we analyzed (Canyon Diablo, Henbury, and Eagle Station), the metal is not homogeneous and consists of kamacite with taenite lamellae. Since we have compared the SARISA data for kamacite with bulk Os concentrations for these three meteorites, it is necessary to consider the effect of Os partitioning between kamacite and taenite. The mass fraction of taenite in Canyon Diablo and Henbury has been measured and is very low (<2%; RASMUSSEN et al., 1988, 1989). Mass balance calculations indicate that the taenite/kamacite partitioning ratio is probably <5 since the reduction in the Os concentrations of kamacite compared to bulk meteorite is less than the $\pm 10\%$ analytical uncertainty.

Useful yield and detection limit

The useful yield (defined here as the ratio of ions detected to atoms sputtered) and the detection limit are two parameters frequently used to characterize an analytical technique. Since these parameters measure two different aspects of a technique, both cannot always be optimized in a single experiment. With SARISA, for example, the useful yield can be maximized by using a narrow primary ion pulse (~ 200 nsec) and low primary ion current ($\sim 2\ \mu A$) which in turn allows a small spot size of $<100\ \mu m$. This procedure reduces the volume filled by sputtered atoms and thus maximizes both the ionization probability and the transmission of photoions through the mass spectrometer. In contrast, the detection limit can be optimized by using a wider primary ion pulse ($\sim 1\ \mu sec$) and higher primary ion current (and spot size) to increase the sputtering rate so that the maximum number of atoms of a trace constituent are sputtered from the sample and fill the photoionization volume.

A primary goal of the present experiment was to determine if we could achieve a high useful yield (and high spatial res-

olution) for high ionization potential elements such as Os. Accordingly, a narrow pulse width and low current of Ar^+ primary ions were used, and no attempt was made to obtain the best possible detection limit for Os. For some applications maximum useful yield and high spatial resolution are not as important as the optimization of detection limits. In one such case it was possible to detect In in a Si matrix at the parts per trillion atomic level by using a wide primary ion pulse (5.6 μsec), a high ion current (~100 μA), and a large spot size (3000 μm) (PAPPAS et al., 1989).

The useful yield is determined from the ratio of Os^+ ions detected per laser shot to the number of Os atoms sputtered from the sample per primary ion pulse. The Os^+ ion yield per ppma for analysis session 2 (Table 1) corresponds to 0.069 counts per ppma per laser shot. The amount of target material sputtered per primary ion pulse can be estimated from the sputter yield of pure Fe and Os under bombardment by 3.5 keV Ar^+ ions, which for both Fe and Os is 2.5 atoms per Ar^+ ion (MATSUNAMI et al., 1984). With a primary ion current of ~2.0 μA and a pulse width of 0.20 μsec, 2.5×10^6 ions strike the target per pulse and, therefore, approximately 6.3×10^6 Fe atoms are sputtered. We assume that trace levels of Os are sputtered at the same rate as the Fe matrix, which is the expected equilibrium condition (LAM and WIEDERISCH, 1987). In this case, 6.3 Os atoms will be sputtered per ppma of Os in the sample during a single primary ion pulse. Dividing the Os counts per laser shot by the number of sputtered Os atoms per primary ion pulse gives a useful yield of 1%. For example, the Os mass spectrum for the 0.34 ppma Os North Chile sample was collected during 5000 primary ion pulses (125 sec) by sputtering 1.1×10^4 Os atoms (1/5 of a monolayer in a 100 μm spot) and detecting 140 Os^+ ions.

The Os^+ ion yield for analysis session 2 (Table 1) and the average background count rate (16 counts per 125 sec) were used to calculate the detection limit for Os from Poisson statistics at the 95% confidence level. Following the approximation derived by ZIEBOLD (1967) we calculate that the detection limit for Os for this experiment is 38 parts per billion atomic (ppba) for a 125 sec analysis and 7 ppba for a 3600 sec analysis. Increasing the UV dye laser power to saturate the first resonant transition would increase the Os^+ signal and reduce the minimum detection limit. For fully saturated transitions the useful yield would be expected to increase to ~5%, as was achieved for Fe analyses using SARISA (PELLIN et al., 1988), and the minimum detection limit should be reduced to ~2 ppba.

DISCUSSION

Resonance ionization of sputtered atoms samples the large neutral fraction of atoms that are sputtered, rather than the much smaller secondary ion fraction sampled by secondary ion mass spectrometry. Matrix-dependent variations in sensitivity should be smaller for photoionization than for sputter-initiated secondary ionization because ionization occurs in the gas phase and is largely independent of the physical properties of the sample. Variations in relative ion yield of several orders of magnitude are common for secondary ion mass spectrometry (e.g., WILLIAMS, 1983) but appear to be much less than a factor of 10 for resonance ionization of sputtered atoms (PARKS et al., 1988). The yield of photoions using SARISA should depend only on 1) the sputtering rate of the sample, 2) the relative sputter yield of neutral atoms, ions, and molecules, and 3) the extent of surface segregation and/or contamination during an analysis.

The Ar^+ ion sputter yields for most elements have been measured as a function of projectile energy and vary by up to a factor of ~3 at 3.5 keV (MATSUNAMI et al., 1984). Sputter yields for more complex multielement matrices are largely unknown and will have to be determined by weight loss or by profilometry of sputtered craters. We have used nonresonant excimer laser ionization to saturate the ionization of atoms and molecules in order to gain a qualitative understanding of the ratio of sputtered atoms to sputtered molecules. For samples of Fe-Ni metal, sulfides, and oxides, we have found that molecules make up <10% of the total sputtered species.

The relative yield of sputtered secondary ions is strongly affected by surface properties such as the extent of oxygen coverage (e.g., HUSINSKY et al., 1987). Secondary ion yields can be higher than 10% for low ionization potential elements but are generally much lower than 10% for high ionization potential elements under ultra-high vacuum conditions (BENNINGHOVEN, 1975). Therefore, the yield of sputtered molecules and secondary ions will not significantly deplete the population of sputtered neutral atoms of Os (or other PGE) that are available for photoionization.

The high useful yield and elemental selectivity of resonance ionization of sputtered atoms allows chemical and isotopic analyses to be made on small numbers of Os (or other PGE) atoms without the need for chemical separation. As discussed by BLUM et al. (1990), the time-of-flight mass spectrometer used in these experiments is adequate for concentration measurements but not appropriate for high precision (< ±1%) isotope ratio measurements of Os due to its low mass resolution. Resonance ionization of sputtered atoms can, in principle, be coupled with a magnetic sector, quadrupole, or high resolution time-of-flight mass spectrometer for high precision isotope measurements. In this case, the precision of Os measurements would be limited primarily by ion counting statistics. Osmium occurs in geological materials dissolved at low concentrations in sulfides, silicates, and spinels and as a major constituent in μm-sized PGE-rich sulfides and alloys. Osmium measurements of geochemical interest can be grouped into the following categories: 1) *in situ* chemical analyses of Os (and other PGE) at low (sub-ppma) concentrations, 2) *in situ* isotopic analyses of Os at low concentrations, 3) *in situ* isotopic analyses of Os in μm-sized PGE-rich sulfides and alloys, and 4) isotopic analyses of Os chemically concentrated from geological materials.

We can use simple counting statistics to calculate the approximate precision of Os concentration and $^{187}Os/^{186}Os$ isotope ratio measurements that are potentially possible using this method. In an earlier section we demonstrated a useful yield of 1%, which corresponds to 0.069 Os^+ counts per laser shot per ppma of Os in a sample. The experiments reported here were run at a 40 Hz repetition rate, but XeCl excimer lasers are available which operate at repetition rates of up to 200 Hz. For a 1 h analysis at 200 Hz we calculate that there would be 5×10^4 Os^+ counts per ppma of Os in a sample.

Based on the calculated count rates and counting statistics, we expect to be able to measure Os concentrations *in situ* with a precision of ±10% down to 2 ppba, and with a precision of ±1% down to 200 ppba. These detection limits will allow the investigation of Os partitioning and solubilities in mineral phases from iron meteorites, terrestrial mafic and ultramafic rocks, and in phases synthesized in laboratory experiments.

Most geological applications of Os isotope studies require the measurement of $^{187}Os/^{186}Os$ ratios with < ±1% precision (ALLÈGRE and LUCK, 1980). Our calculations indicate that this should be possible for *in situ* measurements of samples with ≥15 ppma Os. This is a considerably higher concentration than needed for Os concentration measurements because ^{187}Os and ^{186}Os are minor isotopes (~1.6% abundance) of Os. As a result, *in situ* Os isotope investigations will be limited to materials that are enriched in Os such as iron meteorites and Ni-Fe sulfides in peridotites and mafic-ultramafic intrusions.

Osmium is a major constituent in PGE-rich alloys and sulfides that are commonly found as inclusions in spinels associated with ophiolites and layered mafic-ultramafic intrusions. These inclusions range in size from 1 to 20 μm in diameter and have Os concentrations of up to ~20% (e.g., STOCKMAN and HLAVA, 1984; TALKINGTON et al., 1984). Although the primary Ar^+ ion beam used in our apparatus has a ~70 μm fwhm diameter, small inclusions can still be analyzed for $^{187}Os/^{186}Os$ with a precision of < ±1% if they have high Os concentrations. For example, a 1 μm diameter inclusion with 5% Os or a 5 μm diameter inclusion with 0.2% Os should be adequate for such an analysis. Thus, the Os isotope systematics of PGE-rich alloys and sulfides from most ophiolites and layered mafic-ultramafic intrusives should be amenable to *in situ* Os isotope studies.

Finally, resonance ionization of sputtered atoms can be used to measure the isotopic composition of extremely small samples of Os that have been chemically concentrated from geological materials. Following separation of Os from rocks by acid dissolution and distillation (cf. LUCK and ALLÈGRE, 1983), samples with as little as 10^{-15} g of Os could theoretically be used for $^{187}Os/^{186}Os$ ratio measurements with < ±1% precision if they were deposited as thin films onto a substrate for sputtering. Chemical separation of Os would allow Os isotope analyses of mg-size samples of virtually all rock-types including felsic crustal rocks which have Os concentrations as low as ~0.01 ppba (MORGAN and LOVERING, 1967).

Osmium can quite easily be concentrated by a factor of ~10 from bulk rocks into NiS or Ni metal by fire assay fusion (HOFFMAN et al., 1978). Alternatively, Os can be concentrated by ~10^4 by NiS fire assay fusion followed by acid dissolution and filtration of acid insoluble residues (TENG et al., 1987). These residues could then be sputtered directly or fused with NiS or Ni metal for sputtering. Fire assay concentration of Os would allow Os isotopic analysis of ultramafic rocks which generally contain 1 to 10 ppba Os.

We have shown that resonance ionization of sputtered atoms can be used for quantitative analysis of trace levels of Os in Ni-rich and Fe-rich metal with a spatial resolution of ~70 μm. This technique can be adapted to trace analysis of most high ionization potential elements (including all of the PGE) in a wide variety of natural and synthetic materials by determining the appropriate ionization scheme for each element and tuning the dye laser wavelengths accordingly. To obtain multielement analyses in a single spot, dye laser wavelengths will have to be rapidly tuned to the ionization scheme for each element. The high useful yield and elemental selectivity of resonance ionization of sputtered atoms should eventually allow *in situ* measurement of Os isotope ratios down to concentrations of ~15 ppma without chemical separation.

Acknowledgments—We thank J. Whitten for technical assistance, J. T. Wasson for providing meteorite specimens, G. R. Rossman and E. M. Stolper for the use of furnaces, and L. Brown, G. P. Russ, K. K. Turekian, and an anonymous referee for reviews. This study was performed as part of a doctoral dissertation by the senior author at the California Institute of Technology. (Caltech). Work was supported by the US Dept. of Energy through BES-Material Sciences contract W-31-109-ENG-38 to Argonne National Laboratory and BES-Engineering and Geosciences Grant DE-FG03-88ER13851 to Caltech. Caltech Division of Geological and Planetary Sciences Contribution Number 4817 (687).

Editorial handling: G. Faure

REFERENCES

ALLÈGRE C. J. and LUCK J. M. (1980) Osmium isotopes as petrogenetic and geologic tracers. *Earth Planet. Sci. Lett.* **48**, 148–154.

BENNINGHOVEN A. (1975) Developments in secondary ion mass spectroscopy and applications to surface studies. *Surf. Sci.* **53**, 596–625.

BLUM J. D., WASSERBURG G. J., HUTCHEON I. D., BECKETT J. R., and STOLPER, E. M. (1989) Diffusion, phase equilibria and partitioning experiments in the Ni-Fe-Ru system. *Geochim. Cosmochim. Acta* **53**, 483–489.

BLUM J. D., PELLIN M. J., CALAWAY W. F., YOUNG C. E., GRUEN D. M., HUTCHEON I. D., and WASSERBURG G. J. (1990) Resonance ionization mass spectrometry of sputtered osmium and rhenium atoms. *Anal. Chemistry* **62**, 209–214.

CABRI L. J. (1988) Applications of proton and nuclear microprobes in ore deposit mineralogy and metallurgy. *Nucl. Inst. Meth. Phys. Res.* **B30**, 459–465.

CHRYSSOULIS S. L., ALCOCK R. A., SIZGORIC M. B., and CABRI L. J. (1990) Quantitative trace PGE analyses of phyrrhotite, pentlandite and millerite. *5th Int. Platinum Symp. Geol. Soc. Finland Bull.* (abstr.) (in press).

CROCKETT J. H. and CABRI L. J. (1981) Analytical methods for the platinum-group elements. In *Platinum-Group Elements: Mineralogy, Geology, Recovery* (ed. L. J. CABRI), pp. 71–82. The Canad. Inst. of Mining and Metall.

DAVIS A. M. (1977) The cosmochemical history of the pallasites. Ph.D. dissertation, Yale University.

HERR W., HOFFMEISTER W., HIRT B., GEISS J., and HOUTERMANS F. G. (1961) Versuch zur datierung von eisenmeteoriten nach der rhenium-osmium-methode. *Z. Naturforsch.* **16a**, 1053–1058.

HERR W., WÖLFLE R., EBERHARDT P., and KOPP E. (1967) Development and recent applications of the Re/Os Dating Method. In *Radioactive Dating and Methods of Low-Level Counting*. IAEA Vienna, pp. 499–508.

HOFFMAN E. L., NALDRETT A. J., VAN LOON J. C., HANCOCK R. G. V., and MANSON A. (1978) The determination of all of the platinum group elements and gold in rocks and ore by neutron activation analysis after preconcentration by a nickel sulfide fire-assay technique on large samples. *Anal. Chimica Acta* **102**, 157–166.

HUZINSKY W., WURZ P., STREHL B., and BETZ G. (1987) Cr atoms sputtered from different matrices. *Nucl. Inst. Meth. Phys. Res.* **B18**, 452–457.

LAM N. Q. and WIEDERSICH (1987) Bombardment-induced segre-

gation and redistribution. *Nucl. Inst. Meth. Phys. Res.* **B18**, 471–485.

LINDNER M., LEICH D. A., RUSS G. P., BAZAN J. M., and BORG R. J. (1989) Direct determination of the halflife of ^{187}Re. *Geochim. Cosmochim. Acta* **53**, 1597–1606.

LUCK J. M. and ALLÈGRE C. J. (1983) ^{187}Re-^{187}Os systematics in meteorites and cosmochemical consequences. *Nature* **302**, 130–132.

MATSUNAMI N., YAMAMURA Y., ITIKAWA Y., ITOH N., KAZUMATA Y., MIGAYAWA S., MORITA K., SHIMIZU R., and TAWARA H. (1984) Energy dependence of the ion-induced sputtering yields of monatomic solids. *Atom. Data Nucl. Tables 31.*

MORGAN J. W. and LOVERING J. F. (1967) Rhenium and Osmium abundances in some igneous and metamorphic rocks. *Earth Planet. Sci. Lett.* **3**, 219–224.

PAPPAS D. L., HRUBOWCHAK D. M., ERVIN M. H., and WINOGRAD N. (1989) Atom counting at surfaces. *Science* **243**, 64–66.

PARKS J. E., SPAAR M. T., and CRESSMAN P. J. (1988) Analysis of high purity solids by resonance ionization spectroscopy. *J. Crystal Growth* **89**, 4–15.

PELLIN M. J., YOUNG C. E., and GRUEN D. M. (1988) Multiphoton ionization followed by time-of-flight mass spectroscopy of sputtered neutrals. *Scanning Microscopy* **2**, 1353–1364.

PERNICKA E. and WASSON J. T. (1987) Ru, Re, Os, Pt and Au in iron meteorites. *Geochim. Cosmochim. Acta* **51**, 1717–1726.

RASMUSSEN K. L., MALVIN D. J., and WASSON J. T. (1988) Trace element partitioning between taenite and kamacite; Relationship to the cooling rates of iron meteorites. *Meteoritics* **23**, 107–112.

RASMUSSEN K. L., GREENWAY T. J. L., and GWOZDZ R. (1989) The composition of kamacite in iron meteorites investigated by accelerator mass spectrometry, neutron activation analysis and analytical electron microscopy. *Nucl. Instr. Meth. Phys. Res.* **B36**, 43–52.

RUSS G. P., BAZAN J. M., and DATE A. R. (1987) Osmium isotopic ratio measurements by inductively coupled plasma source mass spectrometry. *Anal. Chemistry* **59**, 984–989.

SIMMONS D. S. (1983) Isotopic analysis with the laser microprobe mass analyzer. *Intl. J. Mass Spec. Ion Proc.* **55**, 15–30.

STOCKMAN H. W. and HLAVA P. F. (1984) Platinum-group minerals in alpine chromitites from southwestern Oregon. *Econ. Geology* **79**, 491–508.

TALKINGTON R. W., WATKINSON D. H., WHITTAKER P. J., and JONES P. C. (1984) Platinum-group minerals and other solid inclusions in chromite of ophiolitic complexes: occurrence and petrological significance. *TMPM Tschermaks Min. Petr. Mitt.* **32**, 285–301.

TENG R. T. D., FEHN U., ELMORE D., HEMMICK T. K., KUBIK P. W., and GOVE H. E. (1987) Determination of Os isotopes and Re/Os ratios using AMS. *Nucl. Instr. Meth. Phys. Res.* **B29**, 281–285.

THONNARD N., WILLIS R. D., WRIGHT M. C., and DAVIS W. A. (1987) Resonance ionization spectroscopy and the detection of ^{81}Kr. *Nucl. Instr. Meth. Phys. Res.* **B29**, 398–406.

WALKER R. J. and FASSETT J. D. (1986) Isotopic measurement of subnanogram quantities of rhenium and osmium by resonance ionization mass spectrometry. *Anal. Chemistry* **58**, 2923–2927.

WALKER R. J., SHIREY S. B., and STECHER O. (1988) Comparative Re-Os, Sm-Nd and Rb-Sr isotope and trace element systematics for Archean komatiite flows from Munro Township, Abitibi Belt, Ontario. *Earth Planet. Sci. Lett.* **87**, 1–12.

WILLIAMS P. (1983) Secondary ion mass spectrometry. In *Applied Atomic Collision Physics 4* (ed. S. DATZ), pp. 327–377. Academic Press.

ZEIBOLD T. O. (1967) Precision and sensitivity in electron microprobe analysis. *Anal. Chemistry* **39**, 858–861.